CONTROL OF HUMAN-OPERATED MACHINERY WITH FLEXIBLE DYNAMICS

A Thesis
Presented to
The Academic Faculty

by

Ehsan A. Maleki

In Partial Fulfillment
of the Requirements for the Degree
Doctor of Philosophy in the
School of Mechanical Engineering

Georgia Institute of Technology
December 2013

CONTROL OF HUMAN-OPERATED MACHINERY WITH FLEXIBLE DYNAMICS

Approved by:

Dr. William Singhose, Advisor
School of Mechanical Engineering
Georgia Institute of Technology

Dr. Michael Leamy
School of Mechanical Engineering
Georgia Institute of Technology

Dr. Jun Ueda
School of Mechanical Engineering
Georgia Institute of Technology

Dr. Dewey Hodges
School of Aerospace Engineering
Georgia Institute of Technology

Dr. William Miller
Georgia Tech Research Institute
Georgia Institute of Technology

Dr. Khalid Sorensen
CAMotion Inc.

Date Approved: October 8, 2013

ACKNOWLEDGEMENTS

I would like to thank Siemens Energy and Automation, the Boeing Company, and the National Science Foundation for their financial support of this work. I would like to thank my committee members, Dr. Leamy, Dr. Ueda, Dr. Hodges, Dr. Miller, and Dr. Sorensen, for their support of this work. I would also like to thank my advisor, Dr. William Singhose, for his continuous support and encouragement. His words of wisdom and contagious enthusiasm have helped me greatly in my research and life.

I would like to thank my friends and lab mates for their help and for making this experience more enjoyable.

I would like to thank my parents, Flora and Hossein, for sacrificing their own lives to give me numerous opportunities. Without their love and support, I would not be where I am today.

Finally, I would like to dedicate this dissertation to my wife, Ta, for her unending love, encouragement, and support. She has helped me in every possible way to achieve everything that I have.

TABLE OF CONTENTS

LIST OF TABLES

LIST OF FIGURES

SUMMARY

Heavy-lifting machines such as cranes are widely used at ports, construction sites, and manufacturing plants in a variety of material-transporting applications. However, cranes possess inherent flexible dynamics that make fast and precise operation challenging. Most cranes are driven by human operators, which adds another element of complexity. For a typical crane operation, the operator must first create a mental map of the task and the desired trajectory to complete that task. Then, the operator has to translate the desired trajectory into button pushes or lever motions on the user interface. Finally, the operator must continually monitor the effect of the commands in real time and modify the trajectory as necessary. Operating a machine with flexible dynamics is very challenging. The human operator will often exhibit erratic and nonlinear behavior in an attempt to control the machine.

The goal of this thesis is to develop controllers that allow human operators to easily and efficiently control machines with flexible dynamics. To achieve this goal, this thesis first analyzes the complex dynamic behavior of two types of machines: boom cranes and dual-hoist bridge cranes. These machines are commonly used in industry; however, they are also two of the most complex types of cranes. To understand their behavior, their response to various input commands, configurations, and types of payloads are analyzed.

To improve the ease of human operation of these machines, various control structures are developed and their effectiveness in aiding the operator are evaluated. Cranes are commonly used to swing wrecking balls that demolish unwanted structures. To aid the operator in such tasks, swing-amplifying controllers are designed and their performance are evaluated through simulations and experiments with real operators. To make maneuvering of these machines in material-transporting operations easier, input-shaping control is used to reduce oscillation induced by operator commands. In the presence of external disturbances, input shaping is combined with a low-authority feedback controller to eliminate unwanted oscillations, while maintaining the human operator as the primary controller of the machine. The performance and robustness of the proposed controllers are thoroughly examined via numerical simulations and a series of experiments and operator studies on a small-scale mobile boom crane and a two-ton dual-hoist bridge crane.

CHAPTER I

INTRODUCTION

Cranes, like the one shown in Figure 1.1, are commonly used in heavy-lifting and transporting applications. These machines have been used for thousands of years at ports, construction sites, and manufacturing plants. However, cranes possess flexible dynamics that make fast and precise operation challenging for their human operators. Cranes carry payloads by attaching them to flexible suspension cables that hang down from their main body. Motion of the crane and external disturbances such as wind induce large-amplitude payload swings. These payload swings decrease efficiency, throughput, and safety. This thesis focuses on understanding the complex dynamics of flexible, human-operated machines and developing methods that make operating

Figure 1.1: Boom Crane at Work

these machines easier. The next section discusses general human control of machinery. Then, three different approaches to improve the performance of human-machine systems are presented and discussed.

1.1 Human Control of Machinery

A human-operated system is defined as a system that possesses the following qualities:

1. The human operator is the main controller.
2. The feedback controller (i.e., the person) is nonlinear.
3. The feedback controller varies from operator to operator.
4. The feedback controller varies from task to task.
5. The input command is not repeatable (i.e., the operator cannot repeat a task exactly the same way).

Human-operated systems are different from computer-controlled systems because humans add an additional element of complexity. The human operator senses the machine state using his/her senses (i.e., sight, hearing, and touch) and uses this feedback in real-time to adjust his/her commands to the machine. Numerous researchers have attempted to model the behavior of the human operator using mathematical equations. For example, McRuer's crossover model provides a simple mathematical description of the combined human-machine system [39],

$$Y_{OL}(j\omega) = Y_p(j\omega)Y_c(j\omega) = \frac{\omega_c}{j\omega}e^{-j\omega\tau_e} \tag{1.1}$$

where Y_{OL} represents the system open loop dynamics, Y_p represents the human dynamics, Y_c represents the controlled-element dynamics, ω_c is the gain crossover frequency, and τ_e is the effective time delay. The crossover model essentially assumes that the human operator adapts to the controlled-element dynamics such that the open loop approximates integrator-like dynamics near the crossover region. McRuer's crossover model has been used to analyze manual control performance in a variety of circumstances. The Simplified Precision Model (SPM) attempts to capture the dynamics of just the human operator [9],

$$Y_p(j\omega) = K_p \frac{(\tau_L j\omega + 1)}{(\tau_I j\omega + 1)} e^{-j\omega\tau_e} \tag{1.2}$$

where K_p is the gain, τ_L is the lead-time constant, τ_I is the lag-time constant, and τ_e is the effective time delay. Although these models have been used with some success, operating a machine with flexible dynamics, especially one with a low damping ratio like a crane, is very difficult. Modeling the human-operator behavior (with mathematical equations) for such machines is more challenging because the operator will often exhibit erratic and nonlinear behavior in a attempt to control the machine [40]. As a result, these simplified models do not work for a wide range of flexible systems.

In order to efficiently operate flexible machines, the most prevalent solution in industry has been using "expert" operators who have years of training and experience. They can use a combination of motions to move the machine without exciting large oscillations. However, the machine velocities are typically reduced to make it easier for the operator to control the machine. In addition, the performance of "expert" operators can vary from day to day and from one machine to another. Different types of machines require different skill sets for efficient operation.

Researchers have proposed various techniques to simplify the operation of complex systems and decrease the dependence on the operators' skill. Some of this research has focused on designing optimal user interfaces [16, 20, 28]. User interface design is a well studied field [8, 41, 43, 53]. The user interface needs to be simple so that the user can immediately detect the status of the machine, yet it needs to provide adequate information so the operator can quickly assess what he/she needs to do to accomplish the task. This requires the UI to convey just the right amount of information to the user. Too little or too much information can make operating conditions challenging [48]. The right amount of information, however, can vary depending on the machine, the task, and the operator.

Another method that can help operators is the use of predictive control elements that predict the response and future states of the machine. Vaughan et al. designed a control element to predict where a crane will come to rest after the operator has issued a stop command [74]. Buzan et al. developed a dynamic user aid to help the operator anticipate the delayed system response of telemanipulator systems by providing predicted force and position feedback using dynamic models of both the manipulator and the environment [15]. By effectively conveying predictive information to the operator, the operator can more precisely plan his/her upcoming actions. This method is especially useful when the operator is remotely operating the machine. Such methods, however, often require an accurate, detailed model of the machine being controlled, which can be challenging to obtain.

Another area of research on improving the performance of human-operated machines focuses on modifying the dynamic behavior of the system to make operation easier. There are three main categories in this area: *i)* mechanical design, *ii)* feedback control, and *iii)* input-shaping control. These three areas are introduced and discussed in the following sections.

1.2 Mechanical Design

One way to improve the response of flexible machinery and make operation easier is to modify their physical design. A practical and economical approach for cranes is altering the rigging scheme. The Rider Block Tagline system (RBTS) [13], illustrated in Figure 1.2, is one such example. The RBTS consists of a rider block and multiple taglines. The operator can control the vertical location of the rider block along the suspension cables by pulling the taglines. This effectively decreases the pendulum length, thereby reducing the horizontal payload swing. However, this method can be troublesome as the taglines can become tangled with one another or with the

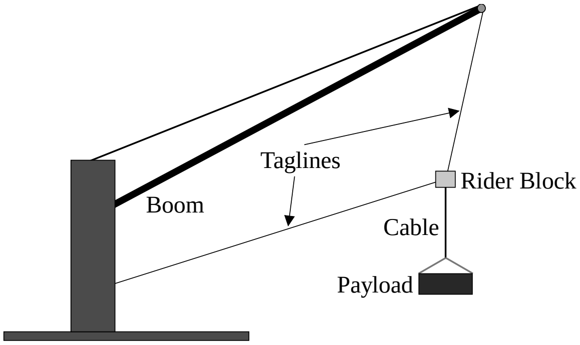

Figure 1.2: Rider Block Tagline System

numerous cables that hang from a typical crane structure. This process also requires additional human effort (in addition to the crane operator) to pull the taglines and move the rider block as necessary (i.e., more degrees of freedom and more required inputs).

Improving the mechanical design of a machine can sometimes be a good solution; however, it is not always feasible. Even if it is possible, it can be very time-consuming and expensive. Therefore, it is often preferable to combat flexibility problems with a good controller.

1.3 Feedback Control

Numerous researchers have proposed using feedback control to limit crane payload oscillation. A survey of various feedback methods in literature can be found in [4]. In this section, some of the more common and effective methods are briefly discussed.

State-feedback control, or pole-placement, is a very common feedback control technique and has been extensively applied to various types of flexible machines. This method allows the designer to place the closed-loop poles of the system at specific locations, effectively making the dynamic response of the system more desirable. Souissi and Koivo proposed a two-tier controller for rotary cranes [66]. A PID controller was used to track the crane motions, and a PD controller was used to dampen the payload oscillation. Numerical simulation demonstrated the effectiveness of the proposed controller. Omar and Neyfeh applied two full state feedback controllers to a tower crane [47]. The controller was effective at reducing payload oscillation when the feedback gains were explicitly designed for the given system parameters. The controller effectiveness decreased for changes in the parameters.

Henry et al. developed a delayed feedback controller for planar ship-mounted cranes [21]. Masoud et al. extended the idea to three-dimensional cranes [38]. Simulation and experiments showed significant payload oscillation reduction. Sorensen et al. proposed a PD feedback controller to eliminate disturbance-induced oscillations of gantry cranes [65]. The effectiveness of the controller was demonstrated through experiments on a 10-ton bridge crane. Neupert et al. proposed a tracking and anti-sway controller for boom cranes [44]. The anti-sway controller was composed of two input/output linearization modules and two disturbance observers. The tracking controller was based on model predictive control. The controller essentially solved an open-loop optimal control problem. The control loop was closed by repeating the optimization process by using state measurements as initial conditions in the optimal control problem. Experiments on an industrial harbor mobile crane showed good tracking behavior with minimal load sway.

Fuzzy logic control is a mathematical system that uses a set of rules to create logical relationships between the inputs and outputs [77]. First, a set of membership functions are defined for each input/output. A membership function is essentially a graphical representation of the fuzzy variable sets for each input/output. Then, rules are created to define how the input variables relate to the output variables. Yasunobu proposed a fuzzy logic controller to the reduce the payload sway and handling time of container cranes [76]. A set of fuzzy rules based on the knowledge of skilled operators was developed. Simulation results showed that the controller was effective in reducing the handling time of typical tasks. Suzuki et al. developed a set of fuzzy logic rules affecting the crane acceleration that allowed the crane to maneuver around obstacles while reducing the induced payload sway and travel time [70].

Another area of feedback control research focuses on neural network control [46]. A neural network is a system with inputs, outputs, and many processing elements. Each processing element has a number of internal parameters called weights. By changing the weights of each element, the behavior of the whole network can be altered. The broad goal of neural network control is to choose the weights (in a process called training) to achieve the desired input/output relationship. Valera et al. proposed the use of neural networks on an industrial crane [72]. One neural network was trained to learn the nonlinear system behavior and another network calculated the control action. The combination of the two was shown to be effective at trajectory tracking and payload sway reduction. Duong et al. designed a neural network control system trained with hybrid evolutionary algorithm for a three-dimensional tower crane [18]. Simulation results demonstrated the superior performance of the controller in reducing payload swing as compared with conventional training algorithms.

Sliding mode control is a nonlinear control method that applies a discontinuous control signal to force the system states to a user-defined surface, called the sliding surface [71]. The control signal is discontinuous because it can switch from one control law (e.g., one set of gains) to another depending on the system state. Ngo and Hong proposed a sliding mode controller for container cranes [45]. The sliding surface was designed by incorporating both the payload swing and the crane trolley dynamics. The effectiveness of the controller and its robustness to uncertainty was demonstrated through simulations and experiments on a scale model of a gantry crane.

Adaptive control is useful in system where the inputs and/or parameters vary significantly over time. Adaptive control techniques adjust the controller parameters (e.g., feedback gains) in real time to adapt to the changing system behavior. Ackermann proposed an adaptive gain scheduling scheme for a state-feedback controller [5]. The feedback gains were scheduled to keep the system states within a stable region. Butler et al. developed a two tier control system consisting of a primary linear state-feedback controller and an adaptive controller to account for any unmodeled dynamics [14]. The performance of the controller was evaluated on a scale model of a gantry crane. It was shown to be effective at reducing the payload swing after a few repetitions of a pre-defined crane trajectory.

Although there has been success, there are several factors that make implementing feedback control on cranes very challenging. One such significant challenge of using feedback control on cranes is the difficulty of measuring the motion of the payload. Two methods that have been used with some success are machine vision and gyroscopes. Machine vision systems can work well in fairly controlled environments, where lighting conditions are fairly constant and background clutter is minimal. However, most cranes operate in conditions that are significantly less ideal. Vision systems will have additional difficulties in the crowded, harsh, and changing environments in which many cranes operate.

Even under ideal conditions, sensing the payload is not trivial. One obvious place to mount a machine vision system is overhead, attached to the crane trolley. This configuration provides the best opportunity to keep the hook and payload in the camera field-of-view. However, the suspension cables and hook can limit the camera's view of the payload.

Other researchers have used gyroscope-based sensing solutions with some success [44, 52]. In this work, the gyroscopic measurements are often coupled with secondary means of sensing, such as potentiometers measuring cable deflection, and observers are used to smooth the resulting signals. The design and implementation of such observers introduces an additional layer of complexity to the system.

Another major challenge of feedback control is that a fundamental conflict exists between computerized feedback control and human operators. For pre-designated or point-to-point motions, feedback control, ignoring the difficulties mentioned above, can work fairly well. However, most cranes are not controlled by a computer or driven through pre-defined trajectories. Rather, they are controlled in real time by human operators. Herein lies the conflict. The human operator provides not only the initial reference command to the crane, but also introduces adjustments and additional feedback as necessary to maneuver the crane through the desired trajectory. The actions of the human operator (the primary controller) must take precedence over the computerized feedback control effort (the secondary controller).

To address this problem, a high-authority control (HAC) low-authority control (LAC) structure can be utilized [51]. This control structure consists of combining two controllers in a dual-loop scheme. The inner loop uses an active damping controller (i.e., low-gain controller) and the outer loop uses a HAC (i.e., high-gain controller) based on a model of the actively-damped system. A mixed high-authority/low-authority control structure was utilized on a control-optimized piezoelectric micro-gripper [19]. The low-authority controller was used as an active damping regulator and the high-authority controller was used to significantly modify the open-loop system poles. Berkhoff and Wesselink used a combination of fixed decentralized feedback control (low-authority control) and multiple-input multiple-output adaptive control (high-authority control) to reduce broadband active noise and vibration [10]. This control structure was applied to a panel with piezoelectric actuators, piezoelectric sensors, and acceleration sensors and the increased robustness and improved performance were demonstrated. Makarov et al. proposed a low-authority/high-authority controller for a flexible-joint robotic arm [35]. The LAC introduced adequate damping and the HAC was responsible for the overall motion of the arm. The effectiveness of the proposed controller was validated experimentally on a lightweight robot arm.

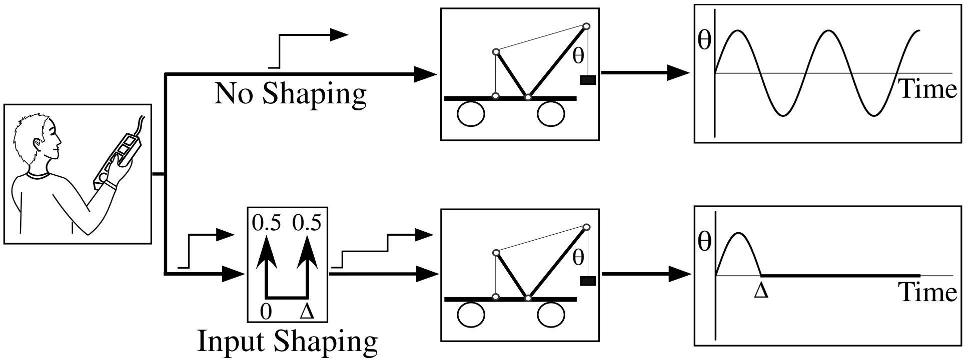

Figure 1.3: The Input-Shaping Process

1.4 Input-Shaping Control

Command shaping [55] is a control method that assists the human operator in effectively controlling flexible machinery, such as cranes. Input shaping [54,63] is a specific type of command shaping that intercepts the operator command and slightly modifies it. The modified command is then used to drive the machine without inducing large residual oscillations.

The input-shaping process is demonstrated in Figure 1.3. When the human operator pushes a button on the control pendent, a velocity-step command is sent to the crane. This command induces an oscillatory response, as shown in the top part of Figure 1.3. However, with input shaping, the original command is convolved with a sequence of impulses called the input shaper. The two-impulse input shaper shown in Figure 1.3 is called the Zero Vibration (ZV) shaper [54, 63]. The result of the convolution is a shaped command that moves the crane, but induces no residual vibration.

Although convolution is a complex mathematical operation, it is rather simple to implement when applied to a sequence of impulses, such as an input shaper. For example, the convolution shown in Figure 1.3 is performed by simply multiplying the reference command by the amplitude of the first impulse and then adding it to the reference command multiplied by the amplitude of the second impulse and shifted forward in time by Δ. Input shaping has been successfully implemented on many types of cranes [24, 31, 34, 37, 49, 65, 67, 69], and it is available in commercial products [1].

1.4.1 Input Shaper Derivation

The challenge with input shaping is to design an appropriate sequence of impulses for use in the input-shaper module. For an underdamped, second-order system, the residual vibration that results from a sequence of impulses (such as those in an input shaper) is described by [54],

$$V(\omega_n, \zeta) = e^{-\zeta\omega_n t_n}\sqrt{[C(\omega_n, \zeta)]^2 + [S(\omega_n, \zeta)]^2} \tag{1.3}$$

$$C(\omega_n, \zeta) = \sum_{i=1}^{n} A_i e^{\zeta\omega_n t_i} \cos(\omega_d t_i) \tag{1.4}$$

$$S(\omega_n, \zeta) = \sum_{i=1}^{n} A_i e^{\zeta\omega_n t_i} \sin(\omega_d t_i) \tag{1.5}$$

where A_i and t_i are the impulse amplitudes and times, respectively, n is the number of impulses in the impulse sequence (i.e., input shaper), ζ is the damping ratio, ω_n is the undamped natural frequency, and ω_d is the damped natural frequency given by,

$$\omega_d = \omega_n\sqrt{1 - \zeta^2} \tag{1.6}$$

Note that Equation (1.3) is nondimensional. It has been normalized by the vibration produced from a single unity-magnitude impulse.

Although there are different types of input shapers, they all share similar characteristics (i.e., constraint equations). In the case of the simplest input shaper, the Zero Vibration input shaper, Equation (1.3) is set equal to zero,

$$V(\omega_n, \zeta) = 0 \tag{1.7}$$

To obtain a normalized result, the impulse amplitudes must sum to one,

$$\sum_{i=1}^{n} A_i = 1 \tag{1.8}$$

This constraint guarantees that the input shaper does not increase or decrease the original command amplitude. The impulse amplitudes are also constrained to be positive,

$$A_i > 0, \quad i = 1, ..., n \tag{1.9}$$

This constraint is imposed to avoid saturating the actuators with large positive or negative impulse amplitudes. To obtain the fastest possible input shaper, the time of the last impulse is minimized,

$$\min(t_n) \tag{1.10}$$

The constraints in (1.8)-(1.10) along with that in (1.7) produce a fully-constrained problem that can be solved analytically to obtain the impulse amplitudes and times of a ZV shaper. The amplitudes and times of the ZV input shaper are given by,

$$\begin{bmatrix} A_i \\ t_i \end{bmatrix} = \begin{bmatrix} \frac{1}{K+1} & \frac{K}{K+1} \\ 0 & 0.5T_d \end{bmatrix} \tag{1.11}$$

where T_d is the damped period of vibration and K is given by,

$$K = e^{\left(\frac{-\zeta\pi}{\sqrt{1-\zeta^2}}\right)} \tag{1.12}$$

To illustrate the input-shaping technique, Figure 1.4 shows the response of a underdamped second-order system ($\omega_n = 3.13$ rad/sec and $\zeta = 0.1$) to only the ZV shaper. The magnitude of the first impulse is A_1, and the magnitude of the second impulse is A_2. The first impulse occurs at time zero, but the second impulse is delayed by $0.5T_d$. Both of these impulses induce an oscillatory response. However, the sum of these two responses, which represents the total response of the system after the shaped command is complete, produces no residual oscillation.

The ZV shaper is designed to produce zero residual vibration at the modeled frequency. If the actual natural frequency of the system is the same as the modeled frequency, then the residual vibration will be greatly reduced. In real machines;

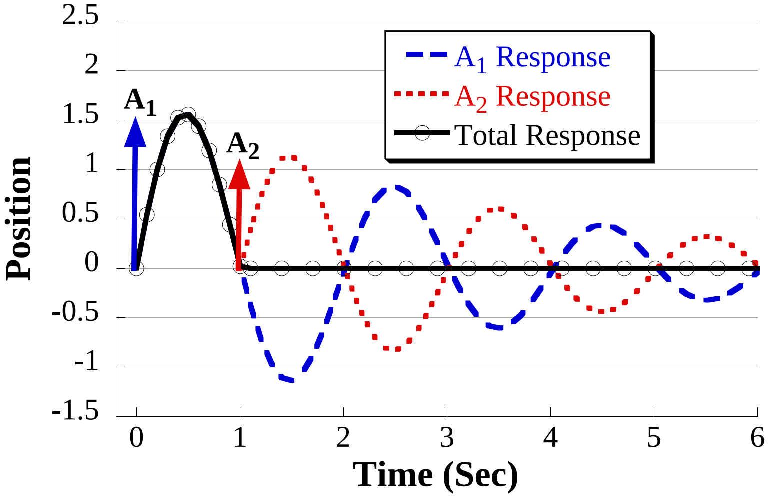

Figure 1.4: Second-Order System Response to ZV Shaper

however, the exact value of the natural frequency is difficult to obtain. Only an estimate of the natural frequency is known. Therefore, it is important to design shapers that are robust to errors or variations in the system parameters. The ZV shaper is not very robust to parameter variation, but there exist many shapers that are robust, such as the Zero Vibration and Derivative (ZVD) shaper [54]. The ZVD shaper is designed by adding an additional constraint and redesigning the impulse sequence. The additional constraint is formed by setting the derivative of the vibration equation (1.3) to zero,

$$\frac{\partial V(\omega,\zeta)}{\partial \omega} = 0 \tag{1.13}$$

The ZVD impulse amplitudes and times are given by,

$$\begin{bmatrix} A_i \\ t_i \end{bmatrix} = \begin{bmatrix} \frac{1}{(1+K)^2} & \frac{2K}{(1+K)^2} & \frac{K^2}{(1+K)^2} \\ 0 & 0.5T_d & T_d \end{bmatrix} \tag{1.14}$$

where K is given in (1.12).

Another robust input shaper is the Extra Insensitive (EI) shaper [60]. The EI shaper is designed by relaxing the zero residual vibration constraint. Instead of setting the vibration equation (1.3) equal to zero, it is set to below some tolerable level, V_{tol},

$$V(\omega, \zeta) < V_{tol} \tag{1.15}$$

The impulse amplitudes and times of the EI shaper are given by,

$$\begin{bmatrix} A_i \\ t_i \end{bmatrix} = \begin{bmatrix} A_1 & 1 - A_1 - A_3 & A_3 \\ 0 & t_2 & T_d \end{bmatrix} \tag{1.16}$$

where,

$$A_1 = 0.2497 + 0.2496V_{tol} + 0.8001\zeta + 1.233V_{tol}\zeta + 0.4960\zeta^2 + 3.173V_{tol}\zeta^2 \tag{1.17}$$

$$A_3 = 0.2515 + 0.2147V_{tol} - 0.8325\zeta + 1.415V_{tol}\zeta + 0.8518\zeta^2 + 4.901V_{tol}\zeta^2 \tag{1.18}$$

$$\begin{aligned} t_2 = (&0.5000 + 0.4616V_{tol}\zeta + 4.262V_{tol}\zeta^2 + 1.756V_{tol}\zeta^3 + \\ &8.578V_{tol}^2\zeta - 108.6V_{tol}^2\zeta^2 + 337.0V_{tol}^2\zeta^3)T_d \end{aligned} \tag{1.19}$$

Figure 1.5 shows the sensitivity curves for the three input shapers discussed above. The horizontal axis is the actual system frequency, ω_a, normalized by the modeled frequency, ω_m. The vertical axis is the percentage residual vibration. A percentage vibration of 100% means that the shaped command will produce the same amount of residual vibration as an unshaped command. The robustness of the input shapers is measured by how much the frequency can deviate from the modeled frequency while the percent residual vibration remains below the tolerable vibration level (V_{tol}). The ZV curve remains below the 5% V_{tol} line for frequencies ±3% of the modeled frequency. The ZVD and EI curves remain below V_{tol} for frequencies ±14.3% and ±20% of the modeled frequency, respectively.

The cost of increasing the robustness of input shaping is a longer shaper duration. Increasing the shaper duration causes a corresponding increase in the command rise time. Specified Insensitivity (SI) shapers [61] provide the maximum amount of robustness for a given shaper duration. Specified Insensitivity shapers are very similar in design to the EI shaper; however, instead of limiting the vibration at one frequency,

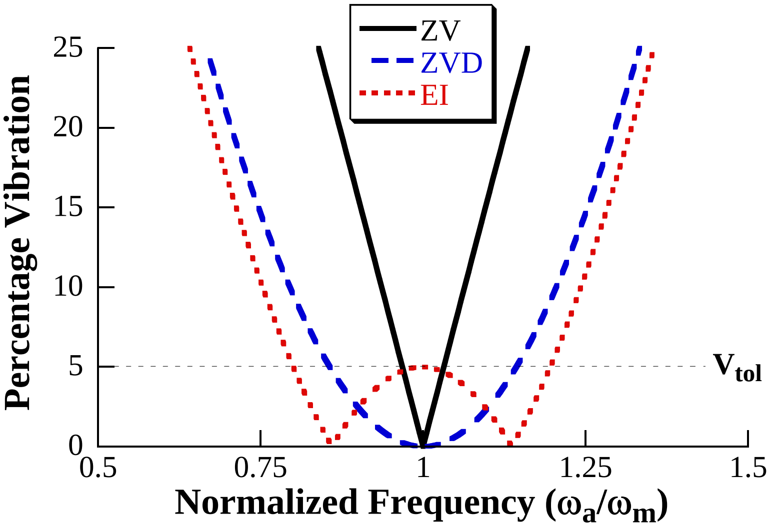

Figure 1.5: Sensitivity Curves for Various Input Shapers

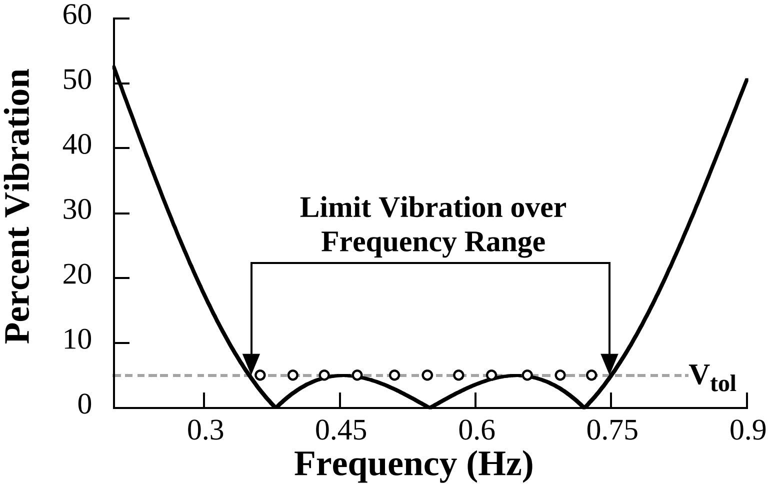

Figure 1.6: Specified Insensitivity Shaper Design Process

the residual vibration is limited to below V_{tol} at several frequencies,

$$V(\omega_1, \zeta) < V_{tol}, \quad V(\omega_2, \zeta) < V_{tol}, \quad V(\omega_3, \zeta) < V_{tol}, \quad \ldots \tag{1.20}$$

The set of constraints that fully define the SI shaper can be solved numerically using the MATLAB optimization toolbox to obtain the impulse amplitudes and times. Figure 1.6 illustrates this design process. The constraints of (1.20) are illustrated by the open circles along the V_{tol} line in Figure 1.6.

If the constraint in (1.9) is removed (i.e., negative impulses are allowed), then the

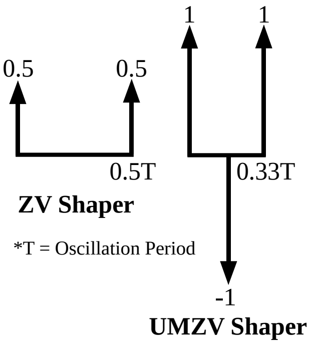

Figure 1.7: ZV Shaper vs. UMZV Shaper

system can be moved more quickly, while still suppressing the unwanted oscillatory behavior. In general, the impulses of a Specified Negative Amplitude (SNA) input shaper can have any value [56]. However, if the negative impulses are limited to unity magnitude, then Unity-Magnitude (UM) input shapers are produced. Figure 1.7 shows a Unity-Magnitude Zero Vibration (UMZV) shaper, along with a positive ZV shaper. By allowing negative impulses, the UMZV shaper can achieve the same vibration-reduction with a smaller rise-time penalty. The duration of the ZV shaper is half the period of oscillation; however, the duration of the UMZV shaper is only a third of the oscillation period. The drawback of negative shapers is that they produce more aggressive commands that can excite unmodeled high modes [58].

Input shapers can also easily handle multiple oscillation modes [31, 37, 58]. The simplest method is to design an input shaper (for example a ZV shaper) for each oscillation mode. Then, convolve the shapers together to produce a multi-mode input shaper. The Specified Insensitivity shaper design process can also be applied to multiple modes by applying the constraints of (1.20) over multiple distinct ranges of frequencies [31, 37, 73].

1.4.2 Vector Diagram Representation

Input shapers can be represented in the phase plane by placing the impulses on a vector diagram [59]. Figure 1.8 shows an example impulse sequence placed on a

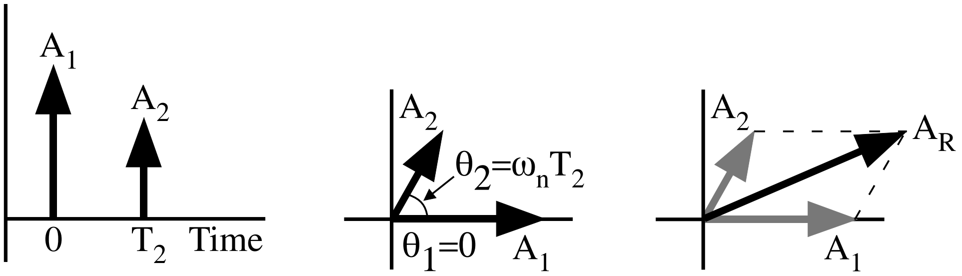

Impulse Sequence Vector Diagram Vector Sum

Figure 1.8: Vector Diagram Representation of an Impulse Sequence

vector diagram. In general, the relationship between the angle of a vector, θ_i, and the time of the i^{th} impulse in a sequence, T_i, is

$$\theta_i = \omega T_i \tag{1.21}$$

where ω is an arbitrary frequency. If instead of an arbitrary frequency, the natural frequency of the system is used ($\omega = \omega_n$), then the magnitude of the resultant vector (A_R) is proportional to the amplitude of the residual oscillation of a second-order system induced by a step command convolved with the impulse sequence [59]. Any arbitrary input can be constructed as a sum of steps; therefore, the magnitude of the resultant vector is a measure of the system response to any input.

Figure 1.9 shows the vector diagram representation of a ZV shaper for an undamped system. The first impulse occurs at time 0; therefore, a vector of magnitude A is placed at an angle of 0°. The second impulse occurs at half the oscillation period, so a second vector of equal magnitude is placed 180° out of phase with the first vector,

$$\theta_2 = \omega_n T_2 = (2\pi f_n)\left(\frac{1}{2f_n}\right) = \pi \tag{1.22}$$

where f_n is the natural frequency (in hertz) of the system. The resultant vector (which represents the induced residual swing) obtained from adding these two vectors is zero.

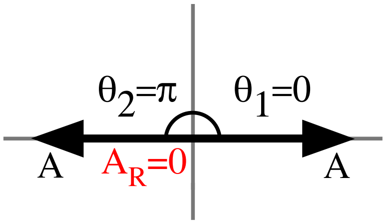

Figure 1.9: Vector Diagram Representation of a ZV Shaper

1.4.3 S-Plane Representation

Input shapers can also be represented in the Laplace domain. This is useful when looking at pole-zero plots of a system containing an input shaper. For simplicity, this analysis will consider a two-impulse ZV shaper, but the analysis can be extended to any other shaper. The general input-shaping process can be represented by,

$$r(t) * i(t) = c(t) \tag{1.23}$$

where $r(t)$ is the initial reference command, $i(t)$ is the input shaper, and $c(t)$ is the shaped command. Taking the Laplace transform of (1.23) yields,

$$R(s)I(s) = C(s) \tag{1.24}$$

where $R(s)$, $I(s)$, and $C(s)$ are the Laplace transforms of their corresponding functions of time. Note that the convolution in the time domain becomes a multiplication in the Laplace domain. As a result, when $I(s)$ is zero, the shaped command, $C(s)$ will also be zero regardless of the input reference command. (Note that this is true except for the special case when $R(s)$ is infinite at the value of s under consideration.) The Laplace transform of the ZV shaper is,

$$I(s) = A_1 + A_2 e^{-t_2 s} \tag{1.25}$$

where A_1, A_2, and t_2 are defined in (1.11). Substituting $s = \sigma + j\omega$ into (1.25) yields,

$$I(s) = A_1 + A_1 e^{\frac{-\pi}{\omega_d}(\zeta\omega_n + \sigma + j\omega)} \tag{1.26}$$

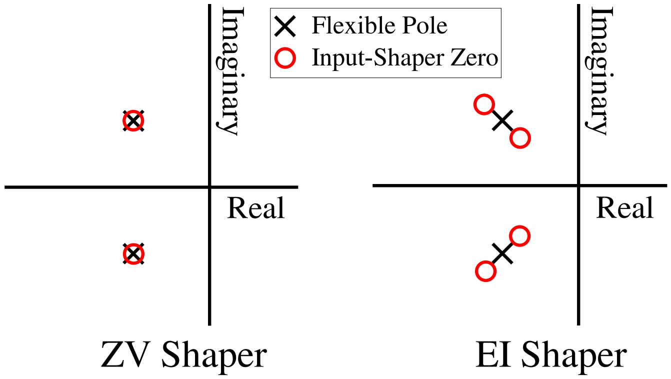

Figure 1.10: S-Plane Representation of Input Shapers

Equation (1.26) will be equal to zero if,

$$e^{\frac{-\pi}{\omega_d}(\zeta\omega_n+\sigma+j\omega)} = e^{\frac{-\pi}{\omega_d}(\zeta\omega_n+\sigma)}e^{j\left(\frac{-\pi\omega}{\omega_d}\right)} = -1 \tag{1.27}$$

For the condition in (1.27) to be true, the real exponential term must be equal to 1 and the imaginary exponential term must be equal to -1. Solving these two equations gives the values of s that make $I(s)$ go to zero,

$$s = -\zeta\omega_n \pm j\omega_d \tag{1.28}$$

These s values correspond exactly to the pole locations of a underdamped second-order system. Therefore, the input shaper has zero frequency content at the poles of the flexible system. This concept is represented in the s-plane in Figure 1.10. The ZV shaper has zeros that lie directly on top of the flexible poles of the system. Figure 1.10 also shows the s-plane representation of the EI shaper. Because the EI shaper limits the vibration below a tolerable level (instead of requiring zero residual vibration like the ZV shaper), the input shaper zeros are not directly on top of the flexible poles. They are placed near the poles, thereby increasing the robustness of the shaper.

1.5 Thesis Contributions

This thesis makes significant contributions to the understanding of the complex dynamics and control of mobile boom cranes and dual-hoist bridge cranes. The main contributions are:

1. The construction of a small-scale mobile boom crane for use in education and research
2. Modeling and analysis of the dynamics of mobile boom cranes and evaluation of various swing-reducing controllers on boom cranes
3. Development of a novel oscillation-amplifying command-shaping method to improve mobile crane applications that require large-amplitude swings, such as demolition with a wrecking ball
4. Modeling and analysis of the dynamic behavior of dual-hoist bridge cranes and evaluation of oscillation-reducing control methods
5. Demonstrating the effectiveness of input shaping in reducing crane payload swing in the presence of some common nonlinear effects
6. Development and analysis of an input-shaped human operator (high authority) and disturbance-rejecting feedback (low authority) control architecture

1.6 Thesis Outline

Chapter 2 presents a small-scale mobile boom crane and the user interfaces used to drive the crane. Then, a numerical model of the crane is derived, and its equations of motion are presented. The boom crane serves as a major testbed for the different controllers designs throughout the thesis. Chapter 3 presents a two-ton dual-hoist bridge crane and then derives a numerical model of the crane. This crane also serves a testbed for evaluating various controllers.

Chapter 4 presents a detailed study of the dynamic response of mobile boom cranes to various configuration and inputs. Input shaping controllers are designed and their performance are evaluated through simulations and experiments. Chapter 5 extends the analysis of boom cranes to double-pendulum payload dynamics. A robust multi-mode input shaper is designed, and its robustness is numerically and experimentally evaluated. Chapter 6 presents novel swing-amplifying controllers designed to help human operators effectively drive boom cranes swinging a wrecking ball. The proposed controller is evaluated by a human-operator performance study.

The dynamic behavior of dual-hoist bridge cranes is explored in Chapter 7. The effect of various parameters and inputs on the crane dynamics are studied and unwanted payload oscillations are combated with input shaping. Experimental results are used to verify key theoretical predictions and the effectiveness of the input-shaping control. Chapter 8 presents a series of operator studies with both the mobile boom crane and the dual-hoist bridge crane. The performance of human operators driving these cranes through different obstacle courses, with and without input-shaping controllers, is evaluated.

Input-shaping control is combined with a low-authority feedback controller in Chapter 9. Various factors affecting the design of the feedback controller are studied. Then, a set of design procedures are extracted that can be applied to other similar flexible systems. Finally, concluding remarks and future work are presented in Chapter 10.

CHAPTER II

SMALL-SCALE MOBILE BOOM CRANE

One of the primary testbeds used to experimentally evaluate the various aspects of this thesis is a small-scale mobile boom crane. This chapter presents the physical structure of the mobile boom crane. Then, the user interfaces of the crane are presented. Finally, numerical simulation models of the mobile boom crane are derived.

2.1 Physical Structure

Figure 2.1 shows the small-scale mobile boom crane. The body of the crane is approximately 115×50 cm. It has two bases: the mobile base and the slewing base. Mobility of the base is provided by two Siemens servomotors. The driving motor is

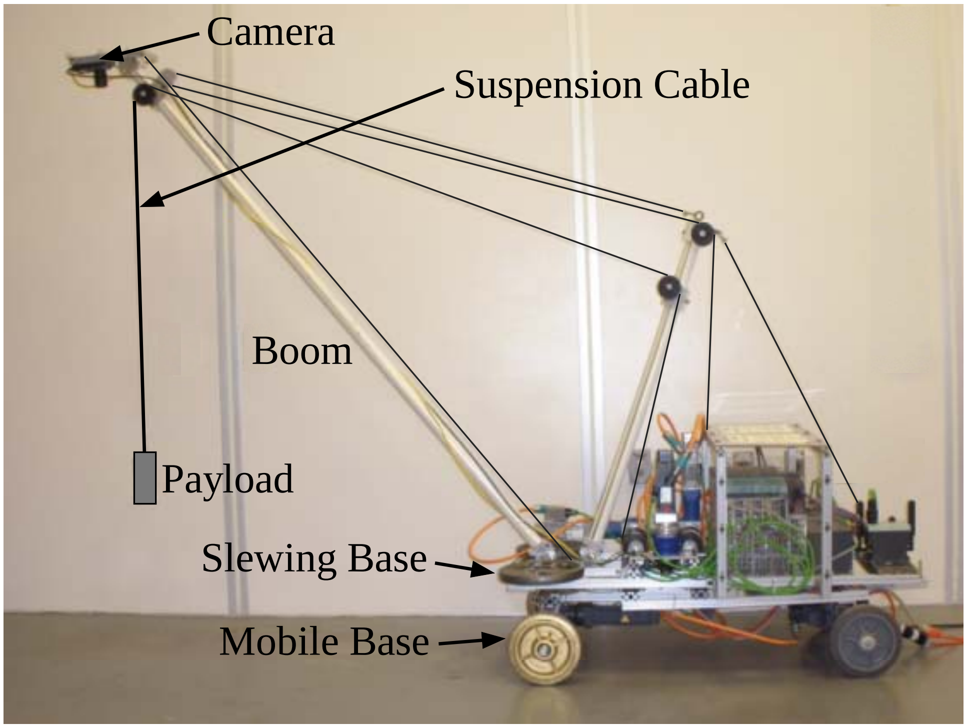

Figure 2.1: Small-Scale Mobile Boom Crane

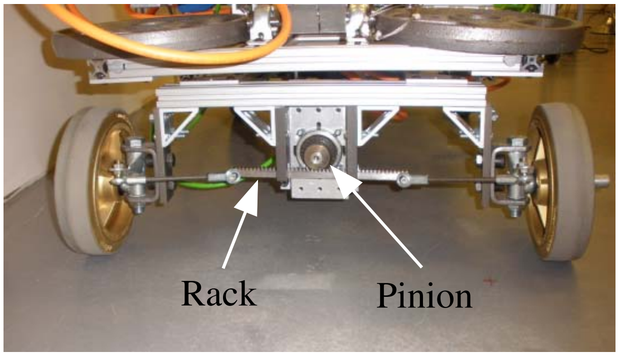

(a) Front

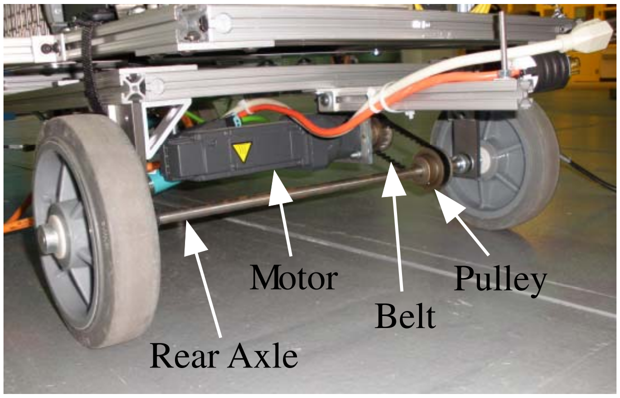

(b) Rear

Figure 2.2: Close-up View of Mobile Base

located near the back of the crane and is connected to the rear wheel axle using a timing belt and one-to-one pulleys. The steering motor is located near the front of the crane and controls steering via a rack-and-pinion. A close-up view of the mobile base is shown in Figure 2.2.

The slewing base can rotate with respect to the mobile base and is capable of 300° slewing rotation. The slewing rotation is supported by a turntable bearing and four ball transfers placed between the mobile and slewing bases. The slewing actuation is driven by a Siemens servomotor attached to a belt-drive system. The boom, which is attached to the top of the slewing base, is 200 cm long. The payload is attached via a suspension cable near the tip of the boom. The payload is moved in and out by moving the boom inward or outward, a rotation called luffing. The luffing angle is controlled via a cable attached to a Siemens servomotor. The suspension cable length

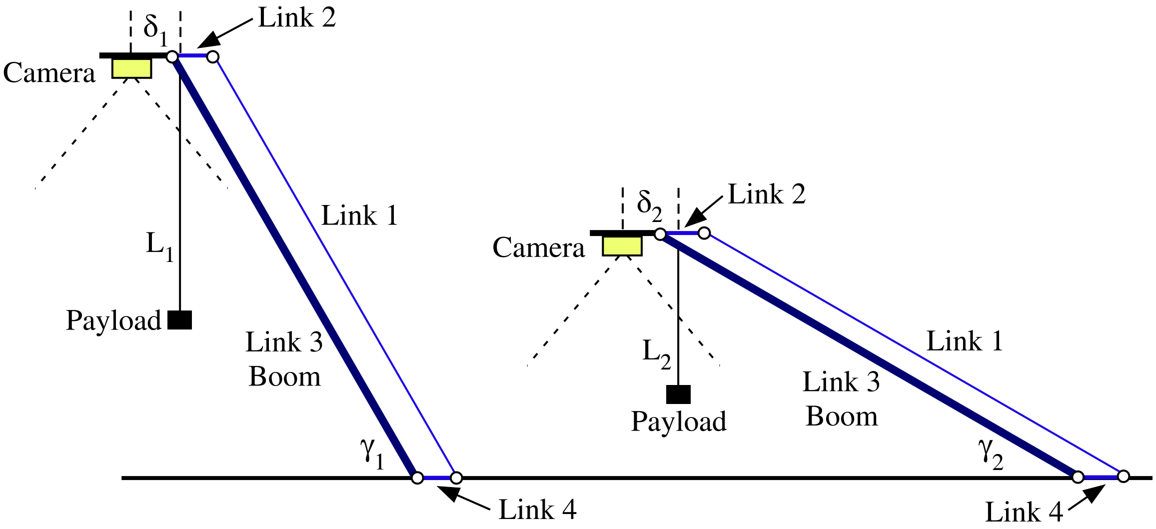

Figure 2.3: Four-bar Mechanism for Camera at the Tip of the Boom

is controlled via another Siemens servomotor.

A Siemens SIMATIC VS732-2 digital camera is mounted at the tip of the boom and records the swing deflection of the hook. The camera is connected using a four-bar mechanism, which allows the camera to rotate with respect to the boom, thereby keeping the payload in the camera field-of-view for a large range of suspension cable lengths and luffing angles. Figure 2.3 shows a sketch of the camera four-bar mechanism. If links 1 and 3 and links 2 and 4 have equal lengths, then the camera will remain parallel to the ground as the luffing angle, γ, varies.

Notice that the hook drifts horizontally across the camera field-of-view as the luffing angle and suspension cable length change. This occurs because the hook is not attached directly below the camera. There is a finite horizontal offset (δ) between them. The value of this offset increases as the luffing angle decreases. To account for the drift when obtaining the hook displacement, a lookup table was generated. The lookup table contains the zero-swing (i.e., equilibrium) payload positions for the entire usable range of luffing angles and suspension cable lengths of the small-scale boom crane. The hook swing deflection at a given luffing angle and suspension cable length is then obtained relative to its corresponding zero-swing reference point from the lookup table.

All actuation of the crane is done by Siemens synchronous, AC servomotors. The motors are controlled via Siemens SINAMICS motor drives with Proportional-Integral control on the reference velocity. Supervisory control of the crane and all of its actuations is done by a Programmable Logic Controller (PLC). A laptop computer communicates with the PLC through a wireless connection.

2.2 User Interfaces

Cranes are driven by user interfaces with joysticks or buttons. The human operator pushes the levers or buttons to send move commands to the crane. For the small-scale mobile boom crane, the operator can move the machine in ten different directions (two different directions for each of the five separate motion axes). This section presents two different methods of controlling the small-scale mobile boom crane: *i)* a Graphical User Interface (GUI), and *ii)* a Siemens touchscreen mobile panel.

2.2.1 Graphical User Interface

The Graphical User Interface (GUI) is shown in Figure 2.4. The right side of the screen contains two input fields. The top field provides buttons that move the crane motions (slewing, luffing, and hoisting) and the bottom-field buttons control the mobile base (driving and steering). The center of the screen provides the on/off button as well as numerical information about the orientation of the crane, such as the slewing angle, the luffing angle, and the suspension cable length. The left side of the screen provides a side view and a top view of the crane. The orientation of the crane in both of these views is updated in real time. The hook is also visible in the top view, and its position varies in real time as well.

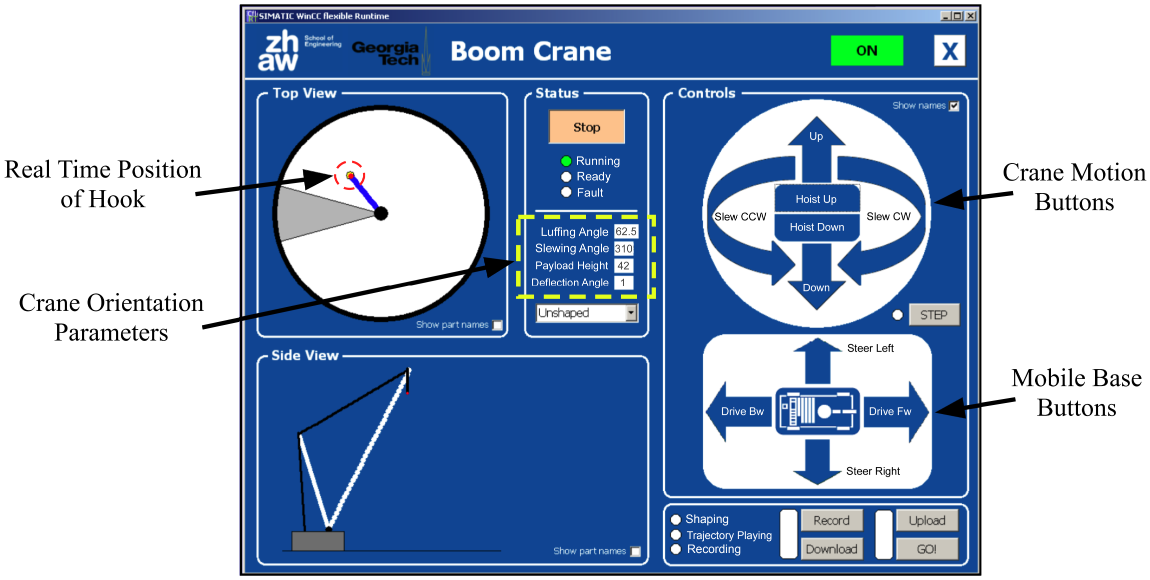

Luffing Angle 62.5
Slewing Angle 310
Payload Height 42
Deflection Angle 1
Unshaped

Figure 2.4: Laptop Graphical User Interface

2.2.2 Siemens Touchscreen Mobile Panel

Figure 2.5 shows the Siemens touchscreen mobile panel used for control of the boom crane. The panel is a Siemens Mobile Panel 277 IWLAN. It has a 7.5 in. TFT-Touch display with a resolution of 640×480 pixels. It has 18 LED functions keys, two illuminated push-buttons, one hand-wheel, and one key-operated switch with three positions. The panel also has 6 MB of internal user memory and PROFINET

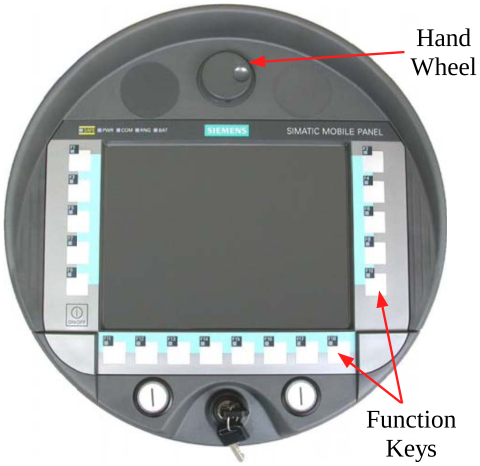

Figure 2.5: Siemens Touchscreen Mobile Panel

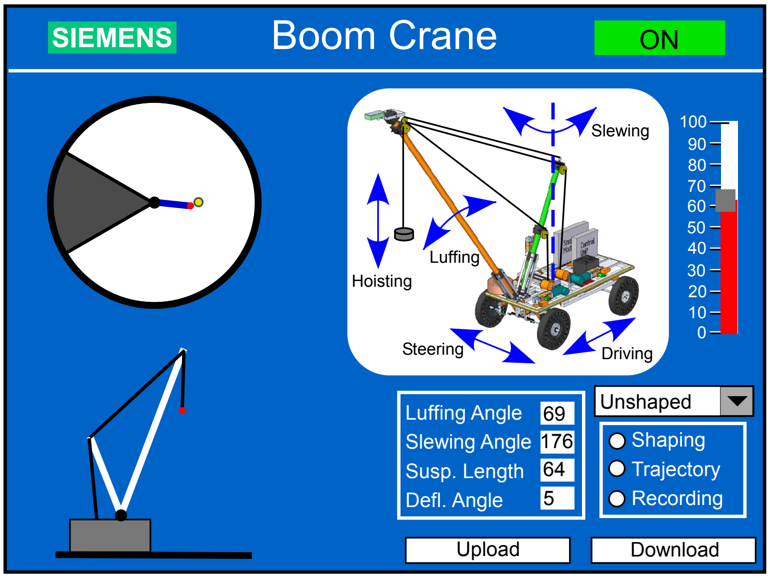

Luffing Angle 69
Slewing Angle 176
Susp. Length 64
Defl. Angle 5

Figure 2.6: Graphical User Interface 1 on Mobile Panel

and USB interfaces. Programming the panel is performed with the Siemens WinCC Flexible software package. The mobile panel was connected to the mobile boom crane through an existing wireless router mounted on the crane.

Two different GUI's were designed for the mobile panel. The first GUI, shown in Figure 2.6, utilizes the hand wheel. The display is used to show the operator information about the mobile boom crane. On the left hand side of the screen are side and top views of the mobile boom crane. These are especially useful if the operator's view of the crane is limited. There is also an additional section that provides numerical values of important crane parameters, such as the luffing angle, the slewing angle, the suspension cable length, and the hook deflection angle.

In order to provide the operator with a better physical understanding of how each motion axis controls the crane, a three-dimensional image of the crane is provided in the top right of the screen. The motion of each axis is clearly labeled on this figure. The operator clicks on the desired axis label (for example, steering, driving, etc.) to select that axis for motion. The selected axis is highlighted to show that it is active. Once the operator has selected an axis, the hand wheel can be turned in either direction to move the crane. For fast maneuvering, the operator can select and move more than one axis at a time. All axes selected are controlled by turning the hand wheel.

Two methods were designed to translate the hand wheel input to system motion. The first method uses the scroll bar on the right side of Figure 2.6 to select the move time associated with one click of the hand wheel. Each axis has a predefined velocity. So when the hand wheel is turned, the active axes will move a distance equal to the selected move time multiplied by their corresponding velocities. Smaller percentages equal smaller move times and are intended for small movements. Larger percentages equal longer move times and are intended for longer movements. The value of the move time is 50 ms when the scrollbar is set to 0% and 450 ms when it is set to 100%.

The second option leaves the selection of the move time to the PLC. The PLC automatically detects whether the operator wants to do a step-by-step motion or a longer motion. The detection is carried out as a function of the system related time delays and the standard cycle time of the PLC. If the user does not carry out more than one click within a cycle time, then the program defines this as a step-by-step motion. Using this method, the operator can turn the hand wheel rapidly to move the payload close to the desired position, and then turn the hand wheel slowly to position it more precisely.

The second GUI designed for the mobile panel is shown in Figure 2.7. This interface uses the function keys (F1-F10) to operate the crane. Although pushing buttons eliminates the physical connection between the interface and the actual motions of the crane, this design makes performing multi-axis motions much simpler.

For each motion axis, there are two corresponding buttons, one for each direction. Buttons for opposing directions of a motion axis are placed across from each other on the screen. The center of the display is again used to show the operator information about the orientation of the mobile boom crane.

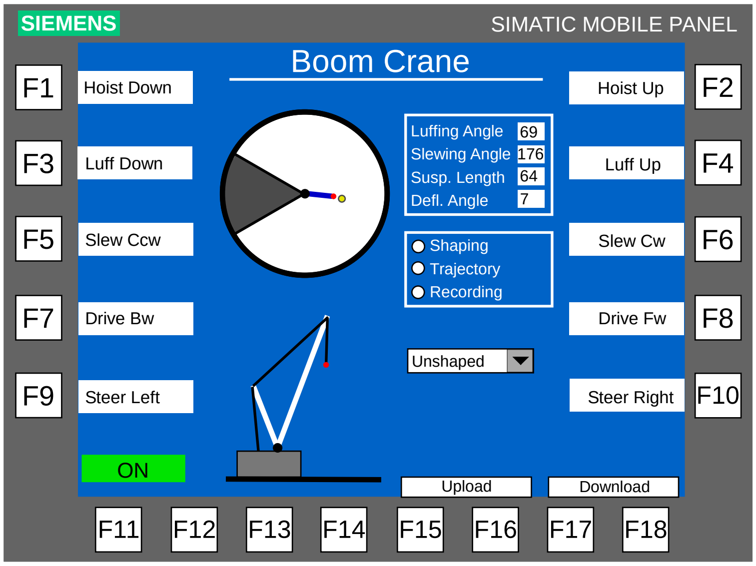

Luffing Angle 69
Slewing Angle 176
Susp. Length 64
Defl. Angle 7

Unshaped

Figure 2.7: Graphical User Interface 2 on Mobile Panel

2.3 Numerical Simulation Models

This section derives the equations of motion of a mobile boom crane with two types of payloads, a single-pendulum and a double-pendulum payload.

2.3.1 Single-Pendulum Model

Figure 2.8 shows a simple sketch of the single-pendulum mobile boom crane model. It has the same basic components as the small-scale mobile boom crane shown in Figure 2.1. The bottom portion is composed of two rectangular bodies. The lower, dark-colored rectangle is the mobile base. The top, light-colored rectangle is the slewing base that rotates with respect to the mobile base. The boom is attached to this slewing base and is capable of rotation in a vertical plane that is perpendicular to the slewing base. The hook is supported by a suspension cable attached near the end of the boom.

The equations of motion for the mobile boom crane were obtained using a multi-body dynamics approach. The mobile boom crane was divided into the five components shown in Figure 2.8. The Mobile Base, the Slewing Base, and the Boom were

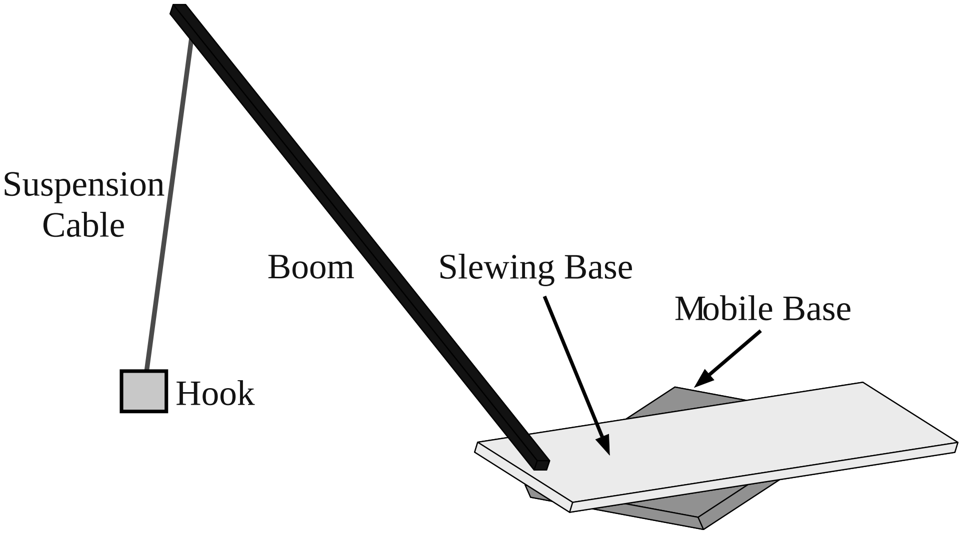

Figure 2.8: Sketch of the Mobile Boom Crane Model

modeled as rigid bodies with mass. The Suspension Cable was modeled as a massless rigid body. The Hook was modeled as a particle.

Figure 2.9 shows a top view of the model. The crane is defined with respect to a Newtonian reference frame, N, with origin at O. The center of the rear axle of the Mobile Base, point A, is located at

$$\vec{P}_{A/O} = x\vec{x}_O + y\vec{y}_O \tag{2.1}$$

The center of the rear axle is chosen as the center of rotation of the Mobile Base because the Mobile Base is modeled as a rear-wheel drive car. The rotation of the Mobile Base about the inertial frame is given by

$$\vec{\omega}_{\text{Mobile Base}/N} = \dot{\alpha}\vec{z}_O \tag{2.2}$$

The geometric center of the Mobile Base, point B, and the slewing center of rotation, point C, are given by

$$\vec{P}_{B/A} = x_{cent}\vec{x}_A + y_{cent}\vec{y}_A \tag{2.3}$$

$$\vec{P}_{C/B} = x_{slew}\vec{x}_A + y_{slew}\vec{y}_A \tag{2.4}$$

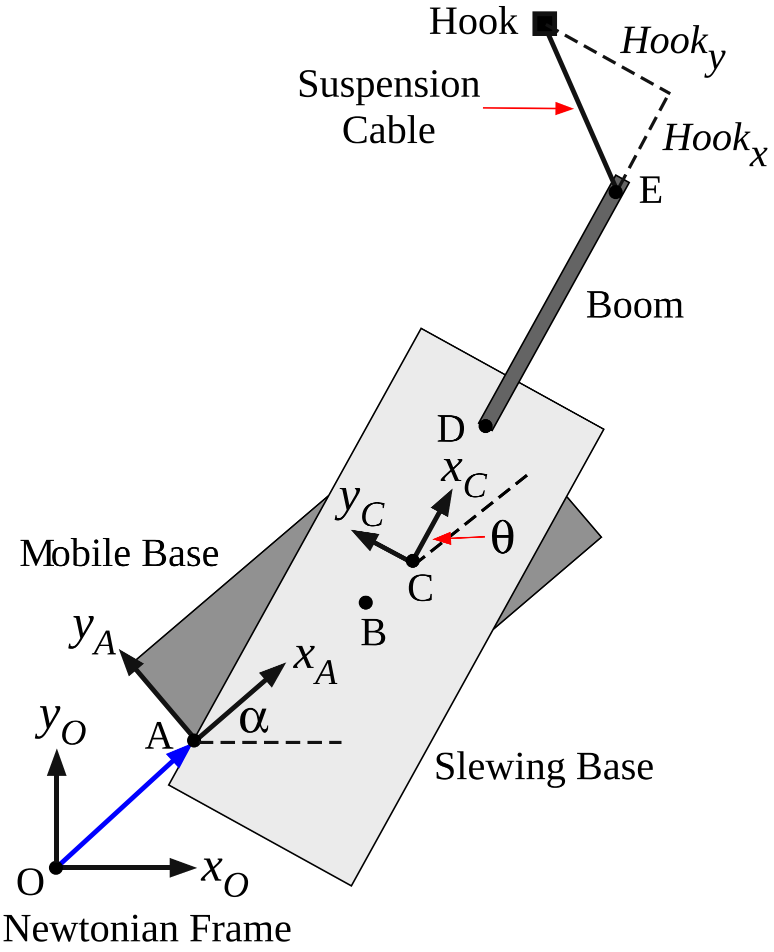

Figure 2.9: Top View of Mobile Boom Crane Model

The Slewing Base can rotate about point C with respect to the Mobile Base with an angular velocity given by

$$\vec{\omega}_{\text{Slewing Base/Mobile Base}} = \dot{\theta}\vec{z}_A \tag{2.5}$$

The luffing center of rotation, point D, is given by:

$$\vec{P}_{D/C} = x_{luff}\vec{x}_C + y_{luff}\vec{y}_C \tag{2.6}$$

As shown in Figure 2.10, the Boom rotates about point D in a vertical plane perpendicular to the Slewing Base

$$\vec{\omega}_{\text{Boom/Slewing Base}} = -\dot{\gamma}\vec{y}_C \tag{2.7}$$

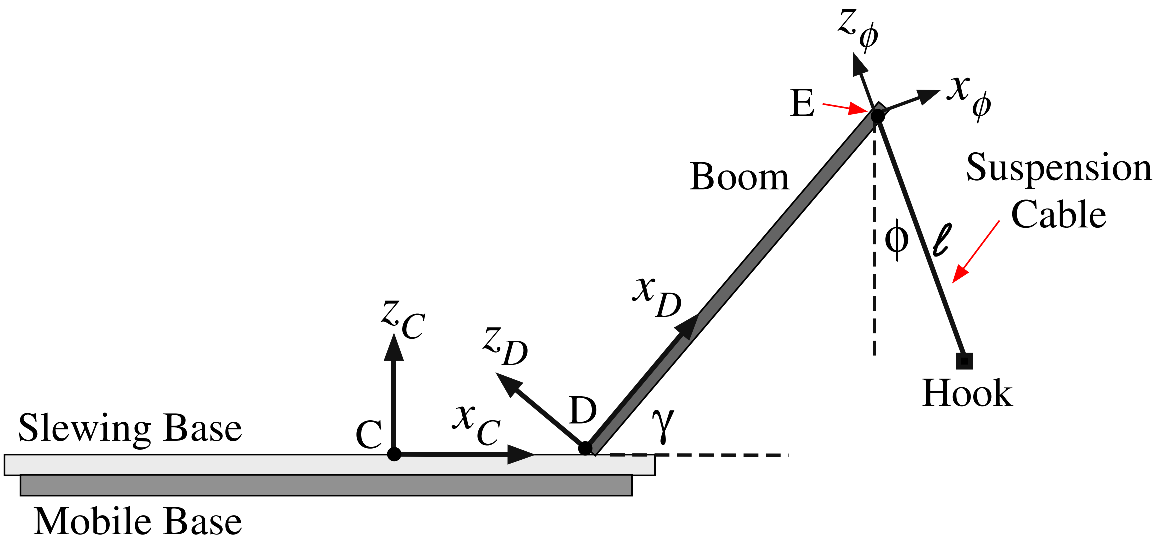

Figure 2.10: Side View of Mobile Boom Crane Model

The negative sign is to ensure that a positive luffing angular velocity will raise the Boom. The Suspension Cable attachment point, E, is given by

$$\vec{P}_{E/D} = \ell_{boom}\vec{x}_D \tag{2.8}$$

The radial swing of the Suspension Cable is defined as

$$\vec{\omega}_{\text{Radial/Boom}} = (-\dot{\phi} + \dot{\gamma})\vec{y}_D \tag{2.9}$$

In order to define the radial swing, ϕ, with respect to a reference frame that is perpendicular to the Slewing Base, the negative of the angular velocity in (2.7) is added to the radial swing. The tangential swing of the Suspension Cable, as shown in Figure 2.11, is defined relative to the radial swing angle

$$\vec{\omega}_{\text{Tangential/Radial}} = \dot{\beta}\vec{x}_\phi \tag{2.10}$$

The Hook is located at the end of the Suspension Cable

$$\vec{P}_{\text{Hook}/E} = -\ell\vec{z}_\beta \tag{2.11}$$

The displacement of the Hook relative to the overhead suspension point E (with

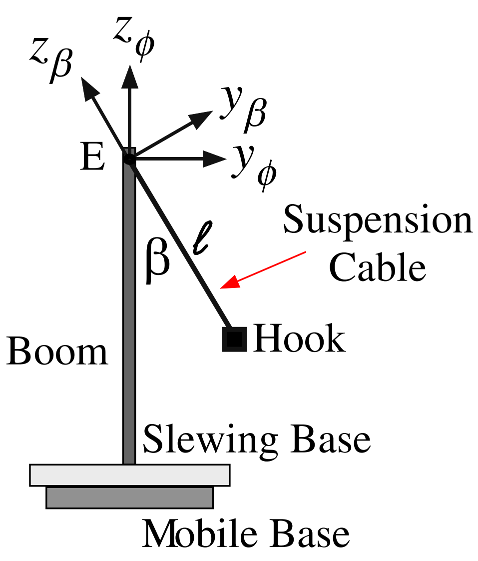

Figure 2.11: Front View of Mobile Boom Crane Model

reference to axes that are parallel to the Slewing Base) is given by

$$Hook_x = \ell \cos(\beta)\sin(\phi) \tag{2.12}$$

$$Hook_y = \ell \sin(\beta) \tag{2.13}$$

Figure 2.12 shows a sketch of the Mobile Base. It is treated as a car with rear-wheel drive and front-wheel steering. The coordinates x and y represent the location of the center of the rear axle with respect to the center of the Newtonian reference frame, ℓ_{axle} is the distance between the front and rear axle, and ρ is the radius of curvature of the arc that is traversed by the center of the rear axle, if the steering angle is constant. The inputs to the Mobile Base are the velocity of the base, v, and the steering angle, ψ. The Cartesian components of the Mobile Base velocity, $\dot{x}$ and $\dot{y}$, as well as the Mobile Base rotation rate, $\dot{\alpha}$, are given by

$$\dot{x} = v\cos(\alpha) \tag{2.14}$$

$$\dot{y} = v\sin(\alpha) \tag{2.15}$$

$$\dot{\alpha} = \frac{v}{\ell_{axle}}\tan(\psi) \tag{2.16}$$

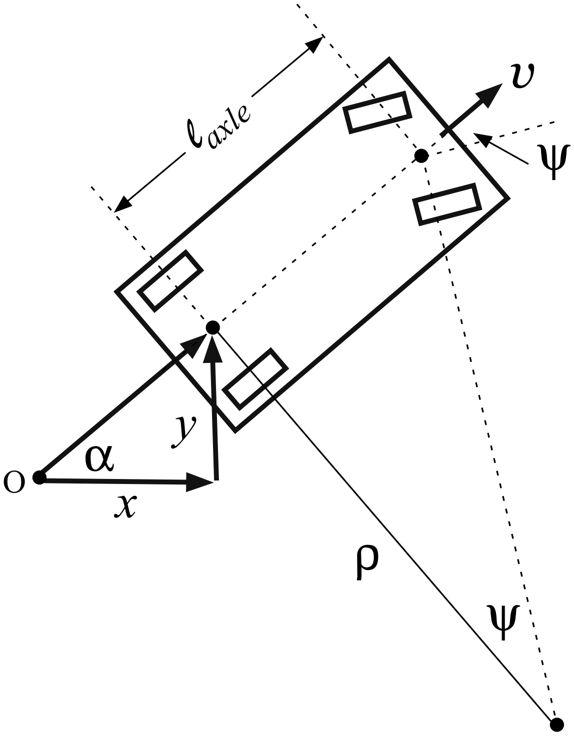

Figure 2.12: Sketch of Mobile Base Parameters

Further details of this derivation are given in [32].

The inputs to the simulation model are the acceleration of the base, $\dot{v}$, and the accelerations for the steering angle, $\ddot{\psi}$, the slewing angle about the mobile base, $\ddot{\theta}$, the luffing angle of the boom, $\ddot{\gamma}$, and the suspension cable length, $\ddot{\ell}$. The important outputs are the hook swing angles in the radial direction, ϕ, and the tangential direction, β.

The model assumes that the body of the crane is significantly more massive than the hook, so that the hook is unable to affect the motion of the crane base. There is no damping in the cable swing. Motor and transmission dynamics are also not modeled. Using a commercial dynamics package [42], the equations of motion for the mobile boom crane were obtained (Appendix A). The equations of motion for the radial and tangential swings are

$$\begin{aligned}
-2\ell\cos(\beta)\ddot{\phi} = {} & 2g\sin(\phi) + 4\dot{\ell}[\cos(\beta)\dot{\phi} - \sin(\beta)\cos(\phi)(\dot{\alpha}+\dot{\theta})] \\
& + [2\cos(\phi)\sin(\alpha+\theta)]\ddot{y} + [2\cos(\phi)\cos(\alpha+\theta)]\ddot{x} \\
& + 2\ell[\sin(\beta)\sin(\phi)\dot{\phi}(\dot{\alpha}+\dot{\theta}) - \sin(\beta)\dot{\beta}\dot{\phi} - \cos(\beta)\cos(\phi)\dot{\beta}(\dot{\alpha}+\dot{\theta})] \\
& - 2\ell[\sin(\beta)\cos(\phi)(\ddot{\alpha}+\ddot{\theta})] - 2\cos(\phi)[x_{luff}(\dot{\alpha}+\dot{\theta})^2 + y_{luff}(\ddot{\alpha}+\ddot{\theta})] \\
& - 2\ell[\dot{\beta} + \sin(\phi)(\dot{\alpha}+\dot{\theta})][\sin(\beta)\dot{\phi} + \cos(\beta)\cos(\phi)(\dot{\alpha}+\dot{\theta})] \\
& - \cos(\phi)\cos(\theta)[(\ell_{axle} + 2x_{slew})\dot{\alpha}^2 + 2y_{slew}\ddot{\alpha}] \\
& - \sin(\theta)\cos(\phi)[2y_{slew}\dot{\alpha}^2 - (\ell_{axle} + 2x_{slew})\ddot{\alpha}] \\
& - 2\ell_{boom}\cos(\gamma-\phi)[\dot{\gamma}^2 + \cos(\gamma)^2(\dot{\alpha}+\dot{\theta})^2] \\
& - 2\ell_{boom}\sin(\gamma-\phi)[\sin(\gamma)\cos(\gamma)(\dot{\alpha}+\dot{\theta})^2 + \ddot{\gamma}]
\end{aligned} \tag{2.17}$$

$$\begin{aligned}
2\ell\ddot{\beta} \quad = \quad & - 2g\sin(\beta)\cos(\phi) - 4\dot{\ell}[\dot{\beta} + \sin(\phi)(\dot{\alpha}+\dot{\theta})] \\
& + 2[\cos(\alpha)(\sin(\theta)\cos(\beta) + \sin(\beta)\sin(\phi)\cos(\theta))]\ddot{x} \\
& + 2[\sin(\alpha)(\cos(\beta)\cos(\theta) - \sin(\beta)\sin(\phi)\sin(\theta))]\ddot{x} \\
& + 2[\sin(\alpha)(\sin(\theta)\cos(\beta) + \sin(\beta)\sin(\phi)\cos(\theta))]\ddot{y} \\
& - 2[\cos(\alpha)(\cos(\beta)\cos(\theta) - \sin(\beta)\sin(\phi)\sin(\theta))]\ddot{y} \\
& - 2\ell\sin(\beta)\dot{\phi}[\cos(\beta)\dot{\phi} - \sin(\beta)\cos(\phi)(\dot{\alpha}+\dot{\theta})] \\
& - 2\ell[\cos(\phi)\dot{\phi}(\dot{\alpha}+\dot{\theta}) + \sin(\phi)(\ddot{\alpha}+\ddot{\theta})] \\
& - 2\sin(\beta)\sin(\phi)[x_{luff}(\dot{\alpha}+\dot{\theta})^2 + y_{luff}(\ddot{\alpha}+\ddot{\theta})] \\
& + 2\cos(\beta)[y_{luff}(\dot{\alpha}+\dot{\theta})^2 - x_{luff}(\ddot{\alpha}+\ddot{\theta})] \\
& + [\cos(\beta)\cos(\theta) - \sin(\beta)\sin(\phi)\sin(\theta)][2y_{slew}\dot{\alpha}^2 - (\ell_{axle} + 2x_{slew})\ddot{\alpha}] \\
& - [\sin(\theta)\cos(\beta) + \sin(\beta)\sin(\phi)\cos(\theta)][(\ell_{axle} + 2x_{slew})\dot{\alpha}^2 + 2y_{slew}\ddot{\alpha}] \\
& + 2\ell_{boom}\sin(\beta)\sin(\gamma-\phi)[\dot{\gamma}^2 + \cos(\gamma)^2(\dot{\alpha}+\dot{\theta})^2] \\
& - 2\ell_{boom}\sin(\beta)\cos(\gamma-\phi)[\sin(\gamma)\cos(\gamma)(\dot{\alpha}+\dot{\theta})^2 + \ddot{\gamma}] \\
& + 2\cos(\beta)[2\ell_{boom}\sin(\gamma)\dot{\gamma}(\dot{\alpha}+\dot{\theta}) - \ell\cos(\phi)(\dot{\alpha}+\dot{\theta})(\cos(\beta)\dot{\phi} \\
& \qquad - \sin(\beta)\cos(\phi)(\dot{\alpha}+\dot{\theta})) - \ell_{boom}\cos(\gamma)(\ddot{\alpha}+\ddot{\theta})]
\end{aligned} \tag{2.18}$$

Table 2.1: Nominal Boom Crane Simulation Parameters

Parameter	Value (m)	Parameter	Value (m)
x_{slew}	0.095	y_{slew}	0
x_{luff}	0.36	y_{luff}	0
ℓ_{boom}	1.85	ℓ_{axle}	0.9

The equations of motion for the boom crane are large and complex. However, they can be represented more simply by

$$M(\Theta)\left[\ddot{\phi},\ddot{\beta}\right]^T + V(\Theta,\dot{\Theta}) + G(\Theta) = U \tag{2.19}$$

where $\Theta = [\phi,\beta,x,y,\alpha,\theta,\gamma,\ell]$, $M(\Theta)$ is a 2×2 mass matrix, $V(\Theta,\dot{\Theta})$ is a 2×1 vector of centrifugal and Coriolis terms, $G(\Theta)$ is a 2×1 vector of gravity terms, and U is a 2×1 input vector given by

$$U = K(\Theta)\left[\ddot{x},\ddot{y},\ddot{\alpha},\ddot{\theta},\ddot{\gamma},\ddot{\ell}\right]^T \tag{2.20}$$

where $K(\Theta)$ is a 2×6 matrix.

Table 2.1 provides the nominal values of the important simulations parameters. These values were chosen to approximately match the physical small-scale mobile boom crane.

2.3.2 Double-Pendulum Model

To study the dynamics of the boom crane with double-pendulum payloads, the model presented above was modified to accommodate double-pendulum payloads. Figure 2.13 shows a three-dimensional sketch of the double-pendulum mobile boom crane model.

An additional Rigging Cable of length ℓ_p that attaches to the Payload, and two swing angles have been added to the model. The Rigging Cable was modeled as a massless rigid body. The Payload was modeled as a particle. The model assumes that the body of the crane is significantly more massive than the payload, so that the

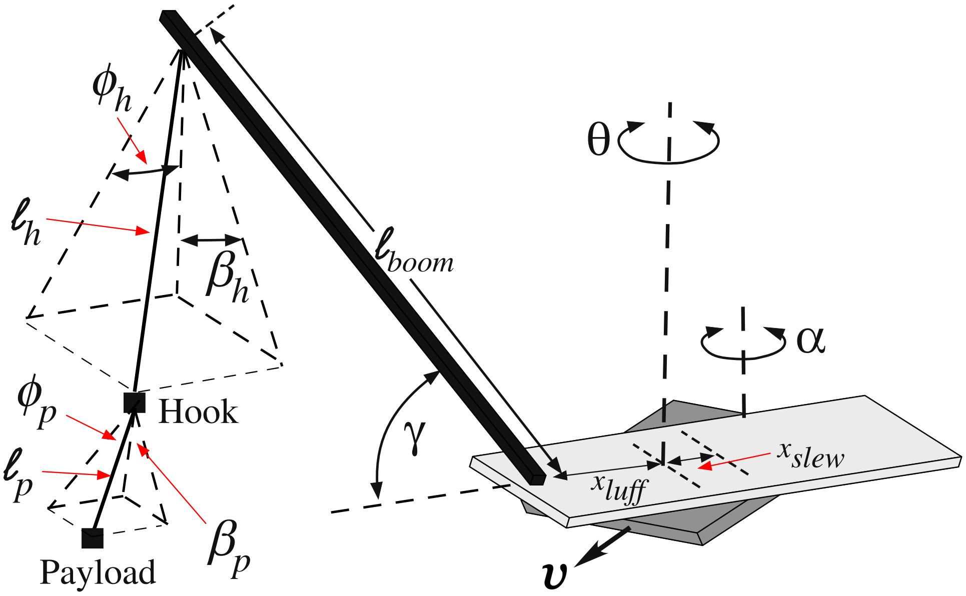

Figure 2.13: Sketch of Double-Pendulum Mobile Boom Crane Model

payload is unable to affect the motion of the crane base. The radial Payload swing, ϕ_p, is defined relative to the tangential Hook swing, β_h, and the tangential Payload swing, β_p, is defined relative to the radial Payload swing. The displacements of the Hook and the Payload relative to the overhead suspension point are given by

$$Hook_x = \ell_h \cos(\beta_h)\sin(\phi_h) \tag{2.21}$$

$$Hook_y = \ell_h \sin(\beta_h) \tag{2.22}$$

$$\begin{aligned} Payload_x = \ell_h \cos(\beta_h)\sin(\phi_h) + \ell_p(\cos(\phi_h)\sin(\phi_p)\cos(\beta_p) - \\ \sin(\phi_h)(\sin(\beta_h)\sin(\beta_p) - \cos(\beta_h)\cos(\beta_p)\cos(\phi_p))) \end{aligned} \tag{2.23}$$

$$Payload_y = \ell_h \sin(\beta_h) + \ell_p(\sin(\beta_p)\cos(\beta_h) + \sin(\beta_h)\cos(\beta_p)\cos(\phi_p)) \tag{2.24}$$

The equations of motion for the double-pendulum mobile boom crane are very complex and long; however, they can be represented by

$$M(\Theta)\left[\ddot{\phi}_h, \ddot{\phi}_p, \ddot{\beta}_h, \ddot{\beta}_p\right]^T + V(\Theta, \dot{\Theta}) + G(\Theta) = U \tag{2.25}$$

Where $\Theta = [\phi_h, \phi_p, \beta_h, \beta_p, x, y, \alpha, \theta, \gamma, \ell_h]$, $M(\Theta)$ is a 4×4 mass matrix, $V(\Theta, \dot{\Theta})$ is a 4×1 column matrix of centrifugal and Coriolis terms, $G(\Theta)$ is a 4×1 column matrix of gravity terms, and U is a 4×1 input column matrix given by

$$U = K(\Theta)\left[\ddot{x}, \ddot{y}, \ddot{\alpha}, \ddot{\theta}, \ddot{\gamma}, \ddot{\ell}_h\right]^T \tag{2.26}$$

where $K(\Theta)$ is a 4×6 matrix.

Double-pendulum payloads have two oscillation modes. The frequencies of oscillation of a double-pendulum payload are functions of the cable lengths and the hook and payload masses. The linearized oscillation frequencies for a planar double-pendulum are [11]

$$\omega_{1,2} = \sqrt{\frac{g}{2}}\sqrt{(1+R)\left(\frac{1}{\ell_h}+\frac{1}{\ell_p}\right) \mp \beta} \tag{2.27}$$

$$\beta = \sqrt{(1+R)^2\left(\frac{1}{\ell_h}+\frac{1}{\ell_p}\right)^2 - 4\left(\frac{1+R}{\ell_h \ell_p}\right)} \tag{2.28}$$

where g is the gravitational acceleration and R is the ratio of the payload mass (m_p) to the hook mass (m_h).

2.4 Summary

This chapter presented the small-scale mobile boom crane used for experiments throughout this thesis. Details of the crane and its user interfaces were provided. Then, a numerical model of the crane was derived and the equations of motion were obtained. It was also shown that the model can be easily modified to simulate double-pendulum payloads.

CHAPTER III

DUAL-HOIST BRIDGE CRANE

Another experimental testbed used to explore the dynamic behavior of complex flexible machinery and evaluate various swing-reducing controllers is a dual-hoist bridge crane. This chapter presents the physical structure of the dual-hoist crane and derives a numerical simulation model for such cranes.

3.1 Physical Structure

Figure 3.1 shows the two-ton dual-hoist bridge crane located in the Aerospace Manufacturing Center at Georgia Tech. The crane operates in a 10×8.5 m rectangular workspace.

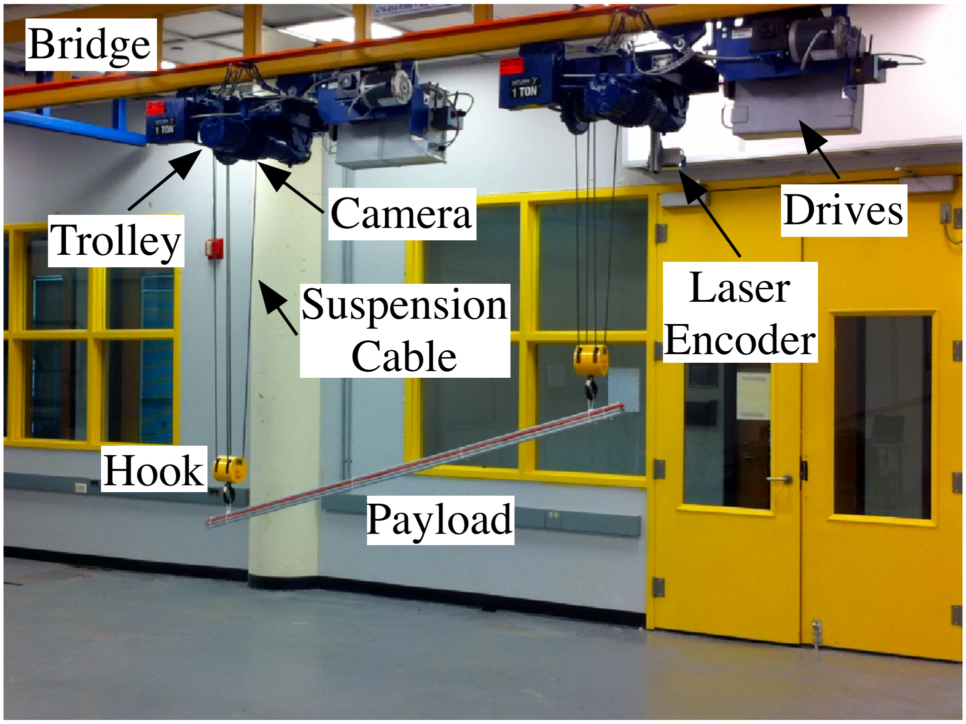

Figure 3.1: Dual-Hoist Bridge Crane

The two trolleys can move independently, or in a coordinated manner, along a bridge. The bridge itself can travel along rails attached at either side of the ceiling. Each trolley is capable of lifting up to 1 ton and can extend its suspension cables to a maximum length of approximately 2.6 m.

All motions of the trolleys and bridge are achieved via Siemens SIMOTION drives. The drives provide Proportional-Integral control of the reference velocities. Supervisory control of the system is provided by a Programmable Logic Controller (PLC). The PLC and drives communicate wirelessly through Siemens wireless access points. The positions of the trolleys and bridge in the workspace are determined by laser encoders attached to the trolleys and one end of the bridge, respectively. The deflection of the hooks is measured using COGNEX cameras attached underneath the trolleys.

The crane can be controlled via a graphical user interface on a Siemens Touch Panel, similar to the mobile panel used to drive the small-scale mobile boom crane presented in Chapter 2. Figure 3.2 shows the GUI used to control the dual-hoist crane. The right-hand side contains the motion buttons for hoisting, the bridge, and both trolleys. The left-hand side contains buttons for selecting controllers and output fields that display useful information, such as the cable lengths.

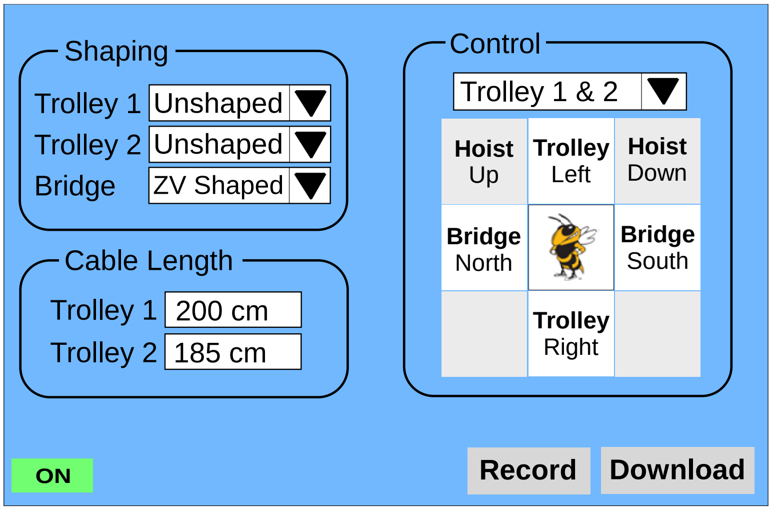
Shaping
Trolley 1 Unshaped
Trolley 2 Unshaped
Bridge ZV Shaped

Cable Length
Trolley 1 200 cm
Trolley 2 185 cm

Control
Trolley 1 & 2

Figure 3.2: Graphical User Interface for the Dual-Hoist Bridge Crane

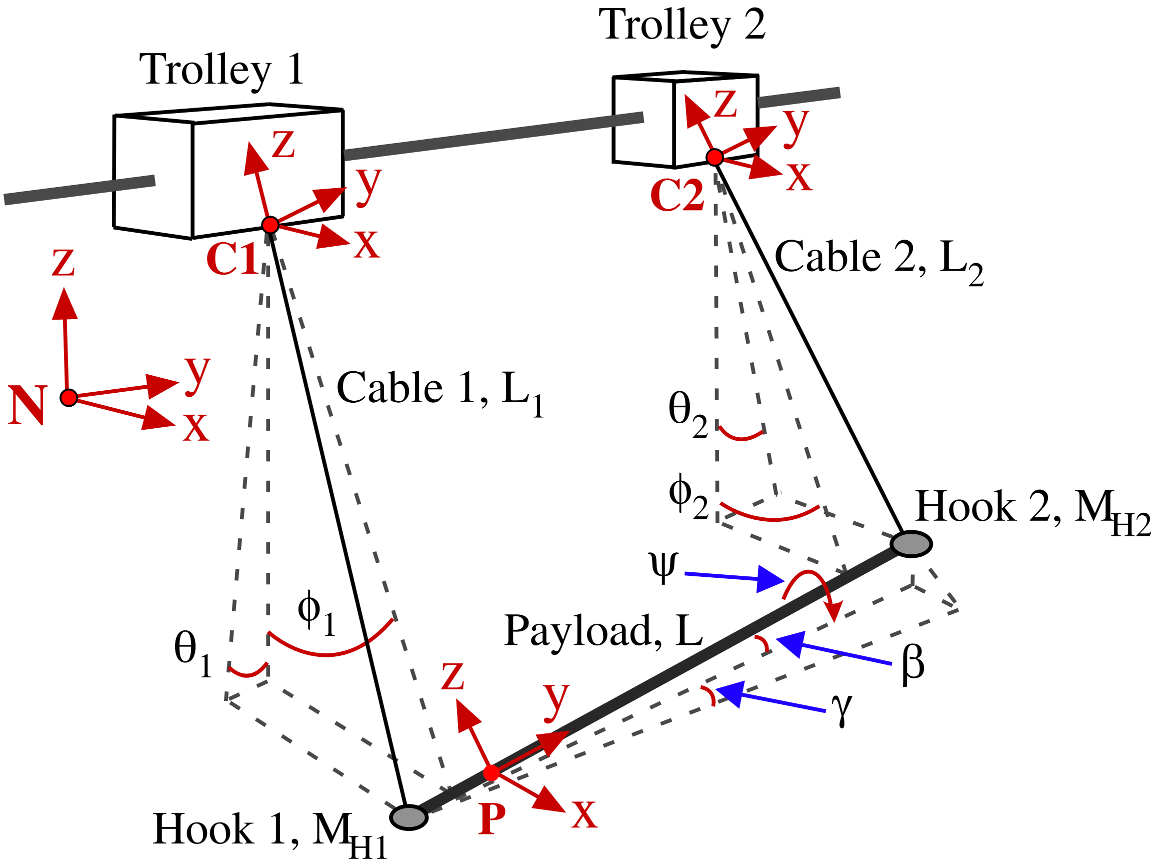

Figure 3.3: Dual-Hoist Bridge Crane Model

3.2 Numerical Simulation Models

A three-dimensional model of a dual-hoist crane system is shown in Figure 3.3. The crane consists of two trolleys. The trolleys can move in the y direction, along a rail that connects the trolleys, and in the x direction, perpendicular to the rail that connects the trolleys. Motion in the perpendicular direction is called bridge motion.

The equations of motion for the dual-hoist bridge crane were obtained using a multi-body dynamics approach. The dual-hoist crane was divided into seven components. The two Trolleys were modeled as massless points. The Suspension Cables were modeled as massless rigid bodies. The two Hooks were modeled as particles and the Payload was modeled as a rigid body with mass and inertial properties.

Trolley 1 and Trolley 2 move relative to a Newtonian frame, N, by

$$\vec{P}_{\text{Trolley } 1/N} = x_1\vec{N}_x + y_1\vec{N}_y \tag{3.1}$$

$$\vec{P}_{\text{Trolley } 2/N} = x_2\vec{N}_x + y_2\vec{N}_y \tag{3.2}$$

The trolleys are constrained to move together in the bridge direction by setting x_1 equal to x_2. Each Trolley has a Suspension Cable attached beneath it. The length of the Trolley 1 and Trolley 2 cables are L_1 and L_2, respectively. Cable 1 and Cable 2 rotate with respect to the Newtonian frame by

$$\vec{\omega}_{\text{Cable } 1/N} = \dot{\theta}_1\vec{N}_x + \dot{\phi}_1\vec{D}_{1y} \tag{3.3}$$

$$\vec{\omega}_{\text{Cable } 2/N} = \dot{\theta}_2\vec{N}_x + \dot{\phi}_2\vec{D}_{2y} \tag{3.4}$$

where $\vec{D}_1$ and $\vec{D}_2$ are intermediate frames of Cable 1 and Cable 2, respectively. There is a Hook attached to the end of each Suspension Cable. The hook masses of Trolley 1 and Trolley 2 are M_{H1} and M_{H2}, respectively. Attached between the two hooks is the Payload, which can rotate with respect to the Newtonian frame by

$$\vec{\omega}_{\text{Payload}/N} = \dot{\beta}\vec{N}_x + \dot{\psi}\vec{A}_y + \dot{\gamma}\vec{B}_z \tag{3.5}$$

where $\vec{A}$ and $\vec{B}$ are intermediate frames produced by each successive rotation.

The model is essentially a hanging four-bar mechanism (the corner points are the two trolley and the two hooks). The four-bar linkage introduces a set of velocity constraints. These velocity constraints are derived by traversing point by point around the four-bar linkage, then differentiating the obtained position constraints,

$$\frac{d}{dt}\left[x_1\vec{N}_x + y_1\vec{N}_y - L_1\vec{C}_{1z} + L\vec{P}_y + L_2\vec{C}_{2z} - x_2\vec{N}_x - y_2\vec{N}_y\right] \bullet \vec{N}_x = 0 \tag{3.6}$$

$$\frac{d}{dt}\left[x_1\vec{N}_x + y_1\vec{N}_y - L_1\vec{C}_{1z} + L\vec{P}_y + L_2\vec{C}_{2z} - x_2\vec{N}_x - y_2\vec{N}_y\right] \bullet \vec{N}_y = 0 \tag{3.7}$$

$$\frac{d}{dt}\left[x_1\vec{N}_x + y_1\vec{N}_y - L_1\vec{C}_{1z} + L\vec{P}_y + L_2\vec{C}_{2z} - x_2\vec{N}_x - y_2\vec{N}_y\right] \bullet \vec{N}_z = 0 \tag{3.8}$$

where $\vec{C}_1$, $\vec{C}_2$, and $\vec{P}$ are body-fixed coordinate axes of Cable 1, Cable 2, and the Payload, respectively.

Table 3.1: **Nominal Dual-Hoist Crane Simulation Parameters**

Parameter	Value
Hook Mass	7.65 kg
Max Trolley Acceleration & Velocity	1 m/s^2 & 0.35 m/s
Max Bridge Acceleration & Velocity	1 m/s^2 & 0.30 m/s

The inputs to the model are the accelerations of the two trolleys in the trolley direction, $\ddot{y}_1$ and $\ddot{y}_2$, and the bridge direction, $\ddot{x}_1$ and $\ddot{x}_2$. The suspension cable lengths are treated as constants during simulation. The mathematical model for this system was obtained using the commercial dynamics package, MotionGenesis [2] (Appendix B). The equations of motion are very complex, but can be represented by

$$M(\Theta)\left[\ddot{\theta}_1, \ddot{\phi}_1, \ddot{\phi}_2, \ddot{\psi}\right]^T + V(\Theta, \dot{\Theta}) + G(\Theta) = U \tag{3.9}$$

where $\Theta = [\theta_1, \theta_2, \phi_1, \phi_2, \beta, \gamma, \psi, x_1, x_2, y_1, y_2]$, $M(\Theta)$ is a 4×4 mass matrix, $V(\Theta, \dot{\Theta})$ is a 4×1 column matrix of centrifugal and Coriolis terms, $G(\Theta)$ is a 4×1 column matrix of gravity terms, and U is a 4×1 input column matrix given by

$$U = K(\Theta)\left[\ddot{x}_1, \ddot{x}_2, \ddot{y}_1, \ddot{y}_2\right]^T \tag{3.10}$$

where $K(\Theta)$ is a 4×4 matrix. Notice that $\ddot{\theta}_2$, $\ddot{\beta}$, and $\ddot{\gamma}$ do not appear in the equations of motion. This is because they are not independent variables. They are obtained from the constraints of the four-bar linkage.

Table 3.1 shows the nominal parameters used to simulate the model. These parameters were chosen to approximately match the parameters of the two-ton dual-hoist bridge crane shown in Figure 3.1.

3.3 Summary

This chapter presented the two-ton dual-hoist bridge crane used for experiments throughout this thesis. Details of the crane and its user interface were provided. Then, a numerical model of the crane was derived using a moving four-bar linkage.

CHAPTER IV

SINGLE-PENDULUM MOBILE BOOM CRANE DYNAMICS AND CONTROL

This chapter explores the complex dynamic response of mobile boom cranes. The effects of various input commands and parameter changes are investigated through simulations and experiments. Input-shaping control is also applied to these motions and its effectiveness is quantified.

The baseline reference command used in this investigation is a trapezoidal-velocity profile (bang-coast-bang acceleration), as shown in Figure 4.1(a). For small motions, the trapezoid reduces to a triangular velocity, as shown in Figure 4.1(b). Bang-coast-bang acceleration was chosen as the reference command because many cranes are driven by human operators pushing on-off buttons on a control pendent. On-off buttons produce a roughly constant acceleration until the velocity limit is reached.

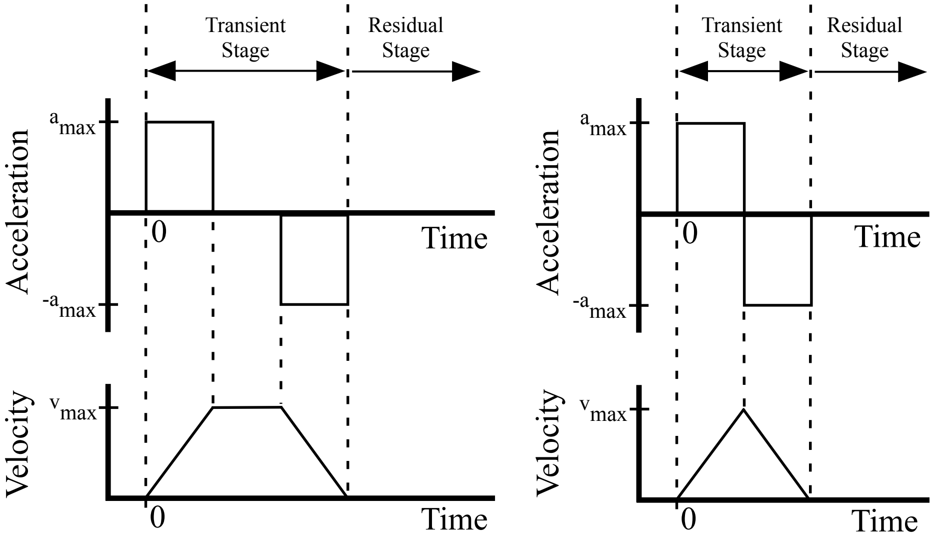

(a) Bang-Coast-Bang Command (b) Bang-Bang Command

Figure 4.1: Bang-Coast-Bang and Bang-Bang Commands

(Most cranes reach their velocity limits in a short period of time.) Releasing the on-off button causes a deceleration to stop. The result is a bang-coast-bang acceleration command.

In this analysis, two important oscillation parameters are measured and discussed: transient deflection and residual vibration amplitude. The transient stage of the response is defined as the time frame from the beginning of the accelerating pulse to the end of the decelerating pulse. The peak-to-peak payload displacement during the transient stage is called the transient deflection. The residual stage is defined as the time frame from the end of the decelerating pulse to the end of the simulation. The maximum peak-to-peak payload displacement during the residual stage is called the residual vibration amplitude.

The next section presents a detailed analysis of the slewing motion. Then, Section 4.2 analyzes the luffing motion, followed by an analysis of level luffing in Section 4.3. Section 4.4 discusses important dynamics of combined slewing and luffing motions. Finally, Section 4.5 investigates the dynamic response of the mobile base of the boom crane.

4.1 Slewing

4.1.1 Numerical Analysis

Slewing motion of the boom crane is defined as the rotation, θ, of the slewing base about the mobile base. During the numerical simulations of the boom crane reported in this section, the maximum slewing velocity was limited to 10°/s and the maximum acceleration was limited to $25^\circ/\mathrm{s}^2$.

The solid line in Figure 4.2 shows the tangential swing of the payload during a 50° slewing motion. The luffing angle was held constant at 45°, and a constant suspension cable length of 1 m was used. The starting acceleration at 0 s initiates some oscillation. At approximately 5 s, the stopping deceleration induces more oscillation. In this

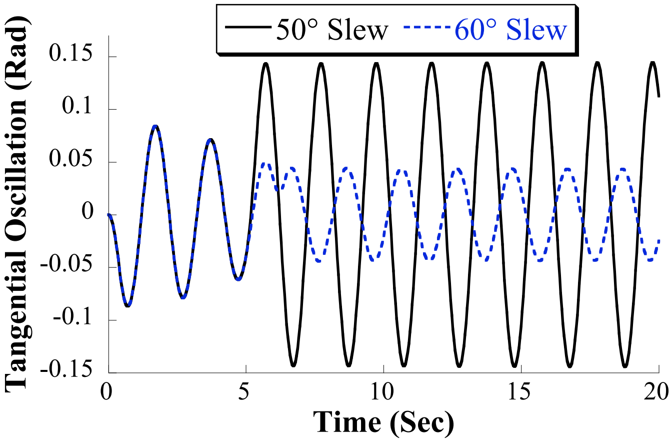

Figure 4.2: Tangential Payload Oscillation for Slewing Distances of 50° and 60°

case, the oscillation induced by stopping the slew is in phase with the swing caused by the initial acceleration. Hence, the residual vibration amplitude is larger than the transient. For some cases, however, the stopping oscillation is out of phase with the starting oscillation and results in reduced residual vibration amplitude. This is demonstrated by the dotted line in Figure 4.2, which shows the tangential swing for a slewing distance of 60°. The stopping deceleration, which occurs at approximately 6 s, partially cancels out the oscillation caused by the starting acceleration, thus resulting in smaller residual oscillation. The results in Figure 4.2 merely offer a glimpse at the complex dynamic nature of boom cranes. The response contains large oscillations that are a complex function of the crane configuration and the operator input.

The tangential and centripetal forces of the slewing motion cause the payload to oscillate in two directions, radial and tangential. This can be traced to coupling terms between the slewing motion and the radial and tangential swing angles, ϕ and β, in the equations of motion. During the slewing motion (transient stage), there are two swing frequencies present in the radial and tangential oscillations [33]. This leads to beating between the two oscillations. This is demonstrated in Figure 4.3, which shows the radial and tangential oscillations for a 360° slewing motion that takes 36 s to complete. Using an FFT analysis, the two frequencies of oscillation were obtained

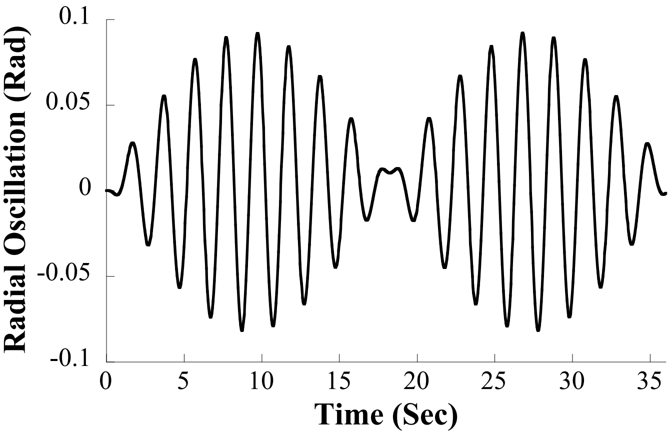

(a) Radial Oscillation

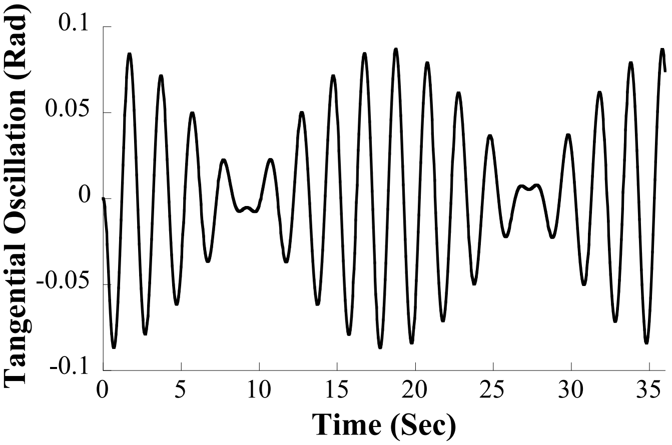

(b) Tangential Oscillation

Figure 4.3: Payload Oscillation During a 360° Slew

as 0.47 Hz and 0.53 Hz. (The oscillation frequency of a simple pendulum with a 1 m suspension cable length is 0.50 Hz.)

Another result of the rotational slewing motion is the precession of the payload. To better demonstrate this effect, the dynamics were simulated for a duration of 1500 s. Figure 4.4(a) shows the radial oscillation and Figure 4.4(b) shows the tangential oscillation resulting from a 10° slewing motion, which is completed in 1.4 s. The maximum residual radial oscillation occurs when the residual tangential oscillation is near its minimum, and vice versa. This effect can be physically interpreted as the oscillation of the payload precessing from one direction to the other. Figure 4.5 shows the location of the payload relative to the suspension point during the 10° slew shown

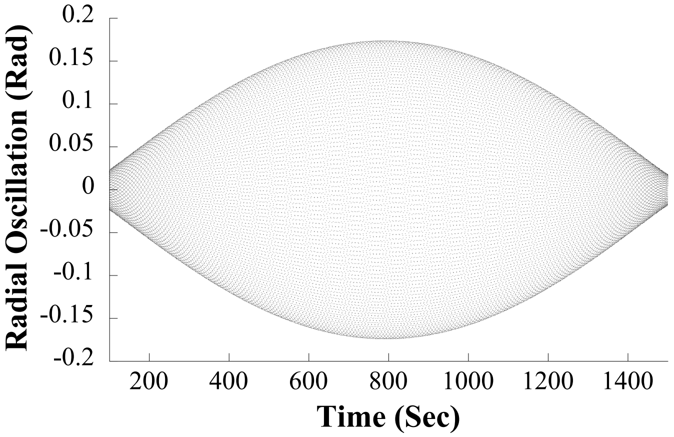

(a) Radial Oscillation

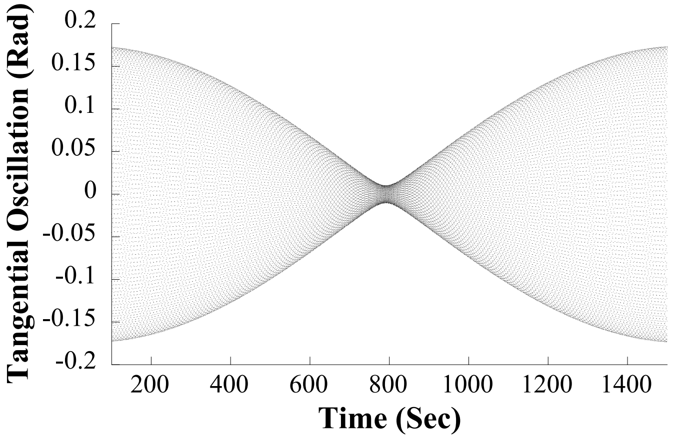

(b) Tangential Oscillation

Figure 4.4: Payload Oscillation Resulting from a 10° Slew

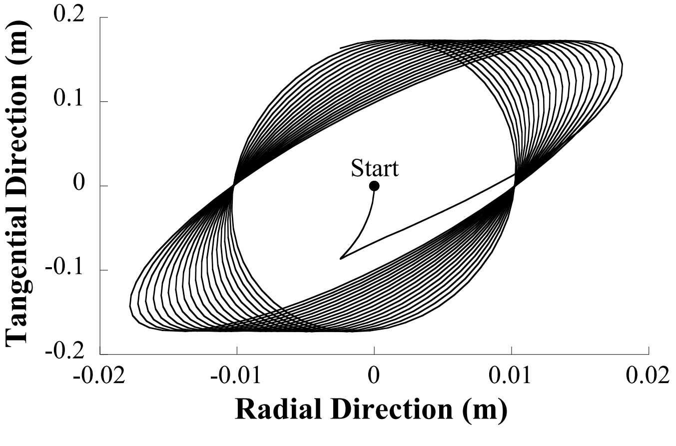

Figure 4.5: Payload Response from a 10° Slew

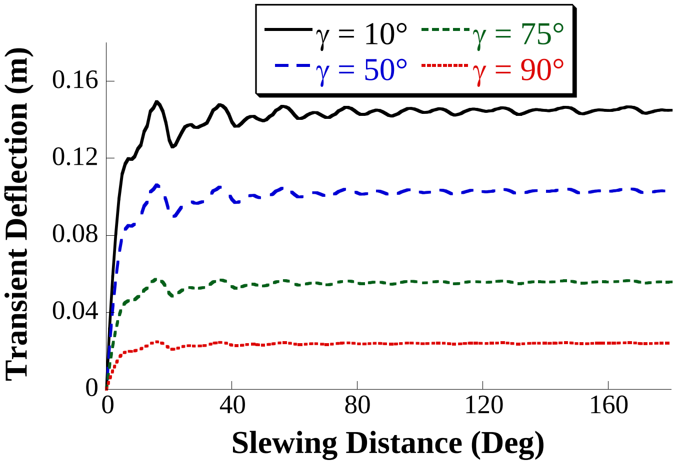

Figure 4.6: Average Transient Deflection vs. Slewing Distance

in Figure 4.4. The payload does not follow a single loop, but oscillates between the radial and tangential directions.

To better understand the dynamics of the slewing motion, the relationship between transient deflection, residual vibration amplitude, slewing distance, and luff angle were investigated. The crane was started from rest at the 0° slew position (with the boom pointing directly forward). Then, it was slewed with a constant luff angle using trapezoidal velocity commands. Figure 4.6 shows how the average transient deflection changes as a function of luff angle (γ) and slewing distance.

The amount of transient deflection depends on the size of the acceleration pulse and the duration of the transient stage. For small slewing distances, the width of the acceleration pulse increases with slew distance. However, once the slew distance is large enough, the maximum velocity is reached and the maximum acceleration pulse for the bang-coast-bang command occurs. For longer moves after this point, the transient deflection is no longer dependent on the acceleration pulse size, but varies as the slewing distance (the transient duration) is increased. This variation is due to the interference between the starting and stopping oscillations during the transient stage (more specifically, during the deceleration pulse of the bang-coast-bang command). As the slewing distance becomes large, however, the starting oscillation

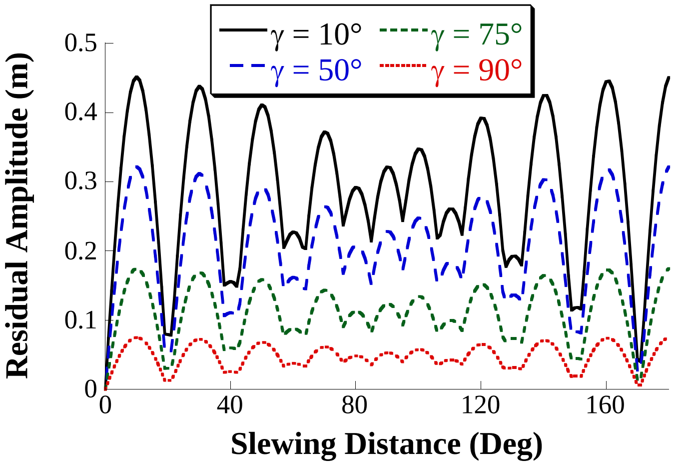

Figure 4.7: Residual Vibration Amplitude vs. Slewing Distance

comprises a larger portion of the transient stage than the oscillation resulting from the interference between the starting and stopping oscillations. As a result, the average transient deflection levels out to a nearly constant value for slew distances greater than 40°-50°.

The relationship between residual vibration amplitude and slewing distance is complex, as shown in Figure 4.7. After a 90° slew, the radial and tangential directions have exactly switched. As a result, the residual vibration amplitude is almost symmetrical about a slewing distance of 90°.

There are numerous peaks and troughs in the residual amplitude curves as the slewing distance varies. Although the slewing motion is nonlinear, the trends in the peaks and troughs can be explained by using a simple, linear second-order model. Assume that the input to such a system is two pulses in acceleration that form a bang-coast-bang command (trapezoidal velocity). Both acceleration pulses have the same magnitude, so they induce the same amount of oscillation. For a linear system, the magnitude of oscillation caused by each pulse is equal in magnitude and sometimes in phase and sometimes out of phase with each other. The amplitude of residual vibration will then contain peaks and troughs as it is plotted versus the move distance. In the nonlinear slewing motion, however, the swings produced by the

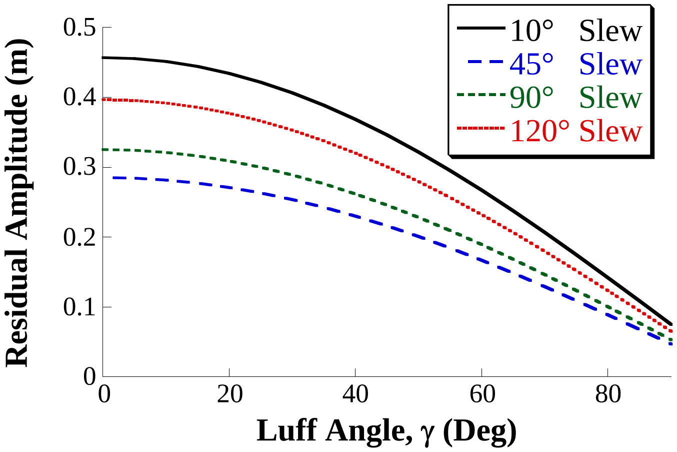

Figure 4.8: Residual Vibration Amplitude vs. Luff Angle

acceleration and deceleration are not quite equal in magnitude. The peaks in residual vibration amplitude arise when the responses from these two pulses are in phase and add up to produce more swing. The troughs occur when the two responses are out of phase and partially cancel each other, resulting in low residual swing. These two scenarios were demonstrated in Figure 4.2. Figure 4.7 shows how the contributions of these two scenarios alternate with slewing distance.

The relationship between residual vibration amplitude and luffing angle is similar to the relationship between transient deflection and luffing angle. Figure 4.8 shows how the residual vibration amplitude changes as a function of the luff angle. As the luff angle decreases, the end of the boom extends farther away from the base, and the residual vibration amplitude increases. When the payload is farther from the rotating base, it travels faster and covers a longer distance for a given change in slewing angle. The higher velocity requires higher tangential and centripetal forces, causing more swing. This relationship, however, is not linear. When the boom is pointing straight up, with a luff angle of 90°, the oscillation is at its smallest; however, it is not zero. This is because the center of slewing and luffing are a finite distance, x_{luff}, apart. Hence, there is a small amount of oscillation induced by slewing even when the boom is straight up.

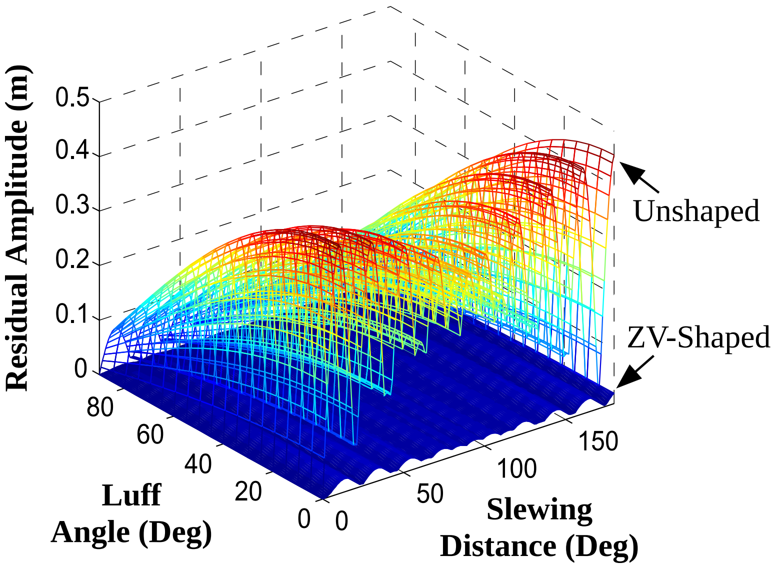

Figure 4.9: Slewing Residual Vibration Amplitude

An iterative simulation routine was performed to find the residual vibration amplitude for a representative subset of all possible slewing commands arising from the bang-coast-bang command that human operators often use. The slewing motion was simulated for distances between 0° and 180°, using constant luffing angles between 0° and 90°. The suspension cable length was kept constant at 1 m. Figure 4.9 shows the residual vibration amplitude for every move as a function of slewing distance and luffing angle. Note that cutting through the surface in Figure 4.9 along a line of constant luff angle would yield a curve similar to those shown in Figure 4.7.

To investigate the effectiveness of input shaping on controlling the oscillation induced by the nonlinear slewing motion, the same maneuvers were repeated, but the reference commands were convolved with a Zero Vibration (ZV) input shaper. The ZV input shaper was designed for a frequency of 0.5 Hz. The damping ratio was assumed to be zero. The solid surface in Figure 4.9 shows the residual vibration amplitude induced by ZV-shaped commands. The residual vibration amplitude from the trapezoidal velocity commands has been overlaid using a mesh. Figure 4.9 demonstrates the effectiveness of input shaping on this nonlinear slewing motion. The

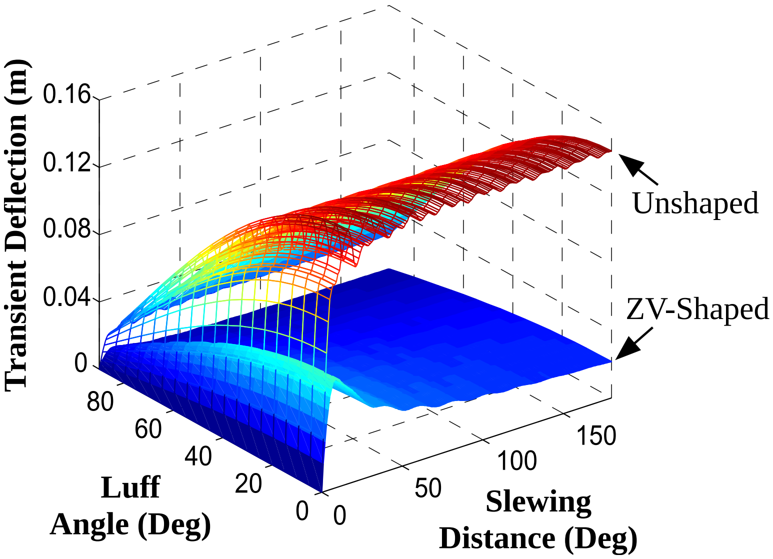

Figure 4.10: Slewing Transient Deflection

residual vibration amplitude was reduced for every slewing distance and luff angle. Over the entire space shown in Figure 4.9, input shaping reduced residual vibration by an average of 95%.

It is also of interest to analyze the transient deflection of the system during the motion. Figure 4.10 shows the unshaped and ZV-shaped average transient deflections. Note that cutting through the surface in Figure 4.10 along a line of constant luff angle would yield a curve similar to those shown in Figure 4.6. The shaped transient deflection is lower than the unshaped transient deflection by an average of 78%.

4.1.2 Effects of Varying the Velocity and Acceleration Limits

The velocity and acceleration limits used in these simulations are relatively low. These velocity and acceleration values, however, correspond reasonably well with those of real boom cranes. For higher velocities, nonlinear effects become more significant and the effectiveness of input shaping decreases. To demonstrate the effect of the velocity limit on the boom crane dynamics, Figure 4.11 shows the unshaped residual vibration amplitude for slewing distances between 0° and 90° for three different maximum velocities: 10°/s, 20°/s, and 30°/s. For each velocity limit, the acceleration and

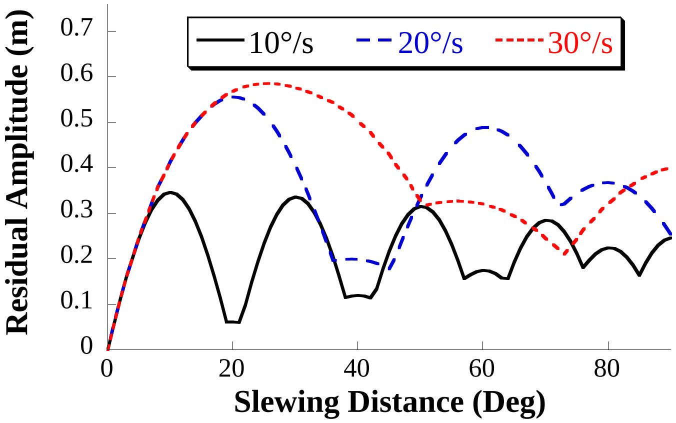

Figure 4.11: Residual Vibration Amplitude vs. Slewing Velocity

deceleration pulse sizes were set accordingly to keep the acceleration limit constant at 25°/s^2.

Increasing the maximum velocity has two effects: *i)* it increases the peak vibration amplitudes and *ii)* it changes the location of peaks and troughs. Even though the acceleration amplitude is held constant, increasing the maximum velocity requires that the crane be accelerated for a longer period of time. Therefore, the payload deflection induced during the acceleration and deceleration periods is larger. To explain the change in the location of the peaks and troughs, assume that the peaks are spaced a time Δt apart. This time is a function of the system period. As the velocity increases, the system can travel a longer distance in that time Δt. Hence, the peaks/troughs are spaced farther apart in move distance as the maximum velocity increases.

The acceleration limit also plays an important role in the dynamic response. Figure 4.12 shows the unshaped residual vibration amplitude for slewing distances between 0° and 90° for three different maximum accelerations: 12.5°/s^2, 25°/s^2, and 37.5°/s^2. For each acceleration limit, the acceleration and deceleration pulse sizes were set accordingly to keep the velocity limit constant at 10°/s. Increasing the acceleration limit increases the peak vibration amplitudes, but the increase is less

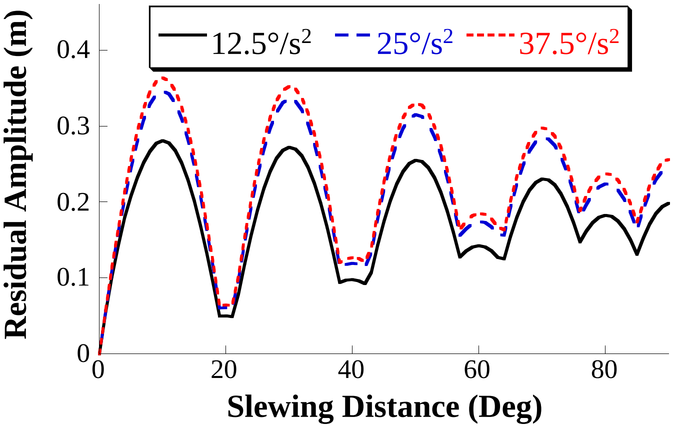

Figure 4.12: Residual Vibration Amplitude vs. Slewing Acceleration

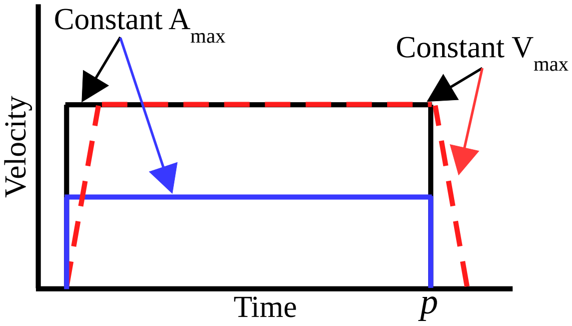

Figure 4.13: Velocity Profiles with Varying Motion Parameters

significant than the results shown in Figure 4.11. In addition, the peaks and troughs occur at approximately the same locations along the move-distance axis. This occurs because the velocity limit is constant, so the system travels approximately the same distance in a given period of the payload oscillation. Figure 4.13 demonstrates this concept. The distances traveled by the two velocity profiles with the same V_{max} (i.e., the area under the curves) are approximately equal. However, the distances traveled by the two velocity profiles with the same A_{max} are very different.

To determine the effectiveness of input shaping, a ZV shaper was designed for the 1 m cable length used in all of these simulations. The ZV-shaped commands reduced the residual vibration amplitude by an average of 95%, 89%, and 83% for velocities of 10°/s, 20°/s, and 30°/s, respectively. The effectiveness of input shaping decreases with increasing maximum velocity; however, shaping still significantly reduces the residual

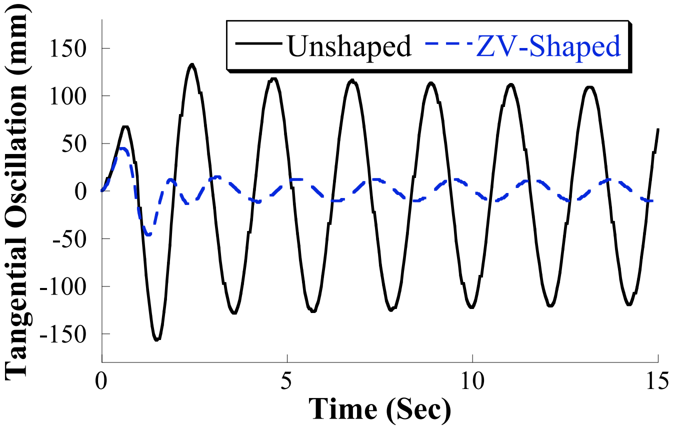

Figure 4.14: Experimental Slewing Response

vibration. The ZV-shaped commands reduced the residual vibration amplitude by an average of approximately 95% for all three acceleration limits tested. Therefore, increasing the acceleration limit does not have a significant effect on the effectiveness of input shaping.

4.1.3 Experimental Evaluation

Experiments were performed to verify the slewing dynamics and the effectiveness of ZV input shaping on boom cranes. The reference command used to drive the crane was a bang-coast-bang acceleration command. As an initial test of input shaping, the crane discussed in Chapter 2 was slewed 5°. Figure 4.14 shows the tangential swing caused by unshaped and ZV-shaped trapezoidal velocity commands. The ZV shaper was designed for a suspension cable length of 1 m (frequency of 0.5 Hz). Besides the nonlinear rotation associated with the slewing motion, the slewing axis of the small-scale boom crane has other sources of nonlinearity such as backlash in the belt-drive system. Nonetheless, the ZV input shaper substantially reduced the payload swing, as predicted by the simulations.

To verify the alternating peaks and troughs in the residual oscillation amplitude as a function of slew distance, the crane was rotated through distances between 0° and 65°, in increments of 2.5°. The luffing angle and suspension cable length were

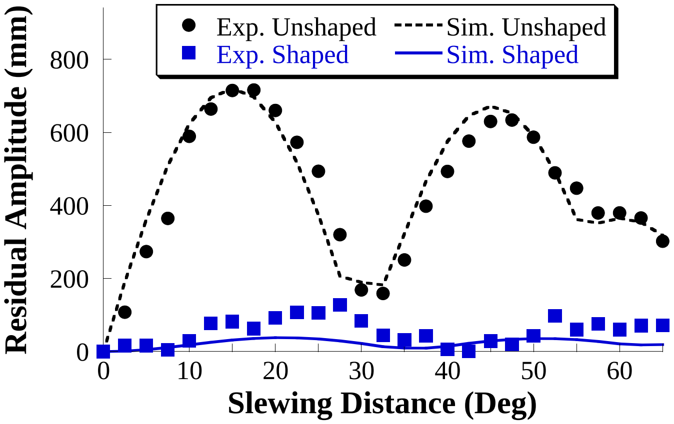

Figure 4.15: Experimental Slewing Residual Vibration Amplitude

held constant at 50° and 1 m, respectively. Figure 4.15 shows the experimental and simulated residual vibration amplitudes. The residual amplitude increases and decreases as the slewing distance is increased, similar to the results obtained through simulation. Figure 4.15 also shows the ZV-shaped residual vibration amplitudes for the same slewing distances. The ZV-shaped commands reduced the residual vibration amplitude by an average of 88%. Notice that this value is somewhat lower than the predicted percent reduction from simulation. The difference can be attributed to the nonlinearities discussed earlier. Nonetheless, the simulated and experimental results are very consistent with one another.

4.2 Luffing

4.2.1 Numerical Analysis

Luffing motion of the boom crane occurs when the boom rotates in a vertical plane. For the simulations discussed here, the maximum luffing velocity was limited to 6.7°/s and the maximum acceleration was limited to 83.3°/s^2.

The boom rotation moves the payload in two directions simultaneously, in the radial and vertical directions. The vertical motion of the payload is typically achieved via a hoisting actuation in most cranes. The same is true in boom cranes; however, the payload can also be lifted by simply luffing. Therefore, to maintain a constant

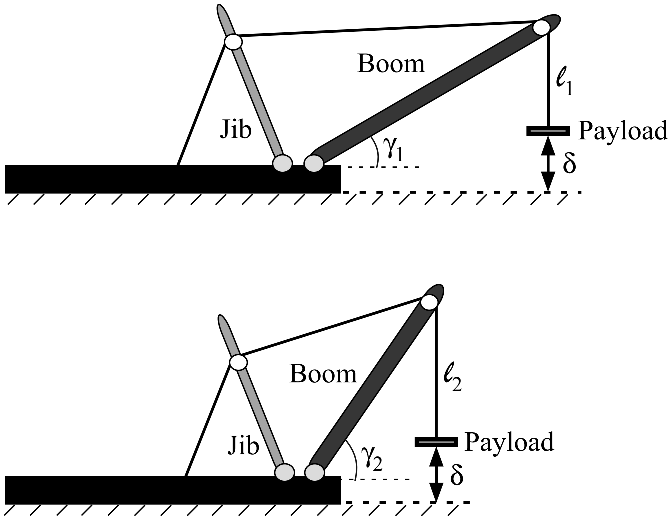

Figure 4.16: Level Luffing

payload distance from the ground when luffing, boom cranes must employ a technique called level luffing, illustrated in Figure 4.16. For level luffing, the suspension length, ℓ, changes in coordination with the luffing angle, γ, in order to keep the payload at the same height, δ, above ground. The model used here can raise and lower the boom both with and without level luffing.

Unlike the slewing motion, luffing results only in oscillation in the radial direction (assuming zero initial conditions). For example, the boom was luffed upward from an initial angle of 30° to a final angle of 60°. The slewing angle was set to zero, and the suspension cable length was kept constant at 1 m (no level luffing). Figure 4.17 shows the radial payload oscillation. The stopping oscillation is in phase with the starting oscillation, thereby increasing the residual vibration amplitude above the transient level. After the transient stage, the payload simply swings back and forth with approximately 13 cm peak-to-peak residual swing. The residual vibration amplitude caused by luffing motions is generally smaller than those produced by slewing commands because some portion of the acceleration is in the vertical direction. This vertical acceleration does not induce pendulum swing like horizontal accelerations.

The luffing dynamics are complicated because the magnitude of payload oscillation

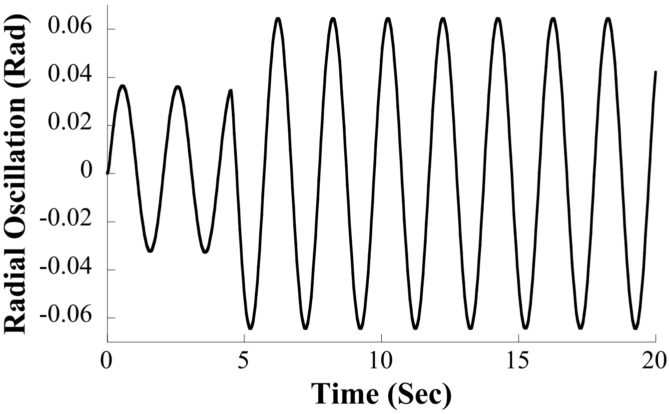

Figure 4.17: Radial Payload Oscillation for an Upward Luff from 30° to 60°

caused by a specific move distance is dependent on both the initial and final luff angles. The direction of motion, upward or downward, can also be significant because the effect of gravity changes. When luffing upward, the payload is moving against the gravitational force; however, when luffing downward, the payload is moving along with gravity. The changes in the net applied forces not only change the oscillation amplitude, but also the oscillation frequency during accelerations [25]. However, this only becomes significant if the luffing acceleration is a substantial fraction of the gravitational acceleration.

Figure 4.18 shows the relationship between average transient deflection and luffing distance for upward luffing from four different initial luff angles, $\gamma(0) = [5°, 20°, 50°, 75°]$. All of the curves do not span the entire Luffing-Distance axis because the luffing angle was limited to between 0° and 90°. For example, if the initial luff angle is 75°, then the maximum allowable upward luffing distance is only 15°, as shown by the dotted line in Figure 4.18.

The amount of transient deflection depends on the size of the acceleration pulse and the duration of the transient stage. For small luffing distances, the width of the acceleration pulse increases with luffing distance. However, once the maximum velocity is reached, the width of the acceleration pulse stops increasing. After this point,

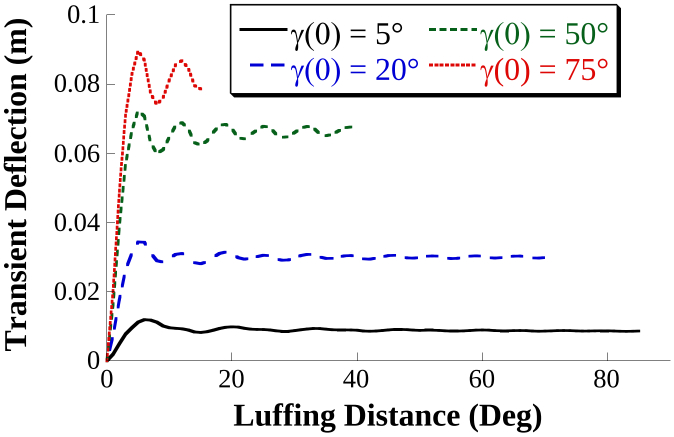

Figure 4.18: Average Transient Deflection vs. Luffing Distance

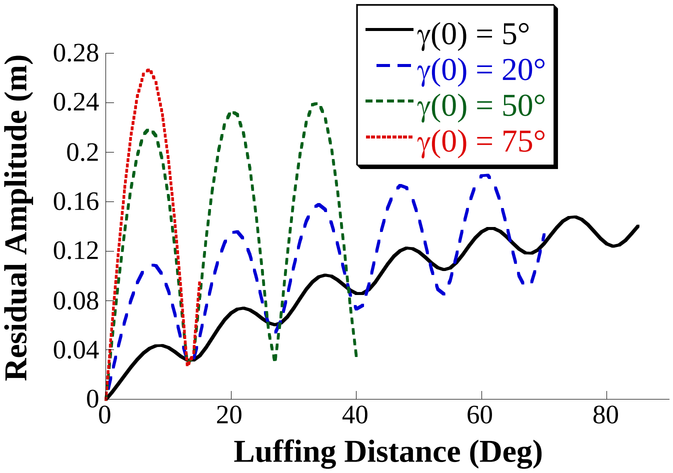

Figure 4.19: Residual Vibration Amplitude vs. Luffing Distance

the transient deflection is no longer dependent on the acceleration pulse size, but still varies as the luffing distance (the transient duration) is increased. This variation is due to the interference between the starting and stopping oscillations during the transient stage. As the luffing distance becomes large, however, the starting oscillation comprises a larger portion of the transient stage than the oscillation resulting from the interference between the starting and stopping oscillations. As a result, the average transient deflection levels out.

Figure 4.19 shows the relationship between residual vibration amplitude and luffing distance for upward motion from four different initial luff angles. As explained

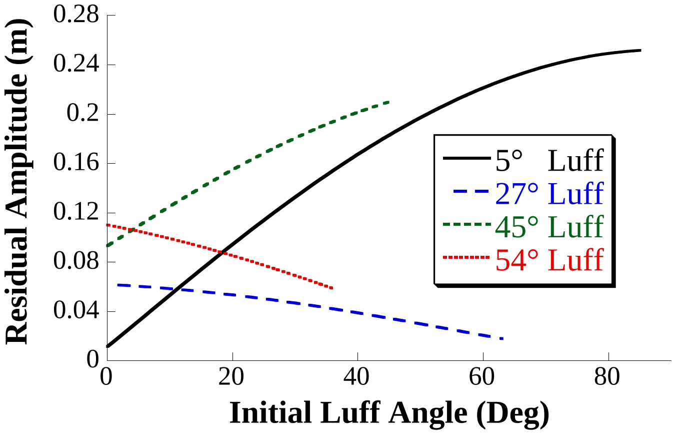

Figure 4.20: Residual Vibration Amplitude vs. Initial Luff Angle

before, the peaks and troughs are created when the starting and stopping oscillations align in phase to create the peaks and occur out of phase to create the troughs.

Figure 4.20 shows the relationship between residual vibration amplitude and initial luff angle for upward luffing. For certain luffing distances, for example 5° and 45°, larger initial luff angles lead to larger residual vibration. This occurs because for small initial luff angles, the boom is mainly in the horizontal plane. In this configuration, the starting motion is mostly vertical and does not contribute significantly to the radial swing of the payload. For large initial luff angles, the starting motion has a larger component in the radial direction and, therefore, results in larger radial payload oscillation. However, for some luffing distances, such as 27° and 54°, the residual vibration amplitude decreases for increasing initial luff angle. These luffing distances correspond to the troughs of Figure 4.19. For these luffing distances, the starting and stopping oscillations are out of phase. At higher initial luff angles, the oscillation induced by the stopping force is able to cancel more of the oscillation induced by the starting force, leading to lower residual vibration.

Luffing downward produces similar relationships to those during upward luffing. For equal luffing distances, luffing upward and downward will produce approximately the same magnitude of residual vibration if the initial and final luff angles are reversed.

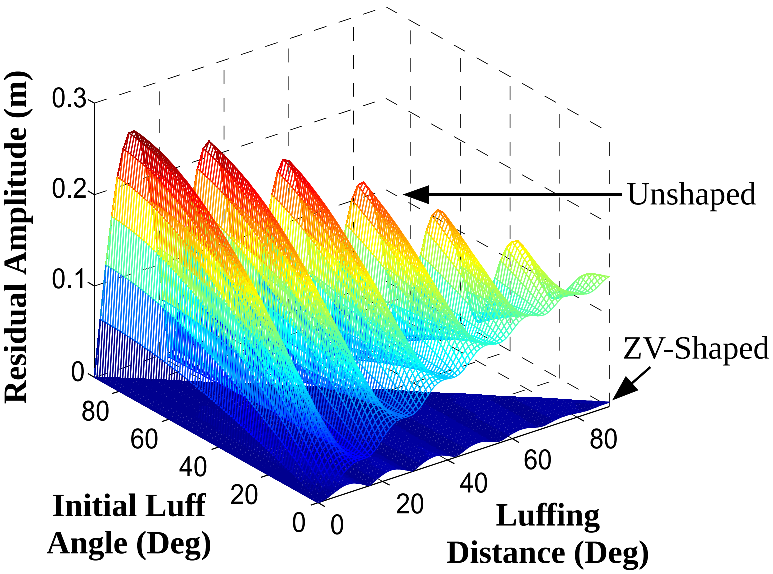

Figure 4.21: Upward Luffing Residual Vibration Amplitude

For example, luffing from an initial angle of 45° to a final luffing angle of 65° produces 0.2208 m of residual vibration. Luffing downward from an initial luffing angle of 65° to a final luffing angle of 45° produces 0.2210 m of residual vibration. The transient deflections of the two scenarios, on the other hand, are different because the amount of transient deflection depends heavily on the initial luff angle.

Iterative simulation routines were carried out for the luffing motion to further investigate the relationship between the oscillation (transient and residual), move distance, and initial luff angle. The suspension cable length was set to 1 m and the initial luff angle and luffing distance were varied between 0° and 90°. Figure 4.21 shows the residual vibration amplitude from upward luffing for unshaped and ZV-shaped commands. The ZV input shaper was designed for a frequency of 0.5 Hz. Input shaping reduced residual vibration by an average of 97% and reduced the transient deflection by an average of 62%.

4.2.2 Effects of Varying the Velocity and Acceleration Limits

Figure 4.22 shows the unshaped residual vibration amplitude for luffing distances between 0° and 80° for three different maximum velocities: 6.7°/s, 13.3°/s, and 20°/s.

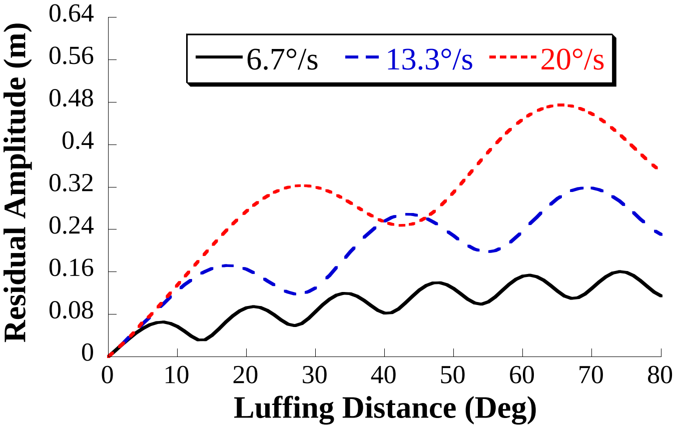

Figure 4.22: Residual Vibration Amplitude vs. Luffing Velocity

The initial luff angle was held constant at 10°. For each velocity limit, the acceleration and deceleration pulse sizes were set accordingly to keep the acceleration limit constant at 83.3°/s^2. Similar to the results of varying the maximum slewing velocity, increasing the maximum luffing velocity has two effects: *i)* it increases the peak vibration amplitudes and *ii)* it changes the location of peaks and troughs.

To determine the effectiveness of input shaping, a ZV shaper was designed for the 1 m cable length used in these simulations. Figure 4.23 shows the percent residual oscillation of the payload resulting from dividing the swing amplitude induced by ZV-shaped commands by the swing amplitude induced by unshaped commands. The ZV-shaped commands reduced the residual vibration amplitude by an average of 95%, 90%, and 85% for velocities of 6.7°/s, 13.3°/s, and 20°/s, respectively. The effectiveness of input shaping decreases with increasing maximum velocity; however, shaping still significantly reduces the residual vibration.

The same analysis was repeated for increasing the maximum luffing acceleration limit. The maximum velocity was held constant at 6.7°/s and three different maximum accelerations were tested: 41.7°/s^2, 83.3°/s^2, and 125°/s^2. The ZV-shaped commands reduced the residual vibration amplitude by an average of approximately 95% for all three acceleration limits tested.

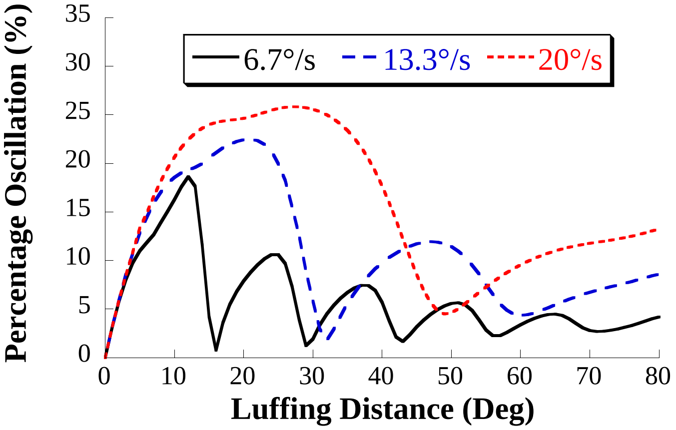

Figure 4.23: Shaped Residual Vibration vs. Luffing Velocity

4.3 Level Luffing

4.3.1 Numerical Analysis

The analysis in Section 4.2 assumed that the luffing motion does not induce a change in the length of the suspension cable length. Because many boom cranes utilize level luffing, it is of interest to analyze how the dynamics change when level luffing is used. During this investigation, the payload was maintained 20 cm above "ground" during the luffing motion. For example, if the initial luff angle was 30° and the boom was luffed upward 60°, then the suspension cable length would change from 0.725 m to 1.65 m. This change in suspension cable length allows the payload to remain at the same vertical level. Figure 4.24 shows the radial payload oscillation for luffing from 30° to 90°, while keeping the payload 20 cm above ground.

The change in cable length has two effects on the transient deflection: *i)* it changes the frequency and *ii)* it changes the swing amplitude. At the start, the suspension cable length is short, so the frequency of oscillation is high. As the suspension cable length increases to accomplish the level-luffing, the frequency is lowered. The decrease in amplitude is a result of the nonlinear dynamics of the crane. Hoisting up and down can either increase or decrease the vibration amplitude [3,12]. In the level-luffing case shown above, the hoisting motion, which occurs simultaneously with luffing, decreased

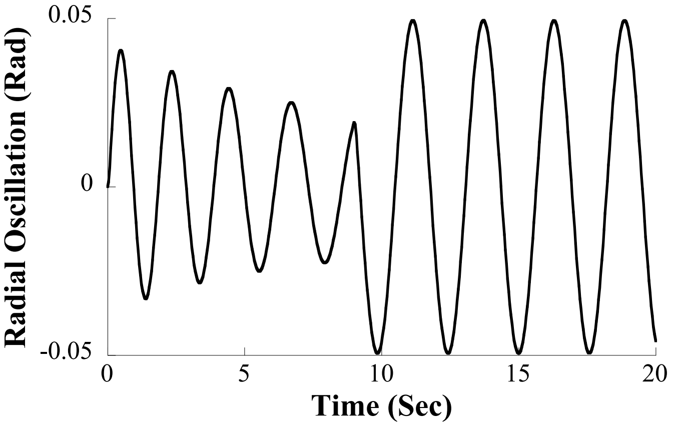

Figure 4.24: Radial Payload Oscillation for Level Luffing from 30° to 90°

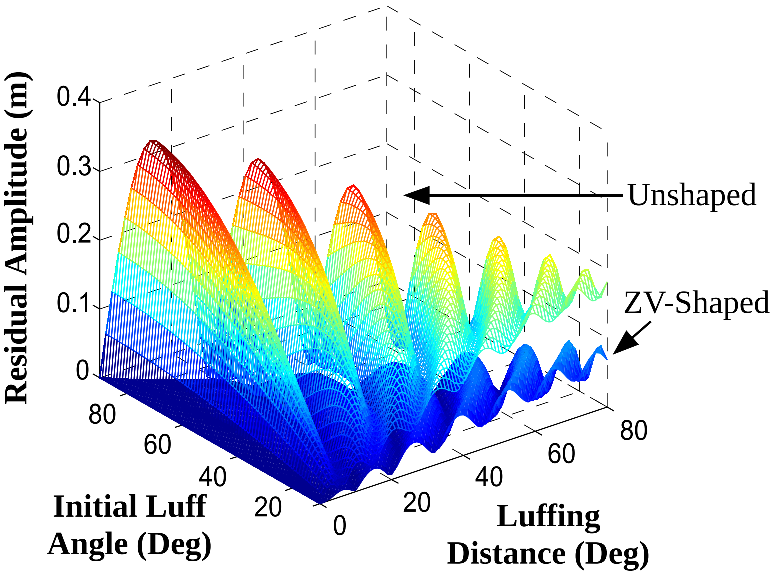

Figure 4.25: Upward Level Luffing Residual Vibration Amplitude

the oscillation amplitude.

Figure 4.25 shows the maximum residual vibration amplitude over a range of conditions when the payload is kept 20 cm above ground during level luffing. The results are a warped version of those for the non-level-luffing case in Figure 4.21. The warping effect is due to the change in the natural frequency induced by the change in the suspension cable length associated with level luffing. The residual vibration amplitude varies in an oscillatory manner; however, this pattern is more complex. This is because the cancellation or addition of the oscillations caused by the starting and stopping accelerations now depends not only on the move distance, but also on the varying frequency of the oscillation.

Input shaping requires little knowledge of the system being controlled. However, it does require a reasonable estimate of the natural frequency of the system. During level-luffing operations, the natural frequency varies. ZV shapers are not very robust to modeling errors; therefore, the ZV shapers used here were designed for the average natural frequency of each motion. For example, for luffing from 30° (0.725 m) to 90° (1.65 m), the ZV shaper was designed for the average frequency of 0.49 Hz. The residual vibration amplitude resulting from these ZV-shaped commands is also shown in Figure 4.25. The shaped commands reduced the residual vibration amplitude by an average of 83%. As expected, ZV shaping is less effective at reducing the residual vibration amplitude when there is a time-varying oscillation frequency during level luffing. However, it still provides substantial vibration reduction. The transient deflection was also investigated for level luffing. ZV shaping reduced the transient deflection by an average of 51%.

4.3.2 Experimental Evaluation

Experiments were performed to verify two important aspects of the simulation results: *i)* the effectiveness of input shaping at reducing the residual oscillation, and *ii)* the alternating peaks and troughs in the residual oscillation amplitude as a function of move distance. As an initial test of input shaping, the crane was luffed from an initial angle of 20° upward by 5°. Figure 4.26 shows the radial swing angle caused by both unshaped and ZV-shaped trapezoidal velocity commands. Input shaping substantially reduced the payload swing, as predicted by the simulations.

To verify the alternating peaks and troughs in the residual oscillation amplitude, the crane was luffed upward from an initial luffing angle of 20° for distances between 0° and 55°. At the initial state, the payload was 20 cm above the ground. The

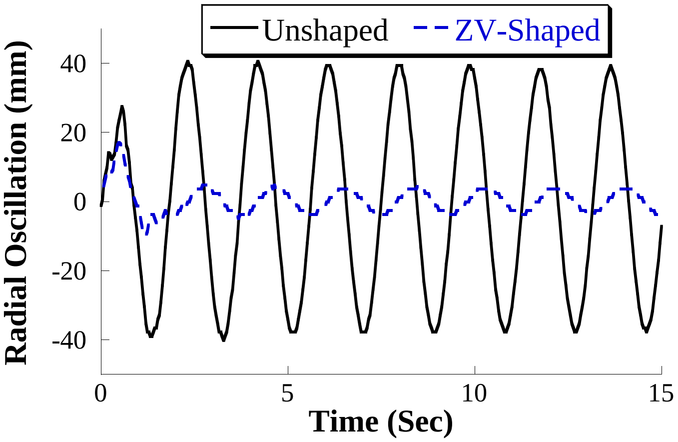

Figure 4.26: Experimental Luffing Response

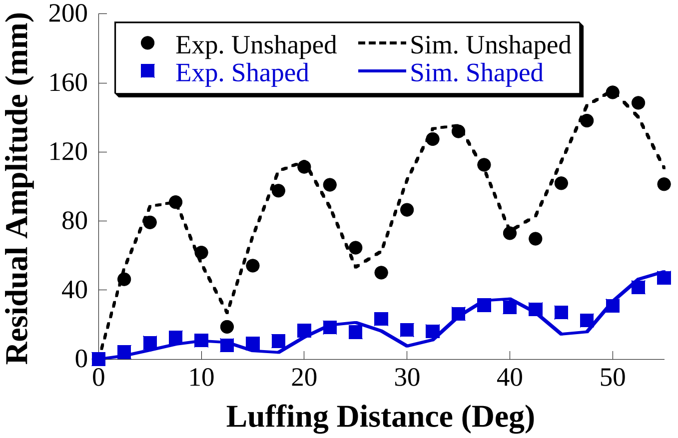

Figure 4.27: Experimental Upward Level Luffing Residual Vibration Amplitude

boom crane has a physical design that provides automatic level luffing as the boom is luffed. The level luffing is optimized to work best in the range of 40° to 70°. Outside of that range, the payload height above ground does not stay perfectly level. However, the suspension cable length does change to provide approximate height compensation. Figure 4.27 shows the experimental and simulated residual oscillation amplitudes. This figure represents a slice through Figure 4.25 at the point where the initial luff angle is 20°. Notice that the simulated results predict the experimental values very closely. The residual vibration amplitude increases and decreases as the luffing distance is increased, similar to the results obtained through simulation. Figure

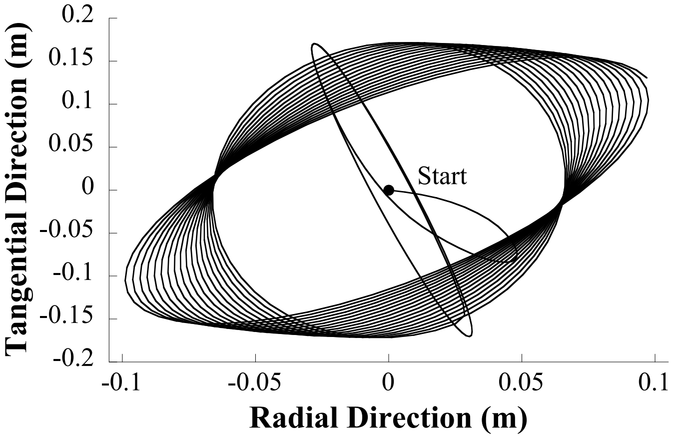

Figure 4.28: Payload Response to 10° Slew and 30° Luff

4.27 also shows the shaped residual vibration amplitude for the same luffing distances. The ZV input shapers were designed for the average natural frequency during the luffing motion. The ZV-shaped commands reduced the residual vibration amplitude by an average of 77%.

4.4 Combined Slewing and Luffing

The boom crane dynamics become even more complex when two rotations are performed simultaneously. Figure 4.28 shows the location of the payload relative to the overhead suspension point during an upward luffing from 45° to 75°, and a simultaneous 10° slewing. The suspension cable length was kept constant at 1 m. The payload motion during the transient stage is a complicated function of the radial, tangential, and centripetal accelerations caused by the slewing and luffing commands. However, once the slewing and luffing commands are complete, the payload moves in symmetric loops, similar to those caused by slewing commands alone.

In order to analyze the effectiveness of input shaping on the combined luffing and slewing motions, both unshaped and ZV-shaped commands were used to drive the boom crane model for luffing distances between 0° and 55°, from an initial luff angle of 35°, and slewing distances between 0° and 90°. Figure 4.29 shows the residual vibration amplitude as a function of slewing and luffing distances. There are varia-

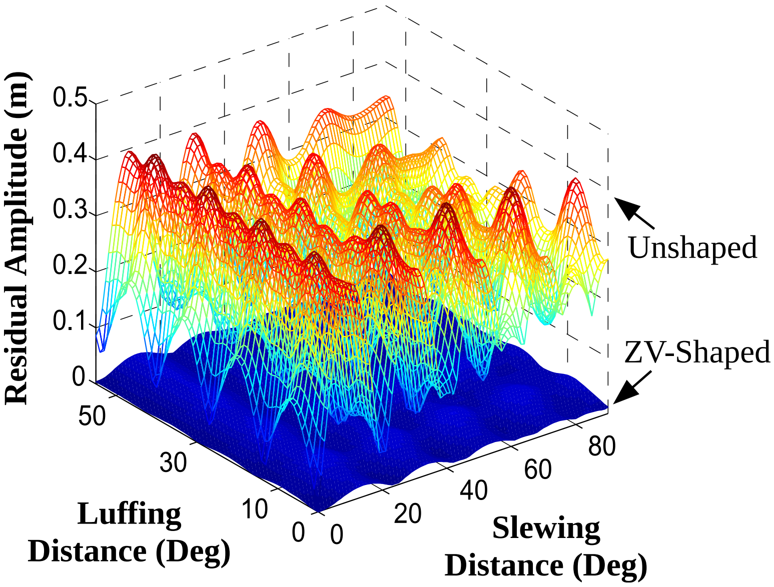

Figure 4.29: Luffing and Slewing Residual Vibration Amplitude

tions in the residual vibration amplitude with respect to changes in luffing distance. However, there are much larger variations in the residual vibration amplitude with respect to slewing distance. As seen in the previous data, slewing commands produce larger residual vibration and are responsible for the majority of the residual vibration amplitude. Even given the complicated dynamics of multiple-axis motion, ZV-shaping is still able to substantially reduce the residual vibration amplitude for all combinations of slewing and luffing commands. For the parameter space shown in Figure 4.29, input shaping reduced residual vibration by an average of 93%.

Figure 4.30 shows the unshaped and shaped average transient deflection for slewing and upward luffing. There are oscillatory variations as the luffing and slewing distances are varied. However, as the slewing and luffing distances become large, these variations begin to level out. The ZV-shaped commands reduced the transient deflection by an average of 76%.

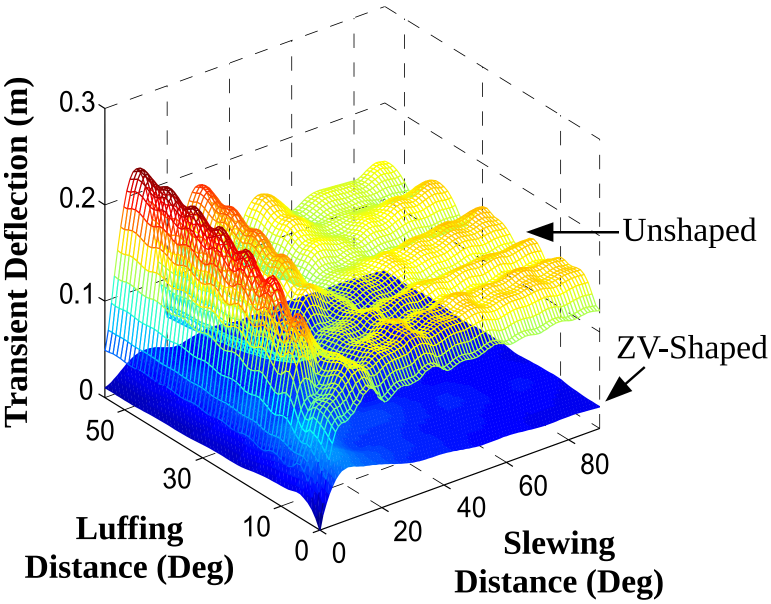

Figure 4.30: Luffing and Slewing Transient Deflection

4.5 Mobile Base Motion

4.5.1 Numerical Analysis

Figure 4.31 shows four possible paths of the mobile boom crane for a 1 m driving motion. For a steering angle of zero, the boom crane moves in a straight line. For nonzero steering angles, the crane follows a curved path whose arc length is the 1-m move distance.

Figure 4.32 shows the simulated payload response induced by a 1 m straight-line motion of the base. The oscillation induced by driving in a straight line depends on the driving distance, velocity, and acceleration. To investigate these relationships, the mobile base was driven for distances between 0 m and 2 m with three different driving velocities [v = 0.15 m/s, 0.35 m/s, and 0.55 m/s]. The acceleration and suspension cable length were held constant at 0.7 m/s^2 and 1 m, respectively. Figure 4.33 shows the residual vibration amplitudes predicted by these simulations.

As the driving distance varies, the oscillation caused by the starting and stopping accelerations are sometimes in phase, thereby causing the peaks shown in Figure 4.33.

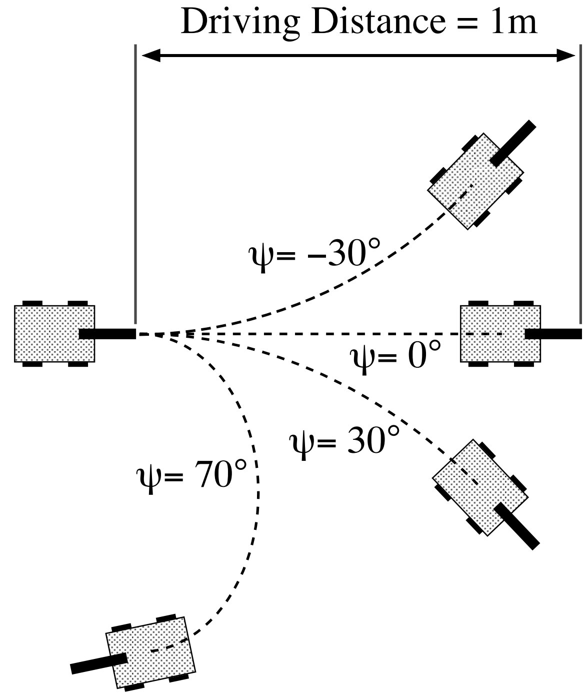

Figure 4.31: Driving Parameters

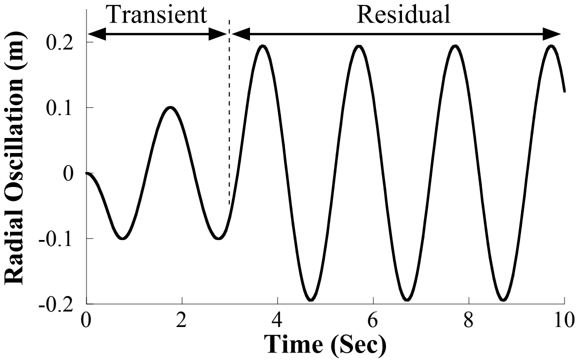

Figure 4.32: Radial Oscillation for Driving Straight 1 m

Sometimes the oscillations are out of phase, thereby causing near-zero residual vibration amplitude. Increasing the velocity has two effects on the residual vibration: *i)* it increases the maximum vibration amplitude, and *ii)* it causes the peaks/troughs to be spaced farther apart along the driving distance axis. Even though the acceleration amplitude is held constant, increasing the maximum velocity requires that the crane be accelerated for a longer period of time. Therefore, the payload deflection induced during the acceleration and deceleration periods is larger. The peaks/troughs occur

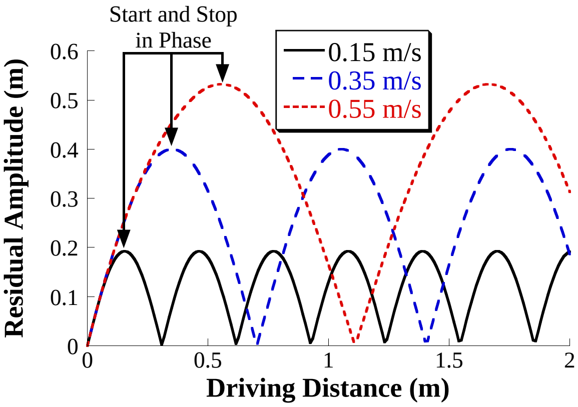

Figure 4.33: Residual Vibration Amplitude vs. Straight-Line Driving for Various Velocities

periodically and are dependent on the oscillation period, which remains constant. For example, if the peaks/troughs occur a time Δt apart, then the system will travel a longer distance in that time Δt when it is moving at a higher velocity. Hence, the peaks/troughs are spaced farther apart in move distance as the maximum velocity increases. Increasing the acceleration (while the velocity is held constant) induces similar trends as those shown in Figure 4.33. The maximum vibration amplitude increases; however, the peaks/troughs will occur at approximately the same locations.

When the steering angle is a nonzero constant during the driving motion, the mobile base travels through a circular arc with an angular velocity, $\dot{\alpha}$, given by (2.16). To analyze the effect of the angular velocity of the mobile base, the steering angle was varied (while the driving velocity was held constant at 0.35 m/s). Figure 4.34 shows the maximum residual vibration amplitude for driving distances between 0 m and 2 m for various steering angles.

As the steering angle increases, the mobile base rotates faster, causing higher centripetal accelerations. For example, a steering angle of 70° produces a rotation rate of the mobile base that is approximately 60°/s. Higher accelerations increase the residual vibration amplitude. In addition, the higher mobile base rotation rates produce more nonlinear effects. The troughs of the curves in Figure 4.34 are not as

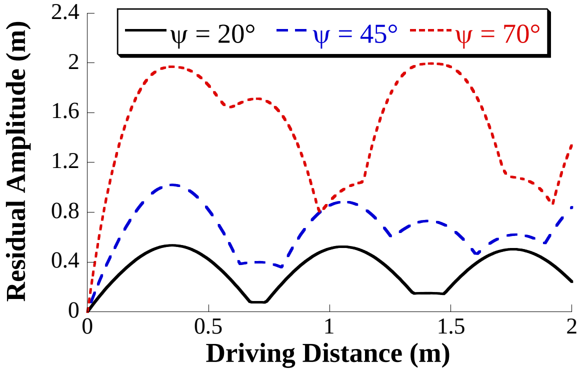

Figure 4.34: Residual Vibration Amplitude vs. Driving Distance for Various Steering Angles

close to zero as the curves in Figure 4.33. In fact, as the steering angle increases, the troughs in Figure 4.34 move farther away from zero. This is a result of the increased nonlinear effects. Because the base rotates, the starting and stopping forces are not applied in the same direction (unless the base goes through a 360° rotation). In addition, during the rotational motion of the base, the frequencies in the radial and tangential directions are slightly different [36]. When the rotational velocity increases, the gap between the two frequencies also increases. As a result, the starting and stopping oscillations in the radial and tangential directions are not in-phase and out-of-phase simultaneously. Therefore, the residual amplitude is not reduced completely to zero at the troughs.

Figure 4.35 shows the average transient deflection for driving distances between 0 m and 2 m for various steering angles [$\psi = 0°$, 20°, 45°, and 70°]. When the crane moves straight forward ($\psi = 0°$), the amount of transient deflection depends on the size of the acceleration pulse and the duration of the transient stage. For small driving distances, the width of the acceleration pulse increases with driving distance. However, once the maximum velocity is reached, the width of the acceleration pulse stops increasing. After this point, the transient deflection is no longer dependent on the acceleration pulse size, but still varies somewhat with the driving distance. These

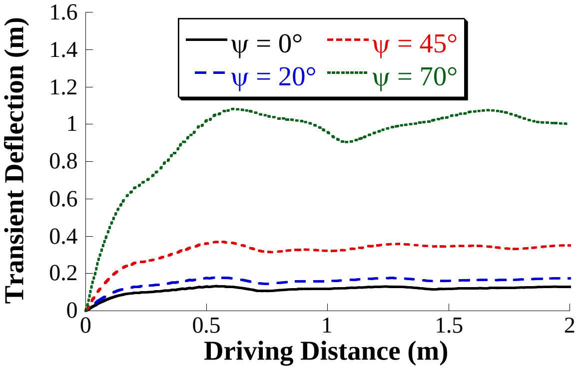

Figure 4.35: Average Transient Deflection vs. Driving Distance for Various Steering Angles

small variations are due to the interference between the starting and stopping oscillations during the transient stage (more specifically, during the deceleration pulse of the bang-coast-bang command). As the driving distance becomes large, however, the starting oscillation comprises a larger portion of the transient stage than the oscillation resulting from the interference between the starting and stopping oscillations. As a result, the average transient deflection levels out as driving distance increases.

The same type of transient dynamics occur in the nonzero steering angle cases shown in Figure 4.35 as well. However, the magnitude of the transient deflection increases with increasing steering angle (i.e., increasing angular velocity). Although not demonstrated in Figure 4.35, the transient deflection also increases with increasing linear velocity similar to the residual vibration amplitude results shown in Figure 4.33.

The dynamic effects presented in this section can be placed into two categories. Driving the mobile base in a straight line induces payload oscillations that vary greatly with motion parameters (i.e., driving distance, driving velocity, etc.). Turning of the mobile base induces larger payload swings and more nonlinear effects. Both of these dynamic effects make it very challenging for human operators to accurately control mobile boom cranes.

To control the payload oscillation caused by driving motions, ZV input shaping was implemented. The ZV shaper was designed for the frequency of a pendulum with

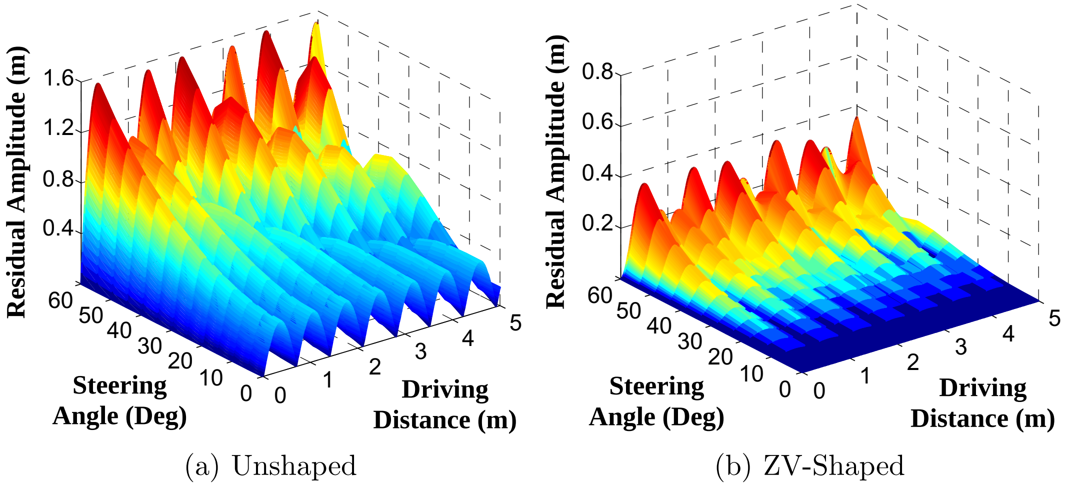

(a) Unshaped (b) ZV-Shaped

Figure 4.36: Residual Vibration Amplitude Induced by Base Motion

a 1 m length. It was assumed that the damping ratio of the system was zero. First, the effectiveness of input shaping on straight-line driving motions was analyzed. Because driving in a straight line induces a response that is approximately linear, increasing the velocity does not impact the effectiveness of input shaping. In fact, ZV-shaped commands reduced the residual vibration amplitude for all three velocities shown in Figure 4.33 by approximately 99.9%. However, as the angular velocity of the mobile base is increased (by increasing the steering angle), the nonlinear effects increase, thereby, degrading the effectiveness of this simple input shaper. For example, for a steering angle of 70°, ZV input shaping reduced the residual vibration by an average of only 62%.

An exhaustive iteration routine was performed for a large range of driving motions. Figure 4.36 shows the maximum residual vibration amplitude for driving distances from 0 m to 5 m and for steering angles from 0° to 60°. Note that the scale on the vertical axis of the unshaped plot, Figure 4.36(a), is two times larger than on the ZV-shaped plot, Figure 4.36(b). As expected, for higher steering angles, the rotation rate of the mobile base increases significantly and the ZV shaper loses some effectiveness.

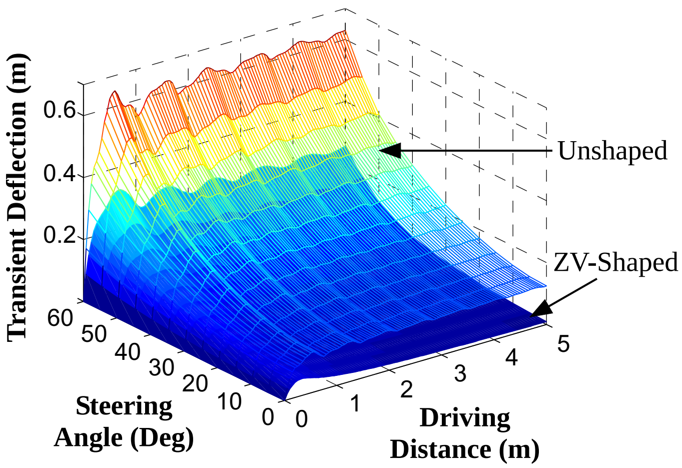

Figure 4.37: Transient Deflection Induced by Base Motion

However, the steering angle of most vehicles, including the mobile base of the small-scale boom crane used for the experiments in this thesis, is generally limited to a range of approximately -45° to 45°. Even with the extreme steering angles included (angles between 0° and 60°), ZV-shaped commands reduced the maximum residual vibration amplitude by an average of 89%.

Figure 4.37 shows the average transient deflection for the same motions. The ZV-shaped data is shown by a solid surface and the unshaped data is overlaid in a mesh. The ZV-shaped commands reduced the transient deflection by an average of 68% over the parameter area shown in the figure.

4.5.2 Experimental Evaluation

Experiments were performed to verify the dynamic phenomenon induced by motion of the mobile base, as well as the effectiveness of input shaping. The mobile base of the small-scale boom crane was driven in a straight line for distances between 10 cm and 200 cm, in increments of 10 cm. Figure 4.38(a) shows the experimental and simulated residual vibration amplitudes induced by trapezoidal and ZV-shaped driving commands. This figure represents a slice through Figure 4.36 where the steering angle, ψ, is zero. The simulated ZV-shaped vibration amplitudes are virtually zero,

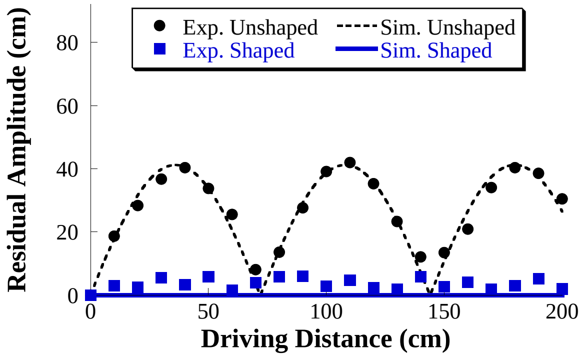

(a) ψ=0°

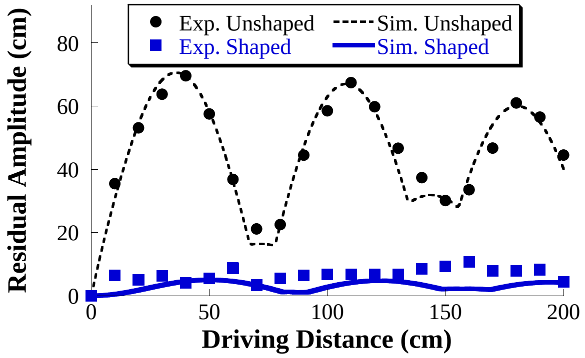

(b) ψ=30°

Figure 4.38: Experimental Driving Residual Vibration Amplitude

but the experimental ZV-shaped vibration amplitudes are slightly larger (with an average of 3.7 cm). This difference results from the nonlinearities of the experimental setup. Nonetheless, the simulated and experimental results match well.

Similar to the simulation results, the unshaped driving residual vibration amplitude contains peaks and troughs as the driving distance is varied. The ZV-shaped commands, however, are much less dependent on the driving distance, as they reduce the residual vibration amplitude to near zero for all move distances. The ZV-shaped commands reduced the residual vibration amplitude by an average of 87%.

Figure 4.38(b) shows the experimental and simulated residual vibration amplitudes induced when the steering angle is 30°. The driving distance was again varied between 10 cm and 200 cm. This figure represents a slice through Figure 4.36 where the steering angle, ψ, is 30°. Increasing the steering angle had two main effects: *i)* it increased the maximum residual amplitude, and *ii)* it increased the nonlinear effects. The increased nonlinear effects correlate to the troughs of the curves in Figure 4.38(b) moving farther away from zero. The shaped commands again significantly reduced the residual vibration amplitude by an average of 85%.

4.6 Summary

Boom cranes exhibit nonlinear dynamic behavior because they have multiple rotational axes that cause the payload to experience radial, tangential, and centripetal accelerations. The complex dynamic responses were investigated for a wide range of slewing, luffing, and driving motions. The major contributions of this chapter are:

- The residual oscillation amplitude was shown to depend on the crane configuration (i.e., the luff angle), the move distance, and the velocity and acceleration limits.
- The oscillation amplitude varies in a periodic manner as the move distance increases. This variation in the residual vibration occurs because the vibration caused by the stopping deceleration can be either in phase or out of phase with the vibration induced by the initial acceleration.
- Even on such a complex, nonlinear crane, input-shaping control was successful in reducing the residual oscillation. Numerous simulations and experiments on a small-scale boom crane verified the effectiveness of input shaping. Input shaping reduced the residual oscillation by 83% or greater in simulations and 77% or greater in experiments.
- Increasing the velocity and acceleration limits not only increased the induced payload swing, but also increased the nonlinear effects. The increased nonlinear effects somewhat decreased the effectiveness of ZV input shaping.

CHAPTER V

DOUBLE-PENDULUM MOBILE BOOM CRANE DYNAMICS AND CONTROL

Double-pendulum dynamics occur in an important subset of crane applications that arise in many material-handling processes. Double pendulums make the dynamics of cranes much more complex because they add an additional flexible mode to the system that is at a higher frequency than the corresponding single-pendulum swing. Unlike single-pendulum cranes, the vibration frequencies of a double pendulum depend not only on the suspension cable length, but also on the rigging cable length and the masses of the hook and payload [11]. Because these parameters will vary from one crane operation task to another, any controller designed for such systems needs to be robust enough to suppress two time-varying oscillation modes that vary nonlinearly.

The goal of this chapter is to characterize the nonlinear swing dynamics and to design a robust input shaper that can eliminate residual vibration across a large range of double-pendulum dynamics. This challenge contains competing objectives: *i)* robustness to changes in the two vibration modes and *ii)* a fast response. There are many input shapers that have robustness to varying system parameters [75]; however, their robustness comes at a cost of increased shaper duration. The longer the shaper, the slower the response of the system.

The baseline reference motion command used in this investigation is a trapezoidal/triangular velocity profile. The components of the system response analyzed are the transient deflection and the residual vibration. The major diameter of the ellipse that encloses the oscillation during the transient stage is referred to as the transient deflection. The major diameter of the ellipse that encloses the oscillation

Table 5.1: Double-Pendulum Simulation Parameters

	ℓ_h (m)	ℓ_p (m)	m_h (kg)	m_p (kg)
Figure 5.1	1	0.5	0.63	2
Figure 5.2	1	1	0.63	0.25

during the residual stage is referred to as the residual vibration amplitude.

The next section presents analysis of the dynamics of boom cranes with double-pendulum payloads. Important parameters, such as payload mass and suspension and rigging cable lengths, are varied and their effects on the dynamic behavior are documented and explained. Section 5.2 describes the process for designing robust input shaping, followed by operator experiments in Section 5.3. Then, numerical and experimental verification of input shaping are presented in Sections 5.4 and 5.5, respectively. Finally, Section 5.6 presents the effects of varying the velocity and acceleration limits.

5.1 Double-Pendulum Dynamics

Before designing vibration control for a specific application, it is important to determine what frequencies cause problematic oscillations. For a double-pendulum boom crane, the important effect to determine is when the second mode is significant enough to necessitate control action. To demonstrate this effect, the double-pendulum boom crane model was slewed using the parameters shown in the top row of Table 5.1. These parameters produce first and second-mode frequencies of f_1=0.42 Hz and f_2=1.71 Hz, respectively. The crane was driven with a trapezoidal velocity command that induced a 5° slew. The solid line in Figure 5.1 shows the tangential payload oscillation resulting from this test. Figure 5.1 also shows the payload responses from two types of input-shaped commands. The first-mode shaper is a ZV shaper designed to suppress the first-mode frequency. The second-mode shaper is a ZV shaper designed to suppress the second-mode frequency. The first-mode shaper substantially reduces the

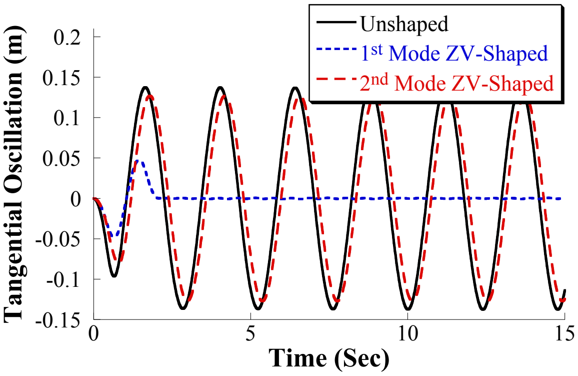

Figure 5.1: Tangential Payload Oscillation [f_1 = 0.42 Hz, f_2 = 1.71 Hz]

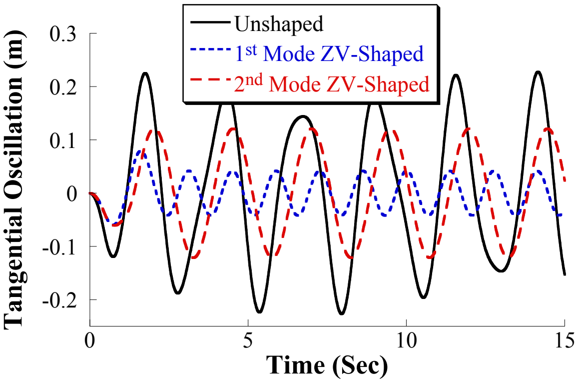

Figure 5.2: Tangential Payload Oscillation [f_1 = 0.40 Hz, f_2 = 0.73 Hz]

residual oscillation (98% reduction), but the second-mode shaper is much less effective (only 8% reduction). These results occur because the contribution of the second mode is small compared to the contribution of the first mode.

If the suspension and rigging cables have similar lengths and the payload mass is small relative to the hook mass, then the second mode can have a significant contribution to the overall oscillation [57]. Second-mode oscillation is also important for cranes moving payloads with large distributed masses [37]. To demonstrate important second-mode effects, the parameters in the second row of Table 5.1 were used. These parameters result in first and second-mode frequencies of f_1=0.40 Hz and f_2=0.73 Hz, respectively. Figure 5.2 shows the tangential payload oscillation for the same slewing motion shown in Figure 5.1. Notice that the tangential oscillation is larger in this case. Two ZV shapers, each designed for one of the two frequencies, were once again applied to the slewing motion. The first-mode shaper is less effective (82% reduction from the total oscillation) at reducing the residual oscillation than in the case shown in Figure 5.1. However, the second-mode shaper is more effective (47% reduction) than in the case shown in Figure 5.1. This indicates that the contribution of the second mode is significant under these conditions.

The goal of this chapter is to understand the complex oscillation dynamics so that input shapers can be designed to robustly eliminate the residual vibration for all realistic values of the crane and payload parameters. These include the cases when the second-mode effects become significant. Therefore, a robust two-mode shaper is designed in the next section.

5.2 Input Shaper Design

The first step in designing a robust input shaper for double-pendulum payloads is to determine the effect of all the varying parameters on the oscillation frequencies. Because there are four different parameters (suspension cable length, rigging cable length, payload mass, and hook mass) that can be varied, it is important to determine how each parameter affects the oscillation frequencies. The frequencies arising from changes in these parameters were obtained using the linearized frequency equations given in Chapter 2.

The second step is to determine what type of input shaper should be used. For example, assume that there is a simple application that requires the suspension cable length to vary from 20 cm to 200 cm. Figure 5.3 shows the first- and second-mode frequencies resulting from this suspension cable range. This application requires a shaper that can suppress frequencies in the range from 0.34 Hz to 0.79 Hz for the low mode and 1.15 Hz to 1.58 for the high mode. Although it is possible to derive a Zero Vibration and Derivative (ZVD) or Extra Insensitive (EI) shaper for each

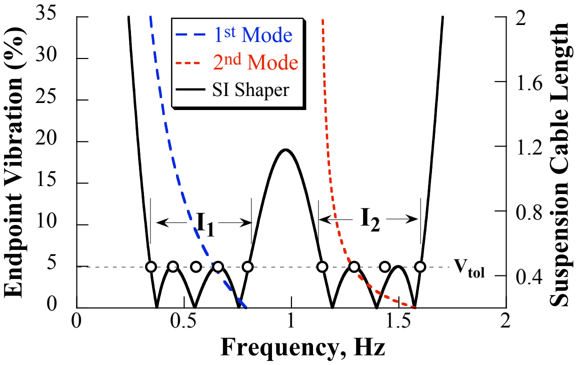

Figure 5.3: Two-Mode SI Shaper Design Process

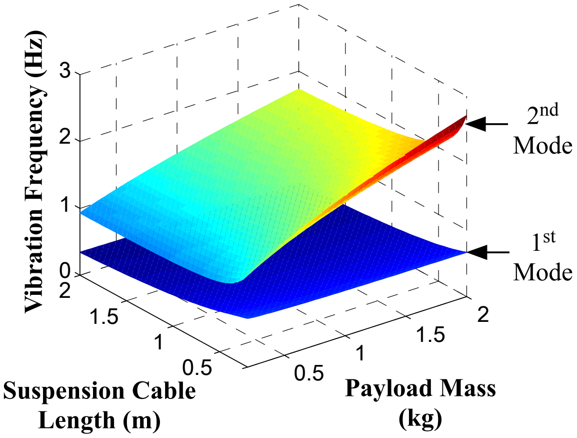

Figure 5.4: Oscillation Frequency vs. Suspension Cable Length and Payload Mass

range with adequate robustness, the Specified Insensitivity (SI) shaper provides the optimal combination of robustness and short shaper duration. The design constraints of a two-mode SI shaper are overlaid on the frequency variations in Figure 5.3. Two frequency suppression ranges, I_1 and I_2, and the tolerable vibration, V_{tol}, over the two ranges are shown in Figure 5.3.

This input-shaping design process was applied to the small-scale boom crane. Figure 5.4 shows the variation in the first and second modes as a function of the suspension cable length and the payload mass. The suspension cable length was varied from 0.20 m to 2 m and the payload mass was varied from 0.2 kg to 2 kg. The

Table 5.2: First and Second Mode Frequency Variations

	Set 1	Set 2
ℓ_h (m)	0.2 - 2	1
ℓ_p (m)	0.4	0.1 - 2
m_h (kg)	0.63	0.63
m_p (kg)	0.2 - 2	0.2 - 2
1^{st} Mode (Hz)	0.33 - 0.73	0.30 - 0.49
2^{nd} Mode (Hz)	0.93 - 2.71	0.62 - 3.34

rigging cable length was fixed at 0.4 m. Short suspension cable lengths are uncommon in crane applications; therefore, suspension cable lengths smaller than 0.2 m are not examined. The second mode clearly undergoes a larger variation than the first mode. The frequency range for each mode resulting from these parameters is listed under "Set 1" in Table 5.2.

The variation in the first and second modes as a function of the rigging cable length and the payload mass was also analyzed. The rigging cable length was varied from 0.1 m to 2 m and the payload mass was again varied from 0.2 kg to 2 kg. The suspension cable length was held constant at 1 m. The results are very similar to Figure 5.4. The second mode rapidly increases with very short rigging cable lengths. For short rigging cable lengths, however, the payload is effectively a single pendulum, and the high mode no longer produces a significant oscillation amplitude [37, 57]. Therefore, short rigging cable lengths (less than 0.1 m) are not examined. The frequency range for each mode resulting from these parameters is listed under "Set 2" in Table 5.2.

Based on this analysis, the range of frequency suppression was chosen to be from 0.3 Hz to 0.7 Hz for the low mode and from 1 Hz to 1.9 Hz for the high mode. The tolerable vibration percentage was chosen to be 5% for the low mode and 10% for the high mode. The impulse amplitudes (A_i) and times (t_i) of the SI shaper meeting these design requirements is:

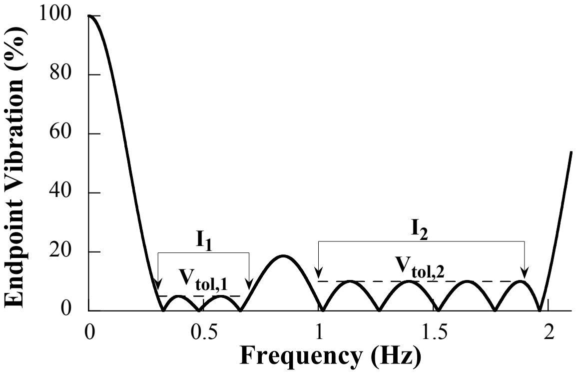

Figure 5.5: Two-Mode SI Shaper Sensitivity Curve

$$\begin{bmatrix} A_i \\ t_i \end{bmatrix} = \begin{bmatrix} 0.0842 & 0.0696 & 0.124 & 0.155 & 0.135 & 0.155 & 0.124 & 0.0696 & 0.0842 \\ 0 & 0.452 & 0.913 & 1.33 & 1.78 & 2.23 & 2.64 & 3.10 & 3.56 \end{bmatrix} \tag{5.1}$$

Figure 5.5 shows the sensitivity curve for the two-mode SI shaper in (5.1). For the frequency range from 0.3-0.7 Hz, the percentage residual vibration (PRV) is below the desired 5% and for the range from 1-1.9 Hz, the PRV is below the desired 10%. This shaper-design procedure can be generalized as [73]:

1. Estimate the range of payloads that the crane will move. (The maximum capacity of the crane can be used.)
2. Estimate the possible ranges of the rigging and suspension cable lengths.
3. Determine the possible frequency ranges for the low and high modes.
4. Set a tolerable vibration percentage, V_{tol}, for each mode.
5. Use numerical optimization to obtain the shaper.

5.3 Example Operator Experiments

As a test of the effectiveness of the input shaper given by (5.1), the payload-maneuvering operation shown in Figure 5.6 was completed by a human operator. The task was to move the payload from its initial position, shown on the left side of Figure 5.6, to its

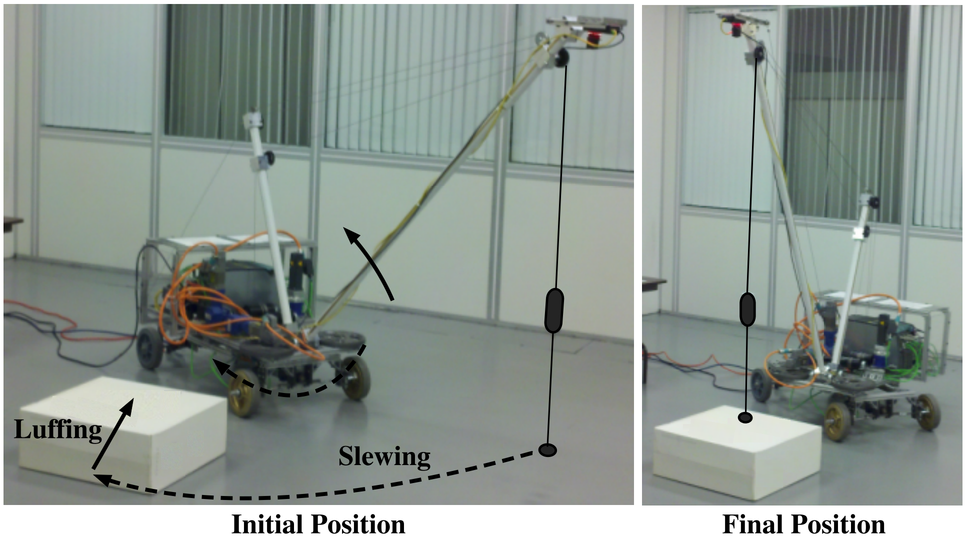

Figure 5.6: Payload-Maneuvering Operation

final position on top of the white box, as shown on the right side of Figure 5.6. To complete the task, the operator had to slew the base and luff the boom upward. The operator issued velocity commands using a wireless pendent and was free to select the order and durations of the inputs. The operator repeated the task several times, with unshaped and SI-shaped commands.

Figure 5.7 shows the results from one of the operator trials. Note that the oscillation shown is the hook oscillation. The unshaped commands induce large oscillations that make completing the task very difficult. The shaped commands, however, drastically reduce the oscillation. The maximum unshaped oscillation is approximately 62 cm, while the maximum shaped oscillation is only about 8 cm.

Figure 5.8 shows another trial from the same operator. The maximum unshaped oscillation is 46 cm, which is smaller than that shown in Figure 5.7. The oscillation induced from unshaped commands is heavily dependent on the inputs from the operator. Hence, even the same operator performing the same task can produce varying results, as illustrated by the results in Figures 5.7 and 5.8. The shaped results, on

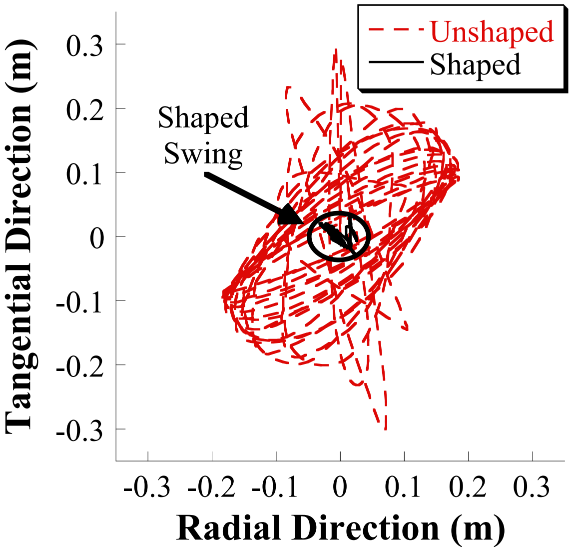

Figure 5.7: Hook Oscillation Resulting from Operator Maneuvers (Trial 1)

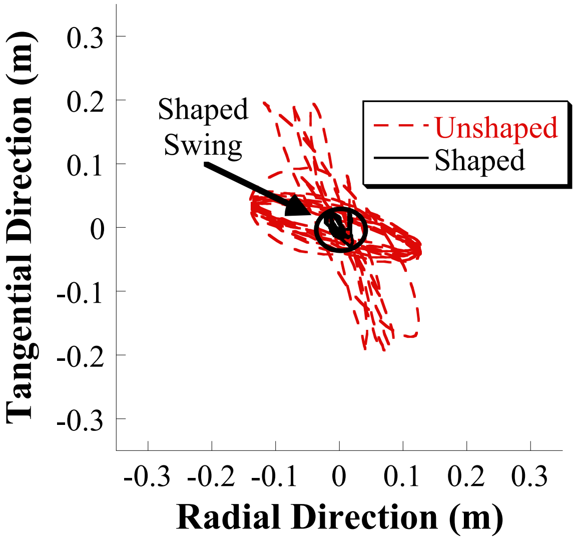

Figure 5.8: Hook Oscillation Resulting from Operator Maneuvers (Trial 2)

the other hand, are very consistent between the trials. The maximum shaped oscillation is only about 7 cm for the case shown in Figure 5.8. The following section presents detailed analysis of a large range of possible slewing and luffing motions and double-pendulum dynamics.

Table 5.3: Velocity and Acceleration Limits

	Velocity Limit (°/s)	Acceleration Limit (°/s^2)
Slewing (Sim.)	10	25
Slewing (Exp.)	15	37.5
Luffing (Sim. and Exp.)	6.67	83.33

5.4 Numerical Input Shaper Verification

Simulations using the double-pendulum model were performed to analyze the performance of input shaping for a variety of parameters and motions. The baseline maximum velocities and accelerations are shown in Table 5.3. These baseline values are used in the following two sections. Then, Section 5.6 demonstrates the effects of varying these motion parameters.

5.4.1 Luffing

The luffing motion is particularly challenging with double-pendulum payloads because, in many boom cranes, a change in the luffing angle produces a change in the suspension cable length. This level-luffing technique for double-pendulum conditions is illustrated in Figure 5.9. The suspension cable length (ℓ_h) changes in conjunction with luff angle changes (γ) to keep the payload the same height (δ) above the ground.

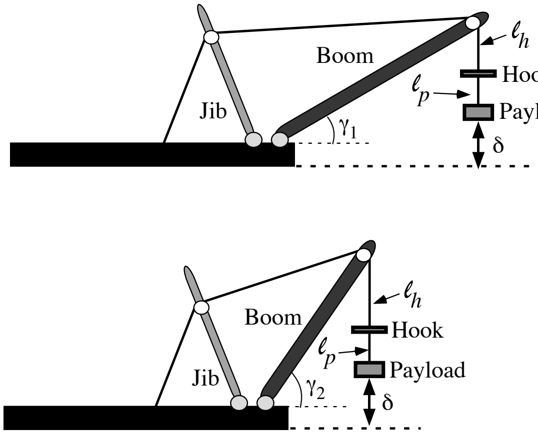

Figure 5.9: Level Luffing with Double-Pendulum Payload

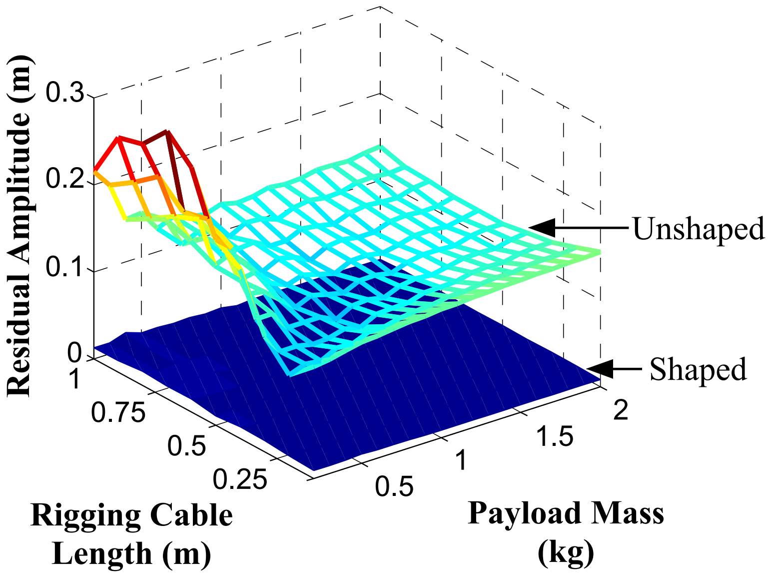

Figure 5.10: Level Luffing Residual Vibration Amplitude vs. Payload Mass and Rigging Cable Length [$\gamma(0) = 35°$, $\gamma_{dist} = 45°$, $m_h = 0.63$ kg]

In the simulations reported here, level luffing was used to keep the payload directly above the ground. Ground is represented by the location of the tip of the boom when the luffing angle is 0°. The initial luffing angle, $\gamma(0)$, and the luffing distance, γ_{dist}, were held constant at 35° and 45°, respectively. The rigging cable length was varied from 0.1 m to 1 m and the payload mass was varied from 0.2 kg to 2 kg. The suspension cable length varied automatically with the rigging cable length to keep the payload at a constant vertical height. Figure 5.10 shows the maximum residual vibration amplitude from these simulations. For very small payload masses and suspension cable lengths close to the rigging cable length, the residual vibration amplitude increases dramatically, as shown on the left side of the plot. In this range of parameters, the contribution of the second mode is significant [57]. However, as the suspension cable length increases beyond the rigging cable length (while the payload mass remains constant), the dynamics approach those of a single-pendulum system. The solid surface labeled "Shaped" in Figure 5.10 indicates the residual vibration amplitude that resulted when the two-mode SI shaper was used. The two-mode SI

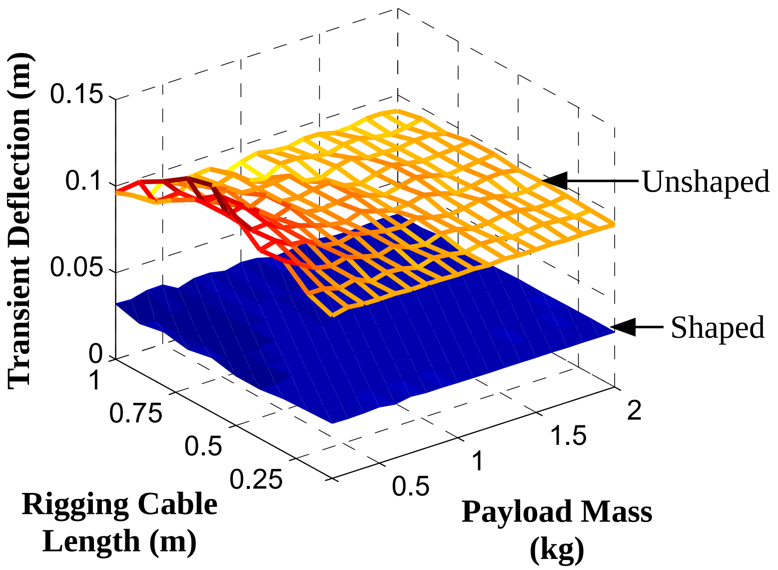

Figure 5.11: Level Luffing Transient Deflection vs. Payload Mass and Rigging Cable Length [$\gamma(0) = 35°$, $\gamma_{dist} = 45°$, $m_h = 0.63$ kg]

shaper was able to reduce the residual amplitude by an average of 93% over the range of parameters shown in Figure 5.10.

The maximum transient deflection induced by the same set of level-luffing motions is shown in Figure 5.11. The two-mode SI shaper reduced the maximum payload transient deflection from an average of 0.106 m down to 0.032 m, a 70% reduction.

5.4.2 Slewing

Simulations were also used to evaluate the dynamics and shaper performance during slewing motions. The luffing angle and the slewing distance, θ_{dist}, were held constant at 45° and 40°, respectively. The suspension cable length was set to 1 m. The 40° slewing motion was repeated for rigging cable length from 0.1 m to 2 m and payload masses from 0.1 kg to 2 kg. Figure 5.12 shows the maximum residual vibration amplitude for this parameter space. For rigging cable lengths close to the suspension cable length and small payload masses, the residual amplitude increases, as shown on the left side of the plot. Nonetheless, the two-mode SI shaper reduced the residual amplitude by an average of 96%. The maximum transient deflection induced by the

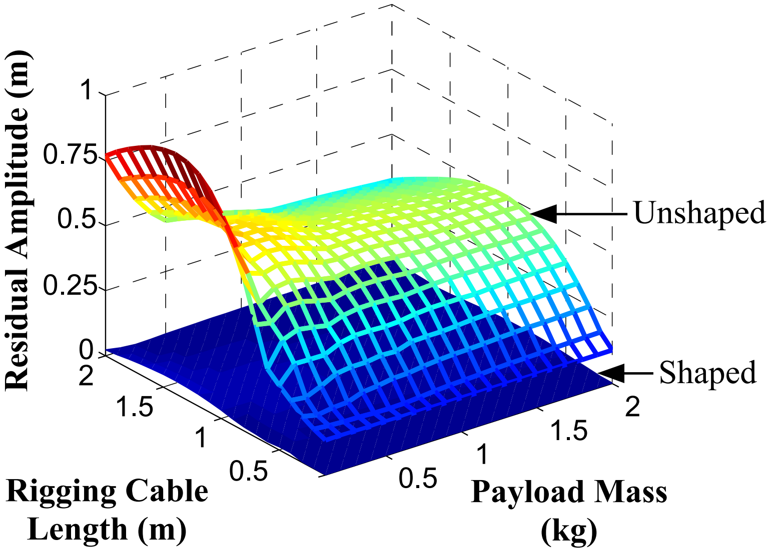

Figure 5.12: Residual Vibration Amplitude vs. Payload Mass and Rigging Cable Length [$\gamma = 45°$, $\theta_{dist} = 40°$, $\ell_h = 1$ m, $m_h = 0.63$ kg]

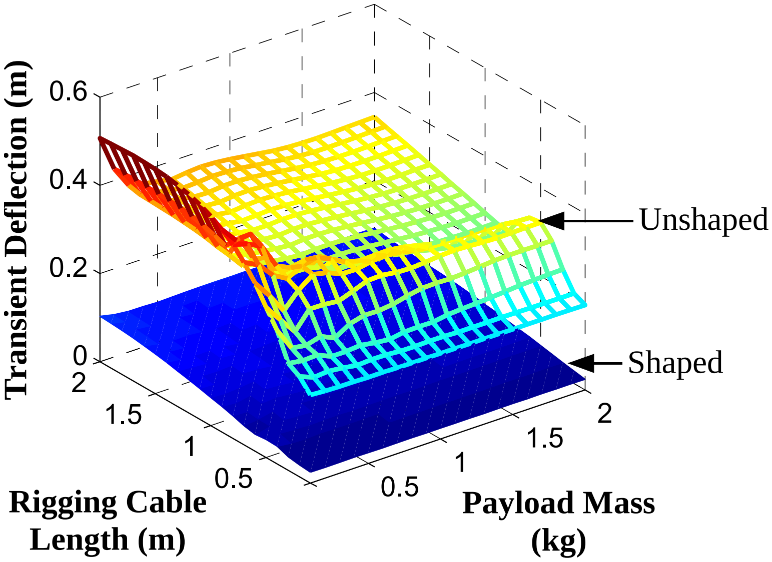

Figure 5.13: Transient Deflection vs. Payload Mass and Rigging Cable Length [$\gamma = 45°$, $\theta_{dist} = 40°$, $\ell_h = 1$ m, $m_h = 0.63$ kg]

same set of slewing motions is shown in Figure 5.13. The two-mode SI shaper reduced the maximum transient deflection by an average of 81%.

In order to test dependence on slewing distance and suspension cable length, the luffing angle was held constant at 45° and the rigging cable length and the payload

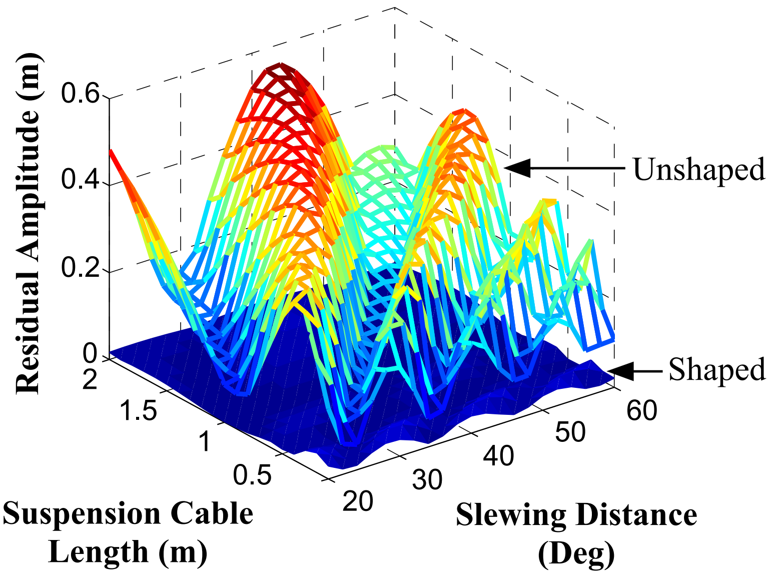

Figure 5.14: Residual Vibration Amplitude vs. Slewing Distance and Suspension Cable Length [$\gamma = 45°$, $\ell_p = 0.3$ m, $m_h = 0.63$ kg, $m_p = 0.2$ kg]

mass were set to 0.3 m and 0.2 kg, respectively. The crane was slewed for distances between 20° and 60°. For each slewing distance, the suspension cable length was varied from 0.1 m to 2 m. Figure 5.14 shows the maximum residual vibration amplitude for this parameter space. The unshaped residual amplitude increases and decreases as the slewing distance changes. This is a result of the interference between the oscillation induced by the acceleration and the oscillation induced by the deceleration [36]. However, the double pendulum makes the dynamics more complex. The two-mode SI shaper reduced the residual amplitude by an average of 95%. The SI shaper also reduced the maximum transient deflection by an average of 83%.

The results displayed in Figures 5.10-5.14 clearly demonstrate the complexity of the dynamic response. Furthermore, the results demonstrate that the two-mode SI shaper in (5.1) can significantly reduce the payload oscillation for a large range of double-pendulum payload dynamics and suspension cable lengths.

Table 5.4: Payload and Rigging Cable Parameters

Payload	m_p (g)	ℓ_p (cm)
A	200	30
B	870	various
C	320	15
D	630	30
E	200	various

5.5 *Experimental Input Shaper Verification*

The next two subsections present experimental responses from the boom crane that was shown in Figure 2.1. The baseline maximum velocities and accelerations were shown in Table 5.3. Two cameras, one at the tip of the boom and another camera placed to the side of the crane, were used to record the hook and payload oscillations.

Five different payloads were used in the experiments. Table 5.4 shows the parameters of these payloads and their rigging cables. These payloads were selected to test a large range of possible dynamics. Payloads A, B, and C were used for the luffing experiments: payload A is a light payload with a long rigging cable, payload B is a heavy payload that is used with rigging cables of various lengths during level-luffing operation, and payload C is a medium-weight payload with a short rigging cable. Payloads D and E were used for the slewing experiments: payload D is a heavy payload with a long rigging cable and payload E is a light payload that is used with various rigging cable lengths.

5.5.1 Luffing

The first set of experiments on the luffing motion investigated the effect of varying luffing distances. The suspension cable length was held constant at 80 cm and payload A was used. The boom was luffed upward from an initial luffing angle of 35° for distances between 5° and 40°. Figure 5.15 shows the payload displacement (with respect to the overhead suspension point) during the residual stage after a 40° luff.

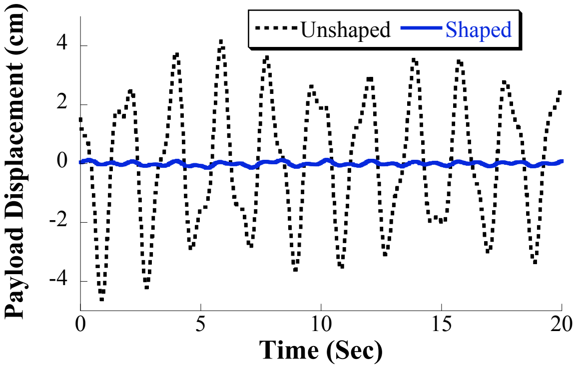

Figure 5.15: Experimental Residual Payload Displacement for 40° Luff

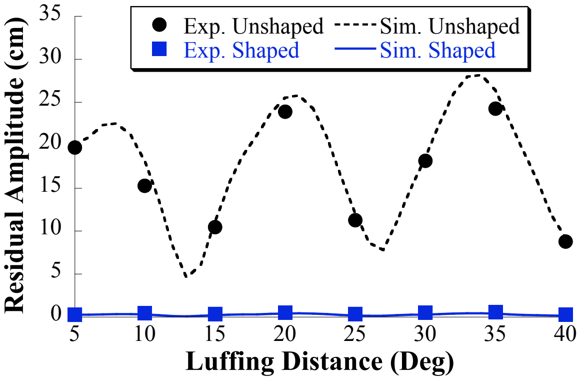

Figure 5.16: Residual Vibration Amplitude vs. Luffing Distance [$\gamma(0) = 35°$, $\ell_h = 0.8$ m, $m_h = 0.63$ kg, Payload A]

Time "0" in Figure 5.15 represents the start of the residual stage. The unshaped response is shown by the dashed line and the shaped response is shown as a solid line. The double-pendulum dynamics are clearly visible in the unshaped response, but the two-mode SI shaper dramatically decreased the residual vibration.

Figure 5.16 shows the experimental and simulated residual vibration amplitudes for various luffing distances. The unshaped residual amplitude varies as the luffing distance increases. On the other hand, the shaped results are essentially independent of the luffing distance because they are near zero for all cases. The two-mode SI shaper reduced the residual vibration amplitude by an average of 98%.

A second set of experiments utilized the level-luffing capabilities of the boom

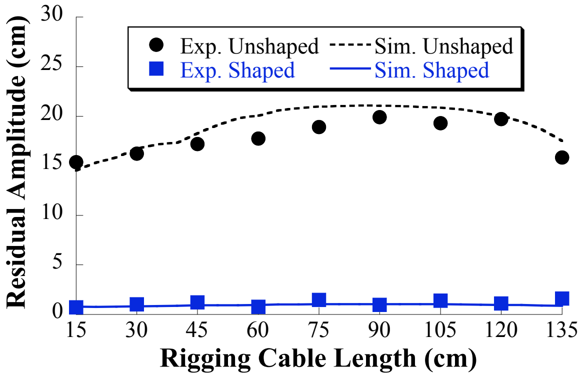

Figure 5.17: Residual Vibration Amplitude vs. Rigging Cable Length [$\gamma(0)$ = 50°, γ_{dist} = 20°, m_h = 0.63 kg, Payload B]

crane. The crane was configured to keep payload B directly above the ground. The rigging cable length was varied between 15 cm and 130 cm. The initial suspension cable length was adjusted according to the rigging cable length to place the payload directly above the ground. A luffing motion from an initial 50° luff angle to a final 70° luff angle was performed during all the tests. Figure 5.17 shows the experimental and simulated residual vibration amplitudes. The results of this figure are similar to a slice through the simulation results of Figure 5.10. The input shaper reduced the residual amplitude by an average of 93% over the range of suspension cable lengths and rigging cable lengths that were tested.

The final set of luffing experiments tested the effects of varying the suspension cable length. The boom crane was configured to move without level luffing, thereby keeping the suspension length constant during the motion. Payload C was used and the initial luff angle and luffing distance were held constant at 50° and 20°, respectively. The suspension cable length was varied from 20 cm to 140 cm. Figure 5.18 shows the resulting experimental and simulated residual vibration amplitudes. There is a local minimum in the unshaped data for a suspension cable length of 40 cm. This local minimum occurs because the starting and stopping oscillations caused by the acceleration and deceleration of the unshaped command were out of phase and

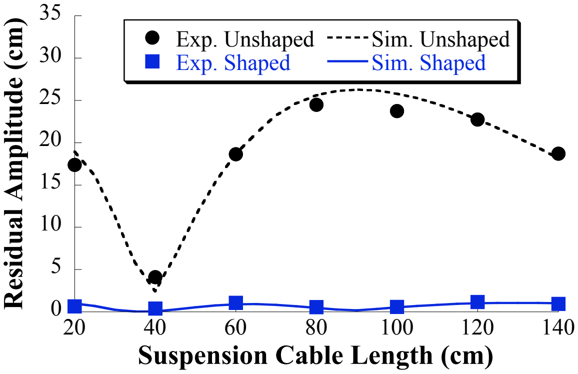

Figure 5.18: Residual Vibration Amplitude vs. Suspension Cable Length [$\gamma(0) = 50°$, $\gamma_{dist} = 20°$, $m_h = 0.63$ kg, Payload C]

partially canceled. The SI shaper was able to reduce the residual vibration amplitude by an average of 96% over the range of suspension cable lengths that were tested.

The large variety of luffing motions represented in Figures 5.16-5.18 demonstrate the complexity of the dynamic response and the effectiveness of the two-mode SI shaper over a large range of suspension cable lengths and double-pendulum parameters. Furthermore, the simulated and experimental results agree very well, even though the simulations neglect several nonlinear effects that are present in the actual crane.

5.5.2 Slewing

The first set of experiments on the slewing motion analyzed the effects of variation in the slewing distance. The luffing angle and suspension cable length were held constant at 60° and 80 cm, respectively. Payload D was used. The boom crane base was slewed for distances between 5° and 55°.

Figure 5.19 shows the experimental and simulated residual vibration amplitudes for various slewing distances. The results of this figure are similar to those presented in Figure 5.14. The unshaped residual amplitude varies as the slewing distance increases. Note that the residual vibration amplitude levels off between 30° and 35°, instead of decreasing to zero. The trough occurs because the starting and stopping

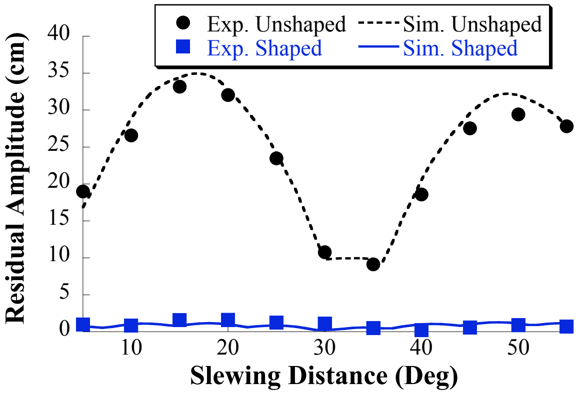

Figure 5.19: Residual Vibration Amplitude vs. Slewing Distance [$\gamma =$ 60°, ℓ_h = 0.8 m, m_h = 0.21 kg, Payload D]

oscillation induced by the acceleration and deceleration are out of phase; therefore, they partially cancel each other out. However, nonlinear effects of the slewing motion at the given velocity and acceleration limits are significant. As a result, the starting and stopping oscillation are not perfectly out of phase and do not have equal magnitudes. The shaped results are essentially independent of the slewing distance because they are near zero for all cases. The two-mode SI shaper reduced the residual vibration amplitude by an average of 96%.

Unlike the experimental luffing results, the experimental slewing results are given in terms of the hook residual amplitude, not payload residual amplitude. The slewing motion causes the payload to oscillate in two directions simultaneously. Therefore, the camera at the tip of the boom was used to record the hook oscillation.

The payload oscillation cannot be recorded with the overhead camera because the suspension cable, hook, and rigging cable obstruct the payload from the field-of-view of the camera. A single camera placed at the side of the boom crane would also be inadequate. To fully capture the oscillation caused by slewing, there would have to be two cameras placed at two sides of the crane. Even then, the camera data would have to be calibrated to account for the fact that the angle of the payload oscillation with respect to the camera changes for various slewing distances. These are just

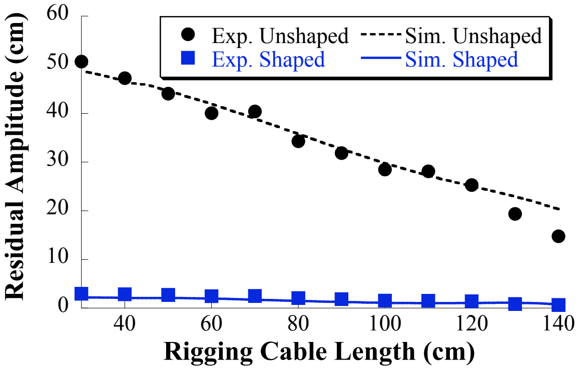

Figure 5.20: Residual Vibration Amplitude vs. Rigging Cable Length [γ = 60°, θ_{dist} = 20°, m_h = 0.21 kg, Payload E]

a few examples of the difficulties of recording the payload position. Therefore, the hook oscillation was recorded instead. Note that the payload oscillation was almost always larger than the hook oscillation reported. This result was confirmed through the numerical simulations performed in Section 5.4. The maximum hook deflection was always smaller than the maximum payload deflection.

A second set of experiments tested varying suspension cable and rigging cable lengths. Payload E was used and the luffing angle and slewing distance were held constant at 60° and 20°, respectively. The rigging cable length was varied from 30 cm to 140 cm. The suspension cable length was varied in order to keep the overall cable length (suspension cable length plus rigging cable length) constant at 170 cm. Figure 5.20 shows the resulting experimental and simulated residual vibration amplitudes. As the suspension cable length increases (rigging cable length decreases), the residual vibration amplitude also increases. This result is to be expected as longer cable lengths allow larger swing distances. However, the SI shaper was able to reduce the residual vibration amplitude by an average of 94% over the entire range of suspension cable and rigging cable lengths tested.

The large variety of slewing motions represented in Figures 5.19-5.20 demonstrate the complexity of the dynamic response and the effectiveness of the two-mode SI

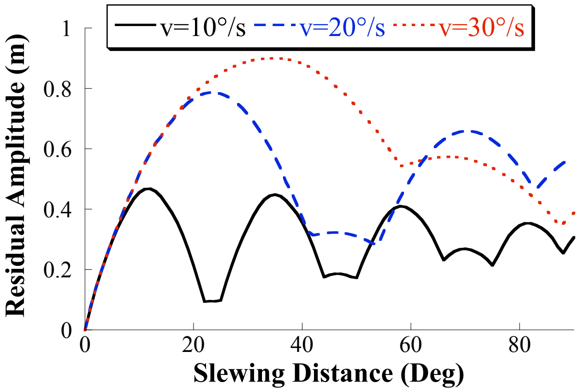

Figure 5.21: Residual Vibration Amplitude vs. Slewing Velocity

shaper over a large range of suspension cable lengths and double-pendulum parameters. Furthermore, the simulated and experimental results agree very well, even though the simulations neglect several nonlinear effects that are present in the actual crane.

5.6 *Effects of Varying the Velocity and Acceleration Limits*

To this point, all simulations and experiments were conducted with constant velocity and acceleration limits. However, varying these parameters has a significant effect on the oscillatory behavior. The effects of these motion parameters were investigated thoroughly for the slewing motion. Similar dynamic behavior can be expected for the luffing motion.

Figure 5.21 shows the residual vibration amplitude as a function of slewing distance for three different slewing velocities: 10°/s, 20°/s, and 30°/s. The acceleration limit was held constant at $25°/s^2$. The other constant parameters were luffing angle=45°, suspension cable length=1 m, rigging cable length=0.5 m, hook mass=0.63 kg, and payload mass=1 kg. These parameters were chosen to produce first and second mode frequencies ($f_1 = 0.43$ Hz, $f_2 = 1.32$ Hz) that fall in the suppression range of the two-mode shaper in (5.1). Therefore, the effectiveness of the two-mode shaper would solely depend on the varying velocity limits.

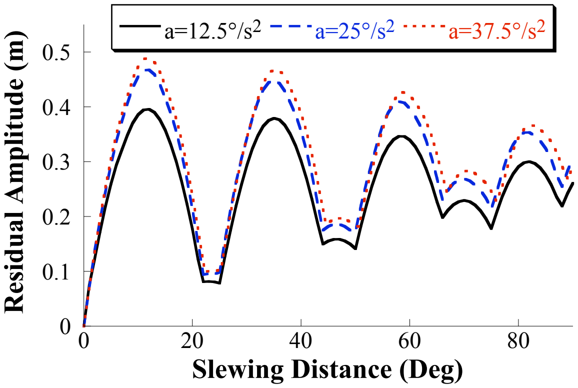

Figure 5.22: Residual Vibration Amplitude vs. Slewing Acceleration

Increasing the maximum velocity has two effects on the residual vibration: *i)* the maximum vibration amplitude increases, and *ii)* the peaks/troughs are spaced farther apart. Even though the acceleration amplitude is held constant, increasing the maximum velocity requires that the crane be accelerated for a longer period of time. Therefore, the payload deflection induced during the acceleration and deceleration periods is larger. To explain the change in the location of the peaks and troughs, assume that the peaks are spaced Δt apart. This time is a function of the system period. As the velocity increases, the system can travel a longer distance in that time Δt. Hence, the peaks/troughs are spaced farther apart in move distance as the maximum velocity increases.

Figure 5.22 shows the residual vibration amplitude as a function of slewing distance for three different accelerations: 12.5°/s^2, 25°/s^2, and 37.5°/s^2. The velocity limit was held constant at 10°/s. All other parameters are the same as those used to produce Figure 5.21. The residual vibration amplitude increases as the maximum acceleration is increased. The locations of the peaks and troughs, however, are approximately equal. This occurs because the velocity limit is constant, so the system travels approximately the same distance in a given period of the payload oscillation.

The simulations were repeated using the two-mode SI shaper given in (5.1). The results demonstrated that the two-mode SI shaper is robust enough to compensate

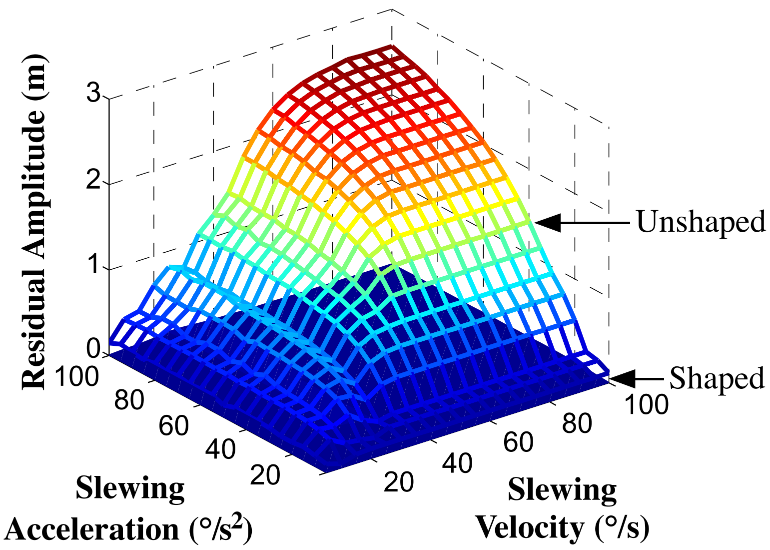

Figure 5.23: Residual Vibration Amplitude vs. Slewing Velocity and Acceleration [γ = 45°, θ_{dist} = 80°]

for the changed dynamics and higher nonlinear effects. For all six cases shown in Figures 5.21 and 5.22, the two-mode SI shaper reduced the average residual vibration amplitude by approximately 96%.

In order to determine the effectiveness of the input shaper over a larger range of maximum velocities and accelerations, the slewing velocity was varied between 5°/s and 100°/s and the slewing acceleration was varied between 5°/s^2 and 100°/s^2. The slewing distance was held constant at 80°. Figure 5.23 shows the unshaped and shaped residual vibration amplitudes for this parameter space. Note that the residual vibration levels off after a certain velocity limit for each acceleration limit. This occurs because after a certain velocity limit, the move is completed before the maximum velocity is reached. Therefore, the command reduces from a trapezoidal velocity command to a triangular command. This command, and therefore the residual vibration amplitude, remains constant even if the maximum velocity is increased. Figure 5.23 also demonstrates that the input shaping is effective at reducing the residual oscillation. For the entire parameter space shown in Figure 5.23, the input shaper reduced the residual oscillation by an average of approximately 98%.

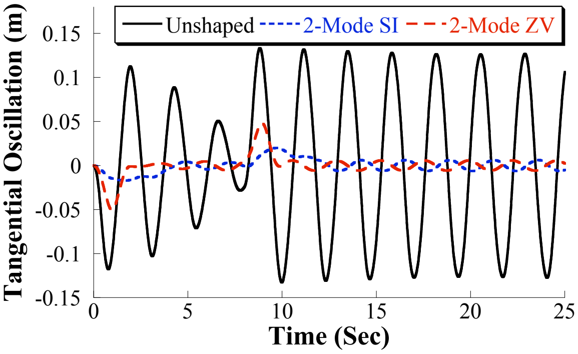

Figure 5.24: Tangential Payload Oscillation [v_{max}**=10°/s and** a_{max}**=25°/s**^{2}]

Increasing the velocity and acceleration limits increases nonlinear dynamic effects. For example, during the slewing motion, the oscillation frequencies also depend on the slewing velocity, in addition to the cable lengths and payload/hook masses [33, 36]. Larger velocities result in more variation from the nominal system frequencies. The two-mode SI shaper is very robust to frequency changes; hence, the effects of increasing the velocity and acceleration limits are reduced. To demonstrate this, Figure 5.24 shows the tangential oscillation resulting from a 80° slewing motion, using three different types of commands: unshaped, two-mode SI shaped, and two-mode ZV shaped. This figure represents the time response of a particular data point from Figure 5.23 where $v_{max} = 10°/\text{s}$ and $a_{max} = 25°/\text{s}^2$. The two-mode ZV shaper was designed for the same system parameters as before ($\ell_h = 1$ m, $\ell_p = 0.5$ m, $m_h = 0.63$ kg, and $m_p = 1$ kg). The impulse times and amplitudes of the two-mode ZV shaper are

$$\begin{bmatrix} A_i \\ t_i \end{bmatrix} = \begin{bmatrix} 0.25 & 0.25 & 0.25 & 0.25 \\ 0 & 0.3784 & 1.1688 & 1.5472 \end{bmatrix} \tag{5.2}$$

As Figure 5.24 demonstrates, for relatively low velocity and acceleration limits, both shapers greatly reduced the residual vibration amplitude. The SI and ZV shapers reduced the oscillation by approximately 95% and 97%, respectively.

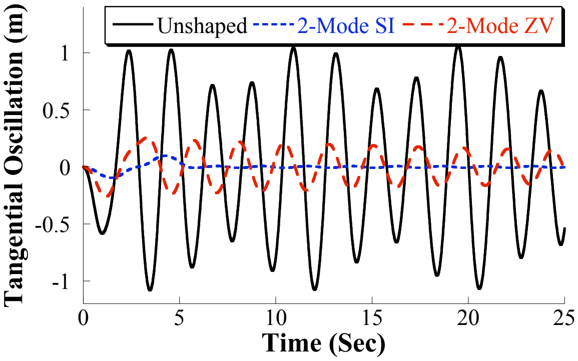

Figure 5.25: Tangential Payload Oscillation [v_{max}=**60°/s and** a_{max}=**80°/s^2**]

In order to demonstrate how the SI shaper's robustness is superior to the ZV shaper's, the velocity and acceleration limits were increased. Figure 5.25 shows the tangential oscillation for the same 80° slewing motion with velocity and acceleration limits increased to 60°/s and 80°/s^2, respectively. The less robust two-mode ZV shaper is much less effective at reducing the residual oscillation. The reduction is only approximately 66%. The more robust two-mode SI shaper, however, reduces the residual oscillation by approximately 99%. Therefore, it is clear that the two-mode SI shaper is robust not only to a large range of double-pendulum dynamic effects, but also to a large range of velocity and acceleration limits.

5.7 Summary

This chapter studied the oscillatory dynamics of boom cranes with double-pendulum payloads. The major contributions of this chapter are:

- If the suspension and rigging cables have similar lengths and the payload mass is small relative to the hook mass, then the second mode can have a significant contribution to the overall oscillation. As a result, a robust two-mode input shaper was required.
- The first- and second-mode swing frequencies for a large range of possible crane and double-pendulum payload configurations were computed. A two-mode

Specified Insensitivity input shaper was designed to suppress vibration over these swing dynamics.

- The robustness of input shaping to parameter variations was demonstrated through numerous simulations and experiments, including a set of operator maneuvers. The SI shaper reduced the residual vibration amplitude by 93% or greater in all cases tested.
- Increasing the velocity and acceleration limits (i.e., using more aggressive commands) increases the nonlinear effects. However, SI shaping was shown to be robust to the increased aggressiveness and nonlinearities.

CHAPTER VI

MAXIMIZING-OSCILLATION CONTROL

Boom cranes are commonly used to swing wrecking balls that demolish unwanted buildings and other structures [27], as shown in Figure 6.1. In such applications, the control goal is *increasing* the pendulum swing. The crane operator moves the machine back and forth to increase the wrecking ball swing and then attempts to direct the swinging ball at the desired point of impact. By increasing the oscillation, the wrecking ball has more damaging force at impact.

The goal of this chapter is to create command shapers that increase the oscillation induced by operator commands, thereby simplifying the task of producing large-amplitude swings for the operator. The next section presents the design of two command shapers that increase the payload swing. Then, Section 6.2 analyzes the robustness of the shapers by using a numerical model of a boom crane. Finally, Section 6.3 evaluates the effectiveness of the shapers through experiments and a set of

Figure 6.1: Boom Crane Swinging a Wrecking Ball [68]

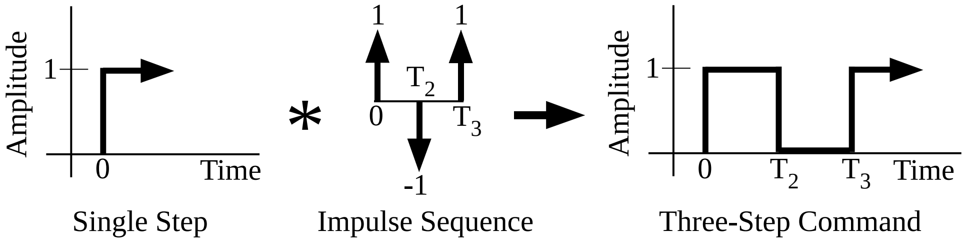

Figure 6.2: Multi-Step Command Generation

human-operator tests on the small-scale mobile crane.

6.1 Swing-Amplifying Command Shaper Design Process

As previous chapters have thoroughly established, boom cranes have complex, nonlinear dynamics that make designing simple and realistic controllers very challenging. Therefore, this section utilizes a simple model of a crane to design input shapers. Then, the performance of the shapers is evaluated on more complex boom crane simulations and experimental hardware in the following sections.

Assume that an undamped second-order system is given a unit step input. The system will oscillate with a peak-to-peak amplitude of two units. To increase the swing, there are two options: *i)* increase the command magnitude, or *ii)* add additional changes to the command. In many physical systems there are actuator limits. For the example system here, a value of one is assumed to be that “physical” limit; therefore, increasing the command magnitude is not possible. Hence, the oscillation must be increased by adding additional changes to the command signal. With every step change in the command, the oscillation can be increased, but at the cost of increased command duration, much like when the operator moves the crane back and forth several times before impacting the wrecking ball.

If we restrict the command to positive values, then a fast-acting command that can excite large swings is the three-step command shown on the right side Figure 6.2. This three-step command can be decomposed into two distinct parts: a single-step command with a magnitude of one and a series of three impulses with magnitudes equal to 1, -1, and 1. The three-step command is produced by convolving these two parts, as shown on the left side of Figure 6.2. As a result of this decomposition, the problem now reduces to designing the impulse sequence, more specifically determining the values of T_2 and T_3.

For an undamped, second-order system, the residual vibration induced by a sequence of impulses is [54]

$$V = \sqrt{\left[\sum_{i=1}^{n} A_i \cos(\omega_n T_i)\right]^2 + \left[\sum_{i=1}^{n} A_i \sin(\omega_n T_i)\right]^2} \tag{6.1}$$

where A_i and T_i are the impulse amplitudes and times and n is the number of impulses in the sequence. The vibration equation in (6.1) is a nondimensional form normalized by the vibration from a single impulse. There are multiple variables in (6.1); however, most of the parameters have already been defined. The number of impulses is $n = 3$, the impulse magnitudes are $A_1 = 1$, $A_2 = -1$, and $A_3 = 1$, the time of the first impulse is $T_1 = 0$, and ω_n is the known natural frequency of the system. As a result, Equation (6.1) is effectively reduced to a function with two unknown variables (T_2 and T_3). The two remaining impulse times can be obtained by computing the maximum of Equation (6.1). This problem can be solving algebraically (by calculating its partial derivatives and setting them equal to zero) or numerically. Although there are an infinite number of solutions, impulse times that minimize the shaper duration are preferred. This yields the solution $T_2 = 0.5P$ and $T_3 = P$, where P is the natural oscillation period.

Alternatively, vector diagrams can be used to graphically determine the impulse times in closed form. Figure 6.3 shows the orientation of three unity-magnitude impulses on a vector diagram that leads to the maximum possible residual oscillation. The first impulse is placed at $\theta_1 = 0$. The second vector must occur at one-half the natural period of the system, which is at an angle of π radians. Because this impulse is negative, it is directed inwardly on the vector diagram and adds constructively to the

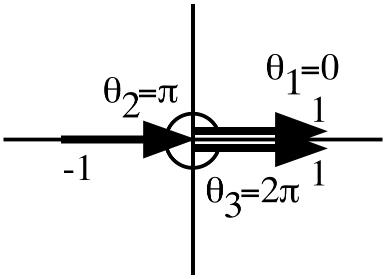

Figure 6.3: Vector Diagram Representation of UM-MV Shaper

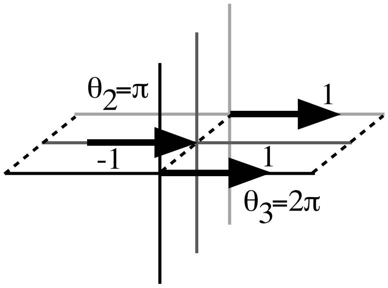

Figure 6.4: 3D Vector Diagram Representation of UM-MV Shaper

first impulse. The final impulse occurs at an angle of 2π radians. The resultant vector (obtained by adding these three impulses) has a magnitude of three, which means that the oscillation is three times the vibration produced with a single impulse. Because the first and third impulses overlap, the standard 2-dimensional vector diagram is not the optimal way of illustrating the shaper impulses. Figure 6.4 shows a 3-dimensional visualization of the vector diagram. The third dimension (in and out of the page) represents the order of the impulses.

The same result can also be obtained by performing a parameter sweep across T_2 and T_3. Because the oscillation is cyclical, the values of T_2 and T_3 that maximize the residual vibration must lie somewhere within one full oscillation period of the system. Figure 6.5 shows the peak-to-peak residual oscillation amplitude of a second-order system driven by the three-step command shown in Figure 6.2 with T_2 and T_3 varying between zero and one times the oscillation period. The flat surface on the bottom right of the figure occurs because the constraint $T_3 \geq T_2$ was enforced. The peak in Figure 6.5 (which has a magnitude of six, three times that of a single-step

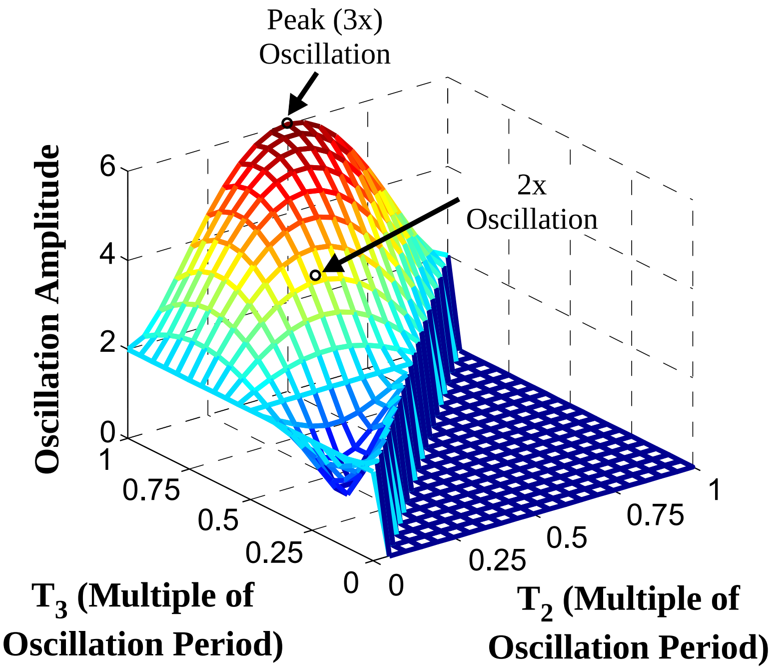

Figure 6.5: Oscillation Amplitude for Varying T_2 and T_3

command) occurs at $T_2 = 0.5P$ and $T_3 = P$.

The three-impulse sequence corresponding to Figures 6.3 and 6.4 is

$$\begin{bmatrix} A_i \\ T_i \end{bmatrix} = \begin{bmatrix} 1 & -1 & 1 \\ 0 & 0.5P & P \end{bmatrix} \tag{6.2}$$

where P is the natural oscillation period of the system. This shaper is called the Unity-Magnitude Maximum-Vibration (UM-MV) input shaper. Equation (6.2) is valid for undamped systems. If the system is damped, then the impulse times must be given as a function of the damped period of oscillation,

$$\begin{bmatrix} A_i \\ T_i \end{bmatrix} = \begin{bmatrix} 1 & -1 & 1 \\ 0 & 0.5P_d & P_d \end{bmatrix} \tag{6.3}$$

where P_d is the damped period given as a function of the natural period, P, and damping ratio, ζ, by $P_d = P/\sqrt{1-\zeta^2}$.

Figure 6.6 shows the response of an undamped second-order system to a unit step command and a UM-MV shaped step command. The maximum oscillation amplitude

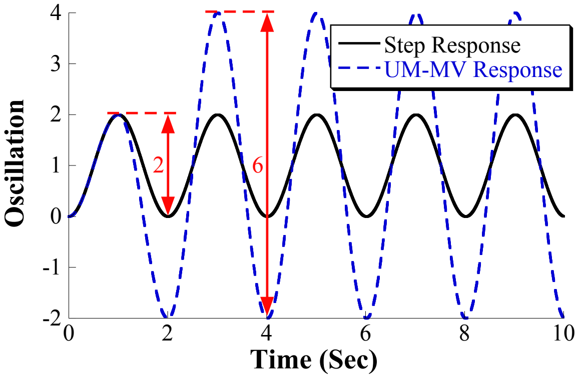

Figure 6.6: Oscillation of an Undamped System

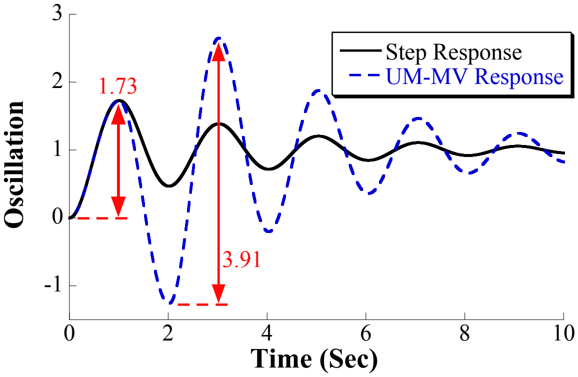

Figure 6.7: Oscillation of an Underdamped System ($\zeta = 0.1$)

of the UM-MV command is three times that of the unit step command. Figure 6.7 shows the response of an underdamped second-order system (damping ratio of 0.1) to a unit step command and a damped UM-MV shaped command. The UM-MV command increased the maximum oscillation by a factor of approximately 2.3. Note that the shaped peak-to-peak amplitude for the damped system (3.91) is smaller than the shaped peak-to-peak amplitude for the undamped system (6) because the damping is actively reducing the swing amplitude.

The shaper given in (6.2) has a duration equal to one period of the system oscillation. Using the vector diagram method, faster shapers can easily be designed by moving the third impulse to an angle less than 360°. This means that the corresponding input shaper will have a duration less than one oscillation period. However, the cost of faster shapers is decreased swing amplification. For example, one such shaper

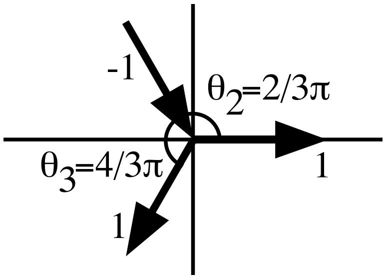

Figure 6.8: Vector Diagram Representation of UM-2xV Shaper

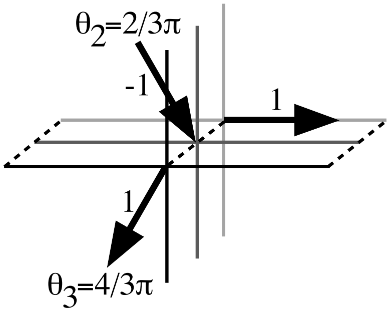

Figure 6.9: 3D Vector Diagram Representation of UM-2xV Shaper

for an undamped system is

$$\begin{bmatrix} A_i \\ T_i \end{bmatrix} = \begin{bmatrix} 1 & -1 & 1 \\ 0 & 1/3P & 2/3P \end{bmatrix} \tag{6.4}$$

This shaper has a duration of only 2/3 the period of oscillation. Figures 6.8 and 6.9 show the 2D and 3D vector diagram representations of this shaper, respectively. The resultant vector has a magnitude of two; therefore, this shaper will double the swing amplitude compared to a single-step command. This shaper is called the Unity-Magnitude Two Times Vibration (UM-2xV) shaper. Its location was also labeled on the oscillation-amplitude surface in Figure 6.5.

6.2 Numerical Evaluation

In Section 6.1, the impulse and step responses of a second-order system were used to illustrate important command-shaping concepts. In this section, the performance and robustness of the swing-amplifying command shapers are evaluated on the nonlinear

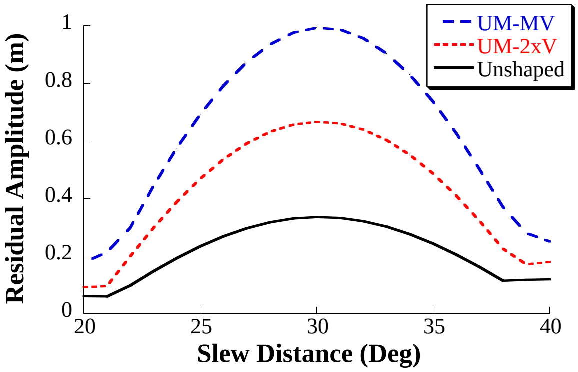

Figure 6.10: Maximum Oscillation vs. Slew Distance

boom crane model using bang-coast-bang acceleration commands.

Robustness is a measure of the effectiveness of the controller at maximizing oscillation in the presence of parameter variations. There are two main sources of variation: the slewing distance and the suspension cable length (swing frequency). Because a human operator will drive the crane, it is unrealistic to assume that the operator can drive the machine back and forth the same distance every time. Hence, it is important to determine the effectiveness of the controller for various move distances. Figure 6.10 shows the maximum peak-to-peak residual swing resulting from the UM-MV shaper, the UM-2xV shaper, and the unshaped trapezoid command. The maximum velocity, maximum acceleration, and luffing angle were set to 10°/s, $25°/s^2$, and 45°, respectively. The peak in the residual oscillation occurs at a slewing distance of 30° for all of the commands. The oscillation amplitude drops off as the slewing distance increases or decreases from 30°. However, throughout the entire range shown in Figure 6.10, both shapers induce significantly larger oscillations than the unshaped command.

Many applications may require the operator to change the suspension cable length, which changes the swing frequency. Therefore, it is also important to demonstrate the robustness to frequency variations. Figure 6.11 shows the sensitivity curves of both the undamped and damped ($\zeta = 0.1$) UM-MV shapers. The vertical axis of the sensitivity plot shows the ratio of the shaped residual amplitude to the unshaped residual

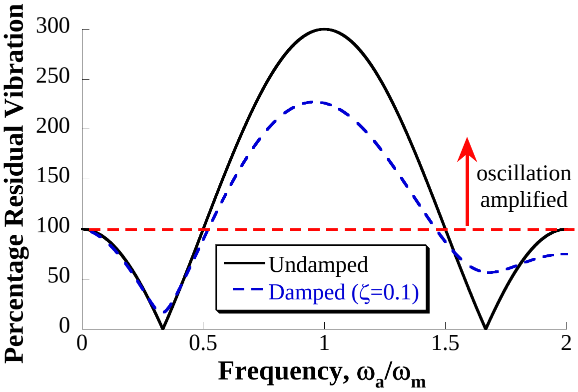

Figure 6.11: Sensitivity Curve for UM-MV Shaper

amplitude. A percent residual vibration (PRV) of 100% means that the shaped command produces the same magnitude of oscillation as the unshaped command. The peak amplitude of 300% occurs when the actual system frequency (ω_a) is equal to the modeled frequency (ω_m). As the actual frequency changes, the peak swing amplitude decreases. However, the percent residual vibration remains above 100% for a large range of the swing frequencies (the actual swing frequency can deviate ±50% from the modeled frequency). Therefore, the shapers will help amplify swing throughout this range of suspension cable lengths.

Figure 6.12 shows the sensitivity curves for the undamped and damped ($\zeta = 0.1$) UM-2xV shapers. The peak in the UM-2xV sensitivity curve does not occur at $\omega_a/\omega_m = 1$. This is expected as the UM-2xV shaper does not maximize the residual amplitude (it doubles the swing amplitude). But the shaper has a shorter duration and provides very good robustness to increases in the swing frequency.

6.3 Experimental Evaluation

6.3.1 Point-to-Point Tests

Three sets of experiments were performed to evaluate the effectiveness of the swing-amplifying shapers and their robustness to parameter variations. In all experiments, the luffing angle was held constant at 55°, the maximum slewing velocity was set to

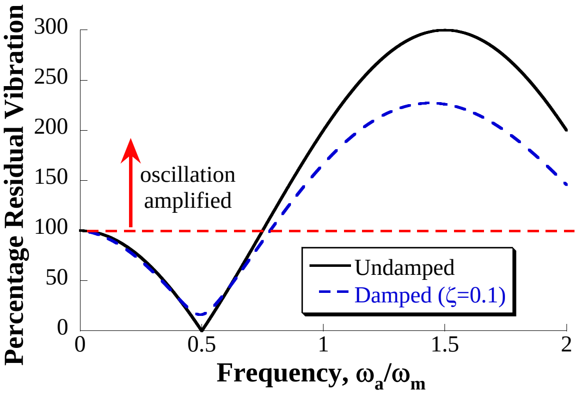

Figure 6.12: Sensitivity Curve for UM-2xV Shaper

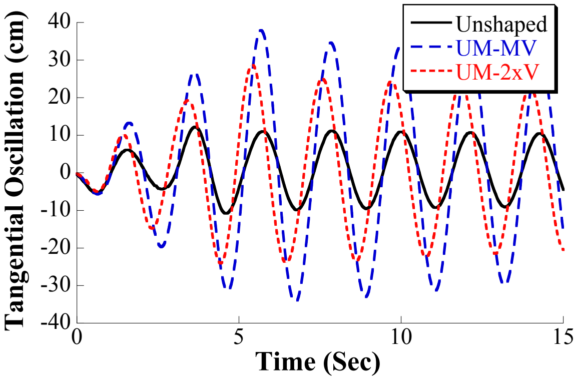

Figure 6.13: Experimental Payload Swing [Slew Distance=20°, Suspension Cable Length=1 m]

6.67°/s, and the maximum slewing acceleration was set to 16.67°/s^2. In the first set of experiments, the suspension cable length was held constant at 1 m and the boom crane was slewed a distance of 20° with unshaped, UM-MV shaped, and UM-2xV shaped trapezoidal velocity commands. For this set of parameters, a 20° slew distance corresponds to the ideal distance that produces the maximum possible residual oscillation. Figure 6.13 shows the tangential oscillation resulting from these tests. The UM-MV shaped command increased the maximum residual oscillation by a factor of approximately 3.1. The UM-2xV shaper increased the residual amplitude by a factor of approximately 2.3.

Next, the robustness of the shapers to varying swing frequency was evaluated. The slew distance was held constant, but the suspension cable length was increased

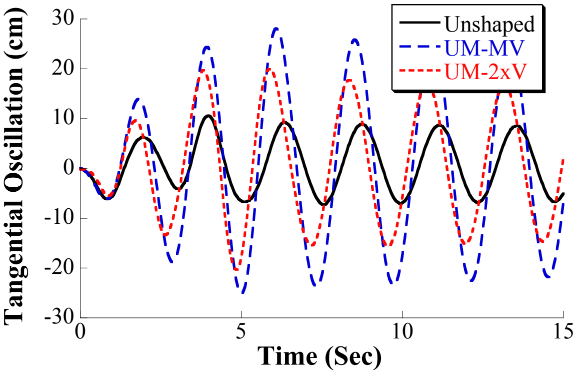

Figure 6.14: Experimental Payload Swing with Longer Suspension Cable Length

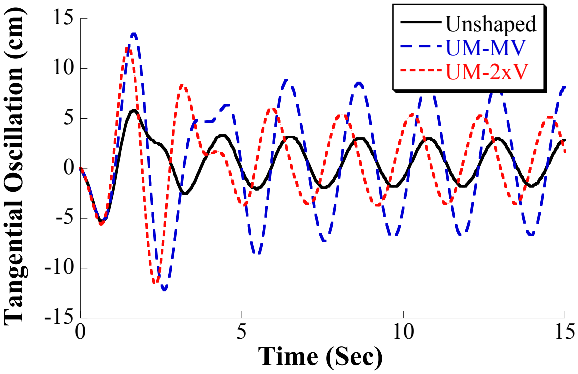

Figure 6.15: Experimental Payload Swing with Shorter Slewing Distance

to 1.3 m (30% change in length and a 12% decrease in frequency). Figure 6.14 shows the tangential oscillation resulting from these tests. Both shapers were still able to substantially increase the residual oscillation. The UM-MV shaped command increased the maximum residual oscillation by a factor of approximately 2.7. The UM-2xV shaper increased the residual amplitude by a factor of approximately 1.9.

Finally, the robustness of the shapers to varying slewing distance was evaluated. The suspension cable was reset to 1 m, and the slew distance was lowered to 13°. Figure 6.15 shows the tangential oscillation resulting from these tests. Note that the residual oscillation amplitudes induced by both shapers are smaller than the oscillation amplitudes induced by the 20° slewing move distance presented in Figure 6.13. Nonetheless, compared to the unshaped command, the UM-MV shaper increased the

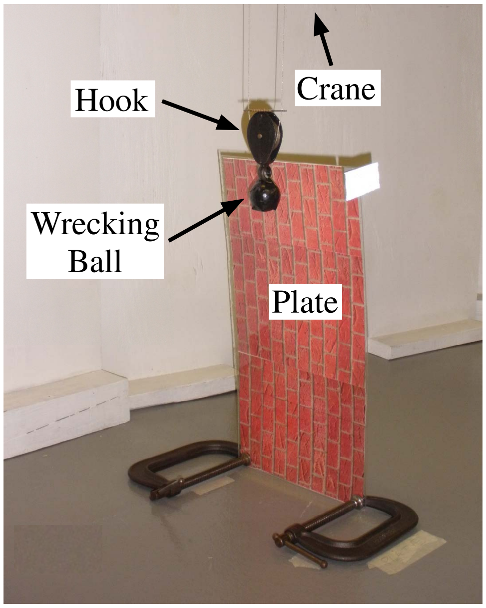

Figure 6.16: Operator Test Set-up

residual oscillation by a factor of approximately 2.6. The UM-2xV shaper increased the residual amplitude by a factor of approximately 1.7.

The results of these experiments clearly demonstrate that oscillation-amplifying command shapers can effectively, and robustly, increase the payload swing. These improvements in swing amplitude occur without any special requirements on the human operators. The operators can use a variety of slew distances and suspension cable lengths.

6.3.2 Operator Tests

To further evaluate the effectiveness of the oscillation-amplifying command shapers, a series of operator studies was conducted. These tests help demonstrate that the controller is truly effective at aiding a human operator to increase the payload swing. Figure 6.16 shows an image of the study set-up. Twelve novice crane operators were asked to slew the mobile crane and swing a wrecking ball into the plate. The deflection of the plate was measured using a camera placed to the side. Each operator was given approximately five minutes of practice time. Then, he/she was asked to

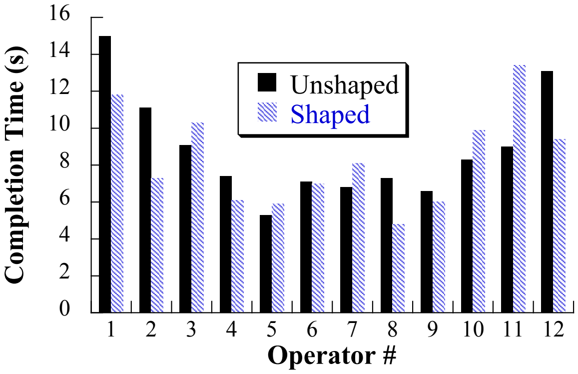

Figure 6.17: Single-Collision Test Completion Times

complete a single-collision test. The completion time, the number of button pushes, and the maximum plate deflection were measured. The completion time was defined as the time period starting with the first button push until a plate collision. The number of button pushes is a measure of the amount of effort the operator exerted to increase the wrecking ball swing and crash into the plate. The operator effort measured here not only represents the physical effort required to push the buttons, but also the mental effort required to continuously update the mental map between button pushes and the actions of the crane. The more buttons an operator pushes, the more physical and mental concentration he/she must exert. The maximum plate deflection measures the effectiveness of the impact.

Figure 6.17 shows the completion times of all 12 operators for both unshaped and UM-MV shaped commands. The average completion time was 8.8 s for the unshaped trials and 8.3 s for the shaped trials. Figure 6.18 shows the number of button pushes for the operators. The average number of button pushes was 6.6 for the unshaped trials. With command shaping, the average number of button pushes was cut nearly in half to only 3.5.

Figure 6.19 shows the maximum plate deflection of all 12 operators. The average plate deflection was 54.9 mm for the unshaped trials and 57.9 mm for the shaped trials. Notice that both the unshaped and shaped trials produced similar plate deflection

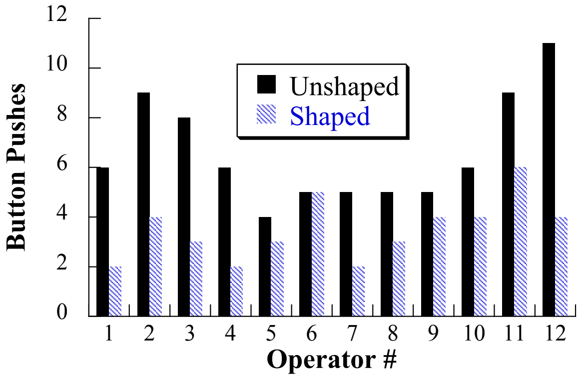

Figure 6.18: Single-Collision Test Button Pushes

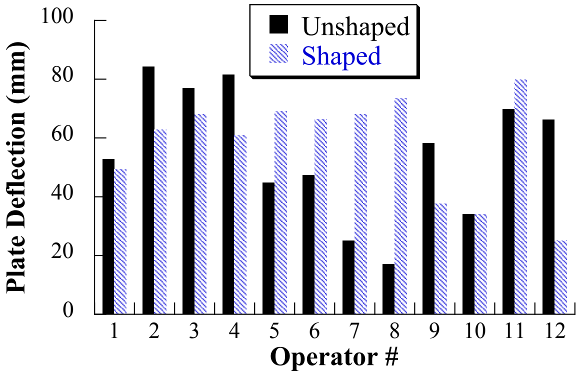

Figure 6.19: Single-Collision Plate Deflection

amplitudes. However, the operators utilized about half as many button pushes and slightly less time to achieve this same level of impact energy.

The above tests only studied the effectiveness of the command shaper in a single-collision scenario. In real wrecking-ball applications, an operator must induce numerous collisions. Therefore, the same 12 operators were given one minute to repeatedly crash the wrecking ball into the plate. The number of button pushes and the total plate deflection were recorded. The total plate deflection was measured by summing the plate deflection amplitude during the entire one-minute duration of the test.

Figure 6.20 shows the button pushes of all 12 operators for the one-minute test. The average number of button pushes was 42.2 for the unshaped trials. With command shaping, the average number of button pushes was again significantly reduced to only 26.3.

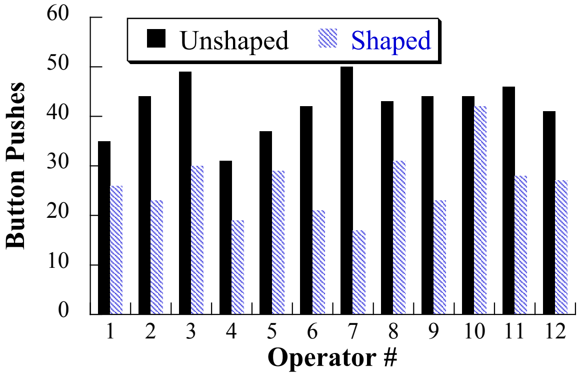

Figure 6.20: One-Minute Test Button Pushes

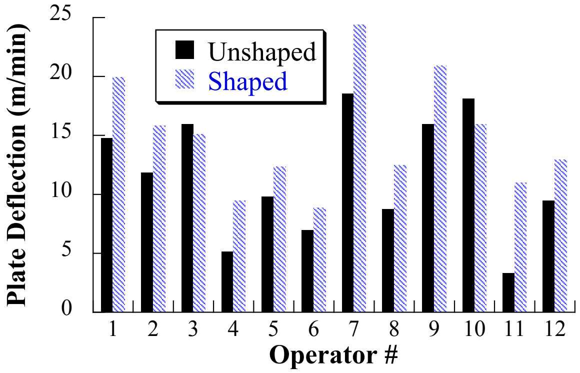

Figure 6.21: One-Minute Test Total Plate Deflection

Figure 6.21 shows the total plate deflection of all 12 operators for the one-minute test. The average total plate deflection is 11.6 m/min for the unshaped trials and 14.9 m/min for the shaped trials. These results demonstrate that the operators were able to increase the total plate deflection, while exerting less effort, as shown by the approximately 40% decrease in the number of button pushes. The results of all the operator tests are summarized in Table 6.1.

Analysis of variance (ANOVA) tests were conducted to measure the statistical significance of the differences between the unshaped and shaped one-minute test results. Because the same group of 12 operators performed both the unshaped and shaped trials, one-way repeated ANOVA tests (Paired t-Tests) were used. A 95% confidence was used for all tests. Table 6.2 summarizes the ANOVA test results. ANOVA tests provide two statistical values, the F-values and the P-values. The F-value is the ratio

Table 6.1: Summary of Operator Test Results

Trial Type	Unshaped Ave.	Shaped Ave.	% Change
Single Collision - Completion Time	8.8 s	8.3 s	-6%
Single Collision - Button Pushes	6.6	3.5	-47%
Single Collision - Plate Deflection	54.9 mm	57.9 mm	+5.5%
One-Minute Test - Button Pushes	42.2	26.3	-37.7%
One-Minute Test - Plate Deflection	11.6 m/min	14.9 m/min	+29%

Table 6.2: Summary of ANOVA Results for One-Minute Test

Trial Type	F-value/F_{crit}	P-value
Button Pushes	10.7	<0.0001
Plate Deflection	4.2	0.0014

of the variation between the two groups (unshaped and shaped data) to the variation within each group. An F-value greater than the F_{crit} value indicates that the variation between the two groups is significant. (The F_{crit} value for a data set with 2 groups and a total sample size of 24 is approximately 4.3.) The P-value measures the probability that there is a statistical difference between the averages of the unshaped and shaped results. Small P-values (less than 0.05) indicate a low probability that the difference between the unshaped and shaped results is due to random chance. The statistical analysis supports the conclusion that the oscillation-amplifying command shapers were able to improve the performance of the operators.

6.4 Summary

The challenging task of using a boom crane for wrecking ball applications was simplified by swing-amplifying command shapers. Two shapers were considered in detail, the Unity-Magnitude Maximum Vibration shaper and the Unity-Magnitude Two Times Vibration shaper. Their effectiveness was demonstrated in simulation and experiments on a small-scale crane. The robustness of the shapers to changes in swing frequency and move distance was analyzed. In addition, their potential benefit in aiding human operators was demonstrated in a series of operator performance studies.

CHAPTER VII

DUAL-HOIST CRANE DYNAMICS AND CONTROL

In certain crane applications (e.g., if the payload is very large) the use of multiple cranes becomes necessary. Simultaneously maneuvering multiple cranes to transport a single payload dramatically increases the complexity and danger of the operation [22, 23, 29, 30]. A dual-hoist bridge crane, such as the one shown in Figure 7.1, is one common example of such cranes. Understanding the complex response of these cranes with various inputs and configurations is an important step in controlling them.

This chapter explores the dynamic behavior of dual-hoist bridge cranes. Although numerous important results are highlighted and explained, this only represents of subset of the full dynamic study on these cranes. The goal of this chapter is not to present an analysis of all the possible responses, but rather explore a few key characteristics that further verify one of the main objectives of this thesis: although

Figure 7.1: Dual-Hoist Bridge Crane

dual-hoist cranes have a complicated and nonlinear response, input shaping can be effectively applied to reduce the nonlinear effects and make human operation easier.

Section 7.1 investigates the crane's response to various trolley and bridge motions and configuration changes. The effects of varying important parameters, such as the cable lengths and payload shape, are investigated. Then, input-shaping controllers are designed and their effectiveness are demonstrated. Section 7.2 examines coordinated trolley-bridge motions necessary to produce L-shaped trajectories to maneuver around obstacles. Finally, Section 7.3 presents experimental results on a two-ton dual-hoist bridge crane to verify key theoretical predictions and demonstrate the effectiveness of input shaping.

7.1 Point-to-Point Motions

Throughout this chapter, several different crane configurations are analyzed. Figure 7.2 demonstrates the various configurations. Configuration A is the simplest, where the cables, the payload, and the trolleys form a rectangle. By changing the payload type, Configurations A.2 and A.3 can be created. These payloads are further explored in Section 7.1.3. Configuration B is produced by keeping the length of Cable 1 constant, and changing the length of Cable 2. Configurations B.2 and B.3 are created by varying the payload length or the trolley separation distance.

7.1.1 Trolley Motion

Figure 7.3 shows the oscillation of both hooks induced by a 1.5 m trolley motion. The hook cable lengths were set to $L_1 = L_2 = 2$ m. The trolley separation distance and payload length were both set to 2 m. The trolleys were moved simultaneously to keep the separation distance constant. This setup corresponds to Configuration A in Figure 7.2. When the crane moves in the trolley direction (planar motion), the system responds very similar to a simple pendulum. The hook swings have a single frequency. In this case, the frequency can be found by using the frequency equation

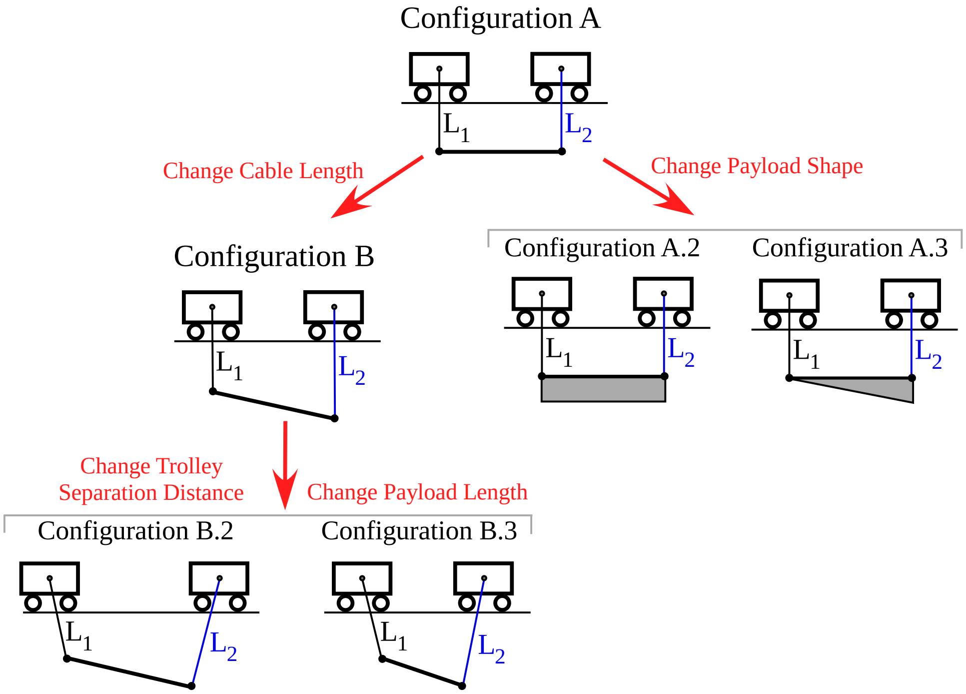

Figure 7.2: Dual-Hoist Bridge Crane Configurations

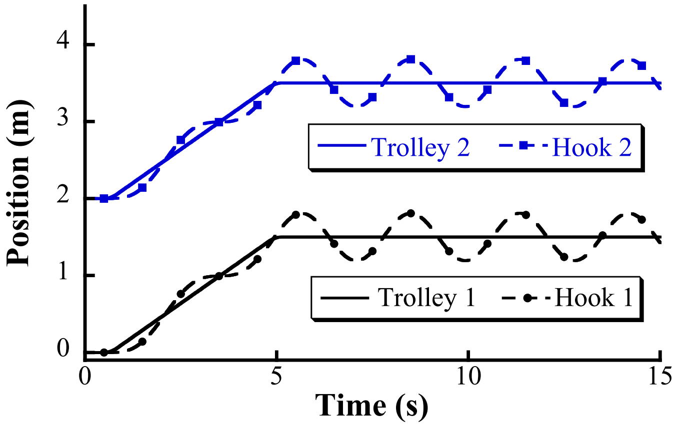

Figure 7.3: Response Induced by 1.5 m Trolley Motion

for a simple pendulum: $f = (\sqrt{g/L})/2\pi$, where L is the pendulum cable length. Note that this equation is derived by linearizing the equation of motion of a simple pendulum using a small-angle approximation. The frequency of swing is 0.35 Hz.

Figure 7.4 shows the maximum peak-to-peak residual swing amplitude of Hook 1 for trolley move distances between 0 m and 3 m. (The swing amplitudes of Hook 2 are very similar to Hook 1.) Varying the move distance results in peaks and troughs

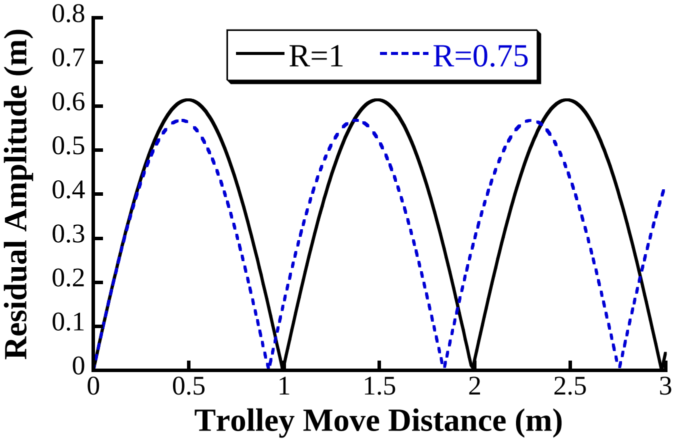

Figure 7.4: Residual Oscillation Amplitude vs. Trolley Move Distance

in the swing amplitude. These peaks and troughs occur because of the constructive and destructive combination of the oscillations caused by starting and stopping the trolley motion.

The length of Cable 1 was reduced to 1.5 m ($L_1 = 1.5$ m, $L_2 = 2$ m). This represents a cable length ratio, $R = L_1/L_2$, of 0.75 (Configuration B). Figure 7.4 also shows the peak-to-peak amplitudes for this case. The swing amplitudes of the two hooks are similar to each other; therefore, only the swing amplitude of Hook 1 is shown. The peaks and troughs occur at different locations compared to the first case ($R = 1$), which indicates that the swing frequency is different. The oscillation frequency of the crane in this configuration is 0.38 Hz. This frequency is approximately the average frequency of the two cables if they were independent single-pendulum systems ($f(2\text{m}) = 0.35$ Hz and $f(1.5\text{m}) = 0.41$ Hz).

To investigate whether the theoretical average frequency can accurately predict the actual system frequency for other cable length ratios, the trolley move distance was held constant at 0.8 m and the cable length ratio was varied between 0 and 2. Figure 7.5 shows the oscillation frequency for this range of cable length ratios. The figure also shows the “average frequency” curve. This curve is the average frequency corresponding to the single-pendulum frequency of each cable length. For the range

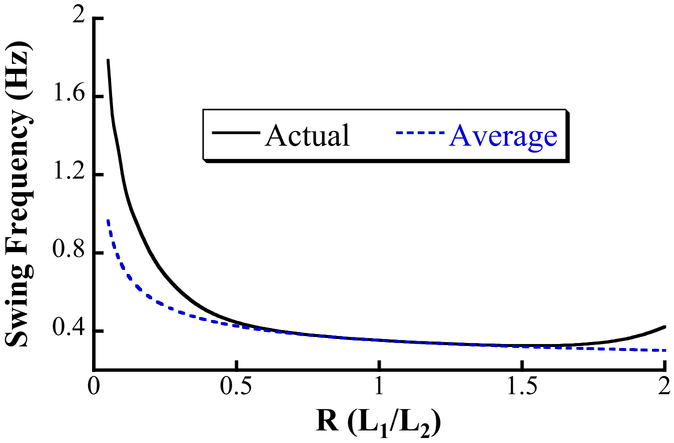

Figure 7.5: Oscillation Frequency vs. Cable Length Ratio (R) for Trolley Motions

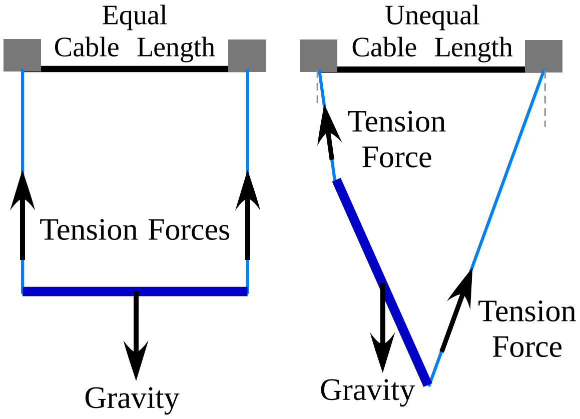

Figure 7.6: Free-Body Diagram of Two Different Crane Configurations

between $R = 0.5$ to $R = 1.5$, the average frequency predicts the effective system frequency quite well. However, outside this range, the frequency increases rapidly and is no longer similar to the average frequency curve. The equation used to compute the frequency of each cable ($f = (\sqrt{g/L})/2\pi$) is derived using a linear approximation. For cable length ratios close to one, this linear approximation is valid. However, as R gets farther away from one, the hook swing angles get larger. As a result, the frequency equation is no longer valid and cannot accurately predict the actual frequency. Alternatively, this can be explained by looking at the forces acting on the system, as illustrated in the free body diagram in Figure 7.6. For $R \approx 1$, the tension forces and gravity act approximately along the same line of action. For very small or

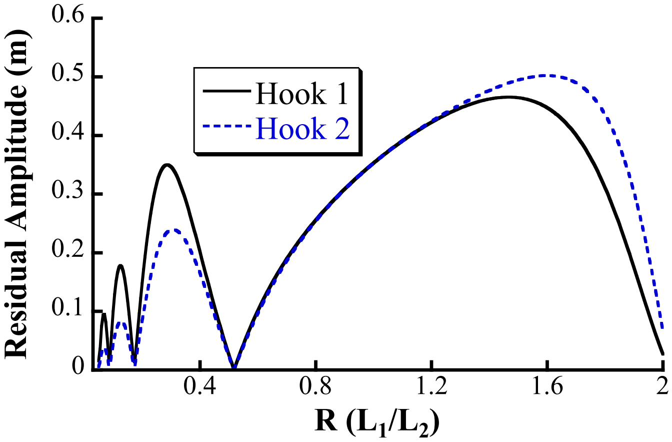

Figure 7.7: Trolley Residual Oscillation Amplitude vs. Cable Length Ratio (R)

very large R, however, the tension forces and gravity are no longer co-linear.

Figure 7.7 shows the swing amplitudes induced by a 0.8 m trolley motion for the same range of cable ratios as in Figure 7.5. The oscillation amplitudes of the two hooks are similar for R close to one, but begin to vary from one another as R increases beyond one or decreases below one. This occurs because the horizontal hook deflections are functions of their cable lengths. Hence, if the two cable lengths vary from one another, then their vibration amplitude will also be different.

As shown thus far, the swing frequency of the dual-hoist crane is heavily dependent on the cable lengths. However, other factors can also effect the oscillation frequency. The payload length (PL) and trolley separation distance (SD) have a significant influence on the oscillation frequency of the system because varying these parameters changes the hook configuration. For example, Figure 7.8 shows sketches of the crane in three different configurations. These sketches correspond to Configurations B, B.2, and B.3 in Figure 7.2. The cable lengths were fixed at $L_1 = 0.5$ m and $L_2 = 2$ m in all three scenarios, but the PL and SD distances were varied. The configuration of the crane is very different in each case, which results in different swing frequencies.

To further investigate the effect of varying the payload length and trolley separation distance, the PL and SD values shown in Figure 7.8 were simulated with cable

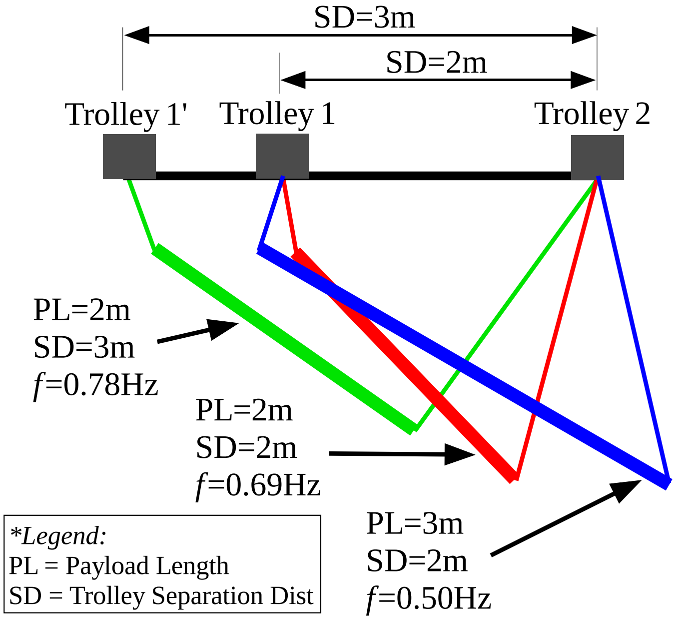

Figure 7.8: Sketches of the Dual-Hoist Crane in Three Different Configurations

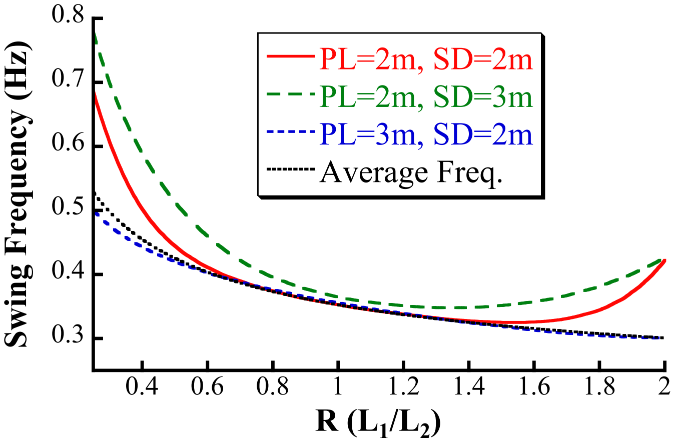

Figure 7.9: Oscillation Frequency for Three Different Configurations

length ratios between 0.25 and 2. The trolley move distance was held constant at 0.8 m. Figure 7.9 shows the oscillation frequency for these cases. For cable length ratios close to unity, the oscillation frequencies are similar for all three cases tested. However, for R values farther from unity, the frequencies of the three cases begin to differ significantly from one another.

It is important to note that the swing frequencies of the three cases shown in

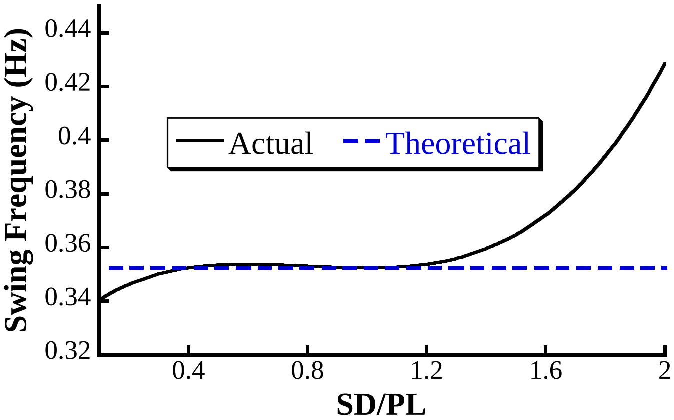

Figure 7.10: Oscillation Frequency vs. Trolley Separation Distance

Figure 7.9 are similar to the theoretical frequency for $R \approx 1$ because the ratio of SD/PL is close to one in all three cases. If this ratio is much greater than or less than one, then even for equal cable lengths, the frequency would deviate from the theoretical frequency. Figure 7.10 shows the swing frequency as a function of varying trolley separation distance. The cable and payload lengths were all held constant at 2 m. The theoretical frequency is also shown. The actual and theoretical frequency are similar for values of SD/PL $\approx$ 1. As the value of SD gets very small or large, the theoretical frequency, which is based on a linear approximation, is no longer valid and does not accurately predict the actual frequency.

A Zero Vibration shaper can be used to effectively reduce the oscillation induced by trolley motions. However, because ZV shapers are not very robust to frequency variations, they would be most effective for applications that do not require large changes to the crane configuration. Note that move distance and payload mass do not have a significant effect on the oscillation frequency. This is not surprising as the response induced by trolley motions is similar to that of a planar, simple pendulum. If a crane application requires significant configuration changes, then the input shaper must be designed to reduce the hook swings for the range of frequencies corresponding to the various expected configurations. The input-shaping design process for such applications is summarized below:

Table 7.1: Input Shapers for Dual-Hoist Bridge Crane

SI	Amplitudes	0.17	0.33	0.33	0.17
	Times (s)	0	1.056	2.089	3.145
EI	Amplitudes	0.26	0.48	0.26	
	Times (s)	0	1.099	2.198	
SI (exp)	Amplitudes	0.26	0.48	0.26	
	Times (s)	0	1.067	2.134	

1. Determine the range of parameters (cable lengths, payload length, and trolley separation distance) required for the application.
2. Compute the swing frequencies resulting from the parameter range in Step 1.
3. Design a Specified-Insensitivity (SI) input shaper to reduce the swing to below a tolerable level in that frequency range.

The advantages of this method are that a single input shaper can be used throughout the crane operation and no sensors are required to measure the system parameters. For example, assume that a certain application requires the following parameter ranges: R = 0.5-2, SD = 2-3 m, and PL = 2-3 m. This corresponds to frequencies in the range from 0.30 Hz to 0.51 Hz. For a tolerable vibration percentage of 5%, the SI shaper satisfying these constraints is given in the top row of Table 7.1. Note that Table 7.1 also provides other input shapers used later in this chapter. Figure 7.11 shows the sensitivity curve for this input shaper. The Percentage Residual Vibration (PRV) is below 5% for the specified range of frequencies.

To evaluate the effectiveness of the SI shaper in Table 7.1, a series of simulations were performed. Figure 7.12 shows the unshaped and shaped residual oscillation amplitude induced by move distances between 0 m and 3 m. Other important parameters were set as follows: R = 1.5, PL = 2.5 m, and SD = 2 m. The SI shaper reduced the oscillation amplitude by an average of 99% throughout this range of parameters.

Figure 7.13 shows the induced residual oscillation by both unshaped and shaped commands for cable length ratios from 0.5 to 1.5. Other important parameters were

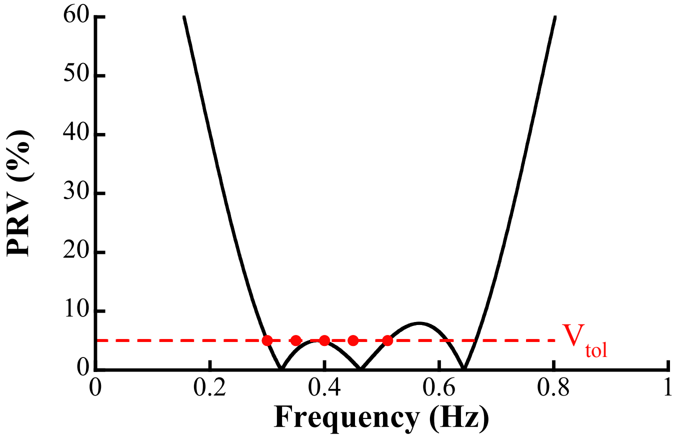

Figure 7.11: Sensitivity Curve of SI Shaper for Trolley Motions

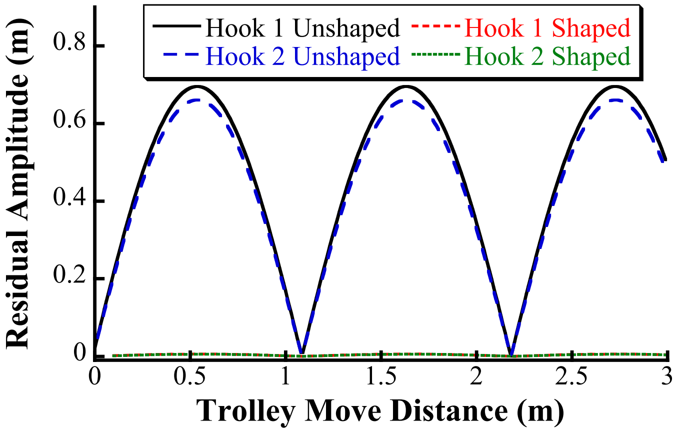

Figure 7.12: Oscillation Amplitude vs. Trolley Move Distance with Input Shaping

set as follows: Move Distance = 1.5 m, PL = 2 m, and SD = 3 m. Input shaping reduced the residual swing by an average of 96%. These simulations demonstrate the effectiveness of input shaping throughout a large range of the crane and payload parameters.

It is also possible to develop an adaptive input-shaping control scheme. Curves similar to those in Figure 7.9 can be obtained for the entire feasible range of parameters for a given system. This essentially produces a look-up table that gives the oscillation frequency as a function of the crane parameters. Then, the amplitudes and times of the input shaper impulses could be adjusted in real time based on the

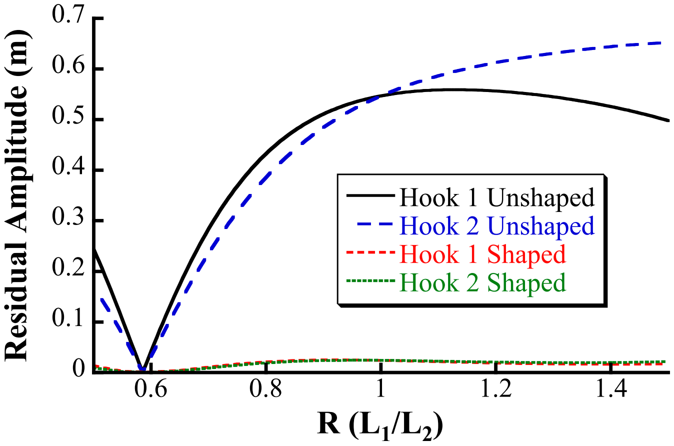

Figure 7.13: Trolley Oscillation Amplitude vs. Cable Length Ratio (R) with Input Shaping

frequency obtained from the look-up table. The advantages of this control scheme is that faster ZV shapers can be used and the vibration amplitude can be kept at a lower level over a wide range of parameters. However, this method requires sensors to accurately measure several parameters. Measuring the parameters of a real crane in its work environment can be very challenging and costly.

7.1.2 Bridge Motion

Figure 7.14 shows the peak-to-peak residual swing amplitude of both hooks for bridge move distances between 0 m and 3 m. Both hook cable lengths were set to 2 m, $R = 1$ (Configuration A). The swing amplitude of both hooks are identical. The results look similar to that of Figure 7.4. When the cable lengths are equal, the swing behavior in the bridge direction is similar to that of a simple pendulum. The swing is approximately linear and only contains one frequency.

Figure 7.14 also shows the residual swing of the hooks for unequal cable lengths: $L_1 = 1.7$ m, $L_2 = 2$ m, and $R = 0.85$ (Configuration B). The hook swing amplitudes are no longer identical. Also, notice that the curves have double-headed peaks (or troughs). This is most obvious in the Hook 1 amplitude curve. This occurs because unlike the equal cable-length case and the trolley motions presented in the previous

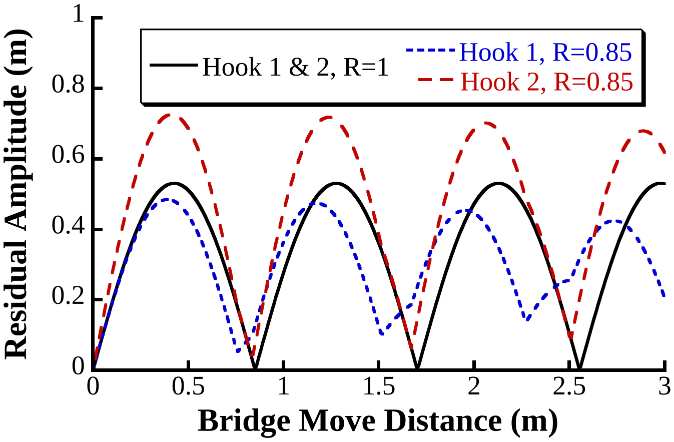

Figure 7.14: Residual Oscillation Amplitude vs. Bridge Move Distance

section, when the two cable lengths are not equal and the crane moves in the bridge direction, the hook oscillations are no longer single-mode. If the two hooks were independent of each other, then each hook would oscillate with a different frequency. However, the hooks are rigidly attached together by the payload. The coupling of these two oscillations results in the two-mode swing behavior. The two frequencies present in the case shown in Figure 7.14 ($R = 0.85$) are 0.40 Hz and 0.36 Hz.

These frequencies approximately correspond to the frequencies of two decoupled, simple pendulums with cable lengths of L_1 and L_2. Figure 7.15 shows the hook swing frequencies for R between 0.30 and 1.65 (the length of Cable 2 was held constant at 2 m). The curve labeled “Cable 1 Freq” represents the frequency of a simple pendulum with a cable length of L_1. The curve labeled “Cable 2 Freq” represents the frequency of a simple pendulum with a cable length of L_2. The circle and square markers represent the actual swing frequencies of each hook. Note that for cable length ratios between $R = 0.65$ and $R = 1.4$, the theoretical frequency curves predict the actual swing frequencies reasonably well. However, for very small or very large R, the system frequencies can no longer be accurately estimated by this trend. This occurs because the “Cable 1 Freq” and “Cable 2 Freq” curves were computed using the linearized frequency equation. For very small or large R, the hook swing frequencies can no

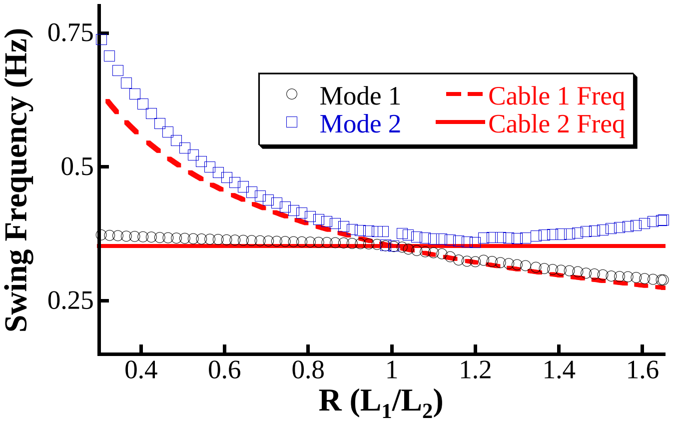

Figure 7.15: Oscillation Frequency vs. Cable Length Ratio (R) for Bridge Motions

longer be estimated by a linear approximation.

Although unequal cable lengths result in two-mode hook swings, the contribution of each mode to the overall swing amplitude is not equal. For example, Figure 7.16 shows the relative FFT magnitude of the first (0.36 Hz) and second (0.40 Hz) modes of the Hook 1 oscillation (for $R = 0.85$) overlaid on top of the Hook 1 swing amplitude for a range of move distances. The sum of the *absolute* contributions of these two modes to the hook oscillation results in the Hook 1 swing amplitude curve. The relative FFT magnitude was obtained by scaling the absolute FFT magnitude of each mode verses the larger of the two. Therefore, one of the two modes always has a FFT magnitude of one. The mode with the larger relative magnitude (magnitude of one) contributes more to the swing amplitude. For the majority of move distances, mode 2 has a larger relative magnitude. In fact, the only move distances that have larger relative mode 1 magnitudes are those corresponding to the troughs of the amplitude curve. Therefore, it is clear that the contribution of mode 2 to the swing amplitude is larger than mode 1. Hence, mode 2 (0.4 Hz) is the dominant frequency present in the Hook 1 oscillation. A similar pattern can be observed in the Hook 2 oscillations, which has a dominant frequency of approximately 0.36 Hz. Hook 1 is attached to the shorter cable; therefore, its dominant frequency is higher than Hook 2, which is

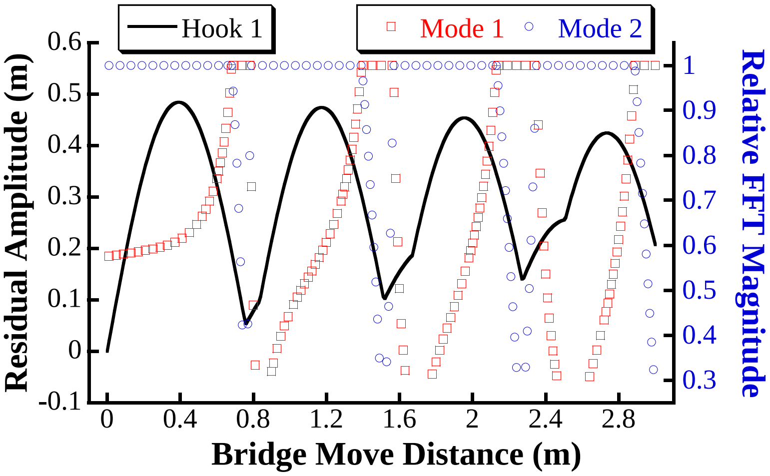

Figure 7.16: Residual Oscillation Amplitude and FFT Magnitude vs. Bridge Move Distance

attached to the longer cable. Because the dominant mode of each hook is different, both modes are significant and must be controlled.

An interesting dynamic phenomenon that occurs if there are two similar frequencies present in the hook oscillations (like the $R = 0.85$ case shown in Figure 7.14) is the beating effect. Figure 7.17 shows the Hook 1 and Hook 2 oscillations induced by a 1 m bridge motion and cable length ratio of $R = 0.85$. The beating frequency is equal to the difference between the two frequencies present in the swing; therefore, the beating frequency is approximately 0.40 Hz - 0.36 Hz = 0.04 Hz. The peaks and troughs of the beat oscillation of the two hooks match. That is, when the Hook 1 beat oscillation approaches a peak (for example at approximately 30 s), the Hook 2 beat oscillation approaches a trough, and vice versa.

Another important dynamic effect caused by bridge motions with unequal cable lengths is out-of-plane oscillations. Moving in the bridge direction causes oscillation in the perpendicular trolley direction. This is an effect that is not present in single-hoist cranes. To understand why this occurs, assume that Hook 1 swings out in the bridge direction. As it swings out, it also lifts up vertically. This deflection in the vertical direction is similar to a change in the cable length. This change in the effective cable

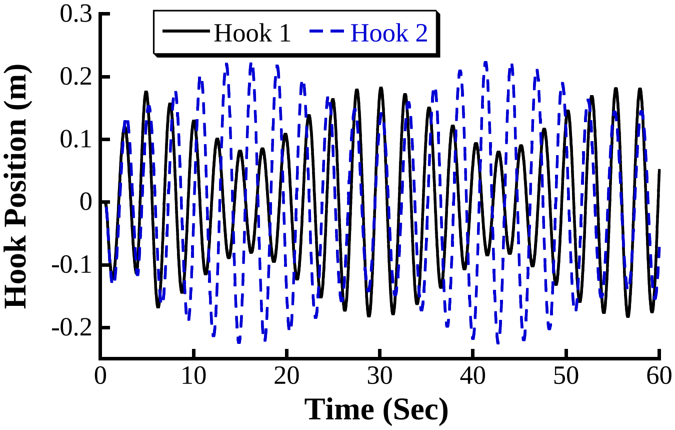

Figure 7.17: Beating Effect Caused by Bridge Motion

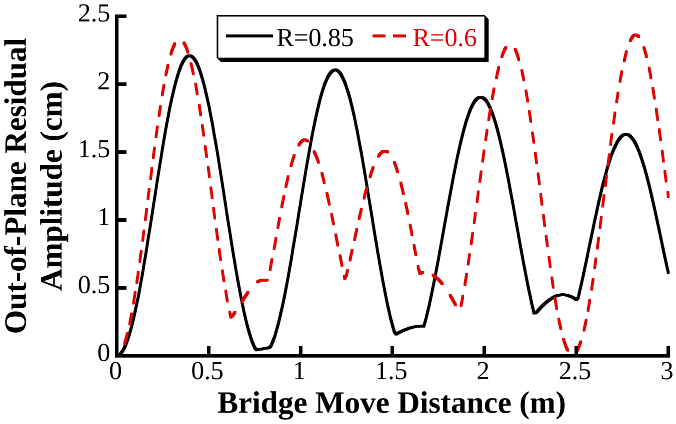

Figure 7.18: Out-of-Plane Residual Oscillation Amplitude vs. Bridge Move Distance

length of Hook 1 (i.e., configuration of the crane four-bar linkage) will cause the hooks to swing in the trolley direction. Figure 7.18 shows the residual swing amplitude in the trolley direction induced by bridge move distances between 0 m and 3 m and two different cable length ratios, $R = 0.85$ and $R = 0.6$. The peaks in the trolley swing amplitude curve (for the $R = 0.85$ case) approximately correspond to the peaks in the bridge swing amplitude curve shown in Figure 7.14. This makes sense because larger swings in the bridge direction correspond to a larger vertical deflection of the payload, thereby causing larger out-of-plane swing. However, note that the out-of-plane swing amplitudes are small relative to the swing induced in the bridge direction.

The behavior of the crane when it moves in the bridge direction strongly depends

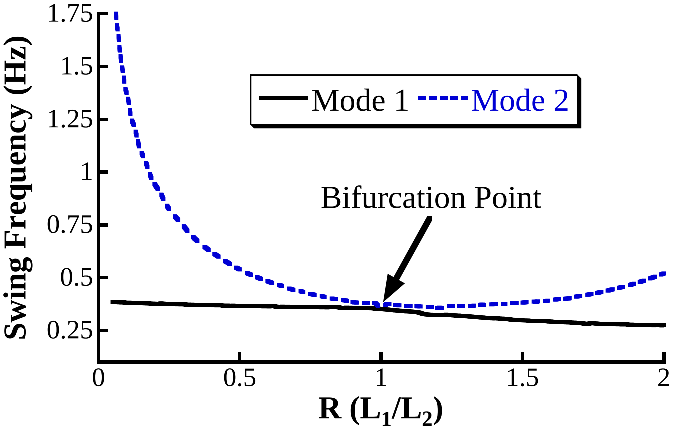

Figure 7.19: Bifurcation of the Swing Frequency Resulting from Varying the Cable Length Ratio

on the cable length ratio. This type of behavior is an example of bifurcation. Bifurcation occurs when changing the parameters of a system can result in a change in the behavior of the system. A small, continuous change in the value of one component (i.e., cable length ratio) results in a dramatic change in the system response. To further study this effect, the move distance was held constant at 2 m, and the cable length ratio was varied between 0 to 2. Figure 7.19 shows the frequencies of both modes in this parameter range. The bifurcation of the system frequency is clear in this figure. When $R = 1$, the system contains one frequency and both hook swings are identical, but as R varies below or above this bifurcation point, the behavior of the crane changes significantly. The response becomes a more complicated multi-mode swing.

The performance of a control system designed for a dual-hoist crane with equal cable lengths (i.e., one oscillation frequency) can begin to degrade as the cable lengths change (i.e., multiple oscillation frequencies arise). However, input shaping can easily deal with a system with a bifurcation. Robust input shapers can be designed to reduce the oscillation in a range of frequencies, regardless of whether both hooks oscillate with one frequency, or if there are multiple frequencies present. This is an example of another nonlinearity whose affects can be attenuated by input shaping.

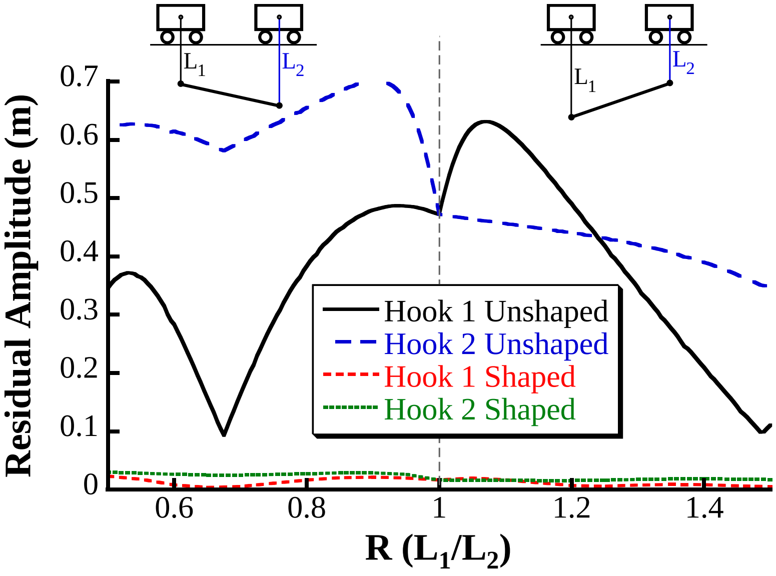

Figure 7.20: Bridge Oscillation Amplitude vs. Cable Length Ratio (R) with Input Shaping

Figure 7.20 shows the residual oscillation amplitude induced by 2 m bridge motions for cable length ratios between 0.5 and 1.5. The frequencies resulting from this range of parameters are approximately within the frequency range used to design the SI shaper in the top row of Table 7.1. Therefore, the same input shaper was used. Figure 7.20 also shows the swing amplitudes induced by shaped commands. Input shaping reduced the residual swing by an average of approximately 96%. Input shaping also reduced the out-of-plane residual swing by an average of approximately 99%.

The frequencies of oscillation induced by bridge motion, similar to the trolley motion, depend on the configuration of the crane (i.e., cable lengths, payload length, and trolley separation distance). In addition to these parameters, the payload mass also has an effect on the oscillation frequency. In the simulations above, the hook masses and payload mass were held constant at 7.65 kg and 2.5 kg, respectively. Increasing the payload mass (relative to the hook masses) increases the hook oscillation frequencies.

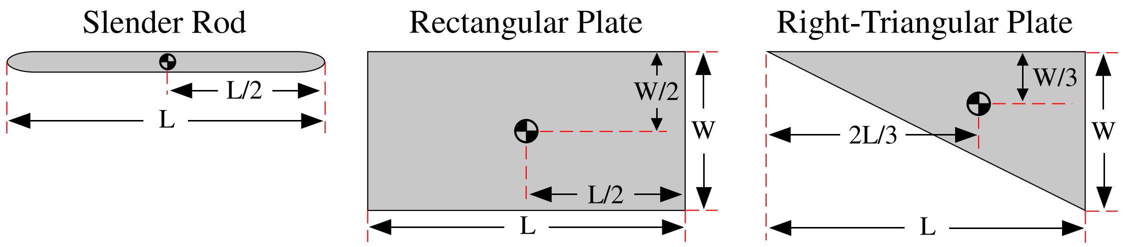

Figure 7.21: Side View of Various Payload Models

7.1.3 Effects of Payload Dynamics

So far in this investigation, the payload has been modeled as a slender rod. Although this simple model represents a large range of possible payloads, certain applications require the dual-hoist crane to lift distributed, or even non-uniform payloads. This section explores the important dynamic effects induced by more complicated payloads. The mass of the payload can also have a significant effect on the swing dynamics. However, this section focuses on analyzing the effects of varying the shape of the payload. The hook masses and payload mass were held constant at 7.65 kg and 2.5 kg, respectively.

Figure 7.21 shows the three different types of payloads used: slender rod, thin rectangular plate, and thin right-triangular plate. The rectangular plate is an example of a distributed payload whose center of mass is below the imaginary horizontal line connecting the two hooks. The right-rectangular plate is another example of a distributed payload whose center of mass is not only below the hooks, but also not centered between the two hooks.

The bridge was moved for a 1 m distance and both cable lengths were set to 1 m. A slender rod, $L = 2$ m, was used as the payload. This setup corresponds to Configuration A in Figure 7.2. Figure 7.22 shows the oscillation of Hook 1 induced by this set up; the oscillation of Hook 2 is identical to that of Hook 1. The hook oscillations strongly resemble a simple pendulum with a particle. The payload swing angles (γ and ψ) remain zero throughout the motion. The oscillation has one frequency of

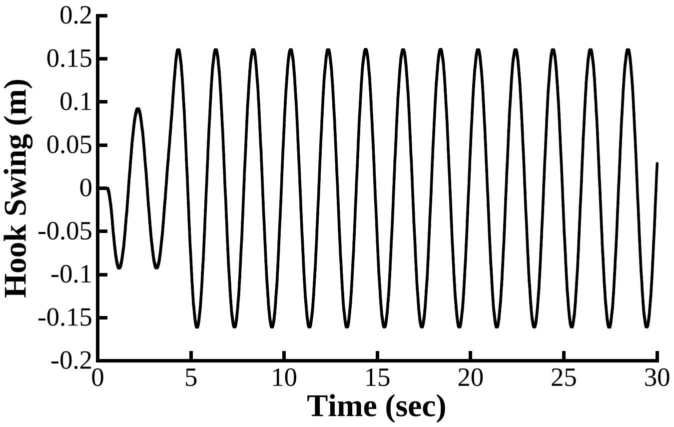

Figure 7.22: Hook Response with Slender Rod Payload

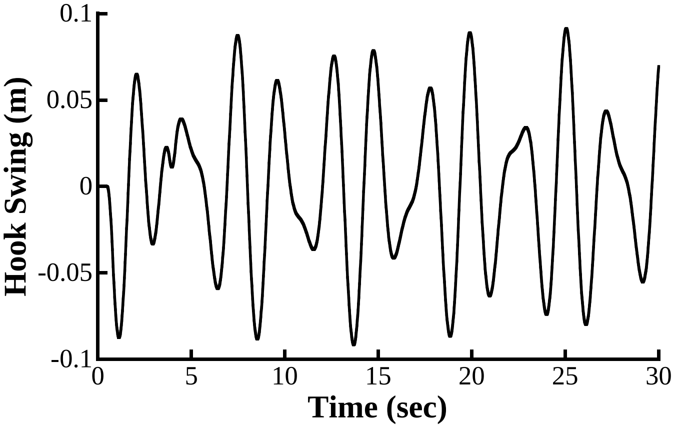

Figure 7.23: Hook Response with Rectangular Payload

approximately 0.5 Hz.

Figure 7.23 shows the oscillation Hook 1 for the same 1 m bridge motion, but with a rectangular plate, $L = 2$ m and $W = 2$ m, as the payload (Configuration A.2). The oscillation of Hook 2 is identical to Hook 1. Although the two suspension cables are equal, the hook oscillations have a two-mode response, with frequencies of 0.40 Hz and 0.57 Hz. The payload oscillates in the bridge direction (ψ) with a maximum peak-to-peak angle of 34° and has a dominant frequency of 0.40 Hz. The payload twist angle, γ remains zero; however, because the center of mass of the payload is equidistant from the two hooks.

Figure 7.24 shows the oscillation of both hooks for a 1 m bridge motion with a

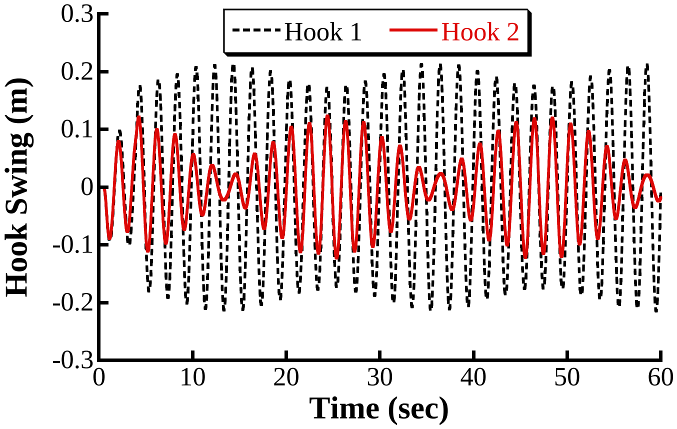

Figure 7.24: Hook Response with Right-Triangular Payload

right-triangular plate, $L = 2$ m and $W = 2$ m, as the payload (Configuration A.3). The hooks oscillate with two dominant frequencies, 0.54 Hz and 0.50 Hz. Notice the beating phenomenon present in the oscillations because the hook swings contain two similar frequencies. The payload swing angle, ψ, is again not zero, and has a dominant frequency of approximately 0.25 Hz. As a result, there are three significant frequencies in this case. In addition, unlike the rectangular-plate payload, the center of mass of the right-triangular payload is not equidistant from the two hooks. Therefore, moving in the bridge direction will not only cause the payload to swing in that direction, but will also produce a moment that will cause the payload to twist about its center of mass. As a result, the payload twist angle, γ, is also not zero (i.e., the oscillations of the two hooks are different).

The main factor that distinguishes a rod-type payload from a plate-type payload is the width. The larger width of the plate adds additional dynamic effects to the system, as shown in Figures 7.23 and 7.24. In order to determine the effect of varying the payload width on the swing frequency of the system, which is the main factor for designing effective input shapers, a 1 m bridge motion was repeated for rectangular plate widths between 0.1 m and 6 m. Figure 7.25 shows the resulting swing frequencies for suspension cable lengths of $L_1 = L_2 = 1$ m.

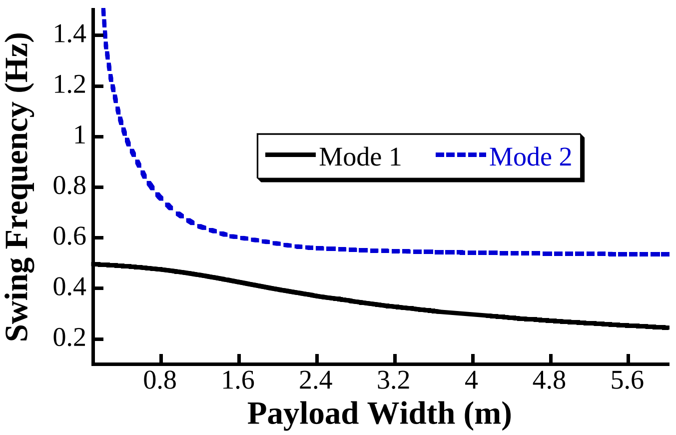

Figure 7.25: Swing Frequency vs. Rectangular Payload Width

There are two swing frequencies present. The Mode 1 frequency is approximately 0.5 Hz for small payload widths. This is the frequency of a simple pendulum with a cable length equal to the crane suspension cables ($L_1 = L_2 = 1$ m). However, as the width gets larger, the effective cable length (the suspension cable length plus the distance from the hooks to the center of mass of the payload) increases, resulting in a decrease in the swing frequency of Mode 1. The second mode frequency is very large when the payload width is small. This high-frequency oscillation of the payload does not significantly contribute to the oscillation of the hooks. However, as the payload width increases, the second mode frequency decreases and its contribution to the hook swings becomes more significant. The contribution of both modes to the dynamic response are most significant when the payload width is approximately two times the cable length (i.e., the distance from the top of the payload to its center of mass is similar to the cable length). In this configuration, the relative FFT magnitude of both modes are approximately equal.

The same analysis was performed with a right-triangular plate payload. Figure 7.26 shows the swing frequencies as a function of payload width for suspension cable lengths of $L_1 = L_2 = 1$ m. Unlike the results shown in Figure 7.25, the oscillation of the two hooks are not identical. This is because the the payload is not symmetric so

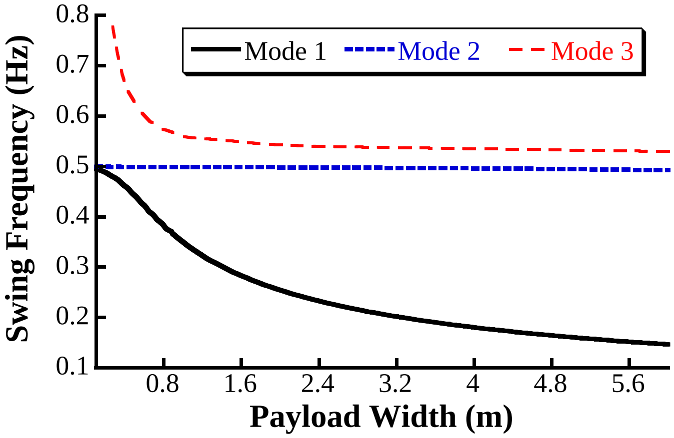

Figure 7.26: Swing Frequency vs. Right-Triangular Payload Width

as it moves along the bridge, it twists about its center of mass. Hook 1 is attached to the thinner end of the right-triangular plate (top, left point of the triangle in Figure 7.21). As a result, there is only one dominant mode present in the Hook 1 swing (labeled as Mode 2) even as the payload width is increased. The frequency of this mode is approximately 0.5 Hz (the frequency of a simple pendulum with a 1 m cable length). Hook 2, on the other hand, is attached to the thick side of the right-triangular plate, so its swing frequency varies as the payload width increases.

Mode 1 is associated with the payload swing and its frequency decreases rapidly as the payload width increases. This contribution of this mode is most significant when the payload width is comparable to the cable length. Mode 2 and Mode 3 are associated with the cable swings and payload twist. Mode 2 has an approximately constant frequency of 0.5 Hz. The Mode 3 frequency is very large for small payload widths (its contribution is small in this range). As the payload width increases, the Mode 3 frequency decreases and its contribution to the swing amplitude increases. This mode is significant throughout the majority of payload widths tested.

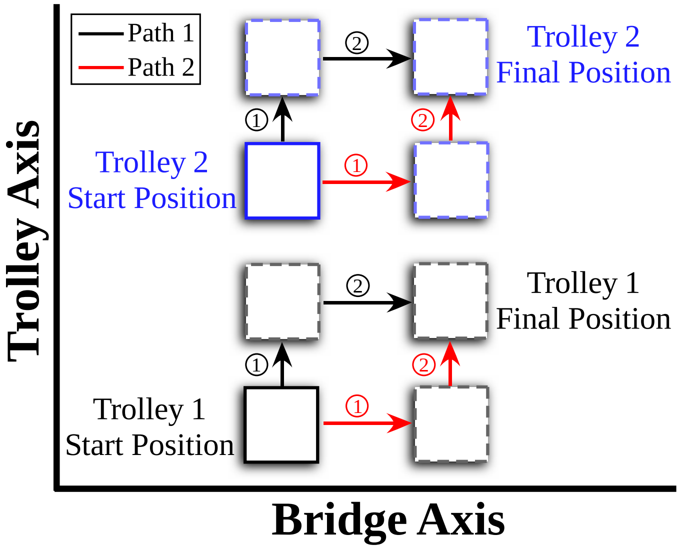

Figure 7.27: Coordinated Trolley-Bridge Movements

7.2 Coordinated Trolley-Bridge Motion

The previous section discussed the dynamic response and control of point-to-point crane motions. This section deals with coordinated trolley and bridge motions necessary to make L-shaped paths, which are commonly used in crane manipulation tasks (e.g., to go around obstacles or along predesignated paths). Figure 7.27 illustrates two possible crane movements that produce L-shaped paths. In one case, the trolleys first move along the trolley axis, then along the bridge axis. In the second case, the trolleys move along the bridge axis first, then along the trolley axis. If the move distances in each direction are kept constant, then both paths result in the same endpoint position of the trolleys.

Figure 7.28 shows the position of Hook 1 throughout the two possible paths shown in Figure 7.27. The trolley and bridge move distances were both set to 0.35 m and the hook cable lengths were set to: $L_1 = 1$ m and $L_2 = 2$ m. The slender rod was used as the payload. This setup corresponds to Configuration B in Figure 7.2. In both cases, the induced maximum residual amplitude is approximately 0.59 m. Therefore, the residual amplitude does not seem to be dependent on the direction of motion (i.e., if

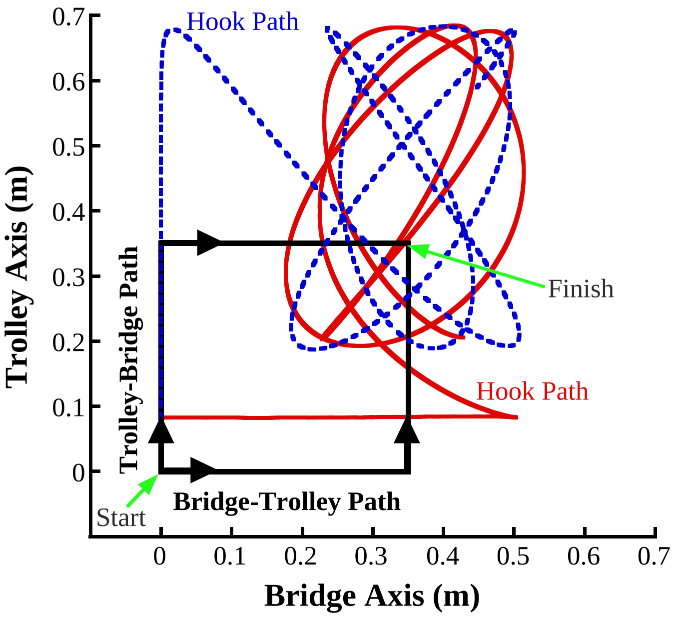

Figure 7.28: Hook Response to Coordinated Moves

the trolley is moved first or the bridge is move first).

To investigate whether the direction of motion affects the induced swing amplitude, the trolley and bridge axes were moved for distances between 0 m and 4 m in a coordinated maneuver. Figure 7.29 shows the induced residual oscillation amplitude. The dependence of the residual oscillation amplitude on the move distance has clearly been established up to this point. The residual oscillation contains peaks and troughs as the move distance varies. Figure 7.29 demonstrates that the direction of motion is not a significant factor on the residual amplitude. This makes sense because for the realistic motion parameters, the out-of-plane hook oscillations induced by bridge motions are small. If the crane moves faster, then the hooks will swing more, and this nonlinear effect will become more significant.

To demonstrate this point, the same L-shaped moves used to generate Figure 7.29 were repeated with double the maximum accelerations of the trolley and bridge (1 m/s^2 to 2 m/s^2) and triple the maximum velocities of the trolley (0.35 m/s to 1.05 m/s) and bridge (0.30 m/s to 0.9 m/s). Figure 7.30 presents the induced oscillation with the faster move parameters. The increased acceleration and velocity have two

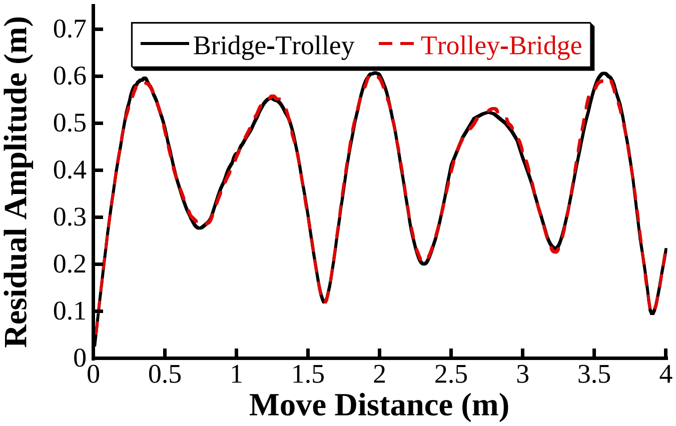

Figure 7.29: Oscillation Amplitude Induced by Various Coordinated Moves

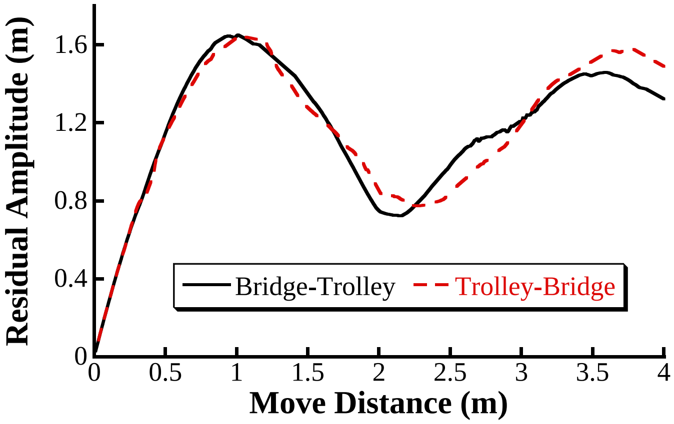

Figure 7.30: Oscillation Amplitude Induced by Various Coordinated Moves with Higher Velocity and Acceleration Limits

effects: *i)* the induced residual oscillation is larger and *ii)* the direction of motion (whether the bridge is moved first or the trolley is moved first) is significant.

The effect of input shaping on coordinated motions was also investigated. For a cable length ratio of $R = 0.5$, the oscillation frequencies are 0.54 Hz and 0.37 Hz in the bridge axis and 0.45 Hz in the trolley axis. These frequencies are relatively close to one another; therefore, an Extra-Insensitive (EI) shaper was designed for all three frequencies. An SI shaper could have been designed for this case as well; however, the EI shaper has closed-from solutions, so it is easier to design than the SI shaper, which has to be solved numerically. The EI shaper was designed for a nominal frequency

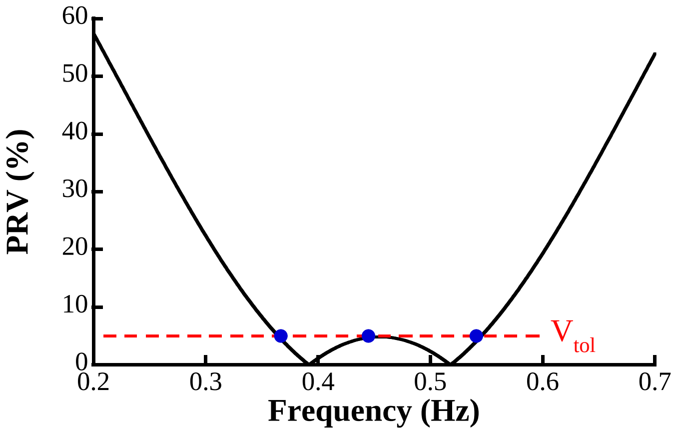

Figure 7.31: Sensitivity Curve of EI Shaper Designed for Coordinated Moves

of 0.455 Hz. The shaper amplitudes and times are given in the second row of Table 7.1. Figure 7.31 shows the sensitivity plot for this input shaper. All three system frequencies, as indicated by circles on the figure, have a percent residual vibration (PRV) of less than 5%.

Figure 7.32 shows the position of Hook 1 throughout the same coordinated motions as those shown in Figure 7.28. However, the trolley and bridge velocities were shaped by the EI shaper given in Table 7.1. The crane travels from its starting position to its final position without inducing large hook swings. The maximum residual swing induced in either case is approximately 0.03 m.

To further test the effectiveness of the EI shaper, it was applied to a larger range of moves. The cable length ratio was held constant at $R = 0.5$, and the coordinated move distance was varied between 0 m and 4 m. Figure 7.33 shows the unshaped and shaped residual oscillation induced by bridge-trolley (BT) and trolley-bridge (TB) motions. The EI shaper reduced the residual oscillation amplitude by an average of approximately 95% in both cases.

The moves were repeated, but with the same higher acceleration and velocity limits as those used to produce Figure 7.30. Figure 7.34 shows the resulting oscillation amplitude for both unshaped and EI-shaped commands. Even though the unshaped

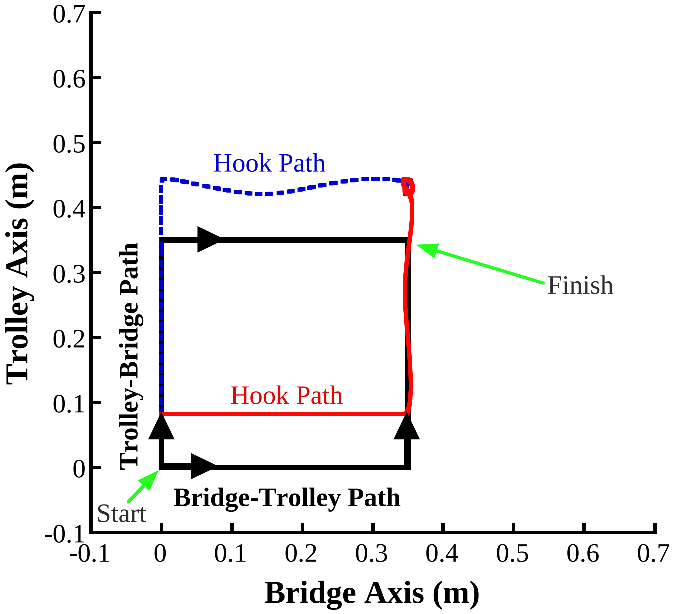

Figure 7.32: Sample Shaped Coordinated Moves

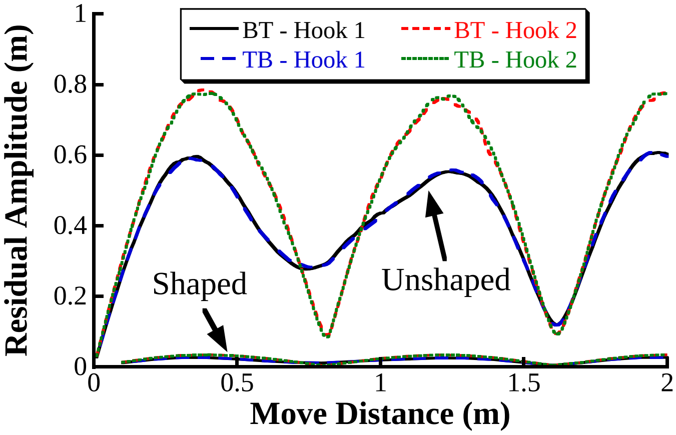

Figure 7.33: Oscillation Amplitude Induced by Various Input-Shaped Coordinated Moves

oscillation amplitude depends on the path, the input shaper reduces the swing to near-zero amplitudes, essentially eliminating the effect of path direction. The EI shaper reduced the residual oscillation amplitude by an average of 95% for the parameters evaluated in Figure 7.34. In this case, the robust EI shaper has essentially removed the nonlinear effects caused by the more aggressive commands. Recall that in Chapter 5, the nonlinear effects introduced by more aggressive slewing commands were also greatly attenuated by using robust input-shaping control.

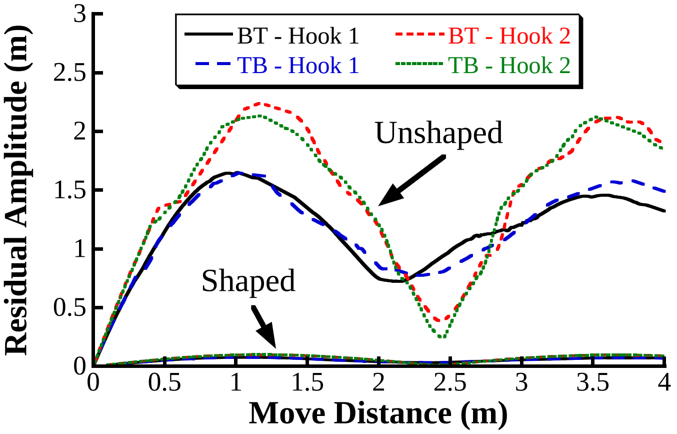

Figure 7.34: Oscillation Amplitude Induced by Various Input-Shaped Coordinated Moves with Higher Velocity and Acceleration Limits

Table 7.2: Nominal Dual-Hoist Crane Experiment Parameters

Parameter	Value
Hook Mass	7.65 kg
Payload Mass & Length	2.2 kg & 2.6 m
Trolley Separation Distance	2.6 m
Max Trolley Acceleration & Velocity	1 m/s^2 & 0.35 m/s
Max Bridge Acceleration & Velocity	1 m/s^2 & 0.30 m/s

7.3 Experimental Testing

The two-ton dual-hoist bridge crane presented in Chapter 3 was used to experimentally verify the simulation model and the dynamic behavior of dual-hoist cranes. A long, slender rod was used as the payload. Table 7.2 gives the nominal crane and payload parameters used throughout these experiments.

Figure 7.35 shows the response of both hooks to a 1 m trolley motion. Both trolleys were moved simultaneously to keep the trolley separation approximately constant. The hook deflection was recorded with a camera attached underneath the trolleys. The suspension cable lengths of both trolleys were held constant at approximately 1.3 m. Note that the hook swing amplitudes decrease slightly over time. This is due to the effect of a small amount of damping presents in the real crane, which was not modeled in the simulation.

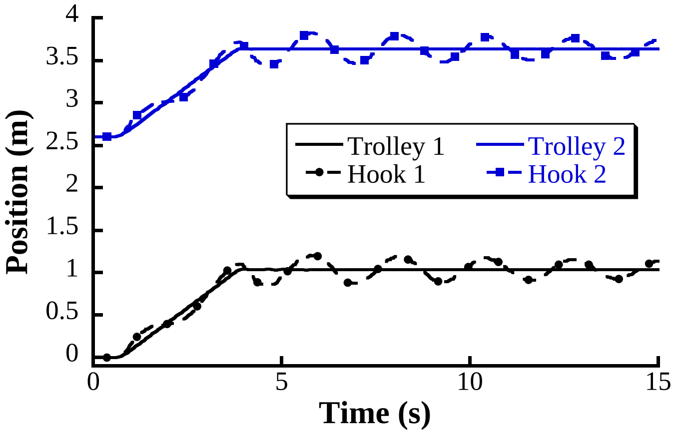

Figure 7.35: Experimental Hook Oscillation Induced by 1 m Trolley Motion

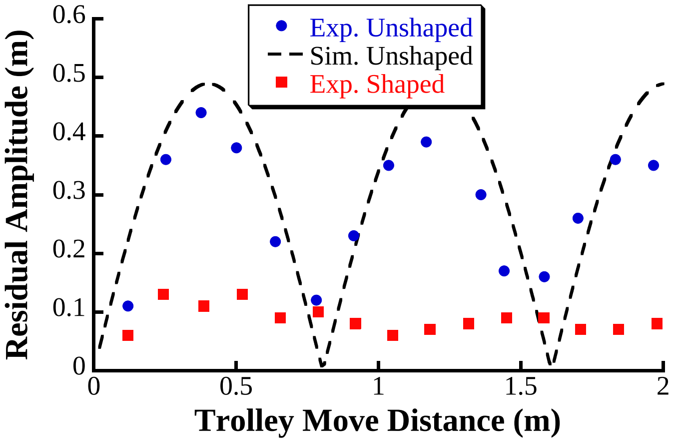

Figure 7.36: Experimental Residual Oscillation vs. Trolley Move Distance

The trolley motion was repeated for distances between 0.1 m and 2 m. Figure 7.36 shows the resulting peak-to-peak residual oscillation amplitude for Hook 1. The figure also shows the simulation results. The experimental and simulation results follow very similar trends. The amplitude curves contain peaks and troughs as the move distance varies. The experimental peaks; however, get smaller as the distance gets larger. This is due to the damping effect. Figure 7.36 also shows the residual swing induced by ZV-shaped commands for the same range of trolley motions. The ZV shaper was designed for a frequency of 0.43 Hz (which is approximately the frequency of a simple pendulum with a 1.3 m cable length). The ZV shaper reduced the residual oscillation

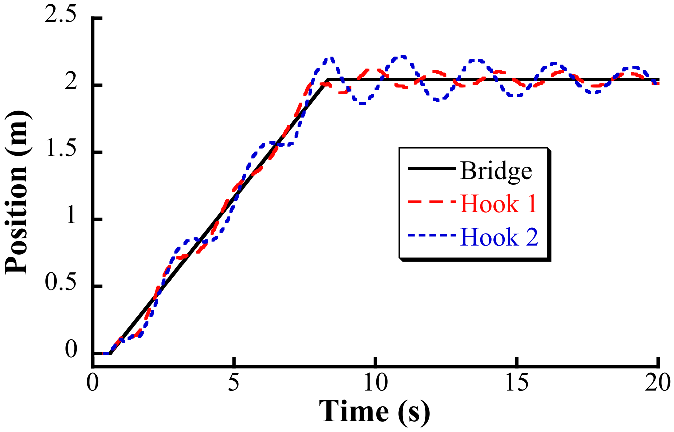

Figure 7.37: Experimental Response Induced by 2 m Bridge Motion

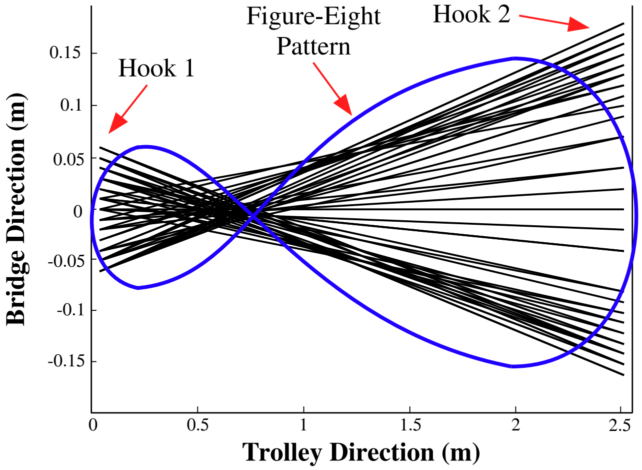

Figure 7.38: Top View of Hook Responses Induced by 2 m Bridge Motion

by approximately 70% over the entire range of move distances.

To investigate the effects of non-planar motion, the trolleys were kept stationary and the bridge was moved 2 m. The suspension cable lengths were set to 1.3 m and 2 m for trolley 1 and 2, respectively. Figure 7.37 shows the system response. The oscillations of the hooks exhibit two-mode behavior and are sometimes in phase and sometimes out of phase. Figure 7.38 shows a top view of the oscillation. The solid lines connecting Hook 1 and 2 represent the payload. Note that oscillation resembles a figure-eight when viewed from above. A figure-eight pattern has been overlaid on top of the figure for clarity.

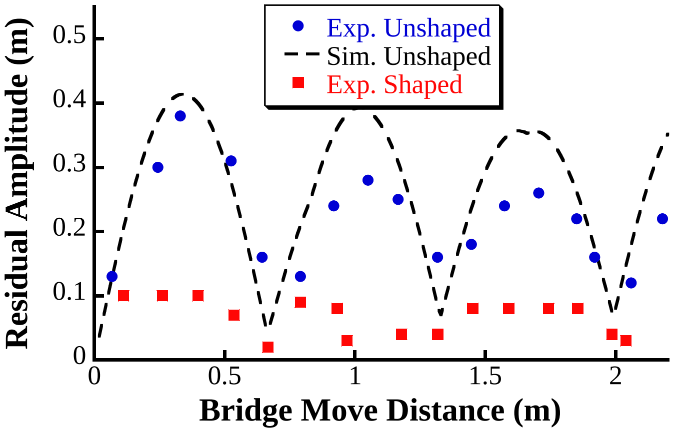

(a) Hook 1

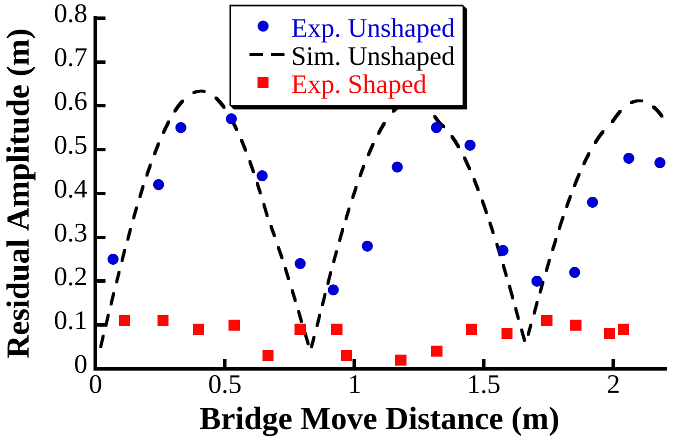

(b) Hook 2

Figure 7.39: Experimental Residual Oscillation vs. Bridge Move Distance

The bridge motion was repeated for distances between 0.1 m and 2.3 m. Figure 7.39 shows the resulting peak-to-peak residual oscillation amplitude for both hooks. There is good correlation between the experimental and simulation results. Note however that because of the damping present in the actual crane, the agreement between the simulation and experimental data slightly decreases for longer move distances. Figure 7.39 also shows the residual oscillation amplitude induced by ZV-shaped commands. The two-mode ZV shaper was designed for frequencies of 0.36 Hz and 0.45 Hz (zero damping was assumed). The ZV shaper reduced the residual oscillation by averages of 70% and 80% in Hook 1 and Hook 2, respectively.

To investigate the performance of a more robust input shaper, the move distance

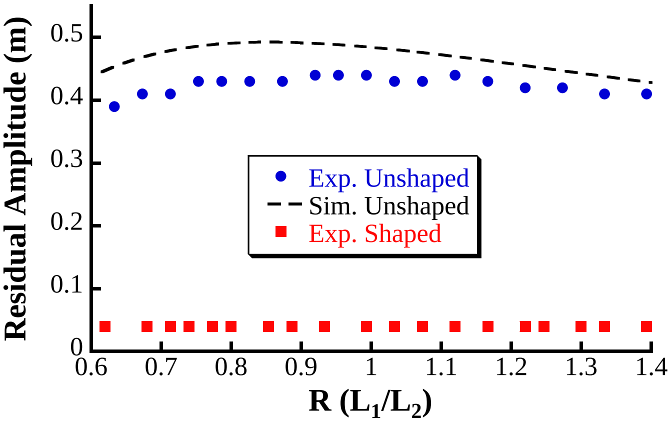

Figure 7.40: Experimental Residual Oscillation vs. Cable Length Ratio for Trolley Motions

was held constant and the suspension cable lengths were varied. Varying the suspension cable lengths changes the oscillation frequency, thereby testing the robustness of the input shaper. Figure 7.40 shows the residual oscillation of Hook 2 induced by a 1.2 m trolley move for cable length ratios (R) of 0.6 to 1.4. The length of Cable 2 was held constant at 1.5 m and the length of Cable 1 was varied. The experimental and simulation data follow very similar trends. To reduce the residual swing, a one-mode SI shaper was designed. Although the system has two oscillation frequencies that vary, the two ranges of frequencies were close enough to be suppressed with a one-mode SI shaper. The SI shaper was designed to suppress the residual oscillation to below 5% of the unshaped value for frequencies between 0.375 Hz and 0.55 Hz. The amplitudes and times of the SI shaper are provided in the last row of Table 7.1. The robust SI shaper reduced the residual amplitude of both hooks by approximately 91% over the range of cable ratios tested.

A similar test was repeated for a bridge move of 1.2 m. Figure 7.41 shows the resulting Hook 2 residual swing for cable length ratios between 0.6 and 1.4. The experimental results correlate well with the simulation data. Input shaping was applied to this set of tests as well. The same SI shaper used to produce the shaped results in Figure 7.40 was used. The SI shaper reduced the residual oscillation by

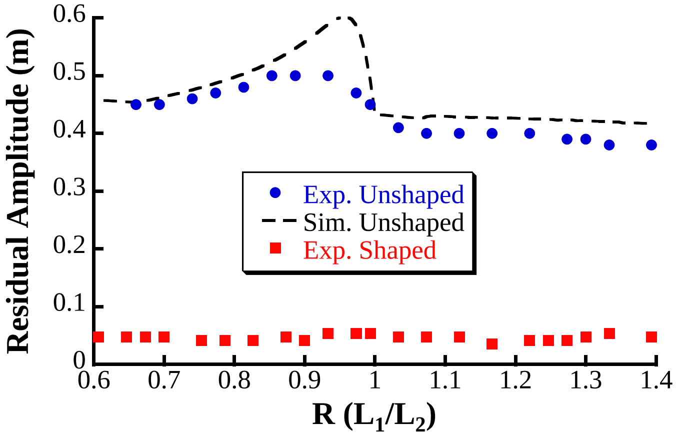

Figure 7.41: Experimental Residual Oscillation vs. Cable Length Ratio for Bridge Motions

approximately 85% and 90% in Hook 1 and Hook 2, respectively.

7.4 Summary

This chapter investigated the dynamic response of dual-hoist bridge cranes. Both planar and out-of-plane motions were studied and the complex dynamic behavior of the crane was analyzed. The major contributions of this chapter are:

- The swing frequency is strongly dependent on the crane configurations. For configurations that do not place the suspension cables at a large initial angle, the actual frequency can be accurately predicted using a linearized pendulum model. Otherwise, the actual frequency deviates significantly from the theoretical prediction.
- Motion in the bridge direction was shown to produce a bifurcation - the dynamics exhibited single-mode or two-mode dynamics depending on if the suspension cables were equal or not. Robust input shaping was shown to be able to mitigate the effects of this nonlinearity and reduce the residual swing across a large range of cable length ratios.
- It was shown that moving the bridge also induced oscillation in the perpendicular direction (i.e., trolley direction) because of the four-bark linkage constraints.

- Three types of payloads were studied. It was shown that more complex payloads, such as rectangular or right-triangular payloads, produce additional oscillation modes related to payload swinging and twisting.
- The dynamics of coordinated trolley/bridge motions were analyzed. It was shown that for aggressive motion commands, the direction of motion became significant. However, the effects of this nonlinearity were essentially eliminated with input shaping.
- Experiments on the two-ton dual-hoist bridge crane were used to verify the theoretical responses and the effectiveness of input shaping. Input shaping reduced the residual oscillation by 70% or greater in every case tested.

CHAPTER VIII

OPERATOR STUDIES

To experimentally evaluate the effectiveness of input-shaping control on human-operated nonlinear cranes, a series of operator performance studies were conducted on the small-scale mobile boom crane and the two-ton dual-hoist bridge crane. The details of the obstacle course and the results of the boom crane operator study are presented in Section 8.1. The course designed for the dual-hoist bridge crane, along with the study results, are presented in Section 8.2.

8.1 Mobile Boom Crane

8.1.1 Obstacle Course

Figure 8.1 shows the obstacle course used for the operator studies presented in this section. Completing the course required driving, steering, and slewing. The opera-

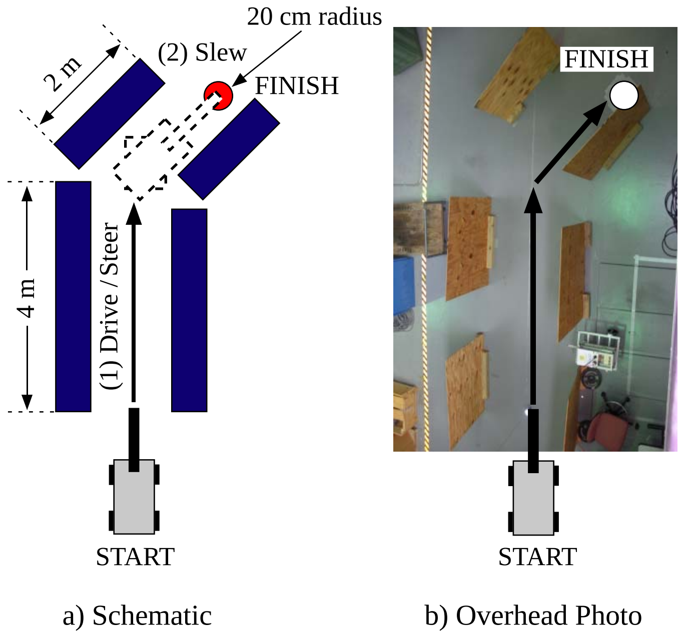

a) Schematic b) Overhead Photo

Figure 8.1: Obstacle Course for Boom Crane

tors were not required to luff or hoist. The course was designed so that during the first stage, the operators used a combination of driving and steering to move the crane approximately 4 m straight through the course. During the second stage, the operators used the slewing motion to position the payload in the target zone. The target was a circle with a 20 cm radius. The task was complete once the payload settled completely within the target zone. The operators were allowed to use any combination of driving, steering, and slewing to complete the course.

Each operator completed the course under four different conditions:

- Unshaped commands with a single-pendulum payload
- One-mode SI shaped commands with a single-pendulum payload
- Unshaped commands with a double-pendulum payload
- Two-mode SI shaped commands with a double-pendulum payload

The single-pendulum payload consisted of the suspension cable and hook (0.63 kg). The suspension cable length was held constant at 155 cm. To create the double pendulum, an additional mass of 0.2 kg was attached to the hook with a rigging cable length of 65 cm. The suspension cable was hoisted up to 90 cm so that the total length remained 155 cm. The luffing angle was held constant at 55° for both payloads. The order of the four tests was chosen randomly for each operator.

Before the operators began the tests, they were provided 15 minutes of basic training in crane operation. In order to provide consistency, all operators completed the same training exercises during the same amount of time. The training tasks and their durations were:

1. Driving with both shapers - 3 minutes
2. Unshaped driving and slewing - 9 minutes
3. Slewing with both shapers - 3 minutes

The first training exercise familiarized the operator with the acceleration and deceleration rates of the mobile base. The second task was vital to help the operator complete the course within a reasonable amount of time using unshaped commands. The operators practiced how to manually break up their unshaped commands into multiple steps in order to reduce the payload oscillation. Task 3 was designed to familiarize the operator with the acceleration and deceleration rates of the slewing motion.

A Siemens Touchscreen Mobile Panel was used as the control interface. The mobile panel communicates wirelessly with the boom crane. Therefore, the operators were free to walk around and stand anywhere in the workspace.

8.1.2 Input Shaper Design

For this operator study, Specified Insensitivity (SI) shapers were utilized. For the single-pendulum payload, a one-mode SI shaper was designed. The tolerable vibration percentage, V_{tol}, was set to 5% for the frequency range from 0.35 Hz to 0.75 Hz. This range corresponds to the swing frequencies that occur throughout a large portion of the crane workspace. It was assumed that the damping ratio of the payload oscillation was approximately zero. The SI shaper times and amplitudes were obtained as

$$\begin{bmatrix} A_i \\ t_i \end{bmatrix} = \begin{bmatrix} 0.158 & 0.321 & 0.0430 & 0.321 & 0.158 \\ 0 & 0.894 & 1.37 & 1.85 & 2.74 \end{bmatrix} \tag{8.1}$$

The frequency range selected suppresses the frequency of a pendulum with a cable length ranging from 0.44 m to 2 m. Although the suspension cable length does not vary during the operator study, the added robustness of the SI shaper can compensate (to some degree) for the nonlinearities that exist in the mobile boom crane.

A two-mode SI shaper was designed for the double-pendulum payload. For frequencies between 0.3 Hz and 0.7 Hz, V_{tol} was set to 5%, and for frequencies between 1 Hz and 1.9 Hz, V_{tol} was set to 10%. The times and amplitudes of the two-mode SI shaper for these suppression constraints are

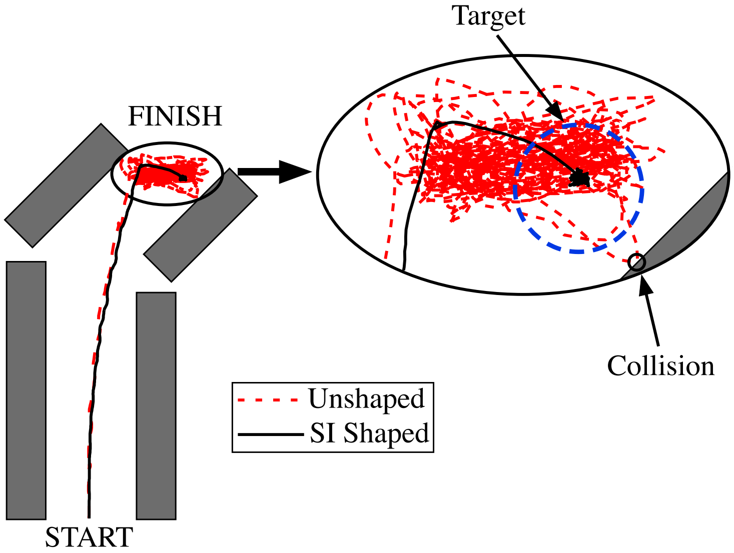

Figure 8.2: Sample Boom Crane Operator Trial

$$\begin{bmatrix} A_i \\ t_i \end{bmatrix} = \begin{bmatrix} 0.0842 & 0.0696 & 0.124 & 0.155 & 0.135 & 0.155 & 0.124 & 0.0696 & 0.0842 \\ 0 & 0.452 & 0.913 & 1.33 & 1.78 & 2.23 & 2.64 & 3.10 & 3.56 \end{bmatrix} \quad (8.2)$$

Note that this is the same input shaper used in Chapter 5. This two-mode suppressing shaper is only 0.82 s longer than the single-mode shaper in (8.1).

8.1.3 Operator Study Results

Figure 8.2 shows the hook position throughout the obstacle course during a typical test. The payload position has been overlaid on a sketch of the obstacle course for reference. Without shaping, the payload experiences large oscillations that make positioning of the payload very challenging, especially when the payload gets close to the target zone, as shown on the right side of Figure 8.2. The large oscillations even led to a collision with an obstacle. Input shaping, however, was able to substantially decrease the payload oscillation. This made it much easier for the operator to maneuver and accurately position the payload.

Figure 8.3 shows a sample timeline of an operator's button-pushing efforts. Buttons pressed simultaneously are shown stacked on top of each other. The top row in the

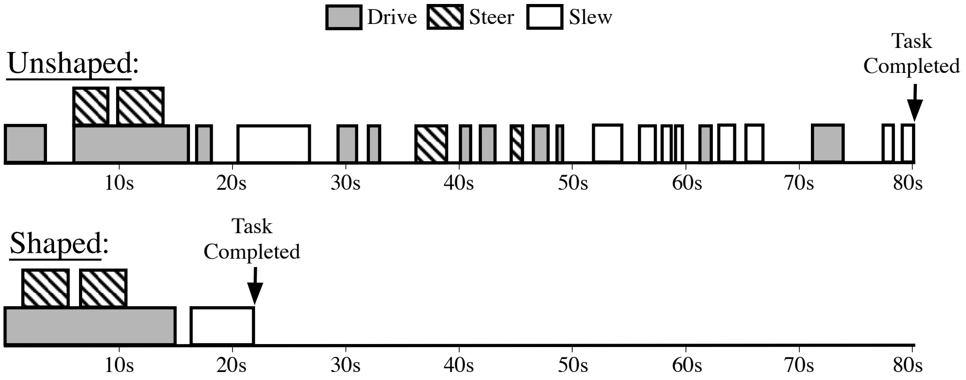

Figure 8.3: Timeline of Button Pushes for a Sample Boom Crane Trial

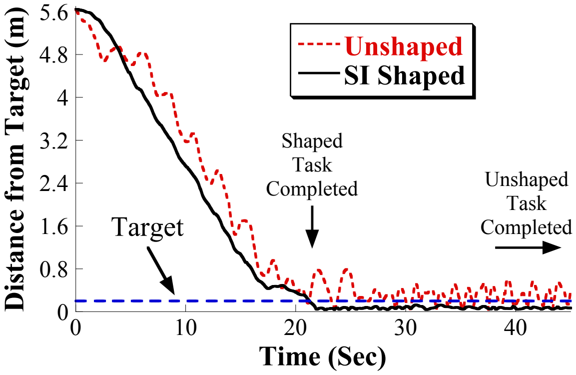

Figure 8.4: Distance to Center of Target During a Sample Boom Crane Trial

figure shows the complex series of button pushes that was used without input shaping. With input shaping, there were very few button pushes. The overall completion time was also much shorter with shaping. In both cases, the majority of the distance was traversed within the first few button pushes, as shown in Figure 8.4. The line labeled "Target" in Figure 8.4 represents a 20 cm distance from the center of the target circle. Therefore, the distance curves must be below this line for the task to be complete. For the unshaped case, the majority of button pushes occurred when the payload was close to the target zone. The operator utilized numerous short button pushes in an attempt to reduce the oscillation. There were also several periods without any button pushes during which the operator was planning his/her next move and waiting for the right time to move the crane.

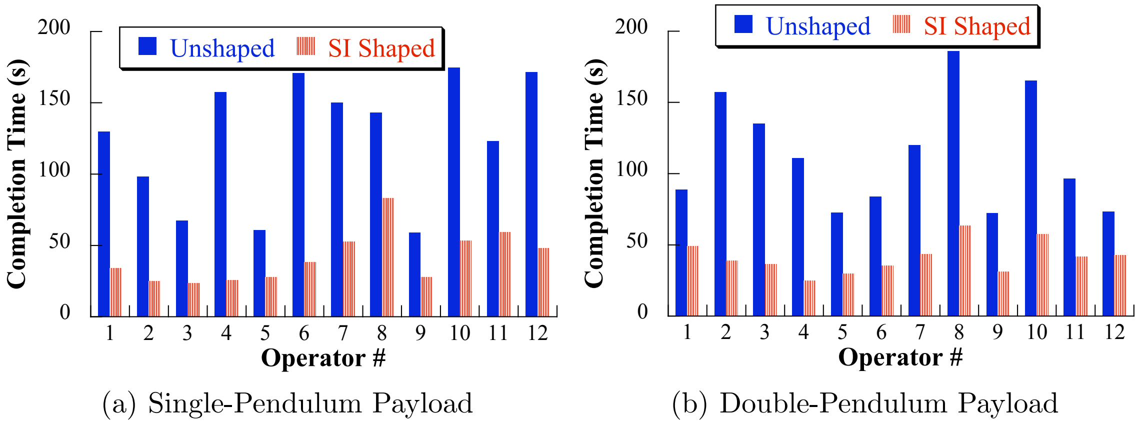

(a) Single-Pendulum Payload (b) Double-Pendulum Payload

Figure 8.5: Boom Crane Completion Times

For every trial, the completion time, the number of button pushes, the maximum peak-to-peak residual vibration amplitude, and the number of collisions were recorded. The completion time is the time from the first button push to when the payload settled within the target zone. The number of button pushes is an indication of the effort the operator exerts to complete the task. The higher the number of pushes, the more effort and concentration the operator must exert in order to complete the task. The maximum residual vibration amplitude is the maximum peak-to-peak payload oscillation once the swing has settled within the target zone. For the double-pendulum payload, the maximum oscillation of the hook was measured.

Figure 8.5(a) shows the completion times for unshaped and SI-shaped single-pendulum trials for all 12 operators tested. The average completion time without shaping was 126 s. It was only 41.5 s when shaping was utilized, a 67% reduction. Operator 4 experienced the greatest improvement (84%) when SI shaping was utilized. Operator 8 experienced the least improvement (42%).

Figure 8.5(b) shows the completion times for unshaped and two-mode SI shaping when the double-pendulum payload was used. The average completion time for the unshaped trials was 113 s. Input shaping reduced the average completion time to 41.2 s, a 64% reduction. Operator 4 again experienced the greatest improvement (78%) when SI shaping was utilized. Operator 12 experienced the least improvement (41%).

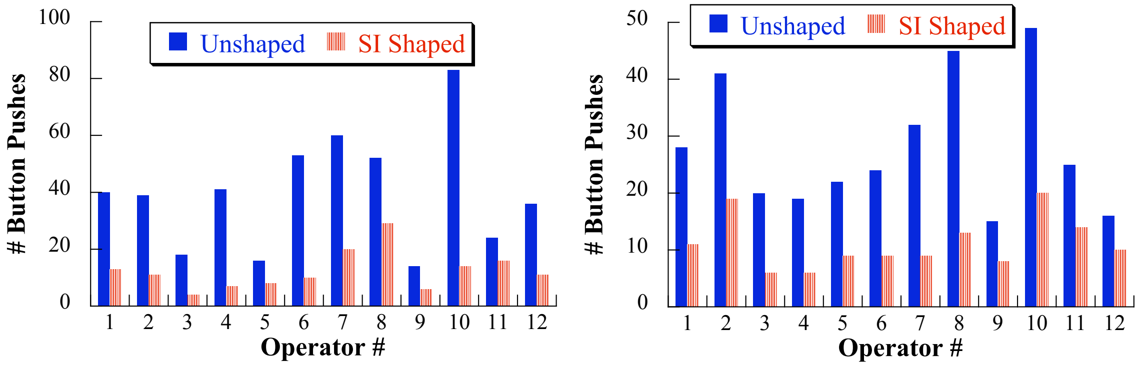

(a) Single-Pendulum Payload (b) Double-Pendulum Payload

Figure 8.6: Boom Crane Button Pushes

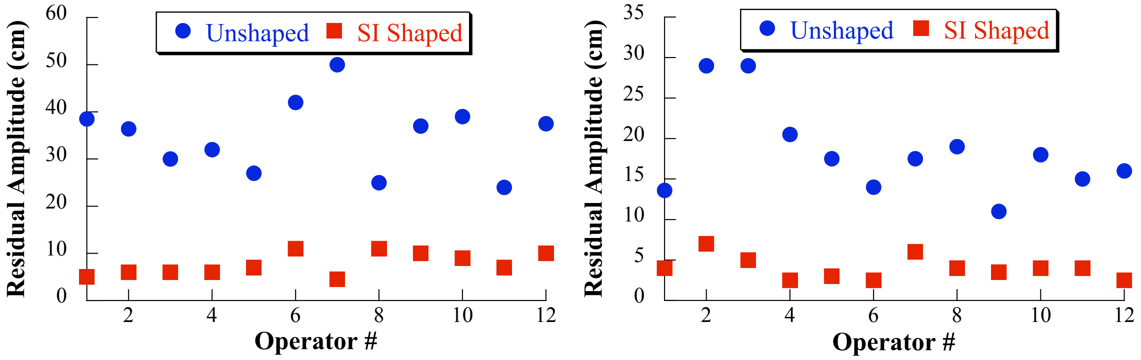

(a) Single-Pendulum Payload (b) Double-Pendulum Payload

Figure 8.7: Boom Crane Residual Vibration Amplitude

Figure 8.6(a) shows the number of button pushes for unshaped and SI-shaped single-pendulum trials. The average number of button pushes without shaping was 39.7, but only 12.4 with shaping, a 69% reduction. Figure 8.6(b) shows the number of button pushes for the double-pendulum trials. The average number of button pushes for the unshaped trials was 28. It was only 11.2 when input shaping was used, a 60% reduction.

Figure 8.7(a) shows the maximum residual vibration amplitude for unshaped and SI-shaped single-pendulum trials. The average maximum residual amplitude without shaping was 34.9 cm and only 7.7 cm with shaping, a 78% reduction. Note that the maximum residual oscillation of operators 6 and 7 exceed the 40 cm diameter of the target zone. In order to avoid frustrating the operators, if they stopped actively trying

Table 8.1: Summary of Boom Crane Operator Study Results

Trial Type	Unshaped Ave.	Shaped Ave.	% Red.
Completion Time, SP	126 s	41.5 s	67%
Completion Time, DP	113 s	41.2 s	64%
Button Pushes, SP	39.7	12.4	69%
Button Pushes, DP	28	11.2	60%
Vibration Amplitude, SP	34.9 cm	7.7 cm	78%
Vibration Amplitude, DP	18.3 cm	4 cm	78%

to reduce the payload oscillation (i.e., pushing buttons on the control panel), the task was considered to be complete. The operators, however, were only allowed to "give up" after trying for at least two minutes. Both operators 6 and 7 had completion times of larger than 150 s, as shown in Figure 8.5(a).

Figure 8.7(b) shows the maximum residual vibration amplitude for the double-pendulum trials. The average maximum residual amplitude for the unshaped trials was 18.3 cm and only 4 cm with shaping, a 78% reduction. Table 8.1 summarizes the results of the operator study. Input shaping provided 60%-78% improvements in all of the performance measures.

There were a total of 39 collisions for the unshaped trials (27 with the single pendulum and 12 with the double pendulum). However, there were only 3 collisions for all the shaped trials (all 3 with the double pendulum). The collisions with input-shaping control occurred when operators overshot the target, whereas the unshaped collisions were caused by the large payload oscillations resulting from unshaped slewing and driving commands.

8.1.4 Statistical Analysis and Discussion

Analysis of variance (ANOVA) tests were conducted to measure the statistical significance of the differences between the unshaped and shaped results. Because the same group of 12 operators performed both the unshaped and shaped trials, one-way repeated ANOVA tests (Paired t-Tests) were used. A 95% confidence was used for all

Table 8.2: Summary of Boom Crane ANOVA Results

Trial Type	F-value/F_{crit}	P-value
Completion Time, SP	13.5	<0.0001
Completion Time, DP	12.9	<0.0001
Button Pushes, SP	6.5	0.0003
Button Pushes, DP	11.9	<0.0001
Vibration Amplitude, SP	30.2	<0.0001
Vibration Amplitude, DP	24.0	<0.0001

tests. The analysis was done on the completion time, button pushes, and maximum residual amplitude data.

Table 8.2 shows the results of the ANOVA analysis. Both the F-values and the P-values are presented. The F-value is the ratio of the variation between the two groups (unshaped and shaped data) to the variation within each group. An F-value greater than the F_{crit} value indicates that the variation between the two groups is significant. (The F_{crit} value for a data set with 2 groups and a total sample size of 24 is approximately 4.3.) The P-value measures the probability that there is a statistical difference between the averages of the unshaped and shaped results. Small P-values (less than 0.05) indicate a low probability that the difference between the unshaped and shaped results is due to random chance. The results of the ANOVA tests provide strong evidence that the one-mode and two-mode SI shapers were effective in decreasing the completion time, lowering the number of button pushes, and reducing the maximum residual swing amplitude.

In addition to the parameters measured, each operator was asked to fill out a questionnaire after completing the testing. The operators were asked to qualitatively evaluate the SI shapers, to compare the single and double-pendulum trials, and to select the task that required the least effort on their part. All twelve operators stated that input shaping made the task much easier to complete. This is not surprising because with shaping, moving the crane body was approximately equivalent to moving the payload. Almost all operators also stated that the double-pendulum payload was more difficult to control than the single-pendulum, and that the shaped single-pendulum trial was the easiest of the four tasks.

8.2 Dual-Hoist Bridge Crane

8.2.1 Obstacle Course

Figure 8.8 shows a sketch of the obstacle course designed to test operators of the dual-hoist bridge crane. The operators were asked to maneuver a long, slender payload along a ∩-shaped path between two obstacles. Initially, the payload was positioned in the start rectangle on the left-hand side of the obstacles. The operators were allowed to use any combination of trolley and bridge motions to move the payload to the finish rectangle on the right-hand side of the obstacles. The task was complete when the payload was settled approximately within the target rectangle. The target rectangle had a length and width of 2.9 m and 0.3 m, respectively. Table 8.3 presents important crane and payload parameters for the study.

Each operator completed the course under four different conditions:

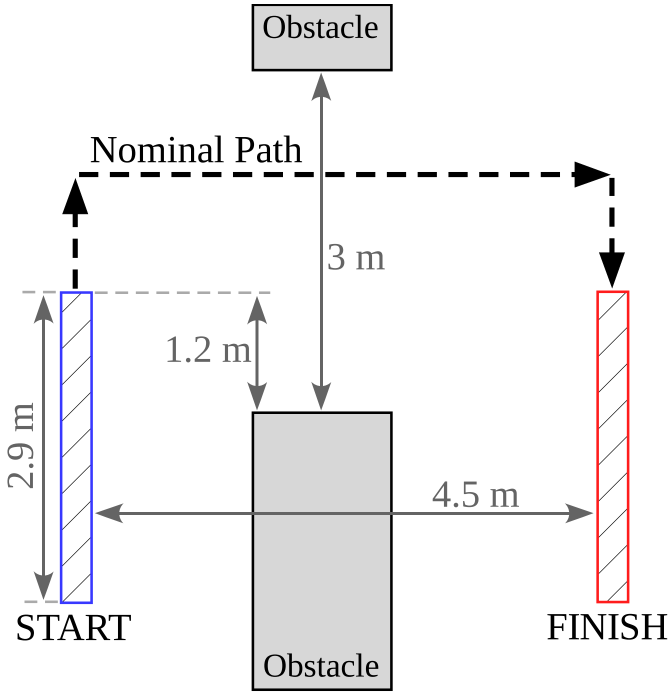

Figure 8.8: Obstacle Course for Dual-Hoist Bridge Crane

Table 8.3: Dual-Hoist Bridge Crane Setup for Operator Study

Parameter	Value
Suspension Cable Length	2.35 m
Cable Length Difference, ΔL	0.40 m
Payload Length & Width	2.6 m & 0.1 m
Payload Mass	2.2 kg
Trolley Separation Distance	2.6 m

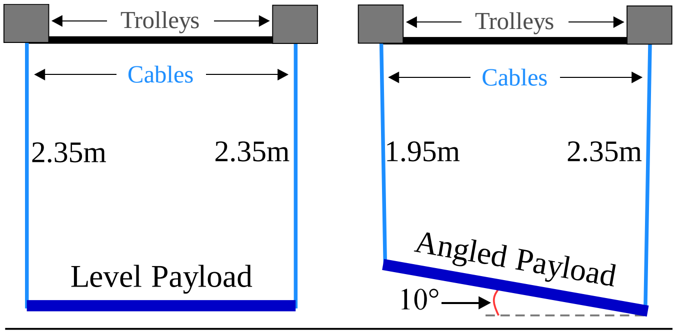

Figure 8.9: Side View of Payloads

- Level payload without input shaping
- Level payload with input shaping
- Angled (10°) payload without input shaping
- Angled payload with input shaping

The level payload was created by setting both suspension cable lengths to 2.35 m, as shown in Figure 8.9. This placed the payload right above the ground. To create the angled payload, the length of one cable was decreased to 1.95 m to create a 10° angle with respect to the ground. The angled payload is also shown in Figure 8.9.

A Siemens Touchscreen Mobile Panel was used to drive the bridge crane. The mobile panel communicates wirelessly with the crane; therefore, the operators were free to walk around and stand anywhere in the workspace. Before the operators began the tests, they were provided with fifteen minutes of basic training in crane operation. During this practice time, the operators moved the crane under all four test conditions outlined above and became familiar with the crane and the user interface.

Table 8.4: **Input Shapers for Dual-Hoist Bridge Crane Operator Study**

ZV, Level	Amplitudes	0.51	0.49		
	Times (s)	0	1.548		
ZV, Trolley & Angled	Amplitudes	0.51	0.49		
	Times (s)	0	1.409		
ZV, Bridge & Angled	Amplitudes	0.26	0.25	0.25	0.24
	Times (s)	0	1.389	1.515	2.904

8.2.2 Input Shaper Design

Zero vibration shapers were designed for this operator study. The swing frequency and damping ratio of the crane for the level-payload configuration in both the trolley and bridge directions were approximately 0.32 Hz and 0.008, respectively. The amplitudes and times of the ZV shaper are presented in the top row of Table 8.4.

For the angled payload, the oscillation frequencies were different in the trolley and bridge direction. The frequency and damping ratio in the trolley direction were approximately 0.35 Hz and 0.008, respectively. The ZV shaper designed for the trolley direction is shown in the second row of Table 8.4. The frequencies and damping ratio in the bridge direction were approximately 0.33 Hz, 0.36 Hz, and 0.008, respectively. Note that there are two frequencies present in the bridge direction. Therefore, a two-mode ZV shaper was designed. The amplitudes and times of the two-mode ZV shaper are given in the last row of Table 8.4.

8.2.3 Operator Study Results

Figure 8.10 shows the position of the hook attached to the shorter suspension cable throughout the obstacle course during a typical angled-payload test. The hook position has been overlaid on a sketch of the obstacle course for reference. Without shaping, the payload experienced large oscillations that made positioning of the payload very challenging. The large oscillations even led to a collision with an obstacle. Input shaping, however, was able to substantially reduce the hook oscillations and

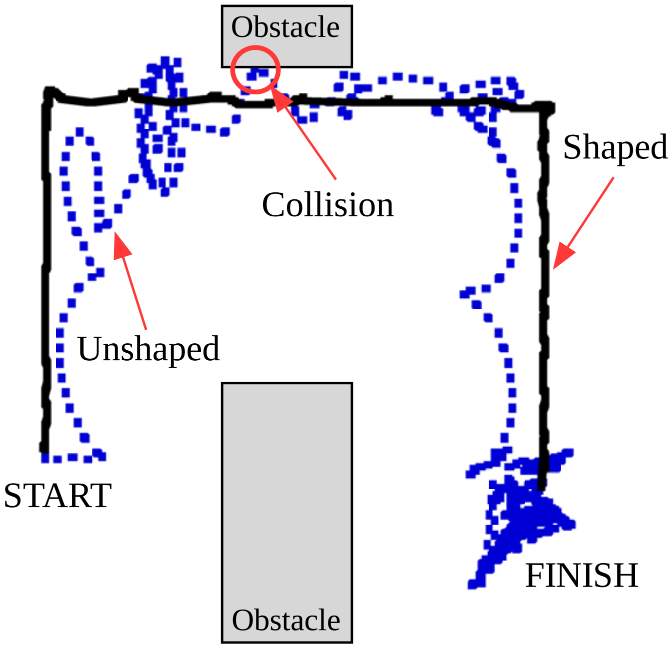

Figure 8.10: Sample Dual-Hoist Crane Operator Trial

made it easier for the operator to drive the crane and accurately position the payload.

For every trial, the completion time, the number of button pushes, and the number of collisions were recorded. The completion time is the time from the first button push to when the payload approximately settled within the target rectangle. The number of button pushes is an indication of the effort the operator exerts to complete the task. The higher the number of pushes, the more effort and concentration the operator must exert in order to complete the task. The number of collisions with obstacles indicates the safety and accuracy of the payload-maneuvering operation.

Figure 8.11(a) shows the completion times for unshaped and shaped level-payload trials for all 8 operators tested. The average completion time without shaping was 65 s. It was only 33 s when input shaping was utilized, a 49% reduction. Figure 8.11(b) shows the completion times for unshaped and shaped angled-payload trials. The average completion time for the unshaped trials was 65.5 s. Input shaping reduced the average completion time to 33.5 s, a 49% reduction.

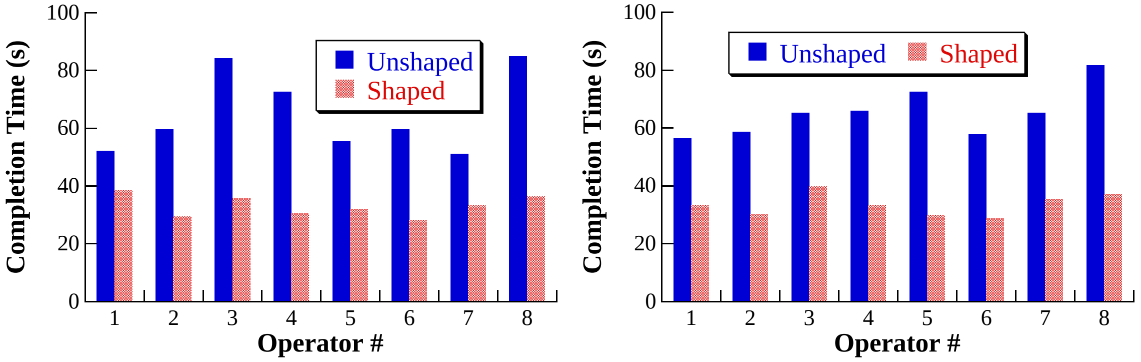

(a) Level Payload (b) Angled Payload

Figure 8.11: Dual-Hoist Crane Completion Times

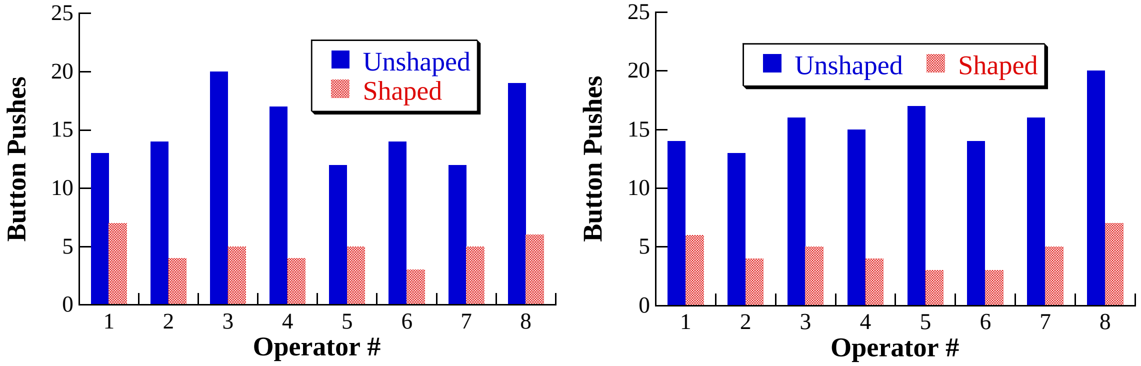

(a) Level Payload (b) Angled Payload

Figure 8.12: Dual-Hoist Crane Button Pushes

Figure 8.12(a) shows the number of button pushes for unshaped and shaped level-payload trials. The average number of button pushes without shaping was 15, but only 4.9 with shaping, a 68% reduction. Figure 8.12(b) shows the number of button pushes for the angled-payload trials. The average number of button pushes for the unshaped trials was 15.6. It was only 4.6 when input shaping was used, a 70% reduction.

Figure 8.13(a) shows the total number of obstacle collisions for unshaped and shaped level-payload trials. The average number of collisions without shaping was 2 and 0.125 with shaping, a 94% reduction. Figure 8.13(b) shows the total number of collisions for angled-payload trials. The average number of collisions for the unshaped trials was 0.75 and only 0.25 with shaping, a 67% reduction. Table 8.5 summarizes

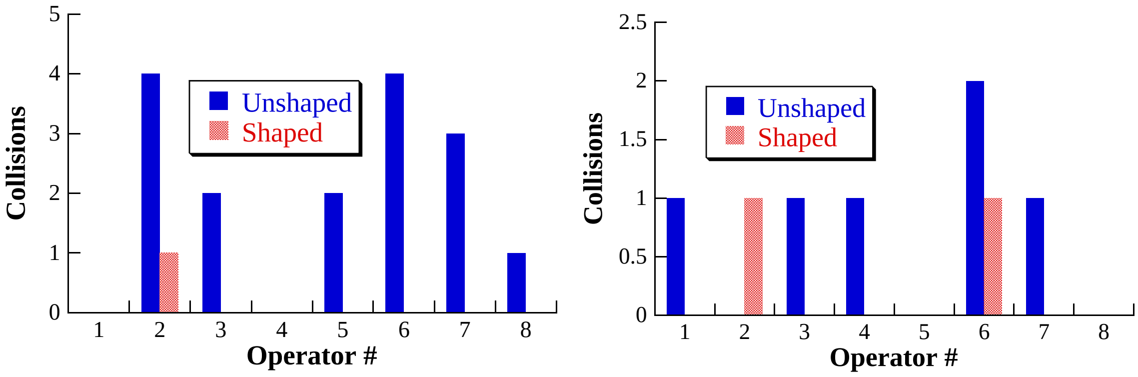

(a) Level Payload (b) Angled Payload

Figure 8.13: Dual-Hoist Crane Collisions

Table 8.5: Summary of Dual-Hoist Crane Operator Study Results

Trial Type	Unshaped Ave.	Shaped Ave.	% Red.
Completion Time, Level	65 s	33 s	49%
Completion Time, Angled	65.5 s	33.5 s	49%
Button Pushes, Level	15	4.9	68%
Button Pushes, Angled	15.6	4.6	70%
Collisions, Level	2 cm	0.125 cm	94%
Collisions, Angled	0.75	0.25	67%

the results of the operator study. Input shaping provided 49%-94% improvements in all of the performance measures.

8.2.4 Statistical Analysis

Similar to the analysis performed for the boom crane operator study results in Section 8.1.4, ANOVA tests were conducted to measure the statistical significance of the differences between the unshaped and shaped results. Because the same group of operators performed both the unshaped and shaped trials, one-way repeated ANOVA tests (Paired t-Tests) were used. A 95% confidence was used for all tests.

Table 8.6 shows the results of the ANOVA analysis. The F/F_{crit} values are large in every case (except for collisions with the angled payload) and the corresponding P-values are small. There were only a few collisions with the angled payload (although mostly without shaping), so the statistical significance of that set of data is

Table 8.6: Summary of Dual-Hoist Crane ANOVA Results

Trial Type	F-value/F_{crit}	P-value
Completion Time, Level	10.0	0.0003
Completion Time, Angled	30.3	<0.0001
Button Pushes, Level	16.7	<0.0001
Button Pushes, Angled	57.4	<0.0001
Collisions, Level	2.9	0.008
Collisions, Angled	0.77	0.10

small. Nonetheless, the ANOVA tests provide strong evidence that input shaping was effective in decreasing the completion time and lowering the number of button pushes for both payload configurations.

8.3 Summary

This chapter analyzed the performance of human operators maneuvering two types of nonlinear cranes, a mobile boom crane and a dual-hoist bridge crane. The boom crane experiments were configured to test the driving, steering, and slewing axes of the boom crane. The operators completed the task with single and double-pendulum payloads, both unshaped and with one-mode and two-mode Specified Insensitivity shapers. The dual-hoist crane experiments were configured to test operators maneuvering a long, slender payload along an approximately $\cap$-shaped path. The payload was placed in two configurations, a level and an angled orientation relative to the horizontal. The operators utilized unshaped and ZV-shaped commands.

In both studies, several performance characteristics, such as the completion time, the number of button pushes, the number of collisions, and the maximum residual oscillation, were measured. The results of both studies demonstrated that the operators improved their performance substantially with input shaping enabled. They were able to complete the task in less time and avoid the workspace obstacles. These improvements occurred even though the operator effort was decreased, as measured by the amount of control effort exerted by the operators.

CHAPTER IX

LOW-AUTHORITY / HIGH-AUTHORITY CONTROL

The effectiveness of input-shaping control on human-operated flexible machines has been well established up to this point of the thesis. However, one of the main shortcomings of input shaping has not been addressed yet. This shortcoming is the inability of input shaping to eliminate oscillations induced by external disturbances, such as a gust of wind. Because input shaping does not require any sensors, it can only eliminate swing caused by intentional operator commands.

Sorensen et al. [65] proposed combining input shaping with feedback control to address this shortcoming. This chapter presents a similar solution approach, but presents a formalized design method for developing such a control structure. In addition, this work assumes that there is a human operator driving the crane. As a result, the input-shaping control module must be combined with a low-authority feedback controller. The low-authority feedback controller eliminates disturbance-induced oscillations, while the input-shaping controller reduces operator-induced oscillations. It is important that the feedback controller be low-authority so that the human operator remains in control of the machine at all times. Essentially, the commands of the operator must take precedence over the computerized feedback effort.

The next section presents the proposed control structure. Then, a step-by-step process for designing the feedback control and input-shaping control modules are presented. Important parameters that affect the design process are thoroughly analyzed. Finally, the effectiveness of the combined controller is experimentally evaluated.

9.1 Feedback Model

Figure 9.1 shows a block diagram of the system with the proposed control structure. The operator continually generates a baseline reference velocity command, V_R, via a control interface. Pushing and releasing a button (or lever) on the interface produces a velocity command. This command is combined with any additional human feedback, V_A, resulting from the sensory feedback the human gets from the machine. This human feedback is essentially a position controller that drives the system to the desired final state. The combined human effort, V_H, is then sent to an input-shaping module. The input-shaping module is primarily in charge of eliminating unwanted dynamics (i.e., payload sway) induced by operator commands. The input-shaped command, V_S, is added to the output of the feedback control module, V_F. The feedback controller is a secondary controller and is in charge of eliminating any payload oscillation induced by external disturbances and modeling errors. (Note that most indoor cranes will rarely be subjected to disturbances. So the feedback component will only rarely play a significant role.) The combined input-shaping and feedback control signal, V_C, is sent to the crane. The crane dynamics are broken up into three blocks,

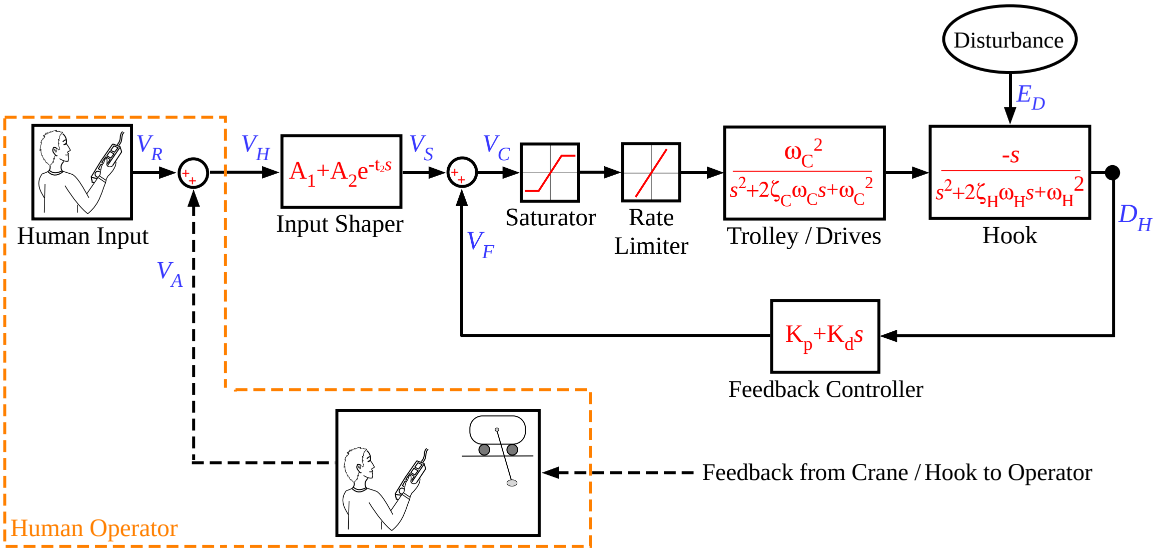

Figure 9.1: System Block Diagram

the saturater (to limit the maximum allowed move velocity, V_{max}), the rate limiter (to limit the maximum allowed move acceleration, A_{max}), and a highly-damped second-order system that represents the trolley and motor drives. The motion of the crane trolley is the input to the hook, which is modeled as a lightly-damped second-order system. The feedback signal, D_H, is the horizontal deflection of the hook relative to its overhead attachment point. There is also an external disturbance, E_D, that can act on the hook.

The complex, nonlinear dynamics of the trolley (including motors and drives) were modeled as a lumped second-order system with a saturater and a rate limiter [50,64]. The second-order trolley transfer function is given by,

$$\frac{\omega_C^2}{s^2 + 2\zeta_C \omega_C s + \omega_C^2} \tag{9.1}$$

where ω_C is the natural frequency of the trolley and ζ_C is the damping ratio of the trolley.

A single-hoist bridge crane model was used to derive the transfer function of the hook. Figure 9.2 illustrates a two-dimensional bridge crane. The model consists of a trolley (modeled as a point), whose horizontal position is given by X, and a hook of mass m (modeled as a point mass), which is attached below the trolley by a suspension cable with length given by L. The deflection of the hook relative to its overhead attachment point O is given by θ. The model assumes that there is damping in the hook swing. Although the trolley of a typical bridge crane can move in two directions, for the purposes of deriving its equation of motion, a planar model is adequate. The equations of motion of the trolley (of a bridge crane) in the two directions are not coupled; therefore, once the equation of motion in one direction is obtained, it can be applied to both directions.

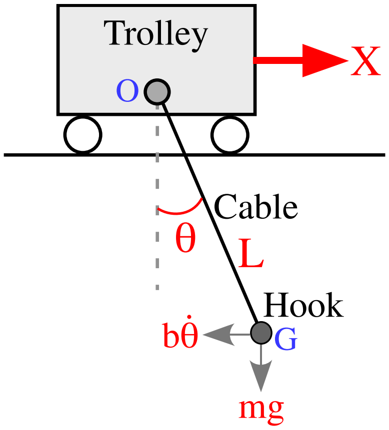

Figure 9.2: Single-Hoist Bridge Crane Model

The equation of motion was obtained using the Newton-Euler method. The moments were summed about point O,

$$\sum M_O = J\alpha + m\overrightarrow{r_{OG}} \times \overrightarrow{a_O} \tag{9.2}$$

where M_O is the sum of the moments about point O, J is the mass moment of inertia of the hook about point O, α is the rotational acceleration of the hook, $\overrightarrow{r_{OG}}$ is the position vector from point O to point G, and $\overrightarrow{a_O}$ is the linear acceleration of point O. The only external forces (as shown in Figure 9.2) are gravity and damping, so the left-hand side of (9.2) simplifies to,

$$\sum M_O = -mgL\sin(\theta) - b\dot{\theta}L\cos(\theta) \tag{9.3}$$

where b is the damping coefficient. The right half of (9.2) simplifies to,

$$J\alpha + m\overrightarrow{r_{OG}} \times \overrightarrow{a_O} = mL^2\ddot{\theta} + mLcos(\theta)\ddot{X} \tag{9.4}$$

Substituting (9.3) and (9.4) into (9.2) and utilizing the small-angle approximation yields,

$$mL^2\ddot{\theta} + bL\dot{\theta} + mgL\theta = -mL\ddot{X} \tag{9.5}$$

Equation (9.5) is the equation of motion of the hook. This equation can be given in terms of the horizontal deflection of the hook by substituting $d_H = L\theta$,

$$mL\ddot{d}_H + b\dot{d}_H + mgd_H = -mL\ddot{X} \tag{9.6}$$

Taking the Laplace transform (assuming zero initial conditions) of (9.6) yields the transfer function of the system,

$$\frac{D_H(s)}{X(s)} = \frac{-s^2}{s^2 + \left(\frac{b}{mL}\right)s + \left(\frac{g}{L}\right)} \tag{9.7}$$

The input to the transfer function in (9.7) is the acceleration of the trolley. However, in most cranes, the input command given to the crane is a velocity signal. Therefore, $X(s)$ is replaced with $V(s) = sX(s)$, which represents the time derivative of the position, $X(s)$ in the Laplace domain. This is mathematically equivalent to multiplying both sides of (9.7) by $\frac{1}{s}$,

$$\frac{D_H(s)}{V(s)} = \frac{-s}{s^2 + \left(\frac{b}{mL}\right)s + \left(\frac{g}{L}\right)} \tag{9.8}$$

Substituting $\omega_H^2 = \frac{g}{L}$ and $2\zeta_H\omega_H = \frac{b}{mL}$ yields the final form of the hook transfer function,

$$\frac{D_H(s)}{V(s)} = \frac{-s}{s^2 + 2\zeta_H\omega_H s + \omega_H^2} \tag{9.9}$$

where ω_H is the natural frequency of the hook and ζ_H is the damping ratio of the hook.

The feedback controller shown in Figure 9.1 is a proportional-derivative controller, where K_p represents the proportional gain and K_d represents the derivative gain. The process used to design this controller is explored in Section 9.2. The input shaper shown in Figure 9.1 is the s-domain representation of a simple ZV shaper. However, it can be replaced with any other type of input shaper. The input-shaping design process is discussed in Section 9.3. Finally, the effects of introducing the human-feedback loop are explored in Section 9.4.

Table 9.1 provides the numerical values of the various parameters of the feedback model shown in Figure 9.1. The system was simulated in SIMULINK. The equations of motion were solved using ODE5. ODE5 is fixed-step, built-in MATLAB function that solves differential equations using the 5th-order Dormand & Prince method (a

Table 9.1: Nominal Feedback Simulation Parameters

Parameter	Value
Trolley Frequency, ω_C	8 rad/sec
Trolley Damping Ratio, ζ_C	0.86
Maximum Trolley Speed, V_{max}	0.3 m/s
Maximum Trolley Acceleration, A_{max}	0.27 m/s^2
Hook frequency, ω_H	2.2 rad/sec
Hook Damping Ratio, ζ_H	0.0074

member of the Runge-Kutta family). The sampling rate was set to 100 Hz (i.e., fixed step length of 0.01 s).

9.2 Feedback Controller Design

There are several important factors to consider when designing a feedback controller for use in a crane-control system. These factors include:

- Stability
- Actuator limits, such as velocity and acceleration limits
- Range of suspension cable lengths
- Response characteristics, such as settling time
- Compatibility with the human operator
- Robustness to payload changes
- Ease of design
- Minimization of sensors
- Reliability

The following sections analyze some of the more important factors affecting the feedback design process. The final result is a set of stable and effective proportional (P) and derivative (D) gains for the feedback controller.

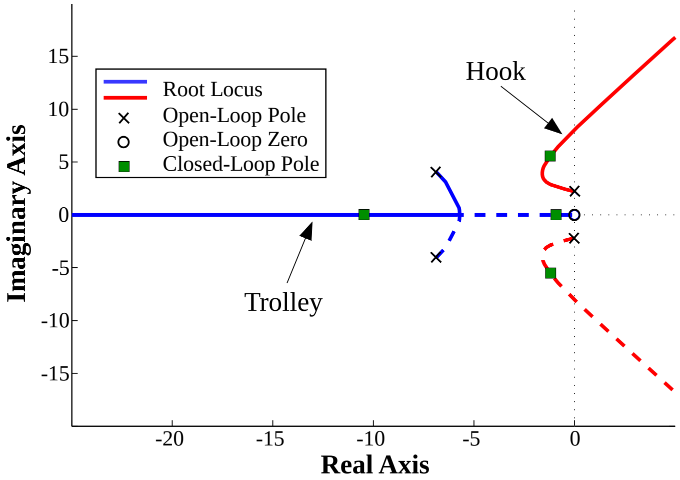

Figure 9.3: Root Locus of Trolley/Hook Plant with Proportional Feedback Control

9.2.1 Stability

This section explores the stability of the trolley/hook system using root locus analysis (the saturator and rate limiter are not considered because they are nonlinear components). Figure 9.3 shows the root locus of the trolley/hook system with only a proportional feedback controller. The closed-loop poles shown on the figure are for a proportional gain of 5. The hook closed-loop poles cross over to the right-hand plane for proportional gains larger than 13. Although there is a range of P gains that produce stable results, adding a derivative gain (i.e., damping) can help further stabilize the system and improve the response characteristics (such as settling time).

Figure 9.4 shows the root locus of the trolley/hook system with a proportional-derivative feedback controller. Notice that an additional zero is added to the root locus. This zero is a result of the PD feedback controller and its location is,

$$s_{zero} = -4 = \frac{-\mathrm{P}}{\mathrm{D}} = \frac{-2}{0.5} \tag{9.10}$$

The entire root locus (for all P and D gains) is in the left-hand plane.

As the P gain increases in Figure 9.4, the hook closed-loop poles move from the complex region (oscillatory poles) to the real axis (overdamped poles). This means that the hook response changes from oscillatory to exponentially decaying. One of

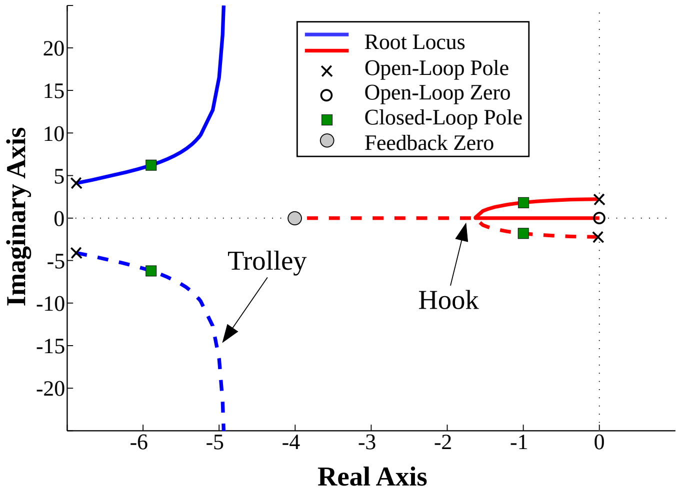

Figure 9.4: Root Locus of Trolley/Hook Plant with Proportional-Derivative Feedback Control - Case One

the hook closed-loop poles approaches the feedback zero and moves farther to the left. The other hook closed-loop pole approaches the zero at the origin. These two real poles correspond to exponential terms in the hook response, with time constants equal to the inverse of their locations on the real axis. The pole approaching the feedback zero becomes less and less significant as it moves to the left (its time constant becomes smaller and smaller). Therefore, the hook response becomes dominated by the exponential term corresponding to the pole close to the origin (which has a very large time constant). The result is that the system dynamics become very sluggish.

One of the fundamental trade-off in the feedback control design is demonstrated in Figure 9.5. The trolley was moved for 3 s with two sets of P and D gains: [P=2, D=1] and [P=40, D=20]. Note that the ratio of the P and D gains (i.e., location of the feedback zero) was held constant. The hook response with higher gains is similar to a second-order overdamped response.

Although the response shown in Figure 9.5 is stable, this type of behavior (i.e., large rise time) is undesirable for human control of cranes. However, increasing the P gain further makes the trolley poles very oscillatory and can even drive the real system unstable. For an infinitely large sampling rate, the simulated system would be stable

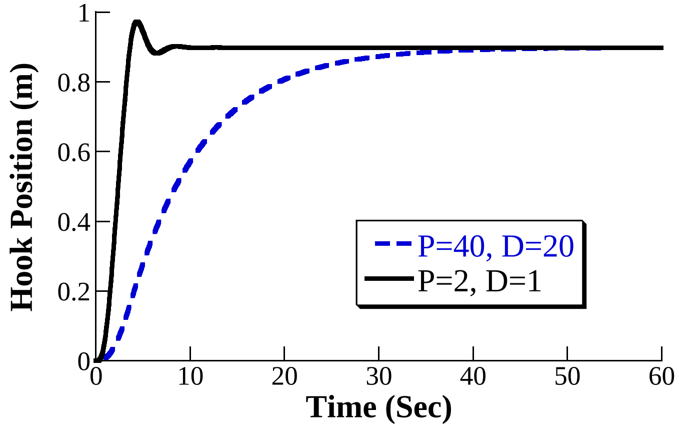

Figure 9.5: Hook Responses with Two Exemplary Sets of Gains

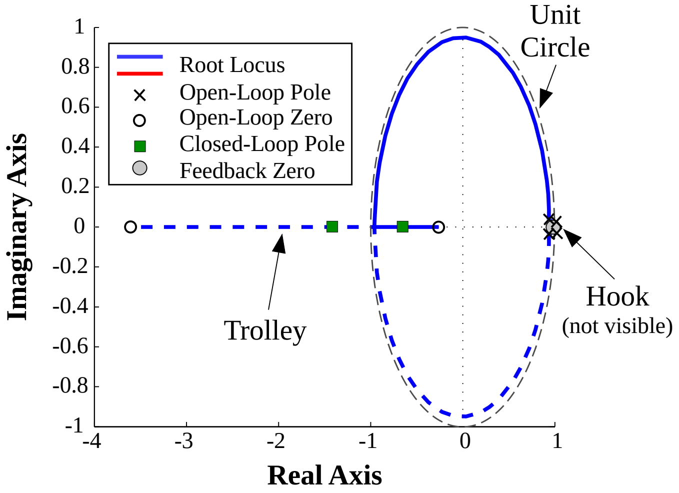

Figure 9.6: Discrete-Time Root Locus of Trolley/Hook Plant with Proportional-Derivative Feedback Control

for all gains because the closed-loop poles are in the left-hand plane. However, real systems have finite sampling rates. As a result, increasing the P gain will eventually drive the real system unstable. Figure 9.6 shows the root locus of the system in the z-plane for a sampling rate of 100 Hz. Note that for large P gains, the trolley closed-loop poles go outside of the unit circle. If the simulation is performed with a low sampling rate, then the instability of the real system can also be captured in the simulated system.

The instability effect for a finite sampling rate (100 Hz) is demonstrated in Figure 9.7, which shows the trolley response to a 3 s straight-line move with two different sets

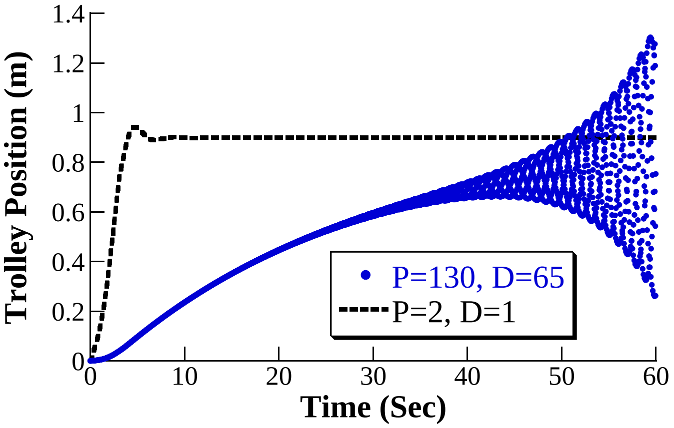

Figure 9.7: Trolley Responses with Two Exemplary Sets of Gains

of P and D gains: [P=2, D=1] and [P=130, D=65]. Note that the ratio of the P and D gains (i.e., location of the feedback zero) was held constant. Although the closed-loop poles are in the left-hand plane for both sets of gains, the system response is unstable with the higher gains. The trolley response is oscillatory and the oscillation amplitude gets larger with time, indicating unstable dynamics. Although not shown in Figure 9.7, the hook deflection is also unstable and increases over time.

Figure 9.4 showed one possible configuration of the root locus for this system. The shape of the root locus depends on the location of the feedback zero. If the feedback zero moves far enough to the left ($|s_{zero}| \geq 13$), the root locus shape changes. Figure 9.8 shows the root locus for an example case where the feedback zero has a large value. The feedback zero is located at,

$$s_{zero} = -15 = \frac{-2}{0.133} \tag{9.11}$$

where P=2 and D=0.13. For large values of the P gain, the hook closed-loop poles become highly flexible (i.e., high frequency and low damping) and can eventually go unstable (cross over to the right-hand plane). Moving the feedback zero to the left pulls the root locus curves of the hook farther into the right-hand plane, increasing the unstable region of the root locus.

To determine the range of stable P and D gains for this system, the trolley was

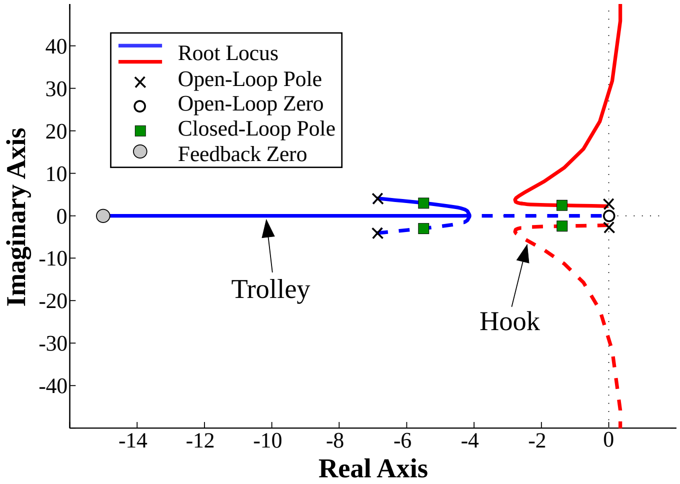

Figure 9.8: Root Locus of Trolley/Hook Plant with Proportional-Derivative Feedback Control - Case Two

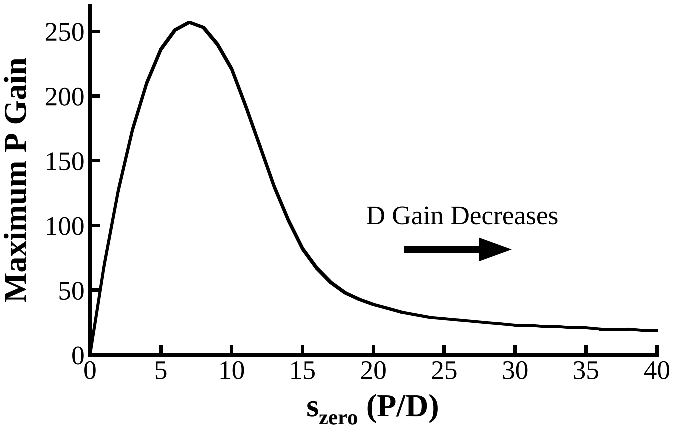

Figure 9.9: Range of Stable Gains for the Trolley/Hook System

given a 10 s move command (i.e., the human operator held down the move button for 10 s) with different feedback gains. The location of the feedback zero (s_{zero}) was varied between 0 and 40 and the maximum stable P gain at each iteration was determined. As the feedback zero moves farther away from the origin, its effect on the system dynamics becomes less significant. This is evident by the fact that for very large values of s_{zero}, the root locus resembles that of a proportional gain shown in Figure 9.3. Therefore, s_{zero} values larger than 40 were not considered in this analysis. Figure 9.9 shows the range of stable gains for the trolley/hook system.

Note that for $|s_{zero}| \leq 13$, there should be no upper bound on the maximum

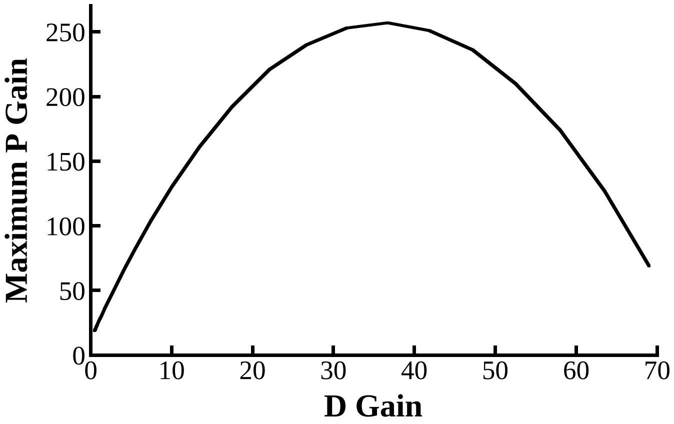

Figure 9.10: Stable P and D Gains for the Trolley/Hook System

stable P gain (assuming an ideal, continuous system). As discussed earlier, however, the system was simulated numerically with a finite sampling rate, so there is an upper bound. This upper bound is realistic because most cranes equipped with feedback control operate in the digital domain with relatively low sampling rates.

The results of Figure 9.9 can be rearranged to show the relationship between the P and D gains more directly, as shown in Figure 9.10. The peak in the maximum P gain occurs at a D gain of approximately 35. Increasing or decreasing the D gain results in a smaller range of stable P gains.

Although the range of stable gains shown in Figure 9.9 was obtained using a 10 s trolley motion, the results are valid in general. This is because the trolley/hook system is linear and satisfies the principle of superposition. The principle of superposition can be represented mathematically as,

$$\begin{aligned} &Hx_1 = y_1 \qquad (9.12)\\ &Hx_2 = y_2 \\ &H(x_1 + x_2) = Hx_1 + Hx_2 = y_1 + y_2 \end{aligned}$$

where x_1 and x_2 are input commands, y_1 and y_2 are their corresponding outputs, and H is the linear system (i.e., transfer function representing the system). Any arbitrary input command can be decomposed into multiple components, one of which

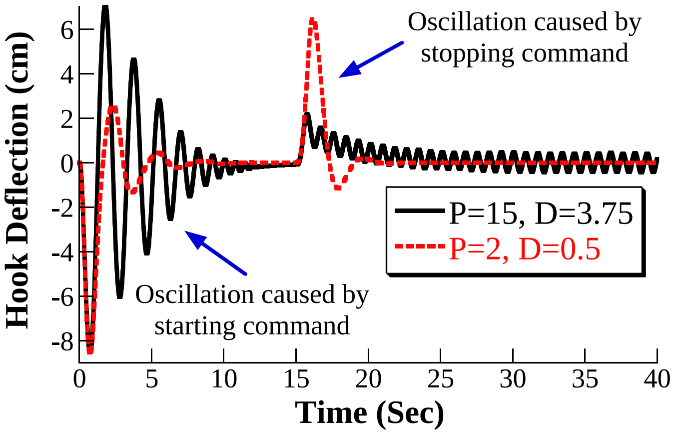

Figure 9.11: Hook Responses Showing Limit Cycle Stability

can always be a 10 s move (for example a 5 s move can be broken up into a 10 s move and a 5 s move in the opposite direction). If the system response (for a certain set of gains) to the 10 s move is unstable, then by the principle of superposition, the system response to any arbitrary input will also be unstable. Therefore, the range of stable gains shown in Figure 9.9 is valid for any input command to the trolley/hook system.

9.2.2 Velocity and Acceleration Limits

The analysis in Section 9.2.1 ignored the velocity and acceleration limits that exist in most physical systems. This section takes these limits into consideration by including the saturator and rate limiter blocks shown in Figure 9.1 in the simulation. As a result, the trolley can no longer follow arbitrarily large inputs (large velocities) or rapid changes in the input (large accelerations).

Enforcing the velocity and acceleration limits introduces another type of instability (other than the one shown in Figure 9.7) present in nonlinear systems called limit cycles. Figure 9.11 demonstrates this concept. The trolley was moved for 15 s with two different sets of P and D gains: [P=2, D=0.5] and [P=15, D=3.75]. The induced hook oscillation is shown in Figure 9.11. With the higher gains, the hook oscillation does not settle over time, as in the stable case, or amplify over time, as in the unstable case. The hook simply oscillates back and forth with a constant amplitude. Although not shown in Figure 9.11, the trolley also oscillates back and forth in a continuous, yet unsuccessful attempt to settle the hook oscillation. This type of behavior is undesirable because the system never settles.

Another interesting dynamic effect introduced by including the velocity and acceleration limits is that the maximum stable P gain (for a constant s_{zero}) is larger during the trolley move command than after the move command is over. In Figure 9.11, the initial hook oscillation (for P=15, D=3.75) is eliminated during the move command. However, the oscillation induced by the stopping command (at approximately 15 s), even though it has a smaller amplitude, drives the system into a limit cycle. This is because during the move command, the total input to the trolley is made up of the move command, which is a pulse at the maximum velocity, and the feedback effort. The move command dominates the total input to the trolley. Therefore, the trolley velocity remains positive (i.e., the crane moves in one direction) for the majority of the time. This results in larger maximum stable P gains. After the move command, the feedback effort makes up the entire input to the trolley. The trolley input oscillates about zero, resulting in the trolley moving back and forth. So the same P-gain value that was stable during the move command can produce unstable results. Note, however, that the maximum stable P gain for a system is the gain that results in a stable response *both* during and after the input.

To determine the stability of a system with nonlinear elements, some researchers have proposed the use of describing functions [6, 7, 62]. Describing functions are a method of linearizing nonlinear elements in a system (quasi-linearization) and using frequency-response techniques to study its stability. The method generally assumes that only one nonlinearity exists; however, it can be extended to systems with multiple nonlinear elements [17]. If the nonlinear elements are adjacent to each other, they can be lumped into a single describing function. Otherwise, they have to be treated

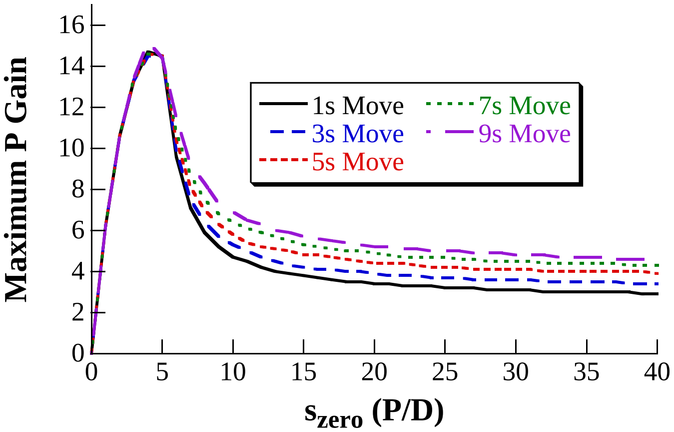

Figure 9.12: Range of Stable Gains for the Trolley/Hook System with Velocity and Acceleration Limits

separately. The process of computing the describing functions of multiple nonlinear elements, and then analyzing the stability of the system can be quite challenging and cumbersome. Also, the nonlinear parameters are well bounded for cranes. As a result, a more direct and effective method is used here.

To determine the range of stable P and D gains with velocity and acceleration limits, a move command was issued to the trolley and the system response (specifically the hook response) was analyzed to determine whether it settled or amplified over time. The maximum stable P gains for s_{zero} between 0 and 40 were obtained. P gains that resulted in limit cycles were also considered “unstable”. Unlike the linear trolley/hook system, the input command to the nonlinear system (the trolley/hook system with a saturator and a rate limiter) is no longer arbitrary. Because the feedback controller must be stable for all possible input commands, the move that results in the smallest range of stable gains must be selected. Therefore, a range of move times was simulated to determine the limiting factor. Figure 9.12 shows the stable gains for the trolley/hook system with velocity and acceleration limits.

For small values of s_{zero}, large D gains, the move time does not have a significant effect on the range of stable gains. However, as s_{zero} increases, i.e., D gain gets smaller, the effect of move time becomes significant. The proportional gain is directly related

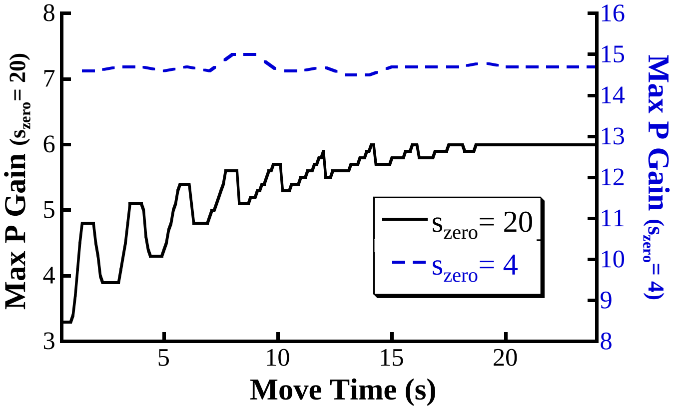

Figure 9.13: Maximum Stable P Gain vs. Move Time

to the amplitude of the hook swing. Larger swing means more proportional feedback effort. However, the derivative gain is inversely related to the hook swing. When the swing is at its maximum, the derivative feedback effort is at its smallest. When the D gain is small, the P gain dominates the feedback effort, so the system becomes more sensitive to the swing amplitude, and therefore, more sensitive to variations in the move time.

To better understand how the move time affects the range of stable gains, Figure 9.13 shows the maximum stable P gains for move times between 0.1 s and 25 s for $s_{zero} = 4$ and $s_{zero} = 20$. Very small move times ($< 0.1s$) are not considered. This is because cranes have a very large inertia. As a result, very short move commands would result in almost no motion of the crane. The smallest move time that results in a crane motion can differ from one machine to the next.

As expected, there is little variation in the $s_{zero} = 4$ data across different move times in Figure 9.13. On the other hand, there are two significant trends in the $s_{zero} = 20$ data: *i)* there are peaks and troughs in the maximum P gain as the move time varies and, *ii)* there is a general upward trend in the maximum P gain as the move time increases.

The peaks and troughs occur as a result of the interference between the oscillation induced by the starting command (i.e., pushing a move button on the control

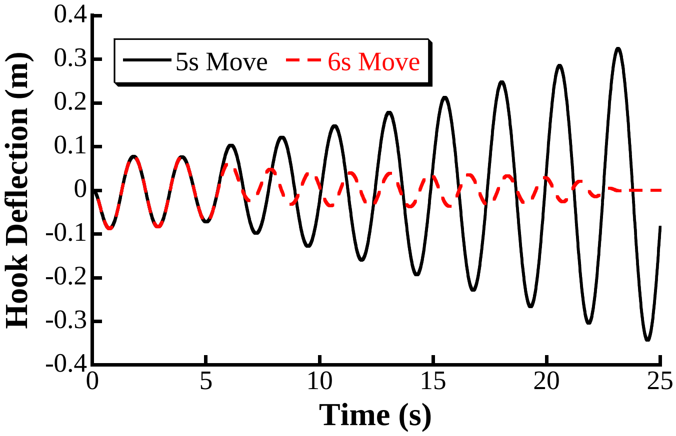

Figure 9.14: Example Hook Deflections Induced by 5s and 6s Moves with P=5.4 and D=0.27

interface) and the oscillation induced by the stopping command (i.e., releasing the button). Note that the stopping command refers to releasing the button on the control interface. This does not mean that the trolley comes to rest as the feedback controller is still active. When the trolley starts to move, it causes hook oscillation, which the feedback controller actively tries to eliminate. The stopping command, however, also induces oscillation. This oscillation can be in-phase with the existing hook swing, thereby increasing the oscillation and reducing the maximum stable P gain. However, the oscillation induced by the stopping command can also be out-of-phase with the existing hook swing, thereby reducing the oscillation and increasing the maximum stable P gain. For example, Figure 9.14 shows the hook responses to 5 s and 6 s trolley moves. The gains were set to P=5.4 and D=0.27 ($s_{zero} = 20$). The hook oscillations induced by the 5 s trolley move increase after the stopping command is issued at approximately 5 s. This drives the system unstable. On the other hand, the hook oscillations induced by the 6 s move decrease after the stopping command is issued. The hook deflections reduce to zero over time, making the system stable.

There is also a general upward trend in the maximum P gains shown in Figure 9.13 as the move time increases. As the move duration increases, the feedback controller is able to eliminate more of the oscillation caused by the starting command before

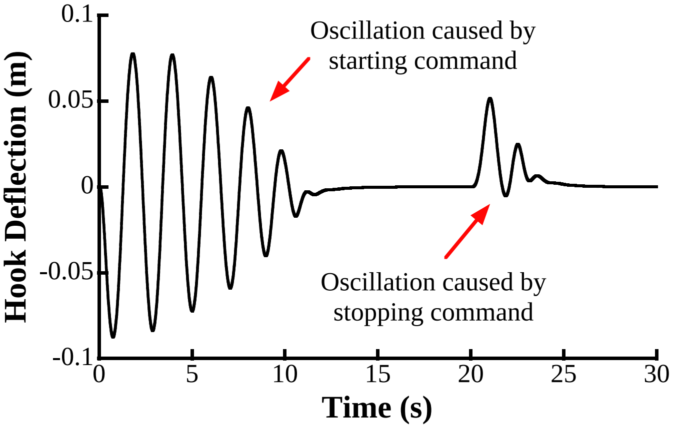

Figure 9.15: Example Hook Deflection Induced by 20s Move with P=5.4 and D=0.27

the end of the input. Because the remaining hook swing is small, the maximum stable P gain increases. If the move time is long enough, the feedback controller can completely eliminate the oscillation caused by the starting command before the end of the input. Because there is no remaining hook swing when the stopping command is issued, there is no interference between the two oscillations. Therefore, the maximum P gain is no longer dependent on the move time. For example, Figure 9.15 shows the hook response to a 20 s trolley move, with gains set to P=5.4 and D=0.27 ($s_{zero} = 20$). After approximately 12 s, the oscillation caused by the starting command is eliminated. Therefore, for any move time larger than 12 s, the induced hook oscillation will be identical to the stable results shown in Figure 9.15 (except that the oscillation caused by the stopping command will occur at a different point in time). Hence, the maximum stable P gain never drops below this value (5.4) for moves larger than 12 s.

Note that the P gain does not increase indefinitely. There is an absolute maximum in the P gain data shown in Figure 9.13. For $s_{zero} = 20$, this value is approximately 6.2. Figure 9.16 shows the hook response to a 60 s move for P=6.3. The system goes unstable (the hook oscillation amplifies over time) during the move command. Hence, the system is unstable regardless of the move time for P gains larger than 6.2.

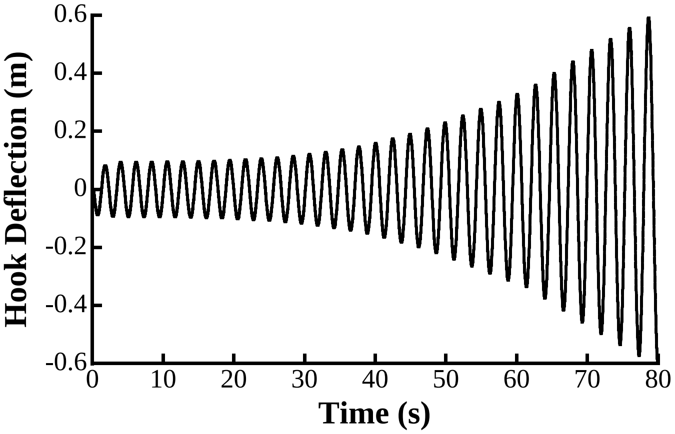

Figure 9.16: Example Hook Deflection Induced by 60s Move with P=6.3 and D=0.32

This gain value, however, is the upper bound. The lower bound, the set of gains that are stable for *all* moves (short or long), is the limiting factor. The lower bound on the stable gains, as shown in Figure 9.13, is obtained from a 1 s trolley move.

In determining the effects of velocity and acceleration limit on the range of stable gains, constant values of 0.3 m/s and 0.27 m/s^2 were used. In most cranes, these parameters are predetermined and do not change during operation. Therefore, similar to the analysis presented here, they can be treated as constants. However, it is of interest to study the effects of varying the velocity and acceleration limits on the range of stable gains. Figure 9.17 shows the maximum stable P gain for s_{zero} set to 5 and 30 and V_{max} between 0.1 m/s and 1 m/s and A_{max} between 0.1 m/s^2 and 2 m/s^2. When the acceleration limit is large relative to the velocity limit, the maximum P gain increases. This makes sense because a higher acceleration means that the trolley can quickly change its speed and eliminate the hook swing. On the other hand, if the velocity limit is large relative to the acceleration limit, then the maximum P gain decreases. This occurs because a higher velocity increases the induced hook swing. This larger hook swing, combined with a small acceleration means that the trolley cannot respond quickly, resulting in a smaller maximum stable P gain.

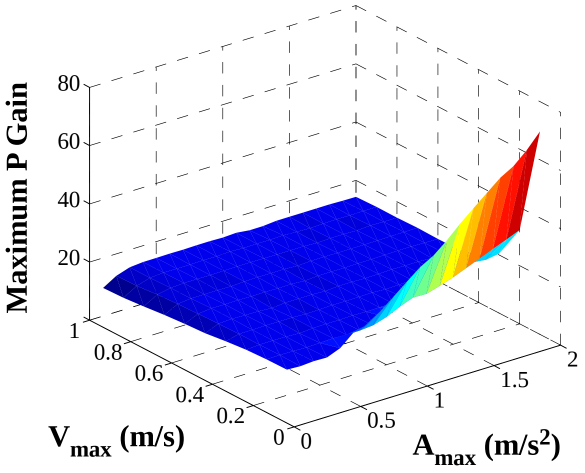

(a) $s_{zero} = 5$

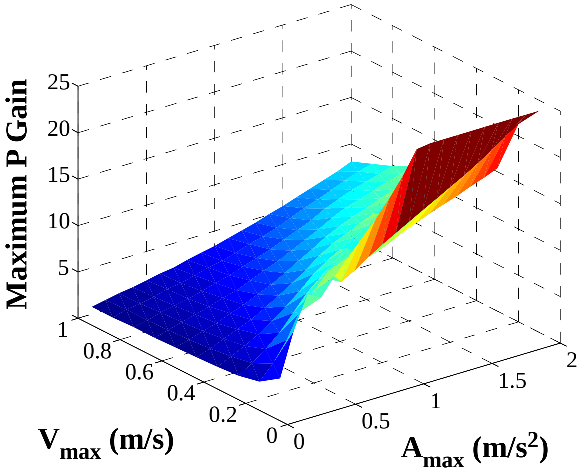

(b) $s_{zero} = 30$

Figure 9.17: Maximum P gain for Varying V_{max} and A_{max}

9.2.3 Suspension Cable Length

Another factor that affects the range of stable gains is the suspension cable length. Because different crane applications require varying suspension cable lengths, it is important to design feedback gains that are stable for all cable lengths being used. To determine the effect of the suspension cable length on the range of stable gains, the 1 s trolley move shown in Figure 9.12 was repeated with three different cable lengths. Figure 9.18 shows the resulting ranges of stable gains. As the cable length increases, the range of stable gains also increases. This is because the hook swing frequency decreases, the period increases, as the cable length increases. This effectively makes

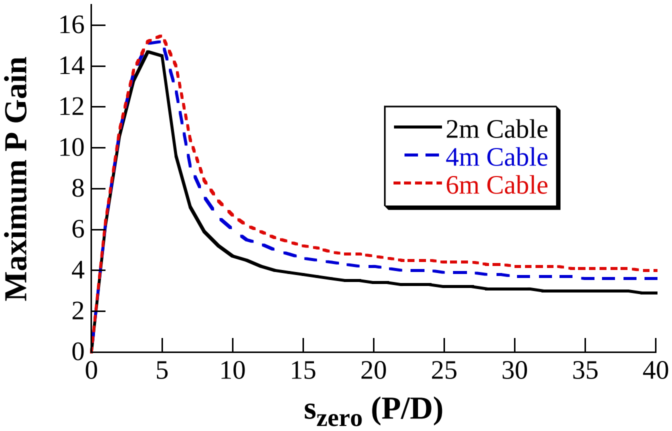

Figure 9.18: Range of Stable Gains for Varying Suspension Cable Lengths

the system slower, giving the feedback controller a longer time to get over the top of hook and eliminate the deflection before the hook changes direction and swings back. Similar to the move time parameter, the goal is to design one feedback controller for all possible configurations of the crane, so the limiting factor is the smallest suspension cable length that the crane will use.

9.2.4 Response characteristics

Response characteristics are another important consideration when selecting feedback gains. The most important characteristic for crane control is the settling time of the hook. Settling time refers to the time duration from the start of the move to the time when the hook deflection has settled to within a tolerable amount. This tolerable amount can be selected by the designer. In this analysis, the tolerable hook deflection is set to ±1 cm.

Figure 9.19 shows the hook settling times across a range of P gains for three different s_{zero} values: 5, 10, and 20. For large P gains, the settling time increases dramatically until the system goes unstable and the settling time goes to infinity. However, the settling time also increases for small P gains. This is because small P gains make the system slow. The trolley cannot respond quickly to the hook

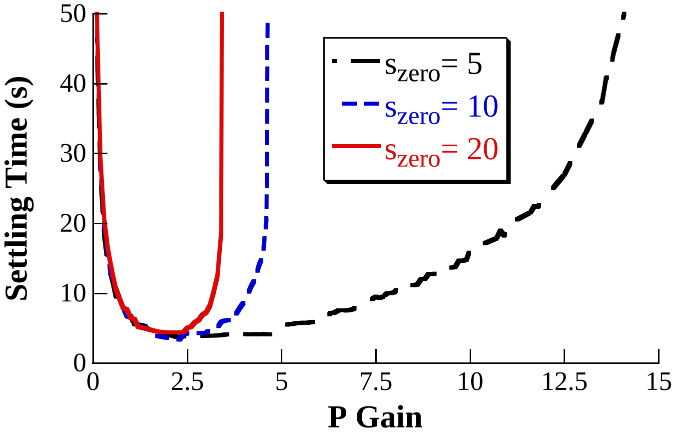

Figure 9.19: Hook Settling Times for Select Gains

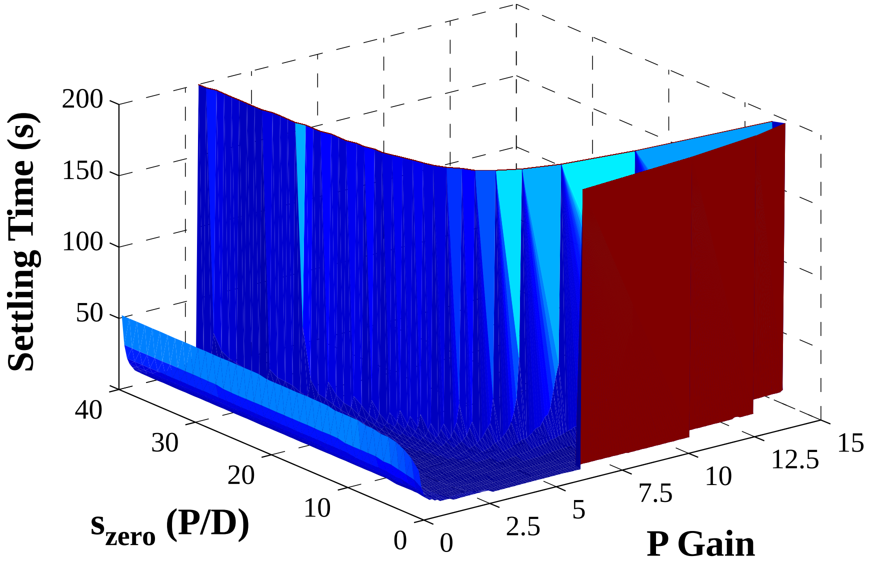

Figure 9.20: Hook Settling Times for a Large Range of Stable Gains

oscillations; therefore, the settling time increases.

Figure 9.20 shows the hook settling times for a large range of stable P and D gains. The patterns observed in Figure 9.19 apply across the entire range of gains. Therefore, it is clear that there is a range of P gains that are not only stable, but produce satisfactory response characteristics (i.e., minimize settling time).

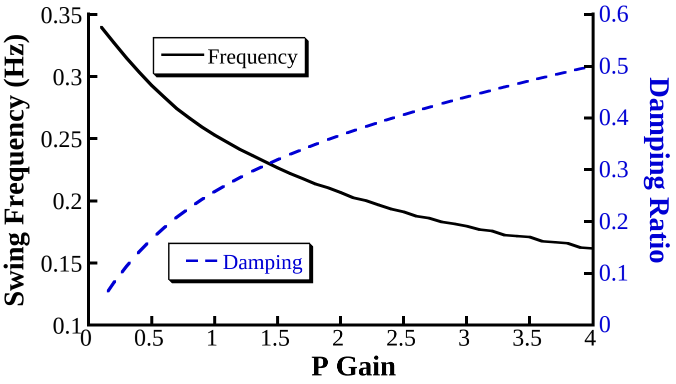

Figure 9.21: Frequency and Damping Ratio vs. P Gain for $s_{zero} = 1$

9.3 Input Shaper Design

The input-shaping module is responsible for eliminating hook oscillations induced by operator commands. Therefore, the input shaper must be designed for the swing frequency and damping ratio of the hook. The frequency and damping ratio can be obtained from the location of the hook closed-loop poles. As was shown in Figure 9.1, the input shaper is outside of the disturbance-rejecting feedback loop, which includes the PD controller and the nonlinear saturator and rate limiter. Changing the feedback gains changes the location of the hook closed-loop poles, resulting in different swing frequencies and damping ratios. For example, Figure 9.21 shows the frequency and damping ratio for various P gains and $s_{zero} = 1$. As the P gain increases, the frequency decreases and the damping ratio increases. This decrease in frequency can also be seen in the root locus plot that was shown in Figure 9.4.

Figure 9.22 shows the corresponding data for $s_{zero} = 20$. The frequency increases as the P gain increases. The damping ratio, however, has a peak at a P gain of approximately 1.7. These results clearly demonstrate that the input shaper must be designed for the frequency and damping ratio of the hook as part of the feedback system. Note that because of the nonlinear elements, the frequency and damping ratio of the system must be obtained numerically through the simulated time response. The swing frequency can be obtained using the Fast Fourier Transform (FFT) and the

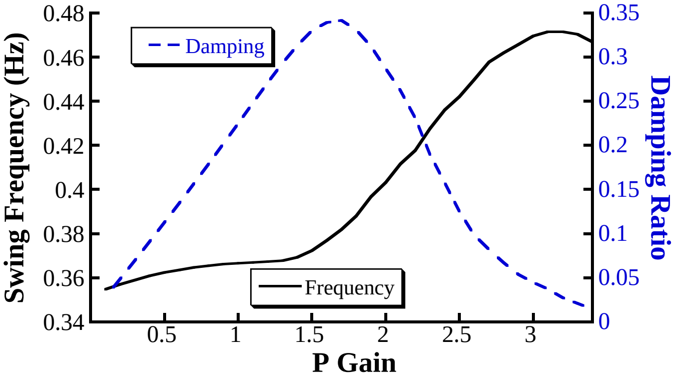

Figure 9.22: Frequency and Damping Ratio vs. P Gain for $s_{zero} = 20$

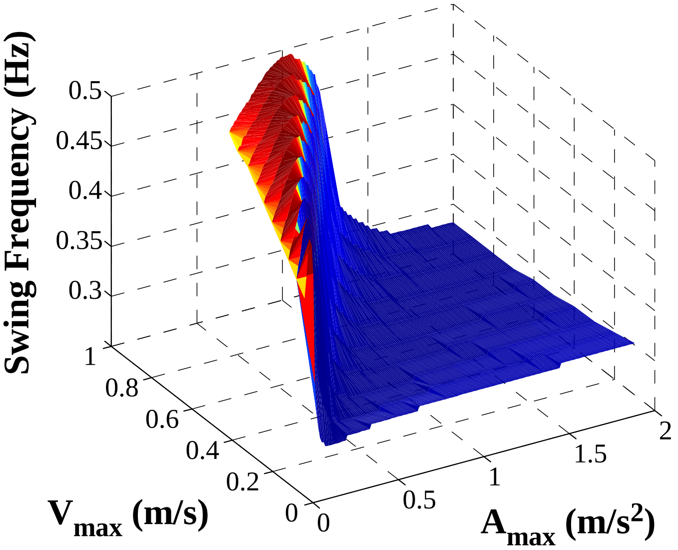

Figure 9.23: Swing Frequency vs. V_{max} and A_{max}

damping ratio can be obtained using the log decrement method.

In Figures 9.21 and 9.22, the velocity and acceleration limits were held constant at 0.3 m/s and 0.27 m/s^2, respectively. However, these limits also have an effect on the swing frequency and damping ratio of the hook. To get an understanding of how varying these move parameters affects the swing dynamics, Figure 9.23 shows the induced swing frequency as a function of varying velocity and acceleration limits. The P and D gains were held constant at P=4 and D=0.40.

For very small acceleration limits, the hook response is unstable. As A_{max} increases, for a constant V_{max}, the swing frequency slightly increases and then begins

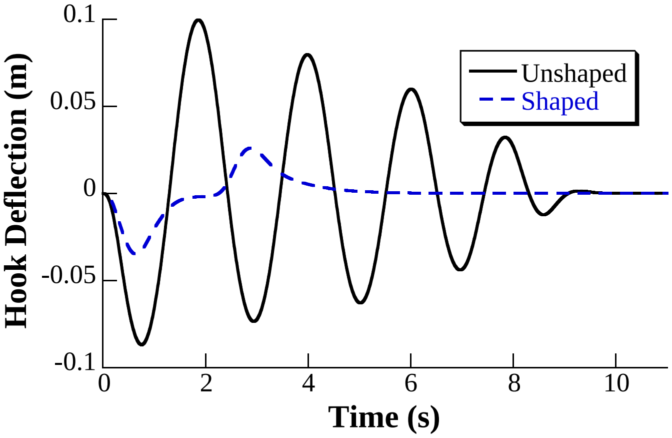

Figure 9.24: Hook Oscillation Induced by Unshaped and Shaped 1s Move with P=4 and D=0.40

to rapidly decrease. This occurs because a higher acceleration allows the trolley to move faster to eliminate the hook swing, resulting in a larger damping ratio. As the damping ratio gets larger, the swing frequency gets smaller. However, as the acceleration limit increases farther (its magnitude relative to the velocity becomes large), the swing frequency flattens out. This occurs because once the acceleration limit is large enough, it is not reached; therefore, the swing dynamics become independent of these limits. This produces the approximately flat region in the right-hand side of Figure 9.23. Essentially, the hook response with very large acceleration limits is similar to the response discussed in Section 9.2.1.

Figure 9.24 shows the response of the hook to a 1 s move with gains set to P=4 and D=0.40 ($s_{zero} = 10$) and the velocity and acceleration limits set to their nominal values given in Table 9.1. Using this hook response, the swing frequency and damping ratio were computed to be approximately 0.48 Hz and 0.036, respectively. Figure 9.24 also shows the hook response induced by a 1 s move with a ZV shaper designed with the obtained frequency and damping ratio.

Without the input shaper, there are large-amplitude hook oscillations that are eliminated by the feedback controller after approximately 10 s. With input shaping, however, there is significantly less swing and the hook is approximately steady after

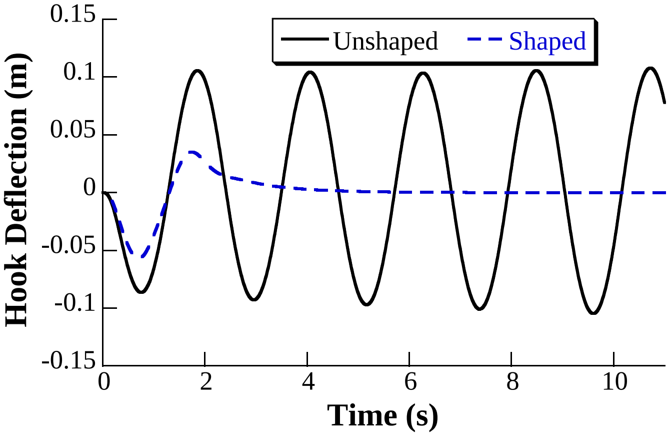

Figure 9.25: Hook Oscillation Induced by Unshaped and Shaped 1s Move with P=5 and D=0.50

only 4 s. The input shaper effectively eliminates oscillation induced by operator commands, removing the oscillation-reduction burden from the feedback controller.

To obtain a faster response, UMZV shapers can be utilized. UMZV shapers have a shorter duration than their positive ZV counterparts. However, they require more actuator effort (the crane must accelerate and decelerate quickly) and can even excite higher modes, such as the trolley vibration mode.

The ZV shaper, whose response was shown in Figure 9.24, can effectively eliminate the oscillation induced by operator commands. However, ZV shapers are not very robust to variations in the system parameters, such as suspension cable length. For applications where the cable length varies significantly, a more robust input shaper, such as the Extra-Insensitive (EI) shaper, should be implemented. The EI shaper design process requires the same information as the ZV shaper, estimates of the swing frequency and damping ratio.

Because input shaping reduces the induced hook swing, when combined with feedback control, it can expand the range of stable gains. For example, Figure 9.25 shows the response of the hook to a 1 s move with gains set to P=5 and D=0.50 ($s_{zero} = 10$). The system is unstable with these gains. However, if input shaping is enabled, the system can be stabilized. The challenge is that because the response is

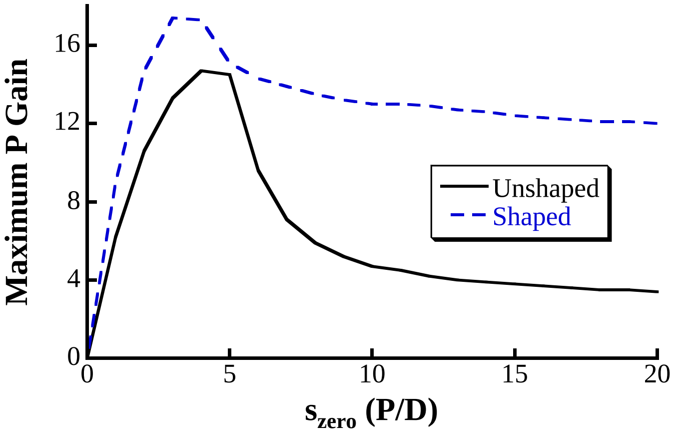

Figure 9.26: Range of Stable Gains With and Without Input Shaping

unstable, the swing frequency and damping ratio cannot be directly obtained from the response (frequency is undefined for an unstable system). Therefore, to obtain the parameters for the input shaper, an iteration routine was executed that looped through a range of frequencies and damping ratios to obtain the parameters that stabilized the system while minimizing the settling time. For the set of gains used in Figure 9.25, the optimal (smallest settling time) input shaper frequency and damping ratio were approximately 0.80 Hz and 0.32, respectively. Figure 9.25 shows the hook response with input shaping. The hook swing is reduced and the system is stable.

To investigate the effect of input shaping on the range of stable gains, the maximum stable P gain both with and without input shaping was obtained for s_{zero} between 0 and 20. A simple ZV shaper was utilized. Figure 9.26 shows the resulting ranges of the P gain. With input shaping, the maximum stable P gain is higher for every value of s_{zero} evaluated. However, note that the maximum P gains have increased for shaped operator motions, not for external disturbances. External disturbances are unaffected by input shaping.

9.4 Compatibility with the Human Operator

Compatibility with the human operator is another significant factor affecting the control design process. The human operator is also a “feedback controller”, as was shown in Figure 9.1. The operator uses his/her sensory feedback (i.e., sight, hearing, etc.) to gather relevant information about the system and adjust his/her commands accordingly to drive the system to the desired final state. Therefore, any computerized feedback controller must be compatible with the human controller. Essentially, the human operator is the high-authority controller (HAC) and is in charge of the overall motion of the system. The computerized feedback controller is the low-authority controller (LAC) and provides active damping.

The gains of the HAC (the human operator) cannot be modified easily and vary from operator to operator and even from task to task. Therefore, the operator commands are modified by an input shaper to eliminate undesired oscillatory dynamics. The parameters of the input shaper are set based on the dynamics of the trolley/hook/feedback system, as was shown in the previous section. As a result, the only remaining control design task is selecting effective feedback gains. Section 9.2 presented the process to obtain a range of stable P and D gains for the trolley-hook system. This section introduces a set of rules for selecting optimal low-authority gains. Then, a simple human-operator model is presented and the effects of the human-feedback loop are explored.

9.4.1 Low-Authority Gain Selection

The disturbance-rejecting feedback controller is designed to be a low-authority controller. By definition, LAC means that the gains of the controller are set low so that the dynamics of the system are not significantly changed. Essentially, the LAC adds a small amount of damping to the crane system to continuously drive the hook oscillation to zero. To determine a specific set of gains from the range of stable ones presented in Figure 9.12, the following set of rules were established:

1. The swing frequency of the system must be within ±20% of the natural frequency of the hook (open-loop hook poles).

2. The damping ratio must be between 0.1 and 0.2.
3. The hook settling time must be minimized.

The first rule is derived directly from the definition of low-authority control. It requires minimal change in the location of the hook closed-loop poles. Keeping the hook closed-loop poles near the stable open-loop poles also helps maintain the stability of the control system. The second rule is important for compatibility with the human operator. Although it is possible to increase the damping ratio to values larger than 0.2, higher damping ratios would mean that the feedback controller effort can make up a larger percentage of the overall control action sent to the crane, reducing the dominance of the operator command. The final rule is necessary to find the optimal set of gains based on the smallest settling time. Note that these rules will result in small gains that will not quickly eliminate the hook swing. However, the feedback controller is in charge of eliminating hook deflections caused by disturbances. The majority of hook swing is caused by the human operator commands, which will be effectively eliminated by the input shaper.

In order to satisfy the design rules, the frequency and damping ratio of the hook response for the entire range of stable P and D gains was computed. Applying the first two rules outlined above narrows the possible range of gains down to a small region. Then, the final rule can be used to select the optimal gains. For the system presented here, the optimal gains were found to be P=0.90 and D=0.056. These gains correspond to a s_{zero} of approximately 16. These optimal gains make sense because the feedback zero is far enough away from the open-loop poles of the system not to have a significant effect on the dynamic behavior of the machine, but it does introduce an adequate level of damping.

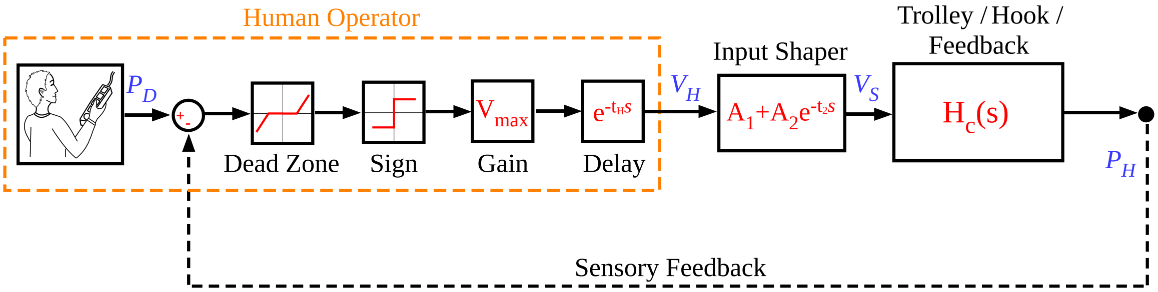

Figure 9.27: System Block Diagram with Detailed Human Operator Model

9.4.2 Human Model

Figure 9.27 shows a block diagram of the overall control system with a detailed human position-control model. The dynamics of the trolley/hook/feedback systems have been lumped into one block, labeled $H_c(s)$ for simplicity. The human operator is in charge of two main tasks, as was shown in Figure 9.1: providing the reference command, V_R, and any additional adjustments, V_A. In the simplified human model presented here, these two tasks have been combined into one model, which consists of five distinct control blocks: human, dead zone, sign, gain, and a time delay. Note that the order of these blocks is important. If the position of any block (except the time delay block) is changed, then the output of the human model becomes incorrect.

The human operator uses his/her vision to detect the actual position of the hook, P_H. This is represented by the feedback line coming out of the trolley/hook/feedback block. The difference between the actual position of the hook and the desired position of the hook, P_D (which is set by the human operator) is passed onto the dead-zone block. This block determines if the current hook position is within an acceptable distance from the desired location. The output of the dead zone block is passed onto a sign block. If the hook position is within the dead zone, then the crane is not moved (the output of the sign block is zero). However, if the crane is outside of the dead zone, the sign block determines which direction the crane should move (the output of the sign block is ± 1). The gain block sets the velocity at which the

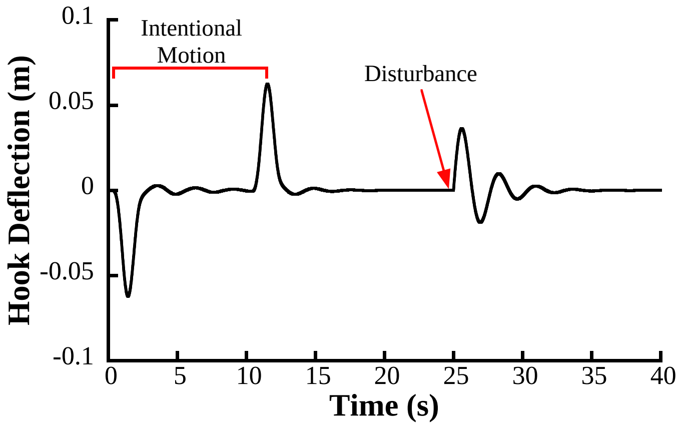

Figure 9.28: Sample Hook Response to 10 s Move with Full Model

crane should move. Because an on/off controller is assumed, the human operator can only produce three velocities: 0, $+V_{max}$, and $-V_{max}$. Finally, the operator command passes through a time delay, given by time constant t_H. This time delay represents the inherent delay present in humans caused by reaction time, neuromuscular delay, etc. This time delay was set to 0.25 s [9].

Note that the human model presented here represents an operator driving a crane with an on/off command. Although many cranes are operated with on/off commands, there are cranes that allow variable speed. One of the main objectives in crane operation is increasing throughput. An on/off command always moves at the maximum allowable speed, so it represents the fastest possible way to drive a crane. In addition, moving at maximum speed induces larger hook swing deflections and hence, represents the worse-case scenario, as was evident in Figure 9.17. For a constant acceleration, as the maximum velocity decreases, the maximum stable P gain increases. Therefore, if the controller is effective for an on/off input, then it will also be effective and stable for variable speed input.

Figure 9.28 shows the simulated hook response to a 3 m commanded trolley motion and an external disturbance at 25 s, using the optimal set of gains obtained in the previous section. For a suspension cable length of 2 m, the optimal gains produced a frequency and damping ratio of approximately 0.36 Hz and 0.20, respectively. A

ZV input shaper was designed for these swing parameters. The input shaper is very effective at reducing operator-induced oscillation, and the feedback controller is effective at eliminating the swing caused by the external disturbance.

9.4.3 Effects of Dead Zone

This section explores the effects of the dead zone. This dead zone is an inherent part of a human driving a crane. Because the crane cannot come to a stop immediately when the operator releases the move button on the pendant, the human operator naturally gives the stop command before reaching the desired location. The presence of the dead zone is necessary to avoid overshooting the desired target or driving the crane into a limit cycle. This can occur because the operator utilizes on/off commands, which move the crane at its maximum velocity. If the operator commands do not have a dead zone, then the operator may be forced to move the crane back and forth in an unsuccessful attempt to position the crane precisely at the desired location. In most practical crane applications, the final hook location is not a precise point, but rather a region, which can be adequately modeled with a dead zone.

The exact value of this dead zone can vary from operator to operator and from task to task. It can also depend on the payload. A smaller payload can be placed more precisely; therefore, a smaller dead zone would be appropriate. But with a large payload, it is difficult for a human operator to precisely position it, so the dead zone is typically larger. To determine the effect of the dead zone, its value was varied and the final position of the hook for each case was obtained. Figure 9.29 shows the final position error (the difference between the desired and actual position) of the hook for various dead zone values for three different moves.

The results of the three cases are nearly identical to each other. The responses are stable for the entire range of parameters shown in Figure 9.29. For the crane parameters used here (listed in Table 9.1), there is a minimum in all cases at a dead

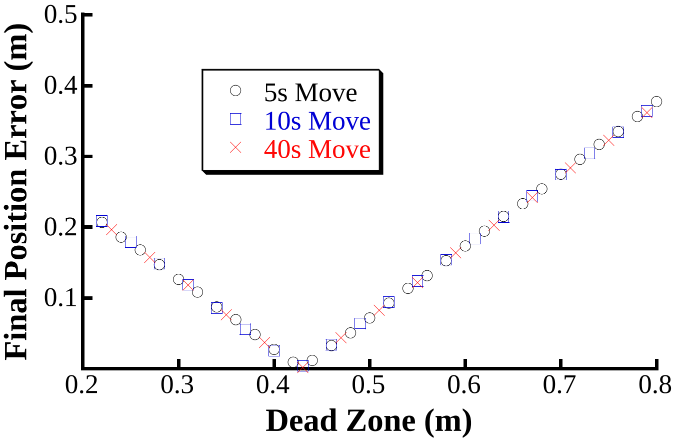

Figure 9.29: Final Hook Position vs. Dead Zone

zone of approximately 0.43 m. If the dead zone is set to this value, then the actual hook position will always be very close to its desired location. Note that the dead zone also depends on the operator's time delay. Increasing the time delay would shift the curves of Figure 9.29 to the right, increasing the optimal dead zone value.

Dead zones of less than 0.2 m led to unstable results. Because the operator can only use on/off commands, such small dead zones will drive the hook into a limit cycle. In such cases when the hook is close to its final position but cannot be positioned precisely with on/off commands, the operator can utilize a few different techniques. One is that he/she can quickly tap the move button, resulting in the crane inching its way towards the desired target. Also, many cranes are equipped with an option to temporarily reduce the crane speed and put the crane in a "crawl" mode. This allows for more precise placement. Alternatively, a secondary operator can assist by manually pushing or pulling on the payload to position it. These types of maneuvers are not considered in the simplified human model presented here.

9.4.4 Human-Feedback Stability

It is important to maintain the overall stability of the system. Adding the human-feedback loop introduces an interesting dynamic effect because the input shaper is now within a feedback loop. Huey and Singhose showed that an input shaper in a closed-loop feedback system will add higher-order dynamics [26]. These high-order dynamics, which are not modeled or controlled, can cause instability as the feedback gains increases. The analysis demonstrated that traditional controllers, such as a lead compensator, can be used to stabilize the system.

There is an important distinction between the analysis in [26] and the system proposed here. The outer feedback loop of the proposed control system contains a human operator, not a computerized feedback controller. It is difficult to mathematically prove the stability of such a human-in-the-loop system. However, the effectiveness and stability of human operators driving lightly-damped, input-shaped cranes has been well established in literature [31, 37, 49, 65] and was demonstrated in Chapter 8 for two types of complex cranes. In addition, the low-authority feedback controller increases the hook damping ratio, which increases the region of stability [26].

9.5 Procedure Summary

Although the controller design process was applied to a specific case of a bridge crane, it can be generalized and applied to other similar human-operated flexible systems. The design process to develop the control structure demonstrated in Figure 9.1 is:

- Define the important parameters of the machine. This includes maximum allowable velocity, maximum allowable acceleration, and minimum oscillation period.
- Compute the range of stable P and D gains for a feedback controller. If the system contains significant nonlinear components, this can be done via simulation. Otherwise, linear control techniques, such as root locus, can be used.
- For the range of possible gains, determine the frequency and damping ratio of the induced system response. These can be computed easily from an experimental or simulated time response. For some linear systems, they can also be obtained theoretically from the root locus.
- Set the acceptable range of frequency and damping ratio. For a low-authority

control, these values should be set to approximately 20% change in the frequency (from the nominal system frequency) and a damping ratio of 0.1 to 0.2.

- Using the requirements for frequency and damping ratio, determine the P and D gains, from the range of stable gains, that produce the fastest settling time. These gains represent an effective set of feedback gains.
- Develop an input shaper based on the frequency and damping ratio induced by the feedback controller. For a system whose configuration does not change significantly, a simple ZV shaper is adequate. However, if the system configuration changes significantly, then a more robust EI or SI shaper must be designed for the range of expected frequencies of the system.

9.5.1 Discussion

The set of rules outlines in Section 9.4.1 lead to a low-authority feedback control system, which is applicable to many other flexible systems. However, these rules can be modified to adapt to different systems. For example, if there are very few external disturbances and the majority of hook oscillations are operator induced, the gains of the feedback controller can be reduced further. This essentially reduces the control system to a human operator and an input shaper. However, if the machine is being operated in conditions that contain frequent external disturbances, such as outdoor environments, the gains (i.e., the maximum damping ratio) can be increased to improve the feedback controller performance and reduce the hook settling time.

9.5.2 Application to Boom Cranes

The feedback control design presented here was applied to a bridge crane. However, it can be extended to more complex cranes, such as a boom crane. The main difference is that the hook model must be altered. The design procedures stay the same. In Figure 9.2, the input to the hook model was the linear acceleration of the trolley (i.e., suspension cable attachment point). In boom cranes, however, the hook is moved

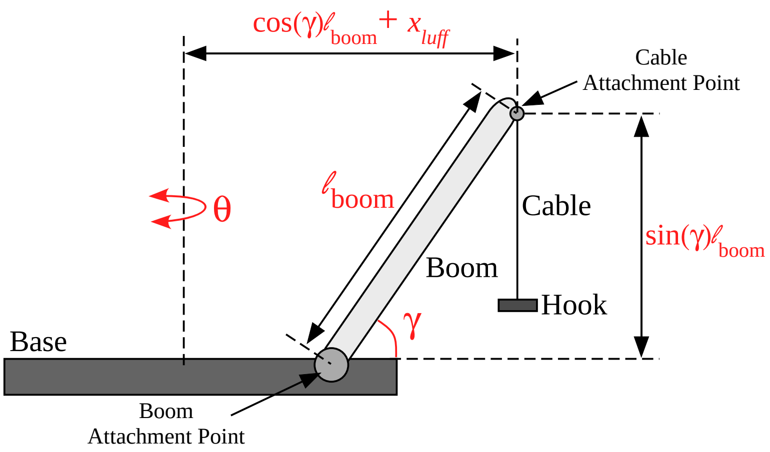

Figure 9.30: Sketch of Boom Crane Model for Feedback Design

by rotation of the base, slewing, and rotation of the boom, luffing. Therefore, the relationship between the input rotation rates and the hook position must be obtained. This relationship is nonlinear and complex.

Alternatively, a more simplified (i.e., linearized) model can be used to find the relationship between the rotations of the base and the boom and the linear acceleration of the cable attachment point. For the small-scale boom crane presented in Chapter 2, and demonstrated again here in Figure 9.30, this relationship in the radial and tangential directions can be represented by,

$$\overrightarrow{a}_{radial} = \ddot{\gamma} \times d_{offset} = \ddot{\gamma}(sin(\gamma)\ell_{boom}) \tag{9.13}$$

$$\overrightarrow{a}_{tangential} = \ddot{\theta} \times d_{offset} = \ddot{\theta}(cos(\gamma)\ell_{boom} + x_{luff}) \tag{9.14}$$

where $\overrightarrow{a}$ is the linear acceleration of the cable attachment point, γ is the luffing angle, θ is the slewing angle, d_{offset} is the distance between the rotation points and the cable attachment point, ℓ_{boom} is the boom length, and x_{luff} is the offset between the slewing rotation point and the boom attachment point. Note that the accelerations are a function of the luffing angle, which can vary during crane operation. For simplicity, the average luffing angle can be used. Otherwise, the feedback gains can be obtained for a range of possible luffing angles and the smallest gains used.

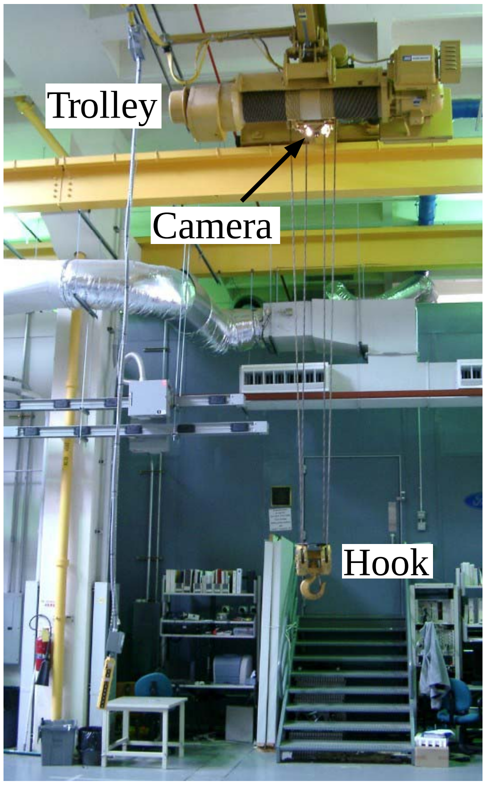

Figure 9.31: Ten-Ton Bridge Crane

9.6 Experimental Evaluation

The proposed controller was experimentally evaluated on the ten-ton bridge crane shown in Figure 9.31 [31, 65]. The crane parameters are similar to those shown in Table 9.1; therefore, the optimal P and D gains (P=0.9 and D=0.06) obtained in Section 9.4.1 were used as the nominal gains of the system. Then, the gains were empirically adjusted to the experimental hardware. This step is naturally required when applying simulation results to a real system. The simulation results provide a good estimate, but the controller parameters must be tuned to the real hardware. For example, the motor drives of the ten-ton bridge crane have velocity dead-zones. As a result, the P and D gains were increased from their nominal values to compensate (to some degree) for this nonlinearity that was not modeled in simulation. The gains selected for the real crane were P=1.5 and D=0.1. These gains are in the stable range of gains presented in Section 9.2. For a suspension cable length of $L = 5$ m,

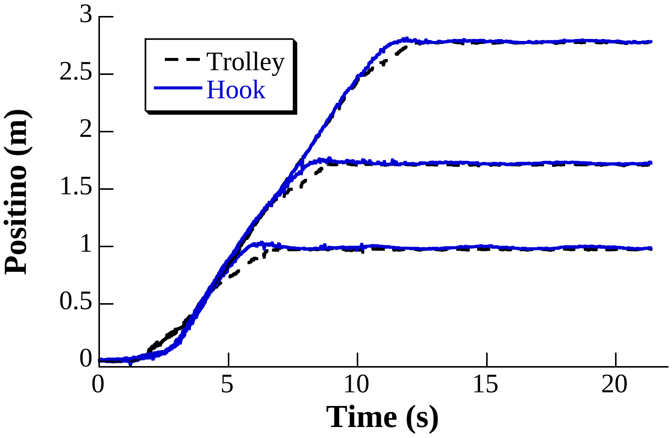

Figure 9.32: Trolley and Hook Responses to Three Different Move Distances ($L = 5$ m)

these gains induced a frequency and damping ratio of 0.24 Hz and 0.12. Note that these swing parameters comply with the low-authority controller rules outlined in Section 9.4.1. A Zero Vibration input shaper was designed according to the obtained frequency and damping ratio.

A human operator drove the ten-ton bridge crane three different move distances. Figure 9.32 shows the resulting hook and trolley responses for all three moves. The input shaper effectively eliminated the hook swing caused by the operator commands. The residual hook swing is near zero in all three cases tested.

The ZV shaper is not very robust to frequency changes. Therefore, changing the suspension cable length can degrade the effectiveness of the input shaper. To demonstrate this concept, the suspension cable length was decreased to $L = 3$ m (approximately a 30% increase in frequency from the case shown in Figure 9.32) and the same three moves were repeated by the operator. Figure 9.33 shows the resulting hook and trolley responses with only input shaping enabled (i.e., without feedback control). The lack of robustness of the ZV shaper is evident by the larger residual hook swing amplitudes.

To test the robustness of the combined controller (input shaping and low-authority feedback control), the same three operator moves were repeated. Figure 9.34 shows

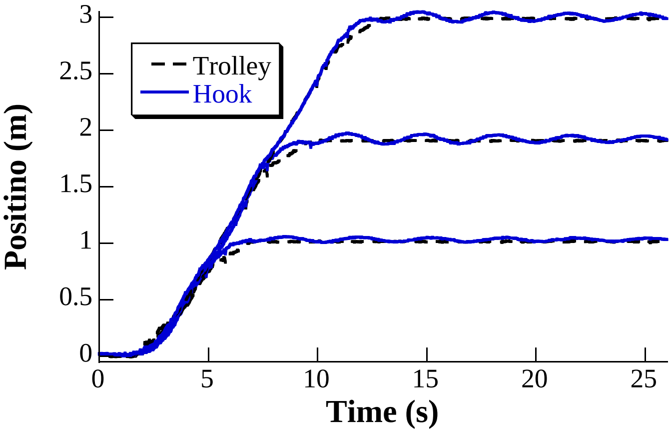

Figure 9.33: Trolley and Hook Responses to Three Different Moves with Only Input Shaping Enabled (L = 3 m)

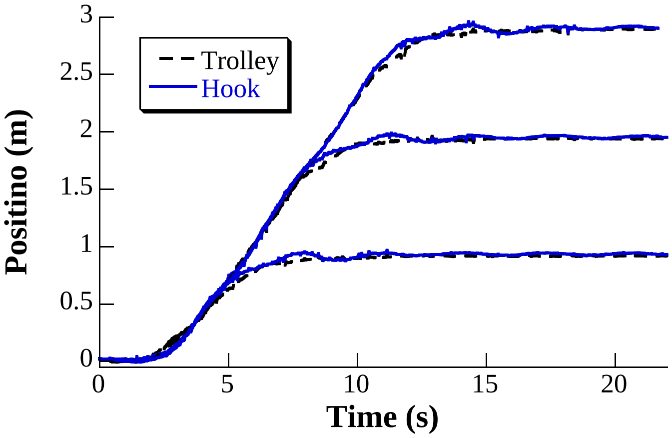

Figure 9.34: Trolley and Hook Responses to Three Different Move Distances (L = 3 m)

the resulting hook and trolley responses. The feedback controller effectively eliminated the hook swing remaining because of the lack of robustness in the ZV shaper. This result demonstrates an important benefit of the feedback control. It can compensate for the decrease in input shaping effectiveness caused by frequency variations.

To test the performance of the controller in the presence of disturbances, the operator drove the crane approximately 2 m while an external disturbance was applied to the hook. The disturbance was a force applied directly to the hook. Figure 9.35 shows the trolley and hook responses resulting from the operator command and an in-plane (i.e., along the direction of motion) disturbance. The feedback controller

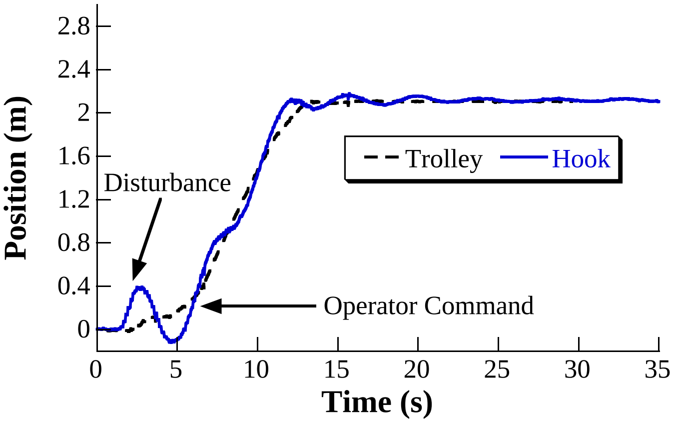

Figure 9.35: Trolley and Hook Responses to In-Plane Disturbance

starts to react to the disturbance-induced hook swing. But when the operator begins to move the crane, the operator's commands take precedence over the low-authority feedback effort and the trolley moves in the desired direction. The actions of the operator have higher authority than the feedback controller. The combined controller was able to reduce the peak-to-peak residual hook swing from approximately 50 cm to under 5 cm within 7 seconds after the completion of the move. This test was repeated ten times with external disturbances of approximately the same amplitude applied at various points along the motion of the trolley. In every trial, the controller successfully reduced the hook oscillations caused by the disturbance and the operator-induced motion to under 5 cm within 6-8 s after the completion of the move.

The effect of non-planar disturbances was also analyzed. The operator drove the crane for approximately 2 m while an external disturbance in the perpendicular direction was applied to the hook. Figure 9.36 shows the trolley and hook responses in the trolley direction (i.e., direction of motion). The out-of-plane disturbance does not have a significant effect on the hook swing in the trolley direction. The input shaper effectively eliminated the operator-induced oscillation.

Figure 9.37 shows the bridge and hook responses in the bridge direction (i.e., perpendicular to the direction of motion). The feedback controller reduced the peak-to-peak residual hook swing amplitude from approximately 40 cm to under 5 cm

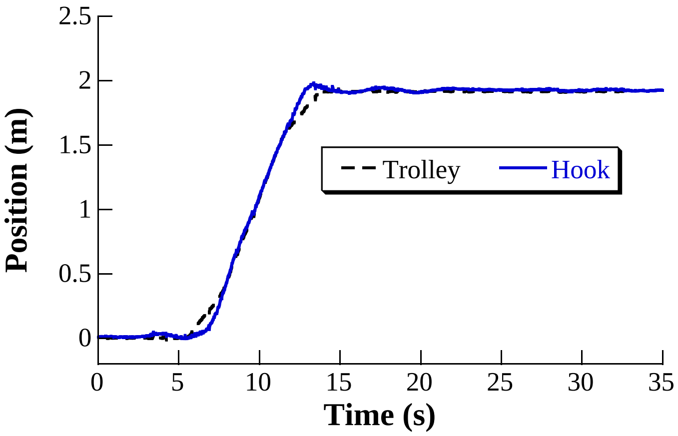

Figure 9.36: Trolley and Hook Responses to Out-of-Plane Disturbance - Trolley Direction

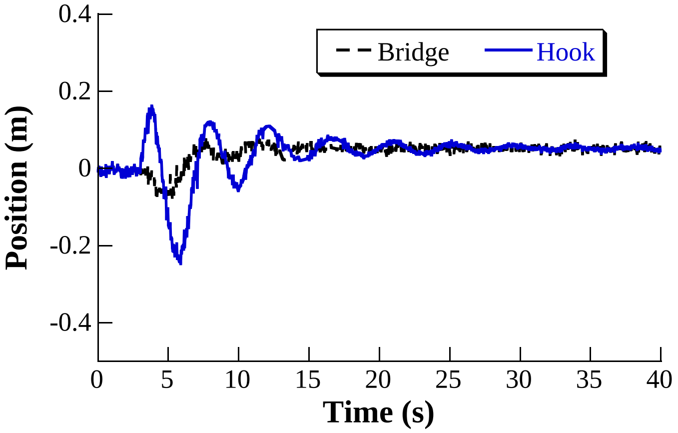

Figure 9.37: Bridge and Hook Responses to Out-of-Plane Disturbance - Bridge Direction

about 6 s after the completion of the move. This test was also repeated ten times with non-planar disturbances at various points along the motion of the trolley. In every trial, the controller successfully reduced the peak-to-peak hook oscillation to below 5 cm within 6-8 s after the completion of the move.

Figures 9.32-9.37 demonstrate the effectiveness of the proposed controller in reducing both operator-induced and disturbance-induced hook oscillations on a human-operated crane.

9.7 Summary

Input shaping can effectively reduce crane payload oscillations and is compatible with human operators. However, if there are external disturbances, then a feedback controller is necessary. To keep the human operator as the high-authority controller in charge of the overall motion of the crane, a low-authority feedback controller was designed and combined with input-shaping control. The major contributions of this chapter are:

- A two-tier control structure was designed. The primary tier consists of an input-shaping controller that eliminates oscillations caused by operator commands. The secondary tier consists of a low-authority proportional-derivative feedback controller that eliminates oscillations caused by external disturbances.
- Using a simple, linear model of a crane, the effect of varying the feedback gains on the system stability were explored. It was shown that a large range of gains lead to stable behavior.
- The effects of imposing velocity and acceleration limits on the trolley was analyzed. It was demonstrated that these motion constraints significantly decrease the range of stable gains. In addition, including these limits created a nonlinear system. As a result, other parameters, such as move distance and suspension cable length, became significant factors that affected stability.
- Input shapers were designed for the crane/feedback system. The effects of varying the feedback gains and the velocity and acceleration limits on the swing dynamics were examined. In addition, it was shown that combining input shaping with feedback controller can increase the range of stable gains.
- A set of rules was outlined to allow a systematic method of selecting gains for a low-authority feedback controller. These rules were designed so the actions of the human operator take precedence over the low-authority feedback effort.

- A simple human model was developed and the effectiveness of the proposed controller with the human model was established. Then, a series of experiments on a ten-ton bridge crane demonstrated the effectiveness of the controller on a real crane.

CHAPTER X

CONCLUSIONS

10.1 Concluding Remarks

This thesis studied the dynamic behavior of human-operated flexible machines. Two useful, yet complex types of cranes were analyzed in detail: mobile boom cranes and dual-hoist bridge cranes. These cranes are fundamental components of construction, manufacturing, and many other material-handling industries. However, payload oscillation inherent to these flexible machine not only decreases efficiency and throughput, but can also create hazardous working conditions. This thesis developed control systems to combat these unwanted dynamics and make it easier for human operators to control these machines.

Chapter 1 presented an overview of existing work in the field of vibration and crane control. It also presented a discussion of human control and modeling for similar systems. Chapter 2 presented a small-scale mobile boom crane constructed to study the dynamics of these complex machines. The important physical components of the machine were explained. Then, a nonlinear, dynamic model of a mobile boom crane was presented and the equations of motion were derived. Chapter 3 presented a two-ton, dual-hoist bridge crane and derived a numerical model of the crane.

Chapter 4 analyzed the dynamic response of the slewing, the luffing, and the mobile base motions of the boom crane. The major contributing factors to the transient and residual oscillation of the payload were presented and analyzed. It was shown that the amplitude of residual vibration does not increase with increasing move distance, but rather contains peaks and troughs and varies periodically. It was also shown that the boom luff angle and the velocity and acceleration limits were significant in determining the vibration amplitude. To eliminate the unwanted oscillatory dynamics of mobile boom cranes, input shaping was utilized. Input-shaping control was shown to be very effective at reducing the transient and the residual vibration for a large range of slewing, luffing, and driving motions. The numerical results were verified by numerous experiments on the small-scale mobile boom crane. The experiments verified the complicated boom crane dynamics, as well as the effectiveness of input-shaping control.

Chapter 5 studied double-pendulum dynamics of the boom crane and analyzed the effectiveness of input shaping on this more complex problem. A two-mode Specified-Insensitivity shaper was designed and the shaper-design process was generalized for other applications. Then, the shaper was tested, numerically and experimentally, on a large set of slewing and luffing commands and double-pendulum payloads. Even with the complex double-pendulum dynamics, the two-mode Specified-Insensitivity shaper significantly reduced the payload oscillation. The effectiveness of the two-mode SI shaper was also analyzed on more aggressive commands. It was shown that robust input shaping can mitigate the increased nonlinear effects introduced by using more aggressive commands.

Chapter 6 presented a solution for a different application of boom cranes. Boom cranes are sometimes used to swing wrecking balls. In these applications, the control goal is increasing the payload swing. Command-shaping design techniques were used to derive swing-amplifying shapers that can aid human operators increase the swing of a wrecking ball. The effectiveness of the proposed controllers were tested in experiments and a series of operator studies.

Chapter 7 investigated the dynamic behavior of dual-hoist bridge cranes. The response of these cranes to point-to-point and coordinated motions were analyzed. The effect of important system parameters on the response dynamics, specifically the swing frequency, was highlighted. It was shown that the swing can contain one or multiple frequencies depending on the cable-payload configuration. However, input shaping was able to eliminate this nonlinear effect. The effects of varying the payload configuration was also discussed. Input-shaping controllers were designed for the system under different conditions and their effectiveness was verified through simulations and experiments.

Chapter 8 presented a series of operator performance studies to test the compatibility of input-shaping controllers with human crane operators. Obstacle courses were created for both the boom crane and the dual-hoist bridge crane. The operators were required to move the payload from a start position to a target location. Important performance characteristics, such as completion time, number of button pushes, and number of collisions were recorded. All operators improved their performance with input shaping enabled. They were able to complete the task in less time and avoid the workspace obstacles. These improvements occurred even though the operator effort was decreased, as measured by the amount of control effort exerted by the operators.

Finally, Chapter 9 presented a procedure for designing a high-authority human, low-authority feedback controller for flexible systems. The high-authority human controlled the overall motion of the system. The operator's commands were shaped to eliminate unwanted oscillatory dynamics. The low-authority feedback controller provided active damping to eliminate oscillations due to modeling errors or external disturbances. The effect of important parameters, such as the feedback gains and the velocity and acceleration limits, on the controller performance were thoroughly investigated. The effectiveness of the proposed control structure was verified numerically using a simple human model and experimentally using a human-driven ten-ton bridge crane.

10.2 Future Work

The work presented in this thesis can be extended in several areas. One area is developing a more detailed human model. Simulating a human operator driving a flexible machine like a crane requires a complex mathematical model. Because the operator's behavior can change depending on the task, the human model must adapt to variations in the crane parameters and task. For example, the inherent human time delay can increase when dealing with more difficult circumstances, such as driving a crane with a double-pendulum payload or maneuvering a crane in a very cluttered workspace. The human dead zone also depends on the task and the payload size/shape and can increase or decrease depending on the task requirements.

The human model must also account for various possible scenarios that require completely different movements. This means that the model must contain several conditional elements that are only executed when necessary. For example, to accurately position a payload close to its final position, many crane operators induce a crawl motion by rapidly tapping the move button on the control interface. The model must be able to recognize when this type of motion is required and execute it if needed. These commonly-used operator techniques can be obtained by studying crane operators performing typical tasks. Such a detailed model would allow a richer study of human-machine behavior, specially when the machine is complex and flexible.

Another area for future work is analyzing complex payload dynamics. This thesis explored this topic by looking at simple double-pendulum payloads on the boom crane and plate-like payloads on the dual-hoist bridge crane. However, there are numerous other possible payload configurations that can lead to interesting dynamic behavior. For example, payloads that have non-uniform mass and non-symmetric shapes can prove challenging, as the payload can oscillate, twist, and spin. More complex payloads can make operation challenging, but also open the door to studying controllers that can combat these unwanted dynamics.

Analyzing large payloads can also lead to studying coordinated crane motions. Cranes, such as the dual-hoist crane, can carry large payloads by attaching them to multiple trolleys that can move independently. By increasing the number of trolleys, additional degrees of freedom are added to the system. While this makes operation more difficult, it also allows for complex payload manipulations necessary in certain crane applications, such as tilting and rotating the payload. Controlling multiple crane trolleys in a coordinated fashion is a very useful area of research.

Finally, the mobility of the boom crane base can be explored further. This thesis presented a dynamic analysis of the mobile base independent of the crane motions. However, moving the crane boom (i.e., slewing and luffing) and the mobile base simultaneously can lead to higher throughput, yet lower stability and safety. Research in this topic can focus on studying various types of controllers (for example, multi-input shaping) for such over-actuated machines. This will also lead to interesting research of macro-micro systems. The mobile base can be used for broad motions, and the crane slewing, luffing, and hoisting can be used for more accurate payload placement. In addition, because driving on rough terrain can induce oscillations, this would allow studying and designing appropriate sensory systems to accurately and robustly measure system disturbances in realistic and cluttered environments typical in many crane workspaces.

APPENDIX A

MOBILE BOOM CRANE MODEL

This code generates equations of motion for a MATLAB simulation of a mobile boom crane using *Autolev*. The lines marked with **DP** indicate additional lines required to produce the double-pendulum boom crane model.

```
%% Default settings
Autoz off     % switching off intermediate variables

%% Frames & Bodies
Newtonian N            % Newtonian reference frame
Frames P               % intermediate frame for defining radial hook swing
Frames Q               % DP - intermediate frame for defining radial payload swing
Bodies CL, CU, B, C    % bodies for carts, boom, and suspension cable
Bodies D               % DP - body for rigging cable

%% Points & Particles
Points RA, CC, SCL, SCU, BA     % important points (defined later)
Particle hook                   % hook as a point mass
Particle payload                % DP - payload as a point mass

%% Constants
Constants mb, mc1, mc2                  % masses (boom, lower cart, upper cart)
Constants bc1, lc1, bc2, lc2, axlel     % dimensions of carts, axle-to-axle length
Constants l1, l2, l3, l4, l5, l6, l7    % distances (look at position vector section)
Constants lb, lbc, lbcom, g             % boom length, length to cable, boom COM, gravity
Constants mhook                         % hook mass
Constants ll, mpay                      % DP - rigging cable length and payload mass

%% Variables
Motionvariables’ phi_h’’, beta_h’’     % hook swings
Motionvariables’ phi_p’’, beta_p’’     % DP - payload swings
Variables x’’, y’’, v’, psi’’, alpha’’, theta’’, gamma’’, l’’
Specified psi_ddot, v_dot, theta_ddot, gamma_ddot, l_ddot
```

```
%% Auxiliary equations
psi'' = psi_ddot                   % steering angle
theta'' = theta_ddot               % slewing angle
gamma'' = gamma_ddot               % luffing angle
l'' = l_ddot                       % suspension cable length
v'=v_dot                           % linear velocity of back wheels (back-wheel drive)
x'' = DT(v*COS(alpha))             % EOM for acceleration in the x-direction
y'' = DT(v*SIN(alpha))             % EOM for acceleration in the y-direction
alpha'' = DT(v/axlel*TAN(psi))     % EOM for angular acceleration

%% Masses & Inertias
Mass CL = mc1, CU = mc2, B = mb, C = 0, hook = mhook
Mass D = 0, payload = mpay                                       % DP - payload-related masses
Inertia CL, mc1/12*bc1^2, mc1/12*lc1^2, mc1/12*(lc1^2+bc1^2)     % lower cart
Inertia CU, mc2/12*bc2^2, mc2/12*lc2^2, mc2/12*(lc2^2+bc2^2)     % upper cart
Inertia B, 0, IB = mb/12*lb^2, IB                                % boom
Inertia C, 0,0,0                                                 % suspension cable
Inertia D, 0,0,0                                                 % DP - rigging cable

%% Position vectors
P_NO_RA> = x*N1> + y*N2>                     % N to center of rear axle
P_RA_CC> =  axlel/2*CL1>                     % center of rear axle to lower cart center
P_RA_CLO> = P_RA_CC> + l1*CL1> + l2*CL2>     % center of rear axle to lower cart COM
P_RA_SCL> = P_RA_CC> + l3*CL1> + l4*CL2>     % center of rear axle to lower cart slewing center
P_RA_SCU> = P_RA_SCL> + l5*CL3>              % center of rear axle to upper cart slewing center
P_SCU_CUO> = -l6*CU1>                        % upper cart slewing center to upper cart COM
P_SCU_BA> = l7*CU1>                          % upper cart slewing center to boom attachment
P_BA_CO> = lbc*B1>                           % boom attachment point to suspension point
P_BA_BO> = lbcom*B1>                         % boom attachment point to boom COM
P_CO_hook> = -l*C3>                          % suspension point to hook
P_hook_payload> = -ll*D3>                    % DP - hook to payload

%% Rotation matrices
Simprot(N,CL,3,alpha)           % rotation of lower cart
Simprot(CL,CU,3,theta)          % slewing of upper cart
Simprot(CU,B,2,-gamma)          % luffing of boom
Simprot(B,P,2,-phi_h+gamma)     % radial hook swing (front to back)
Simprot(P,C,1,beta_h)           % tangential hook swing (side to side)
Simprot(C,Q,2,-phi_p)           % DP - radial payload swing (front to back)
Simprot(Q,D,1,beta_p)           % DP - tangential payload swing (side to side)
```

```
%% Angular velocities
W_CL_N> = alpha'*CL3>                                   % of lower cart in N
W_CU_N> = W_CL_N> + theta'*CU3>                         % of upper cart in N
W_B_N> = W_CU_N> - gamma'*B2>                           % of boom in N
W_C_N> = W_B_N> + (-phi_h'+gamma')*P2> + beta_h'*C1>    % of suspension cable in N
W_D_N> = W_C_N> + (-phi_p')*Q2> + beta_p'*D1>           % DP - of rigging cable in N

%% Angular accelerations
ALF_CL_N> = DT(W_CL_N>,N)     % of lower cart in N
ALF_CU_N> = DT(W_CU_N>,N)     % of upper cart in N
ALF_B_N> = DT(W_B_N>,N)       % of boom in N
ALF_C_N> = DT(W_C_N>,N)       % of suspension cable in N
ALF_D_N> = DT(W_D_N>,N)       % DP - of rigging cable in N

%% Velocities
V_RA_N>=DT(P_NO_RA>,N)                 % of center of rear axle in N
V_CC_N> = DT(P_NO_CC>,N)               % of lower cart center in N
V_CLO_N> = DT(P_NO_CLO>,N)             % of lower cart COM in N
V_CUO_N> = DT(P_NO_CUO>,N)             % of upper cart COM in N
V_hook_N> = DT(P_NO_hook>,N)           % of hook in N
V_payload_N> = DT(P_NO_payload>,N)     % DP - of payload in N
V2pts(N,CL,CLO,SCL)                    % of point SCL in N
V2pts(N,CU,CUO,SCU)                    % of point SCU in N
V2pts(N,CU,CUO,BA)                     % of point BA in N
V2pts(N,B,BA,BO)                       % of boom COM in N
V2pts(N,B,BO,CO)                       % of suspension point in N

%% Accelerations
A_RA_N> = DT(V_RA_N>,N)               % of center of rear axle in N
A_CC_N> = DT(V_CC_N>,N)               % of lower cart center in N
A_CLO_N> = DT(V_CLO_N>,N)             % of lower cart COM in N
A_CUO_N> = DT(V_CUO_N>,N)             % of upper cart COM in N
A_hook_N> = DT(V_hook_N>,N)           % of hook in N
A_payload_N> = DT(V_payload_N>,N)     % DP - of payload in N
A2pts(N,CL,CLO,SCL)                   % of point SCL in N
A2pts(N,CU,CUO,SCU)                   % of point SCU in N
A2pts(N,CU,CUO,BA)                    % of point BA in N
A2pts(N,B,BA,BO)                      % of boom COM in N
A2pts(N,B,BO,CO)                      % of suspension point in N
```

```
%% Forces
Gravity(-g*N3>)     % gravity force

%% Cartesian positions
hook_x = dot(express(P_CO_hook>,CU),CU1>)           % hook x-direction
hook_y = dot(express(P_CO_hook>,CU),CU2>)           % hook y-direction
payload_x = dot(express(P_CO_payload>,CU),CU1>)     % DP - payload x-direction
payload_y = dot(express(P_CO_payload>,CU),CU2>)     % DP - payload y-direction

%% Equations of motion
Zero = Fr() + FrStar()
Kane()

%% Generate MATLAB code
UnitSystem kg, meter, sec
Output T sec, psi rad, alpha rad, theta rad, gamma rad, l m, x m, y m, v m/sec
Output phi_h rad, beta_h rad, hook_x m, hook_y m
Output phi_p rad, beta_p rad, payload_x m, payload_y m     % DP - payload-related outputs
CODE Dynamics() MobileBoomCrane.m
```

APPENDIX B

DUAL-HOIST BRIDGE CRANE MODEL

B.1 Equilibrium Model

This code generates a set of equilibrium equations for the dual-hoist bridge crane model. The MATLAB program produced by this code must be executed before the full crane model to initialize the system and satisfy all four-bar linkage constraints.

```
%% Default settings
SetAutoZee(ON)     % switching on intermediate variables


%% Frames & Bodies
NewtonianFrame N             % Newtonian reference frame
RigidFrame Cable1, Cable2    % rigid, inflexible cables
RigidBody Link               % rigid payload between cables


%% Points & Particles
Point T1(Cable1), T2(Cable2)    % trolleys
Particle P1, P2                 % two ends of rigid link


%% Constants
Constant LE+, LW+, LC+, g+              % cable lengths and gravity (limit to positive)
Constant MC+, ME+, MW+                  % masses (limit to positive)
Constant B_cable1, B_cable2             % cable damping
Constant Ixx, Iyy, Izz, Ixy, Iyz, Izx   % moments and products of inertia of payload
Constant LCx, LCy, LCz                  % distances to COM of payload


%% Variables
Variable theta_1'', theta_2'', beta''   % cable angles for trolley motion
Variable phi_1'', phi_2'', gamma''      % cable angles for bridge motion
Variable psi''                          % payload rotation angle
Variable y1'', y2''                     % trolley accelerations
Variable x1'', x2''                     % bridge accelerations (same for both trolleys)
Specified a_trol1, a_trol2, a_bridge    % input accelerations
```

```
%% Variables in equations of motion
SetGeneralizedSpeed(theta_1',theta_2',beta',phi_1',phi_2',gamma',psi')

%% Auxiliary equations
setDt( y1'' = a_trol1)
setDt( y2'' = a_trol2)
setDt( x1'' = a_bridge)
setDt( x2'' = a_bridge)

%% Inertial properties
P1.SetMass(ME)
P2.SetMass(MW)
Link.SetMass(MC)
Link.SetInertia( LinkCM, Ixx, Iyy, Izz, Ixy, Iyz, Izx )

%% Kinematics
T1.Translate(No, x1*Nx> + y1*Ny>)                % trolley 1
T2.Translate(No, x2*Nx> + y2*Ny>)                % trolley 2
P1.Translate(No,p_No_T1> - LE*Cable1z>)          % hook 1
P2.Translate(No,p_No_T2> - LW*Cable2z>)          % hook 2
Cable1.Rotate(N, BodyXYZ, theta_1, phi_1, 0)     % cable 1
Cable2.Rotate(N, BodyXYZ, theta_2, phi_2, 0)     % cable 2
Link.Rotate( N, BodyXYZ, beta, psi, gamma )      % payload
LinkCM.Translate( No, (p_No_P1> + LCx*Linkx> + LCy*Linky> + LCz*Linkz>) )

%% Cartesian positions
P1_x = Dot( p_No_P1>, Nx> )
P1_y = Dot( p_No_P1>, Ny> )
P1_z = Dot( p_No_P1>, Nz> )
P2_x = Dot( p_No_P2>, Nx> )
P2_y = Dot( p_No_P2>, Ny> )
P2_z = Dot( p_No_P2>, Nz> )

%% External forces
System.AddForceGravity( -g*Nz> )                              % gravity force
Cable1.AddTorque( -B_cable1 * Cable1.GetAngularVelocity(N) )     % cable 1 damping
Cable2.AddTorque( -B_cable2 * Cable2.GetAngularVelocity(N) )     % cable 1 damping
```

```
%% Set up four-bar linkage
Dependent[1] = Dot( Dt( p_No_T1> - LE*Cable1z> + LC*Linky> + LW*Cable2z> - p_No_T2>, N), Nx>)
Dependent[2] = Dot( Dt( p_No_T1> - LE*Cable1z> + LC*Linky> + LW*Cable2z> - p_No_T2>, N), Ny>)
Dependent[3] = Dot( Dt( p_No_T1> - LE*Cable1z> + LC*Linky> + LW*Cable2z> - p_No_T2>, N), Nz>)

%% Constraint equations
Constrain(Dependent[theta_2', beta', gamma'])

%% Equations of motion
Dynamics = System.GetDynamicsKane()
Solve( Dynamics, theta_1'', phi_1'', phi_2'', psi'')

%% Equilibrium equations
eq[1] = Dot(p_No_T1> - LE*Cable1z> + LC*Linky> + LW*Cable2z> - p_No_T2>, Nx>)
eq[2] = Dot(p_No_T1> - LE*Cable1z> + LC*Linky> + LW*Cable2z> - p_No_T2>, Ny>)
eq[3] = Dot(p_No_T1> - LE*Cable1z> + LC*Linky> + LW*Cable2z> - p_No_T2>, Nz>)
     %-- torque generated about P1 in the YZ plane (about the x axis) --%
eq[4] = 0.5*g*LE*(2*ME*sin(theta_1)+2*MW*sin(theta_2)*cos(beta-theta_1) ...
    ... /cos(beta-theta_2)+MC*(2*sin(theta_1)-cos(beta)*sin(theta_1-theta_2)/cos(beta-theta_2)))

%% Initial conditions
Input theta_1 = 15 deg, theta_2 = 15 deg, beta = 0 deg
Input phi_1 = 0 deg, phi_2 = 0 deg, gamma = 0 deg, psi = 0 deg

%% Generate MATLAB code
CODE Nonlinear(eq, theta_1, theta_2, beta, gamma) DualHoistCrane_Equil.m
```

B.2 Full Dynamic Model

This code generates equations of motion for a MATLAB simulation of a dual-hoist bridge crane using *MotionGenesis*.

```
%% Default settings
SetAutoZee(ON)     % switching on intermediate variables

%% Frames & Bodies
NewtonianFrame N             % Newtonian reference frame
RigidFrame Cable1, Cable2    % rigid, inflexible cables
RigidBody Link               % rigid payload between cables

%% Points & Particles
Point T1(Cable1), T2(Cable2)     % trolleys
Particle P1, P2                  % two ends of rigid link

%% Constants
Constant LE+, LW+, LC+, g+               % cable lengths and gravity (limit to positive)
Constant MC+, ME+, MW+                   % masses (limit to positive)
Constant B_cable1, B_cable2              % cable damping
Constant Ixx, Iyy, Izz, Ixy, Iyz, Izx    % moments and products of inertia of payload
Constant LCx, LCy, LCz                   % distances to COM of payload

%% Variables
Variable theta_1'', theta_2'', beta''    % cable angles for trolley motion
Variable phi_1'', phi_2'', gamma''       % cable angles for bridge motion
Variable psi''                           % payload rotation angle
Variable y1'', y2''                      % trolley accelerations
Variable x1'', x2''                      % bridge accelerations (same for both trolleys)
Specified a_trol1, a_trol2, a_bridge     % input accelerations

%% Variables in equations of motion
SetGeneralizedSpeed(theta_1',theta_2',beta',phi_1',phi_2',gamma',psi')

%% Auxiliary equations
setDt( y1'' = a_trol1)
setDt( y2'' = a_trol2)
setDt( x1'' = a_bridge)
setDt( x2'' = a_bridge)
```

```
%% Inertial properties
P1.SetMass(ME)
P2.SetMass(MW)
Link.SetMass(MC)
Link.SetInertia( LinkCM, Ixx, Iyy, Izz, Ixy, Iyz, Izx )

%% Kinematics
T1.Translate(No, x1*Nx> + y1*Ny>)                % trolley 1
T2.Translate(No, x2*Nx> + y2*Ny>)                % trolley 2
P1.Translate(No,p_No_T1> - LE*Cable1z>)          % hook 1
P2.Translate(No,p_No_T2> - LW*Cable2z>)          % hook 2
Cable1.Rotate(N, BodyXYZ, theta_1, phi_1, 0)     % cable 1
Cable2.Rotate(N, BodyXYZ, theta_2, phi_2, 0)     % cable 2
Link.Rotate( N, BodyXYZ, beta, psi, gamma )      % payload
LinkCM.Translate( No, (p_No_P1> + LCx*Linkx> + LCy*Linky> + LCz*Linkz>) )

%% Cartesian positions
P1_x = Dot( p_No_P1>, Nx> )
P1_y = Dot( p_No_P1>, Ny> )
P1_z = Dot( p_No_P1>, Nz> )
P2_x = Dot( p_No_P2>, Nx> )
P2_y = Dot( p_No_P2>, Ny> )
P2_z = Dot( p_No_P2>, Nz> )

%% External forces
System.AddForceGravity( -g*Nz> )                                % gravity force
Cable1.AddTorque( -B_cable1 * Cable1.GetAngularVelocity(N) )     % cable 1 damping
Cable2.AddTorque( -B_cable2 * Cable2.GetAngularVelocity(N) )     % cable 1 damping

%% Set up four-bar linkage
Dependent[1] = Dot( Dt( p_No_T1> - LE*Cable1z> + LC*Linky> + LW*Cable2z> - p_No_T2>, N), Nx>)
Dependent[2] = Dot( Dt( p_No_T1> - LE*Cable1z> + LC*Linky> + LW*Cable2z> - p_No_T2>, N), Ny>)
Dependent[3] = Dot( Dt( p_No_T1> - LE*Cable1z> + LC*Linky> + LW*Cable2z> - p_No_T2>, N), Nz>)

%% Constraint equations
Constrain(Dependent[theta_2', beta', gamma'])
```

```
%% Equations of motion

Dynamics = System.GetDynamicsKane()

Solve( Dynamics, theta_1'', phi_1'', phi_2'', psi'')


%% Generate MATLAB code

Output t, x1 m, x2 m, y1 m, y2 m, P1_x m, P1_y m, P2_x m, P2_y m

Output theta_1 deg, theta_2 deg, beta deg, phi_1 deg, phi_2 deg, gamma deg, psi deg

ODE() DualHoistCrane.m
```

REFERENCES

[1] "Camotion crane control," August 2013, Online: *http://www.camotion.com.*

[2] "Motiongenesis," August 2013, Online: *http://www.motiongenesis.com.*

[3] Abdel-Rahman, E. M. and Nayfeh, A. H., "Pendulation reduction in boom cranes using cable length manipulation," *Journal of Nonlinear Dynamics*, vol. 27, no. 3, pp. 255–269, 2002.

[4] Abdel-Rahman, E. M., Nayfeh, A. H., and Masoud, Z. N., "Dynamics and control of cranes: A review," *Journal of Vibration and Control*, vol. 9, no. 7, pp. 863–908, 2003.

[5] Ackermann, J., "Parameter space design of robust control systems," *IEEE Transactions on Automatic Control*, vol. 25, no. 6, pp. 1058–1072, 1980.

[6] Amato, F., Iervolino, R., Panditt, M., Scala, S., and L.Verde, "Analysis of pilot-in-the-loop oscillations due to position and rate saturations," in *IEEE Conference on Decision and Control*, (Sydney, Australia), December 12-15 2000.

[7] Anderson, M. R., "Pilot-induced oscillations involving multiple nonlinearities," *Journal of Guidance, Control, and Dynamics*, vol. 21, no. 5, pp. 786–791, 1998.

[8] Apple, Inc., *Apple Human Interface Guidelines*, August 2009.

[9] Beerens, G. C., Damveld, H. J., Mulder, M., van Paassen, M. M., and van der Vaart, J. C., "Investigation into crossover regression in compensatory manual tracking tasks," *Journal of Guidance, Control, and Dynamics*, vol. 32, no. 5, pp. 1429–1445, 2009.

[10] Berkhoff, A. and Wesselink, J., "Combined mimo adaptive and decentralized controllers for broadband active noise and vibration control," *Journal of Mechanical Systems and Signal Processing*, vol. 25, pp. 1702–1714, July 2011.

[11] Blevins, R., *Formulas for Natural Frequency and Mode Shape.* New York, NY: Van Nostrand Reinhold Co., 1979.

[12] Bockstedte, A. and Kreuzer, E., "Crane dynamics with modulated hoisting," *Proceedings in Applied Mathematics and Mechanics*, vol. 5, pp. 83–84, 2005.

[13] Bostelman, R. and Goodwin, K., *Survey of Cargo Handling Research.* NIST: Intelligent Systems Division, Gaithersburg, MD, July 1998.

[14] Butler, H., Honderd, G., and van Amerongen, J., "Model reference adaptive control of a gantry crane scale model," *IEEE Control Systems*, vol. 11, no. 1, pp. 57–62, 1991.

[15] Buzan, F. and Sheridan, T., "A model-based predictive operator aid for telemanipulators with time-delay," in *IEEE International Conference on Systems, Man, and Cybernetics*, (Cambridge, MA), November 14-17 1989.

[16] Dam, S. V., Mulder, M., and van Paassen, M., "Ecological interface design of a tactical airborne separation assistance tool," *IEEE Transactions on Systems, Man, and Cybernetics - Part A: Systems and Humans*, vol. 38, no. 6, p. 12211233, 2008.

[17] Davison, E. J. and Constantinescu, D., "A describing function technique for multiple nonlinearities in a single-loop feedback system," *IEEE Transactions on Automatic Control*, vol. 16, no. 1, pp. 56–60, 1971.

[18] Duong, S. C., Uezato, E., Kinjo, H., and Yamamoto, T., "A hybrid evolutionary algorithm for recurrent neural network control of a three-dimensional tower crane," *Automation in Construction*, vol. 23, p. 5563, 2012.

[19] Grossard, M., Boukallel, M., Chaillet, N., and Rotinat-Libersa, C., "Modeling and robust control strategy for a control-optimized piezoelectric microgripper," *ASME Transactions on Mechatronics*, vol. 16, no. 4, pp. 674–683, 2011.

[20] Guerlain, S., Jamieson, G. A., Bullemer, P., and Blair, R., "The mpc elucidator: A case study in the design for humanautomation interaction," *IEEE Transactions on Systems, Man, and Cybernetics - Part A: Systems and Humans*, vol. 32, no. 1, pp. 25–40, 2002.

[21] Henry, R. J., Masoud, Z. N., Nayfeh, A. H., and Mook, D. T., "Cargo pendulation reduction on ship-mounted cranes via boom-luff angle actuation," *Journal of Vibration and Control*, vol. 7, no. 8, pp. 1253–1264, 2001.

[22] Hino, H., Kobayashi, Y., Higashi, T., and Ota, J., "Motion planning method for two stacker cranes in an automated storage and retrieval system," *International Journal of Automation Technology*, vol. 6, no. 6, pp. 792–801, 2012.

[23] Hirsch, P., Palfi, A., and Gronalt, M., "Solving a time constrained two-crane routing problem for material handling with an ant colony optimisation approach: An application in the roof-tile industry," *International Journal of Production Research*, vol. 50, no. 20, pp. 6005–6021, 2012.

[24] Hong, S.-W., Bae, G.-H., and Kim, B.-G., "Development of miniature tower crane and payload position tracking system using web-cam for education," in *Proceedings of the IASTED International Conference on Robotics and Applications*, (Cambridge, MA), November 1-3 2010.

[25] Huey, J. and Singhose, W., "Effect of vertical acceleration on the frequency of a pendulum: Impact on input shaping," in *IEEE Conference on Control Applications*, (Istanbul, Turkey), June 23-25 2003.

[26] Huey, J. and Singhose, W., "Trends in the stability properties of clss controllers: A root-locus analysis," *IEEE Transactions on Control Systems Technology*, vol. 18, no. 5, pp. 1044–1056, 2010.

[27] Iversen, L., "Wrecking ball begins transbay terminal demolition," *San Francisco Chronicle*, pp. A–1, December 4, 2010.

[28] Jamieson, G. A., "Ecological interface design for petrochemical process control: An empirical assessment," *IEEE Transactions on Systems, Man, and Cybernetics - Part A: Systems and Humans*, vol. 37, no. 6, pp. 906–920, 2007.

[29] Jung, S. H. and Kim, K. H., "Load scheduling for multiple quay cranes in port container terminals," *Journal of Intelligent Manufacturing*, vol. 17, no. 4, pp. 479–492, 2006.

[30] Kang, S.-C. and Miranda, E., "Computational methods for coordinating multiple construction cranes," *Journal of Computing in Civil Engineering*, vol. 22, no. 4, pp. 252–263, 2008.

[31] Kim, D. and Singhose, W., "Performance studies of human operators driving double-pendulum bridge cranes," *Control Engineering Practice*, vol. 18, no. 6, pp. 567–576, 2010.

[32] LaValle, S. M., *Planning Algorithms.* Cambridge University Press, 2006.

[33] Lawrence, J. and Singhose, W., "Command shaping slewing motions for tower cranes," *ASME Journal of Vibration and Acoustics*, vol. 132, no. 1, p. 011002, 2010.

[34] Lewis, D., Parker, G. G., Driessen, B., and Robinett, R. D., "Command shaping control of an operator-in-the-loop boom crane," in *American Control Conference*, (Philadelphia, PA), June 24-26 1998.

[35] Makarov, M., Grossard, M., Rodriguez-Ayerbe, P., and Dumur, D., "Active damping strategy for robust control of a flexible-joint lightweight robot," in *IEEE International Conference on Control Applications*, (Dubrovnik, Croatia), October 3-5 2012.

[36] Maleki, E. and Singhose, W., "Dynamics and control of a small-scale boom crane," *Journal of Computational and Nonlinear Dynamics*, vol. 6, no. 3, p. 031015, 2011.

[37] Manning, R., Clement, J., Kim, D., and Singhose, W., "Dynamics and control of bridge cranes transporting distributed-mass payloads," *Journal of Dynamic Systems, Measurement, and Control*, vol. 132, no. 1, p. 014505, 2010.

[38] Masoud, Z., Nayfeh, A., Henry, R., and Mook, D., "Cargo pendulation reduction on ship-mounted cranes via boom-luff and slew angles actuation," in *Structures, Structural Dynamics, and Materials Conference*, (Atlanta, GA), April 3-5 2000.

[39] Mcruer, D. and Weir, D. H., "Theory of manual vehicular control," *IEEE Transactions on Man-Machine Systems*, vol. 10, no. 4, pp. 257–291, 1969.

[40] McRuer, D. T. and Krendel, E. S., "The man-machine system concept," *Proceeding of the IRE*, vol. 50, no. 5, pp. 1117–1123, 1962.

[41] Microsoft Corporation, *Windows User Experience Interaction Guidelines*, August 2009.

[42] Mitiguy, P. and Reckdahl, K., *Autolev Tutorial.* OnLine Dynamics, Inc., Sunnyvale, CA, 2005.

[43] NASA-STD-3000, *Man Systems Integration Standard*, July 1995.

[44] Neupert, J., Arnold, E., Schneider, K., and Sawodny, O., "Tracking and anti-sway control for boom cranes," *Control Engineering Practice*, vol. 18, no. 1, pp. 31–44, 2010.

[45] Ngo, Q. H. and Hong, K.-S., "Adaptive sliding mode control of container cranes," *IET Control Theory & Applications*, vol. 6, no. 5, pp. 662–668, 2012.

[46] Nguyen, D. H. and Widrow, B., "Neural networks for self-learning control systems," *International Journal of Control*, vol. 54, no. 6, pp. 1439–1451, 1991.

[47] Omar, H. M. and Nayfeh, A. H., "A simple adaptive feedback controller for tower cranes," in *ASME Design Engineering Technical Conferences*, (Pittsburgh, PA), September 9-12 2001.

[48] Parasuraman, R., Sheridan, T., and Wickens, C., "A model for types and levels of human interaction with automation," *IEEE Transactions on Systems, Man, and Cybernetics - Part A: Systems and Humans*, vol. 30, no. 3, p. 286297, 2000.

[49] Parker, G. G., Groom, K., Hurtado, J. E., Feddema, J., Robinett, R. D., and Leban, F., "Experimental verification of a command shaping boom crane control system," in *American Control Conference*, (San Diego, CA), June 2-4 1999.

[50] Peng, K., "Interfaces and control systems for intuitive crane control," M.S. thesis, Georgia Institute of Technology, 2009.

[51] Preumont, A., *Vibration Control of Active Structures: An Introduction*, vol. 179. Springer, 2011.

[52] Sawodny, O., Aschemann, H., and Lahres, S., "An automated gantry crane as a large workspace robot," *Control Engineering Practice*, vol. 10, no. 12, pp. 1323 – 1338, 2002.

[53] Shneiderman, B., *Designing the User Interface: Strategies for Effective Human-Computer Interaction.* Boston, MA: Addison-Wesley, 1986.

[54] Singer, N. C. and Seering, W. P., "Preshaping command inputs to reduce system vibration," *Journal of Dynamic Systems, Measurement, and Control*, vol. 112, no. 1, pp. 76–82, 1990.

[55] Singhose, W., "Command shaping for flexible systems: A review of the first 50 years," *International Journal of Precision Engineering and Manufacturing*, vol. 10, no. 4, pp. 153–168, 2009.

[56] Singhose, W., Biediger, E. O., Chen, Y.-H., and Mills, B., "Reference command shaping using specified-negative-amplitude input shapers for vibration reduction," *Journal of Dynamic Systems, Measurement and Control*, vol. 126, no. 1, pp. 210–214, 2004.

[57] Singhose, W., Kim, D., and Kenison, M., "Input shaping control of double-pendulum bridge crane oscillations," *Journal of Dynamic Systems, Measurement, and Control*, vol. 130, no. 3, p. 034504, 2008.

[58] Singhose, W. and Seering, W., *Command Generation for Dynamic Systems.* Lulu, 2008.

[59] Singhose, W., Seering, W., and Singer, N., "Shaping inputs to reduce vibration: A vector diagram approach," in *IEEE Internatinal Conference on Robotics and Automation*, (Cincinnati, OH), May 13-18 1990.

[60] Singhose, W., Seering, W., and Singer, N., "Residual vibration reduction using vector diagrams to generate shaped inputs," *ASME Journal of Mechanical Design*, vol. 116, no. 2, pp. 654–659, 1994.

[61] Singhose, W., Seering, W., and Singer, N., "Input shaping for vibration reduction with specified insensitivity to modeling errors," in *Japan-USA Symposium on Flexible Automation*, (Boston, MA), July 7-10 1996.

[62] Slotine, J.-J. E. and Li, W., *Applied Nonlinear Control.* Prentice-Hall, Inc., 1991.

[63] Smith, O. J. M., "Posicast control of damped oscillatory systems," *Proceedings of the IRE*, vol. 45, no. 9, pp. 1249–1255, 1957.

[64] Sorensen, K., *Operational Performance Enhancement of Human Operated Flexible Systems.* Ph.D. thesis, Georgia Institute of Technology, 2008.

[65] Sorensen, K., Singhose, W., and Dickerson, S., "A controller enabling precise positioning and sway reduction in bridge and gantry cranes," *Control Engineering Practice*, vol. 15, no. 7, pp. 825–837, 2007.

[66] Souissi, R. and Koivo, A. J., "Modeling and control of a rotary crane for swing-free transport of payloads," in *IEEE Conference on Control Applications*, (Dayton, OH), September 13-16 1992.

[67] Starr, G. P., "Swing-free transport of suspended objects with a path-controlled robot manipulator," *Journal of Dynamic Systems, Measurement and Control*, vol. 107, no. 1, pp. 97 – 100, 1985.

[68] Steinhoff, K., "Trinity hall meets wrecking ball," April 2012, Online: *http://www.capecentralhigh.com/trinity-lutheran/trinity-hall-meets-wrecking-ball.*

[69] Strip, D. R., "Swing-free transport of suspended objects: A general treatment," *IEEE Transactions on Robotics and Automation*, vol. 5, no. 2, pp. 234–236, 1989.

[70] Suzuki, Y., Yamada, S.-I., and Fujikawa, H., "Anti-swing control of the container crane by fuzzy control," in *Conference of IEEE Industrial Electronics*, (Maui, HI), November 15-19 1993.

[71] Utkin, V., "Variable structure systems with sliding modes," *IEEE Transactions on Automatic Control*, vol. 22, no. 2, pp. 212–222, 1977.

[72] Valera, J., Irigoyen, E., Gomez-Garay, V., and Artaza, F., "Application of neuro-genetic techniques in solving industrial crane kinematic control problem," in *IEEE International Conference on Mechatronics*, (Malaga, Spain), April 14-17 2009.

[73] Vaughan, J., Kim, D., and Singhose, W., "Control of tower cranes with double-pendulum dynamics," *IEEE Transactions on Control Systems Technology*, vol. 18, no. 6, pp. 1345–1358, 2010.

[74] Vaughan, J., Smith, A., Kang, S. J., and Singhose, W., "Predictive graphical user interface elements to improve crane operator performance," *IEEE Transactions on Systems, Man, and Cybernetics - Part A: Systems and Humans*, vol. 41, no. 2, pp. 323–330, 2011.

[75] Vaughan, J., Yano, A., and Singhose, W., "Comparison of robust input shapers," *Journal of Sound and Vibration*, vol. 315, no. 4-5, pp. 797–815, 2008.

[76] Yasunobu, S., “Automatic container crane operation based on a predictive fuzzy control,” *Transactions of the Society of Instrument and Control Engineers*, vol. 22, no. 10, pp. 1066–1073, 1986.

[77] Zadeh, L. A., “Fuzzy sets,” *Jouranl of Information and Control*, vol. 8, pp. 338–353, 1965.